UNIVERSITY OF CALIFORNIA, SAN DIEGO

Subnanosecond control of excitons in coupled quantum well nanostructures: Photonic storage and Exciton Conveyer devices

A dissertation submitted in partial satisfaction of the
requirements for the degree
Doctor of Philosophy

in

Physics

by

Alexander Graham Winbow

Committee in charge:

Professor Leonid V. Butov, Chair
Professor John Goodkind
Professor Yu-Hwa Lo
Professor Shayan Mookherjea
Professor Sunil Sinha

2010

The dissertation of Alexander Graham Winbow is approved, and it is acceptable in quality and form for publication on microfilm and electronically:

_____

_____

_____

_____

_____

Chair

University of California, San Diego

2010

DEDICATION

To the graduate student and scientist who finds beauty and elegance alike in the lathe and the mill, the network analyzer, the faint gleam of photons piercing the darkness, the pitter-patter of signals on a detector, the rising edge of a pulse, the bracing chill from a dewar, and the wondrous vistas latent in the equations and Physics that underlie the
Universe.

And to my sister, my mother and father, and my dear, dear friends, whose love and support sustained me throughout, lo,
these many years of graduate school.

EPIGRAPH

You see, wire telegraph is a kind of a very, very long cat. You pull his tail in New York and his head is meowing in Los Angeles. Do you understand this? And radio operates exactly the same way: you send signals here, they receive them there. The only difference is that there is no cat.
—Einstein

High-speed designs require expensive, high-performance probes. Once you obtain a decent probe, immediately pin a big red tag to it that reads, "Out of calibration — do not use." . . . If the probe doesn't already have a serial number, engrave your mark onto the connector. *—Howard Johnson,*
High Speed Digital Design: A Handbook of Black Magic

Frogs: *Brekekekex, ko-ax, ko-ax.*
Dionysius: *Hang you, and your ko-axing too!*
There's nothing but ko-ax with you!
—Aristophanes, The Frogs

And from the eastern boundary of this vast golden flower-bed rose the mighty Sierra, miles in height, and so gloriously colored and so radiant, it seemed not clothed with light but wholly composed of it, like the wall of some celestial city. . . . Then it seemed to me that the Sierra should be called, not the Nevada or Snowy Range, but the Range of Light. *—John Muir*

A semidesert with a desert heart *—Walter P. Webb*
via Marc Reisner, Cadillac Desert

If you can't take a little bloody nose, maybe you ought to go back home and crawl under your bed. It's not safe out here. It's wondrous, with treasures to satiate desires both subtle and gross. But it's not for the timid. *—Q*

This Treasury paper, by its very length, defends itself against the risk of being read.
—Churchill

TABLE OF CONTENTS

LIST OF FIGURES

LIST OF TABLES

PREFACE

Dear Reader:

This dissertation describes a body of research undertaken 2006–2010, comprising both a set of several physics experiments leading to publications as well as a very great deal of engineering detail to build the experimental setups. The dissertation is rather lengthy. As a guide for readers interested in a particular aspect of the work, I suggest as follows:

Chapter 2 is intended as a simple, clear, perhaps longwinded introduction to CQW exciton systems for a student just starting out with the literature, something of the kind I would have liked to have read on day 1, as a lead-in to other references.

For descriptions of the *physics experiments, results and analysis*, see principally Chapter 3 and Chapter 5 (in Part II) and Chapter 8 and Chapter 10 (in Part IV).

For descriptions of cryogenic (& RF) mechanical engineering, see principally Chapter 6 and Chapter 7 (in Part III), and some descriptions of RF electronics in Chapter 9 (in Part IV).

The dissertation may be nearly as long as a book, but it is not a completed reference work. These five years have been a rollercoaster ride of practical physics and the more arcane branches of electrical and cryogenic engineering. If future readers have questions about the equipment built and described herein, or about life above a MHz or below liquid nitrogen or the especially messy intersection thereof, I would be glad to answer.

Good luck!

ACKNOWLEDGEMENTS

First, I thank my advisor, Professor Leonid Butov, for taking me into his research group and for fostering a vibrant experimental environment. In the course of working on genuinely exciting physics, Leonid provided and supported the opportunities to build many kinds of apparatus, which allowed me to follow my passions as an experimentalist and develop skills in optics, spectroscopy, high speed electronics, mechanics, and cryogenics. Leonid is an advisor who cares about results, not clocking up hours, and his profound knowledge of exciton physics and competence as a research scientist have been inspiring in developing as a physicist.

Sen Yang, Aaron Hammack, Alex High, Mikas Remeika, Jason Leonard, and Yuliya Kuznetsova have been my lab colleagues and my friends, and I thank them all not merely for help as physicists but for the wonderful camaraderie of spirit inside and outside the lab. In particular, I thank Sen for patient explanations of exciton physics and Aaron for invigorating and inspirational discussions of experimental techniques, and both for offering guidance on how to be an effective graduate student. Jason has been my partner through much of the conveyer experiments, preserving our friendship despite many a long night in the dark figuring out how to get or analyze the data. Alex and Mikas's toils in the cleanroom fabricated the device samples that go into recent experiments, and I thank them and Yuliya for their wry and indefatigable senses of humor that preserve all our sanity and have made the research group such a pleasure.

I am grateful to Professor Arthur Gossard at UCSB, and his former students Micah Hanson and Ken Campman, who grew the high-quality III-V semiconductor quantum well samples that make our research possible.

The experiments described in this work required a great deal of mechanical and electrical design. George Kassabian has taught me tremendously about the practicals of electronics, especially high-frequency work, and I thank him for his tireless help with design and assembly and his cheerful generosity. Mike Rezin, Clem Demmitt, and Allen White have offered not merely technical skill and equipment loans but made the UCSD Physics Electronics Shop a welcoming sanctuary.

One of the greatest pleasures of my graduate research has been becoming a

machinist, and Bob Parker has been as wonderful a mentor as one could imagine, not to mention a grand teller of stories. Brian Naberhuis, formerly of Prof. Goodkind's research group, also taught me plenty. The physics machine shop, with its whirring geartrains, the smell of lubricating oils, and the stream and scream of metal chips really has been a second home.

The UCSD Campus Research Machine Shop has been a great resource over the years, and Don Johnson and Tad Linfesty, in particular, have been generous with their advice and parts and even tooling. Ken Duff of the Scripps Institute of Oceanography machine shop was also magnanimous in machining, especially computer-aided machining, many of the components of the Octopus.

Rachael (Heron) Floyd and Janis Research Co. have been wonderfully helpful with cryogenics, answering countless technical questions and sharing unstintingly the inner details of their trade and their superb product.

Doug Jorgesen, in the Esener Group and Alexander Simic, in the Fainman Group, both of the UCSD ECE department, and Roger Issacson of the Schultz Group at UCSD Physics have kindly loaned valuable electronics; it's a little nerve-racking carrying expensive VNAs around campus on (golf) carts, and I thank them for their trust.

The Physics facilities staff, especially Jeff Phillips and Lester Brooks, and Kevin Smith and Bryan Hill in computing, have been unfailingly and unstintingly helpful on countless occasions and very short notice, and bring a sharp sense of humor with their technical competence. Thanks also to Jeff Patterson and Brad Hanson for their support and trust with the teaching labs.

I am deeply grateful to Charmaine Samahin-Manns, Hilari Ford, David Norris, and Debra Bomar in Physics Student Affairs; they have been incredibly supportive over the past eight years, helping me navigate and weather the twists of the university though all storms and seasons.

A surprisingly gratifying aspect of graduate school has been teaching. Grading endless lab reports is not much fun, but I am grateful to a number of excellent students over the years for bringing, not necessarily background knowledge, but genuine inquisitiveness, of wanting to understand *how* and *why* the physics or the

universe works. They have taught me how to be a better teacher to many kinds of students. Nothing can be more rewarding as a teacher than when a student tells you, after the course is over, that it was *your* class that changed their minds about physics, or that they are now joining summer research programs or considering graduate school, and I wish them the greatest success.

Finally, I cannot find words enough to express gratitude to my sister Victoria, my mother and father, and my dearest friends — especially Alan, Anne, Brian, Cheryl, Glenn, Jon, Katie, Kristina, Matt, and Yaniv. Their love and support in every form, even across spans of distance and time, have been the bedrock sustaining me throughout the long and winding path of graduate school, and life itself.

The text of chapter 3, in part, is a reprint of the material as it appears in A.G. Winbow, A.T. Hammack, L.V. Butov, & A.C. Gossard, *Photon Storage with Nanosecond Switching in Coupled Quantum Well Nanostructures*. Nanoletters, **7**, 1349-1351. © 2007 American Chemical Society, where the dissertation author was the first author.

The text of chapter 5, in part, is a reprint of the material as it appears in A.G. Winbow, L.V. Butov, & A.C. Gossard, *Photon storage with subnanosecond readout rise time in coupled quantum wells*. J. Appl. Phys., **104**, 063515. © 2008 American Institute of Physics, where the dissertation author was the first author.

Elements of chapter 8 and chapter 10, in part, appear in A.G. Winbow, J.R. Leonard, M. Remeika, A.A. High, E. Green, A.T. Hammack, L.V. Butov, M. Hanson, A.C. Gossard. *Electrostatic Conveyer for Excitons*, in Quantum Electronics and Laser Science Conference, OSA Technical Digest (CD) (Optical Society of America, 2010), paper QFI3, where the dissertation author was the first author and presenter.

VITA

2000-2001	Research Assistant Department of Physics, Prof. Karol Lang University of Texas at Austin
2001	Bachelor of Science in Physics, University of Texas at Austin
2006	Master of Science in Physics University of California, San Diego
2002-2010	Graduate Teaching Assistant, Department of Physics, University of California, San Diego
2006-2010	Graduate Research Assistant, Department of Physics, Prof. Leonid V. Butov University of California, San Diego
2010	Doctor of Philosophy in Physics, University of California, San Diego

PUBLICATIONS

K. Lang, J. Day, S. Ellerts, S. Fuqua, A. Guillen, M. Kordosky, M. Lang, J. Liu, W. Opaska, M. Proga, P. Vahle, A. Winbow, G. Drake, J. Thomas, C. Andreopoulos, N. Saoulidou, P. Stamoulis, G. Tzanakos, M. Zois, A. Weber, and D. Michael. *Characterization of 1600 Hamamatsu 16-anode photomultipliers for the MINOS Far detector*. Nucl. Instrum. Methods Phys. Res. Sect. A-Accel. Spectrom. Dect. Assoc. Equip., 545(3):852–871, JUN 21 2005.

A.G. Winbow, A.T. Hammack, L.V. Butov, & A.C. Gossard, *Photon Storage with Nanosecond Switching in Coupled Quantum Well Nanostructures*. Nanoletters, **7**, 1349-1351 [2007].

A.G. Winbow, L.V. Butov, & A.C. Gossard, *Photon storage with subnanosecond readout rise time in coupled quantum wells*. J. Appl. Phys., **104**, 063515.

A.G. Winbow, J.R. Leonard, M. Remeika, A.A. High, E. Green, A.T. Hammack, L.V. Butov, M. Hanson, A.C. Gossard. *Electrostatic Conveyer for Excitons*, in Quantum Electronics and Laser Science Conference, OSA Technical Digest (CD) (Optical Society of America, 2010), paper QFI3.

ABSTRACT OF THE DISSERTATION

Subnanosecond control of excitons in coupled quantum well nanostructures: Photonic storage and Exciton Conveyer devices

by

Alexander Graham Winbow

Doctor of Philosophy in Physics

University of California, San Diego, 2010

Professor Leonid V. Butov, Chair

Indirect excitons in GaAs coupled quantum well nanostructures are a versatile system for fundamental study of cold neutral bosonic gases and demonstration of novel optoelectronic devices based on excitons — a bound electron–hole pair — rather than electrons. Indirect exciton lifetimes range from nanoseconds to microseconds and cool rapidly after photoexcitation to the lattice temperature. Lithographically-patterned electrodes enable design of potential energy landscapes, and both energy and lifetime can be controlled *in situ*, rapidly, on timescales much shorter than the exciton lifetime. Such intrinsically *opto*electronic devices can operate at speeds relevant to optical networks, and later be fabricated in other semiconductors for higher-temperature operation. Two different kinds of devices are demonstrated:

Photon storage — an optical memory — with 250 ps rise time of the readout optical signal and storage time reaching microseconds was implemented with indirect excitons in CQW. The storage and release of photons was controlled by the gate voltage pulse, and the transient processes in the CQW studied by mea-

suring the kinetics of the exciton emission spectra. This control of excitons on timescales much shorter than the exciton lifetime demonstrates the feasibility of studying excitons in *in situ* controlled electrostatic traps.

The Exciton Conveyer is a laterally moving electrostatic lattice potential for actively transporting excitons. Generated by laterally modulated electrodes, the potential velocity and depth are controlled *in situ* by frequency and voltage. We observed exciton transport characterized by average exciton cloud spatial extension over several tens of microns, and observed dynamical localization-delocalization transitions for the excitons in the conveyer: In the localization regime of deeper potentials and moderate exciton density, excitons are moved by the conveyer; in the delocalized regime of shallower lattice potential or high exciton density, excitons do not follow the conveyer motion. We explore conveyer velocities both slower and faster than phonon velocities.

Realizing subnanosecond manipulations of exciton energy and lifetime required versatile control of pulsed and multiple AC RF electrical signals in optical, liquid helium cryogenic systems. Considerable detail is presented of design, construction, and test of flexible experimental apparatus.

Part I

Background

Chapter 1

Introduction and Motivation

1.1 Semiconductor electronics and optical telecommunication

Silicon

The elemental semiconductors Germanium and Silicon come from column IV of the periodic table, underneath Carbon. Silicon is a particularly useful semiconductor in industry, because it can be grown with great purity and because silicon dioxide, the natural oxide layer that forms whenever silicon is exposed to air, is a convenient insulator and naturally compatible with silicon. This makes it relatively easy to form complex semiconductor structures of heterogeneous layers (heterostructures), such as the layer cakes that make up integrated circuits. Silicon is thus the principal material of modern electronics.

Optical interconnects

However, silicon suffers one particular drawback: it is purely electronic, not optical.[1] The modern world of "electronics" consists typically of complicated electronic devices on a local scale (computers and networking interfaces of order 1 m in size), interconnected by network links at scales of meters to thousands of kilometers. The network links are increasingly not electronic, but *optical*. Optical connections are preferred for a number of reasons: the much higher frequencies of light permit a much larger bandwidth of signals to be carried on a single "wire", and valuable copper is replaced by thin strands of pure glass. These optical fibers can be manufactured in lengths of hundreds of kilometers to carry signals with minimal diminishment, and bundles of optical fibres carrying a cacophony of signals suffer little extraneous signal leakage or crosstalk.

The modern world of telecommunications has moved largely from links comprised of copper wires (at all scales) and radio (for very long distances) to optical links for any distance much beyond a single building, and, increasingly, even optically within a single cabinet. Electronics, then, is built around a dichotomy: silicon

[1] Silicon is an "indirect bandgap" semiconductor; in fact, there are active efforts to construct silicon photonic devices, but these are not yet in common use.

integrated circuits within a single computer (or single node of a supercomputer), operating electronically, and optical links between computers, with the concomitant necessity to keep transforming back and forth between electrical signals and optical signals. Such electrical-optical interconnects are bulkier and slower than a typical integrated circuit chip.

Worse off are attempts to switch optical interconnections without recourse to electrical intermediaries. Mass optical switches have been constructed which use arrays of mechanical micromirrors to divert signals among optical fibers. Mechanical devices are inherently limited in speed and difficult to miniaturize or manufacture at low cost.

Gallium Arsenide

Instead of a column-IV element, a semiconductor can also be formed from one element from column III of the periodic table, and one from column V; the chief representative is Gallium Arsenide. GaAs has long been an attractive semiconductor for electronics and integrated circuits, with higher electron mobility and saturation velocity than silicon. Lacking a natural insulating oxide, it is not as easy to manufacture into heterostructures; however, the semiconductor AlGaAs serves well as an insulator analogue to SiO_2.[2] Decades of heavy investment in low-cost silicon processing by the semiconductor industry maintain it as the principal semiconductor of modern electronics, but GaAs is preferred for certain applications, e.g., ultra-high-speed electronics in electronic test equipment.[3]

GaAs's greatest intrinsic advantage, however, is that it is not only an electronic semiconductor, but also *optically* active: it can absorb and emit light. GaAs and related compounds are thus essential for the telecommunication revolution due to fast, miniature, inexpensive lasers and photodetectors.

It would be convenient if it were possible to directly marry digital-processing electronics with optical-processing electronics.

[2]CMOS devices have also been demonstrated in GaAs [Hong et al., 2000].

[3]For example, in the HP 54111D digital oscilloscope used in the experiments of Part II, which achieved 1 gigasample/second in 1985!

1.2 Motivations for studying 'Indirect' Excitons in GaAs coupled quantum wells

1.2.1 Physics of cold bosonic gases

Solid-state physics, generally, and semiconductor physics in particular have principally been concerned with the dynamics and control of electrons and their counterpart 'holes'. Electrons, much like other elementary particles of normal matter (protons and neutrons) all belong to the mathematical class of entities named fermions; a key property is that they obey the Pauli Exclusion Principle. A different class of entities, bosons, do not, and and as a result exhibit fundamental behavior peculiar to normal experience but of enormous interest and possible use, including superconductivity and superfluidity. For decades, the photon (in the form of a maser or laser) and liquid ^{4}He were the main accessible systems for exploring coherent boson physics. In 1995, a long-predicted new state of coherent bosonic matter, the Bose-Einstein Condensate (BEC), was realized in nanokelvin dilute atomic gases and lead to Nobel prizes [Cornell and Wieman, 2002; Ketterle, 2002]. Nanokelvin temperatures, however, present formidable experimental challenges and require considerable bulk of equipment, and creation of potential energy landscapes can require complex tuned counter-propagating laser systems [Bloch, 2005].

Excitons — a bound electron-hole pair — are also bosonic particles, but can be realized in semiconductor nanostructures grown by techniques from the commercial semiconductor industry. 'Indirect' excitons in GaAs coupled quantum wells operate at ordinary liquid helium temperatures; are long-lived, with lifetimes ranging from nanoseconds to microseconds; and cool rapidly (within about one nanosecond) to the lattice temperature. They interact repulsively as dipoles, their energy and lifetime are controllable *in situ* by bias voltage, and both are manipulable on timescales much shorter than the excitons' lifetime. Quantum degeneracy effects arise at a few Kelvins, and Bose-Einstein Condensation is expected at temperatures of hundreds of millikelvins, accessible in dilution refrigerators. Thus, indirect excitons in GaAs coupled quantum well nanostructures provide an alter-

native and experimentally convenient system for exploring the fundamental physics of bosons, using standard techniques of experimental condensed-matter physicists.

1.2.2 Optical and optoelectronic devices

Not only are indirect exciton energy and lifetime controllable *in situ* on timescales much shorter than the excitons' own lifetime, but they can be manipulated at subnanosecond speeds. Electrode structures, patterned by techniques from the commercial semiconductor industry, enable the design of complex potential energy landscapes. Combining rapid control with designable energy landscapes can yield excitonic devices – devices that use *excitons* instead of *electrons*, and are intrinsically *opto*electronic: they directly absorb or emit optical signals, and are directly controllable by electrical or optical signals. Devices realized thus far include photonic storage (optical memory) [Winbow et al., 2007]; analogues to the field-effect transistor [High et al., 2007; Kuznetsova et al., 2010b]; exciton integrated circuit [High et al., 2008]; and a scheme for actively transporting excitons laterally across semiconductor nanostructures: the exciton conveyer [Winbow et al., 2010]. They can operate at speeds relevant to modern optical networking [Winbow et al., 2008], and optical polarization control may lead to *spin* devices [Leonard et al., 2009]. Initially demonstrated in GaAs and operating in the near-infrared, they can later be fabricated in other semiconductors for operation at higher temperatures [Grosso et al., 2009]. In the future, such *excitonic* devices might lead toward fundamentally new kinds of industrial optoelectronics in an increasingly optical world.

In turn, such optoelectronic devices of potential industrial interest, plus optical [Hammack et al., 2007] and electrical excitonic traps [High et al., 2009a,b; Kuznetsova et al., 2010a] and lattices [Remeika et al., 2009] develop our broader abilities to manipulate these bosons, and hence may lead to new opportunities for experimentally studying the fundamental physics of interacting bosons.

1.3 Chronology of research and organization of the dissertation

Chronology

The body of research described in this dissertation took place from 2006-2010, leading to several publications. First, the initial excitonic photonic storage experiment, which lead to beginning understandings of pulsed RF electronics and the need for construction of custom equipment to properly connect such signals to a cryogenic optical sample. That improved setup was used to produce the second photonic storage experiment. Further experiments called for the capability to send many (at least seven) simultaneous pulsed or sinusoidal RF signals to cryogenic samples; a considerable period of time followed to design, construct, and test such a multifunctional RF cryogenic optical sample system, and also to design a system for generating a particular set of RF signals. Those new setups were then used for the exciton conveyer.

Organization

This dissertation is thus organized into four parts:

Part I describes background material: introductory motivation, and the basic physics of our system: excitons in GaAs coupled quantum well semiconductor nanostructures.

Part II describes the photonic storage experiments. First, the original proof of principle device, published in *Nanoletters*. Second, a brief description of an improved experimental system – our first-generation high-speed cryogenic sample insert. This experimental setup was used to improve photonic storage and further investigate rapid control of excitons, published in *Journal of Applied Physics*.

Part III describes the building of the Octopus, a multichannel RF optical cryostat sample insert.

Part IV describes the work leading to the exciton conveyer, portions of which were presented at and published in the proceedings of Quantum Electronics and Laser Science Conference (QELS/CLEO) 2010. First, the theory of the

conveyer, then an additional intermediary engineering chapter on the RF driving system, then the conveyer experiment results and analysis.

The chapters mostly follow the chronological order of the research, except that since most of the descriptions of RF electronics and cryogenic engineering have been centralized in Part III, the first several chapters of Part III are a prerequisite to (and took place before) the later material in Part II.

Readers initially deluged by this dissertation may possibly find helpful the remarks in the **Preface**.

1.4 Remark on units

Although modern science preferably employs SI (Système international) units, nearly all of the mechanical hardware used within this body of research, either commercially manufactured or custom built with compatibility in mind, is constructed in US customary units. Measurements are generally given in their native system to their native precision, rather than converted unnecessarily.

Although machine shops indeed employ fractional- and various letter- or number-indexed measurement standards which initially may seem archaic and confusing, as a practical matter, design and machine work is similarly (in)convenient in either system for at least two reasons: (a) For both metric and US customary fasteners and components, lengths and diameters and thread depths and the like have precise values not nearly as simple as their named *nominal* values, so when designing or machining metric hardware it is often equally necessary to consult lengthy tables of apparently arbitrary decimals. [Oberg et al., 1988] (b) *Decimal* inches and *thou* constitute a kind of metric system, with actually more conveniently-sized basis units of length.[4]

Metric machine screws are named (amongst other properties) by the diameter in millimeters then the number of millimeters between threads, not necessarily integer. US Customary machine screws are named by the diameter then the (in-

[4]This is a (kind of) *metric* system. The author intends no defense of practices such as mixing feet and inches and yards and miles, or performing thermodynamics calculations in Imperial units.

Table 1.1: Conversions between US Customary and SI metric lengths

$1\,\text{inch} = 1'' = 1000\,\text{thou} = 25.4\,\text{mm}$ (exactly)
$1\,\text{thou} = 1/1000\,\text{in} = 0.0254\,\text{mm} = 25.4\,\mu\text{m}$ (exactly)
$1\,\text{mm} \approx 40\,\text{thou}$
$1\,\text{thou} \approx 25\,\mu\text{m}$

teger) number of threads per inch; diameters below $\frac{1}{4}$ inch are index-numbered, starting from #12 and running smaller.[5] As a guide to length scales in this work, note that the common ordinary "large" US machine screw 1/4–20 is similar to the metric M6–1.0. The smallest screw employed in this work is the #0–80, slightly smaller than a M1.6–0.35.

[5]Screw length in inches or millimeters is delimited by '×', but is rarely relevant as a design constraint — one can almost always *cut* down an overlength screw to fit an awkward need.

Chapter 2

Semiconductor physics: Excitons in GaAs coupled quantum well nanostructures

2.1 (Direct) Excitons

If light shines on certain kinds of semiconductors[1], the absorbed photons can provide sufficient energy to excite electrons from the valance band across the energy *band gap* into the conduction band. In GaAs, the energy band gap is about 1.5 eV, corresponding to photons of wavelength near 800 nm, at the very near-infrared. Thus, even at very low temperatures, GaAs can become partly conductive. Left behind in the the valance band is the absence of an electron – a "hole". That hole constitutes a space for a different nearby valance band electron to move into, that electron in turn leaving its former space available for occupation; holes are thus mobile pseudoparticles in themselves, with charge +1 (Figure 2.1). Thus, semiconductors support two kinds of mobile charge carriers – electrons and holes. [2] The electron and hole are free to wander about the lattice. Eventually, an electron and hole will meet again and recombine and annihilate; the liberated energy is emitted either as a photon, or as phonons (sound wave packets or pseudoparticles of sound).

If there are very many mobile excited electrons and holes, we can speak of an *electron hole plasma*; at sufficient densities, an electron may recombine with a different hole than its original photoexcitation partner.

A free electron and hole can also bind via their Coulomb attraction to form a hydrogen-like pseudo-atom, called an *exciton*. (It is also possible for two electrons and a hole to bind to form a pseudoatom of three components, called a *trion*, but trions and biexcitons or more complicated entities are not discussed in this work.) Excitons can be closely bound and small in radius (Frenkel excitons), but in semiconductors, the dielectric screening leads to comparatively weak binding and a large binding radius, much larger than the interatomic spacing (Wannier-Mott excitons).

These experiments employ excitons in GaAs, whose lattice constant $a \sim 0.28$ nm. Although these Wannier-Mott excitons are large in the sense that their

[1] *Direct* band-gap semiconductors, like GaAs, but unlike Silicon

[2] Actually, in this approximation, the electron is not a vacuum electron, but a pseudoelectron with effective mass typically smaller than that of a vacuum (bare) electron.

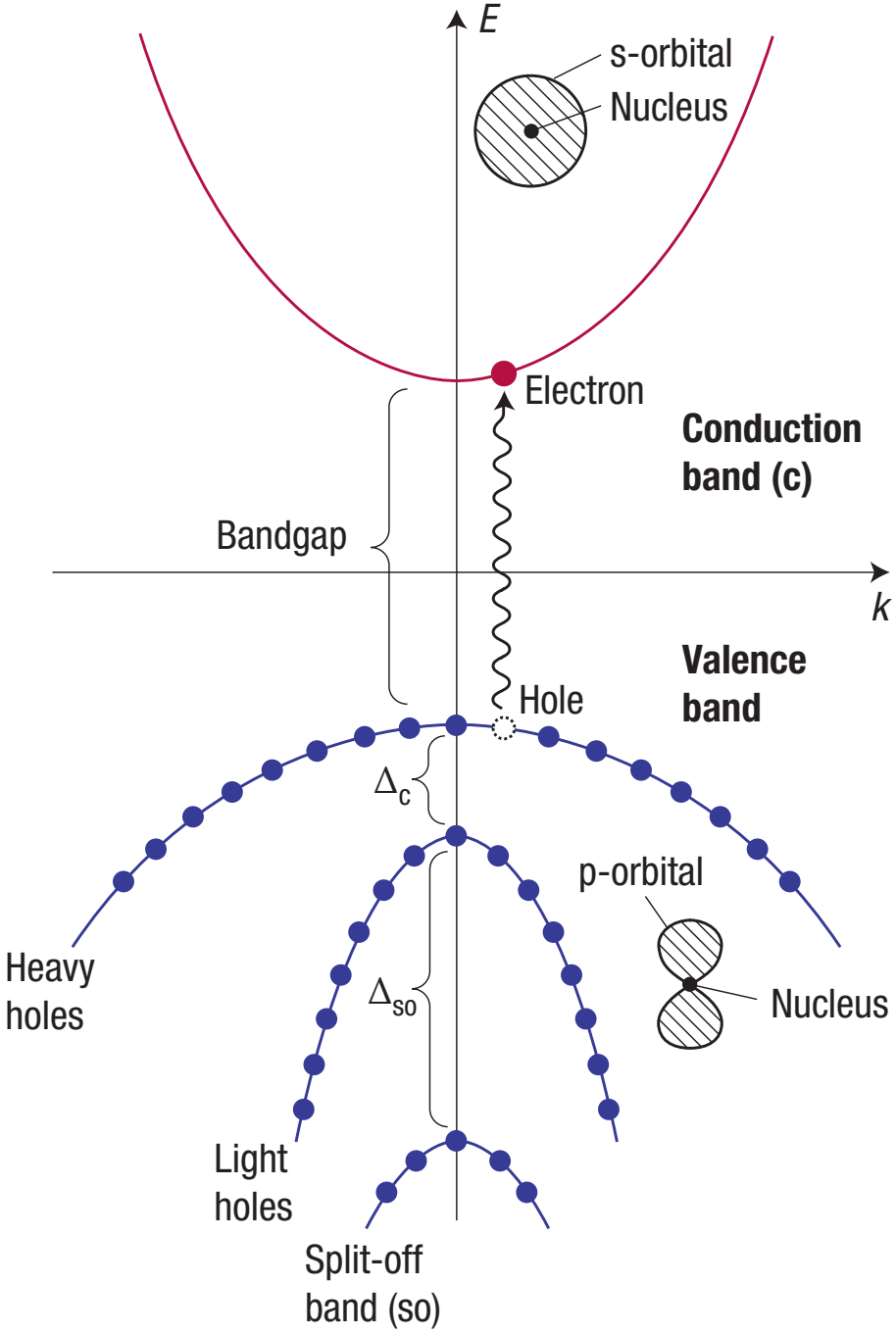

Figure 2.1: Bandstructure of bulk GaAs. An electron is photoexcited from the valance band into the conduction band, leaving behind a 'hole' in the valance band; the electron–hole pair can bind (if at sufficiently low temperature) to form an exciton. The valance bands are split by spin; the experiments in this work use excitons formed from 'heavy holes'. The energy bandgap between valance and conduction, $E_g \approx 1.5\,\text{eV}$, corresponds to absorption or emission of photons around 800 nm (the very near infra-red). From Burkard [2008].

Bohr radius (∼10 nm) spans many atomic sites, at typical working densities in these experiments of order $10^{10}/\mathrm{cm}^2$, individual excitons are separated on the order of 100 nm. (Figure 2.2 is an illustrative cartoon.) Thus, an electron from one exciton is likely to remain with and eventually recombine with its partner hole, not the hole from another electron. These "direct" excitons have effective masses about 20% of the free electron mass, and lifetimes of tens to hundreds of picoseconds.

Excitons are a relative ground state for disassociated electrons and holes, but the fraction of electrons and holes that are actually bound into excitons (vs. a free electron-hole plasma) depends on the temperature and the binding energy, and is appreciable for temperatures roughly below E^{binding}/k_B; for the samples and excitons in this work, around 40 K [Chemla and Miller, 1985; Szymanska and Littlewood, 2003].

In these experiments, the excitation of the lattice is provided by a laser spot. The photoexcited electrons and holes form excitons initially not at the bath temperature (as low as 1.4 K in these experiments), but at the local lattice temperature near the laser spot, towards 6 K [Hammack et al., 2009]. Traveling away from the laser spot, hot excitons can cool towards the bath temperature by emission of longitudinal acoustic phonons, but the need to satisfy energy-momentum conservation slows the cooling time to order nanoseconds [Ivanov et al., 1999]. Since this is much longer than the (direct) exciton lifetime, (direct) excitons remain a hot gas in GaAs.

2.2 GaAs/AlGaAs coupled quantum well structures

Instead of bulk GaAs semiconductor, a three-dimensional medium, one can form thin layers a few nanometers (few tens of atoms) thick. Such layers are commonly grown in a sandwich by molecular beam epitaxy upon a thick foundation of electrically insulating material as a substrate. Free electrons and holes in a thin layer of GaAs semiconductor are confined to that effectively two-dimensional layer, called a *quantum well* (QW). Light can still penetrate other layers of material above

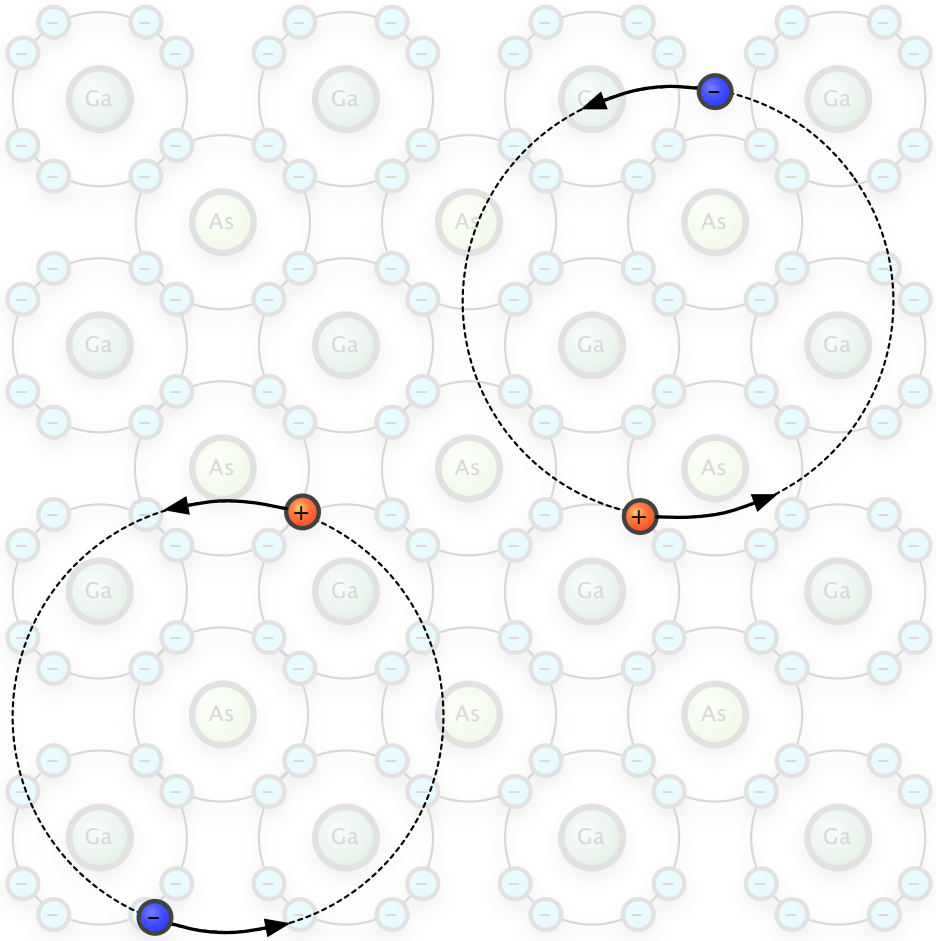

Figure 2.2: Cartoon showing mobile photoexcited electrons and holes in GaAs binding to form excitons, composite bosonic quasiparticles. A flat projection of the GaAs lattice (formed from from two interlocking regular FCC (face-centered cubic) lattices, for each of Gallium and Arsenic, is visible in the background.) These Wannier-Mott excitons have comparatively weak binding energy, leading to a hydrogen-like atom with Bohr radius much larger than the GaAs lattice spacing. From Hammack [2010].

even hundreds of nanometers thick (if transparent), and so excitons can form in the quantum well layer and be confined to that layer.

Coordinate notation

In these experiments, the planer quantum well heterostructure is excited by a laser beam perpendicular to the planar surface. It is thus convenient to adopt the notation throughout that the x–y axis are in the plane of the quantum wells, and the z–axis perpendicular and along the laser beamline, extending macroscopically to optical equipment even meters away. For the exciton conveyer experiments described in Chapter 10, the x–axis is in the direction of transport, which was vertical relative to the optical table.

Coupled quantum wells

A more complicated heterostructure can also be grown, where two such thin quantum well layers are separated by a thin layer of insulation (and in turn surrounded above and below by thicker cap layers). Excitons can form in either layer, but these *coupled quantum well* (CQW) heterostructures can exhibit more complicated behavior: If the intervening insulating layer is sufficiently thin, electrons and holes can quantum-mechanically *tunnel* between quantum wells. A new type of exciton can form, where the electron is in one QW and the hole in the other; still a bound quasiparticle, but with increased separation between the electron and hole (reduced overlap of the wavefunctions), and hence less likely to recombine and longer-lived.

The energy band structure can be altered by applying an electric field. To facilitate this, the semiconductor heterostructure is grown with electrodes on the top and bottom, beyond the insulating layers that surround the QWs. The electrodes can either be made of metal or of semiconductor material that has been heavily doped (typically n^+) to increase the conductivity to give much the same effect as a metal. A voltage difference can then be applied across between the upper and lower electrodes, imposing an electric field in the z–direction. Electrons and holes are driven to tunnel between the quantum wells, until the electrons have

migrated into the QW closer to the more positive electrode and holes the more negative. This creates an electron-hole bilayer. A cartoon of such a device is shown in Figure 2.4.

2.3 Indirect excitons

2.3.1 Formation and interaction

An *indirect exciton*[3] is formed by the binding of an electron and hole in separate layers. To a first approximation, the separation distance d between the electron and hole can be taken to be about the distance between the quantum well centers. The overlap between the e- and h- wavefunctions, thus the indirect exciton lifetime, is controlled by both the geometry (the thickness of the QW layers and any intervening insulation, fixed when grown by MBE) and by the strength of the perpendicular electric field F_z. Indirect excitons are dipoles, and thus their energy

$$\mathcal{E}_I = E_g - E_I^{\text{binding}} - eF_z d$$

is also controlled by the electric field, lower than that of the direct exciton,

$$\mathcal{E}_D = E_g - E_D^{\text{binding}}$$

by

$$\delta\mathcal{E} = eF_z d + (E_I^{\text{binding}} - E_D^{\text{binding}}) \approx eF_z d$$

and hence becomes the preferred ground state. (For typical $GaAs/Al_{0.33}Ga_{0.67}As$ CQW used in this research, $E_I^{\text{binding}} \approx 5\,\text{meV}$ and $E_D^{\text{binding}} \approx 10\,\text{meV}$, and $eF_z d \approx$ 20–50 meV.)

Indirect excitons interact with each other via dipole-dipole repulsion, and thus their energy is additionally increased at higher (areal) densities. In our samples, typical exciton densities are of order $10^{10}/\text{cm}^2$, and the exciton emission wavelength can shift shorter by several nanometers. This shift of the emission

[3] *a spatially*-indirect exciton

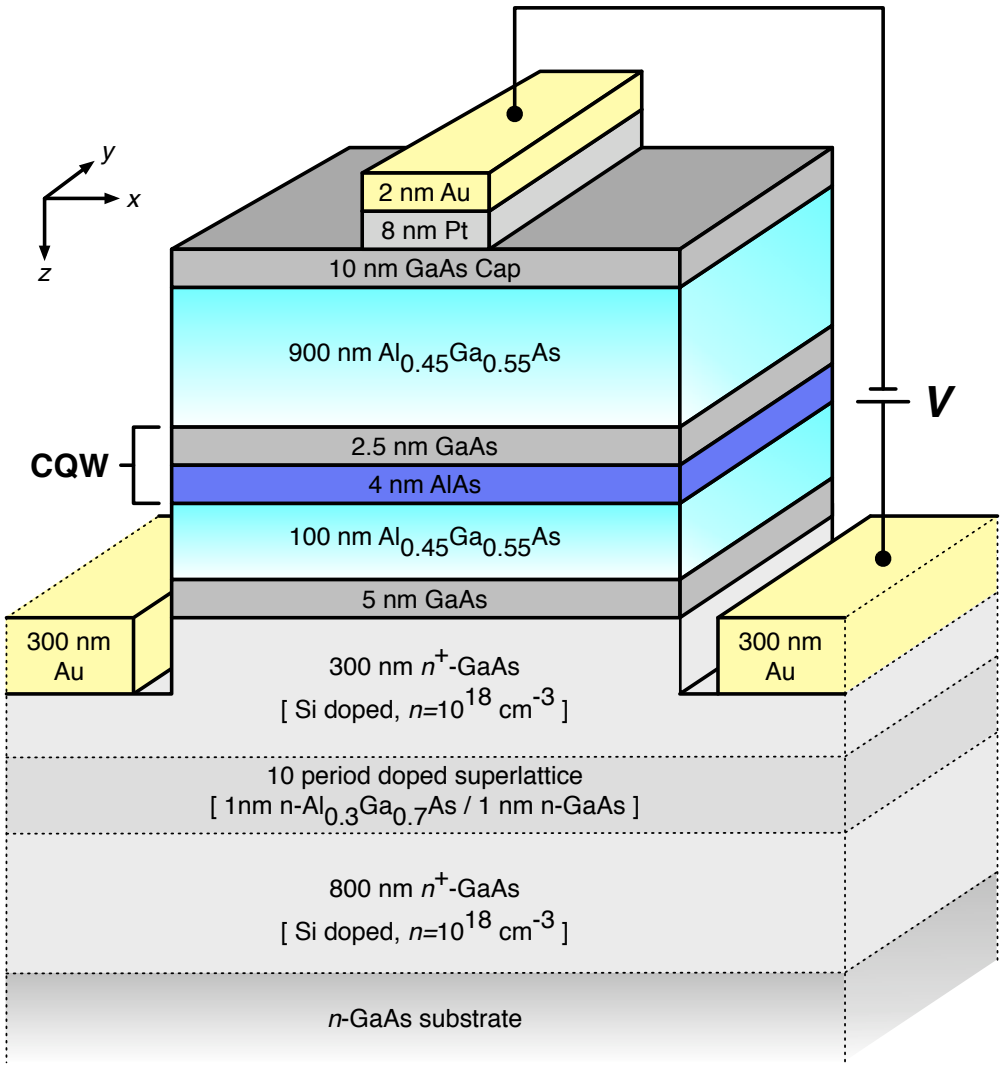

Figure 2.3: Diagram of an example heterostructure device, constructed by molecular beam epitaxy and photolithography. The CQWs (in this case GaAs/AlAs rather than GaAs/$Al_{0.33}Ga_{0.67}As$) are embedded in 1000 nm of $Al_{0.33}Ga_{0.67}As$, protected from above by a thin GaAs cap layer and lie atop a substrate of various and many layers of doped GaAs and $Al_{0.33}Ga_{0.67}As$. The substrate layers provide a monoatomically-smooth foundation for high-quality growth of the CQW structure, and the substrate is doped to function as a conductive bottom ("back") ground plane. The foregoing is all grown (in the z–direction) by molecular beam epitaxy. Later, devices are fabricated by photolithography. Gold electrodes are deposited on the back plane and atop the cap layer, allowing application of a gate voltage and hence electric field across the CQWs. The devices used in this dissertation are constructed analogously, with differing CQW and electrode geometry and materials. From Grosso et al. [2009].

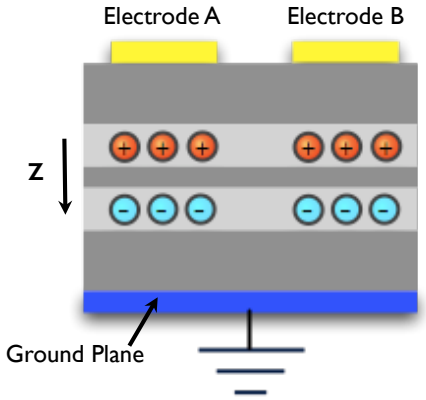

Figure 2.4: Cartoon of indirect excitons in CQWs. Electrons and holes initially formed in either QW are caused by the electric field in the z–direction to migrate to separate quantum wells, forming an electron-hole bilayer. These out-of-plane separated electrons and holes bind to form *indirect* excitons if the temperature is considerably below E^{binding}/k_B. Use of multiple top electrodes makes it possible for F_z to differ at different in-plane locations (here A, B), giving the indirect excitons different energies. From High et al. [2008]; High [2007].

wavelength, spatially-resolvable even in cases of spatially-nonuniform exciton distribution, can be employed as an estimate of the local exciton density. An additional benefit of the repulsive interaction is that modest exciton densities can screen out in-plane inhomogeneous disorder potentials arising from the slight imperfections inherent to MBE-grown QW layers.

2.3.2 Lifetime and cooling

The increased e-h separation gives the indirect exciton a much longer lifetime, of order nanoseconds to microseconds. The two-dimensional quantum wells break translation symmetry in the z–direction, so phonon momentum need not be conserved and indirect excitons of any energy $E \geq 2m_x v_s^2$ are free to cool directly toward the ground state by LA-phonon emission. [Ivanov et al., 1999, 1997; Tikhodeev, 1989, 1990; Zhao et al., 1997]. They cool to the 1.5 K lattice temperature within about 1 ns, much shorter than the indirect exciton lifetime, either while traveling away from the laser spot or after switching the laser off [Hammack et al., 2009]. Thus, indirect excitons — quite unlike direct excitons in either bulk GaAs

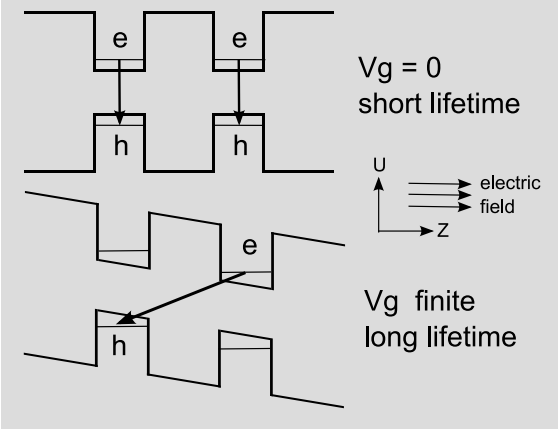

Figure 2.5: Energy band structure of excitons in GaAs CQWs. The horizontal axis is spatial depth (distance in the z–direction) — note that the figure is in some sense rotated 90° from the more photographic cross-section in e.g. Figure 2.4 or Figure 2.3. The vertical axis is *energy*. Photoexcited electrons and holes always lie in the conduction (upper) and valence (lower) bands respectively. With $V_{\rm g} = 0$ (top figure), *direct* excitons are formed from the binding of electrons and holes in the *same* quantum wells. With application of a gate voltage in the z–direction, the energy levels tilt, electrons and holes move into separate quantum wells, and *indirect* excitons are formed by the binding of electrons and holes in *separate* quantum wells. The electrons and holes of indirect excitons are more spatially separated than for direct excitons, leading to reduced wavefunction overlap and probability of recombination and hence longer lifetime.

or in QWs – can form a *cold* bosonic gas.[4] (The possibility of forming cold *direct* excitons by way of controlled indirect excitons is briefly discussed in Winbow et al. [2008] and Section 5.6.

An additional feature of indirect excitons in GaAs CQW is that conditions for Bose-Einstein condensation appear experimentally accessible. The thermal de Broglie wavelength is $\lambda_{\rm dB} = \sqrt{2\pi\hbar^2/(mk_BT)}$, and the temperature at which the interexcitonic separation $\sqrt{n_{\rm 2D}}$ becomes comparable to the de Broglie wavelength is $T_{\rm dB} = 2\pi\hbar^2 n_{\rm 2D}/(k_B m_x g) \approx 3\,{\rm K}$. Below this temperature, quantum coherence effects can become apparent [Yang et al., 2006]. The critical temperature for complete condensation of N particles into the spatial and momentum ground state

[4]The complete thermalization and cooling hierarchy beginning with e.g. absorption of HeNe laser photons 400 meV *above* the bandgap and ending with coldest indirect excitons moving slowly inside the phonon cone spans some five orders of magnitude in energy and several steps.

is $T_{\mathrm{dB}}/\log N$, around 0.2 K for $N \sim 10^5 - 10^6$, which is anticipated to be accessible in a helium dilution refrigerator. The experiments described in this work are performed at temperatures 1.4-5 K.

2.3.3 In situ-controllability

The electric field in the quantum wells is set by the voltage applied between top and bottom electrodes ("gates"), and so the indirect exciton energy and lifetime are both *dynamically* controllable *in situ*, without need to grow another lattice sample with different layer geometry. If the gate voltage is set to (nearly) zero, the electrons and holes are free to tunnel into either QW, and the ground state is again the direct exciton. The direct exciton energy and hence emission wavelength remain largely unaffected by the gate voltage.

The gate voltage need not be uniform; the top surface may be spatially patterned with a (possibly complicated) design [Hammack et al., 2006; High et al., 2007, 2008, 2009a; Remeika et al., 2009; High et al., 2009b; Grosso et al., 2009; Winbow et al., 2010; Kuznetsova et al., 2010b] using multiple electrodes driven by multiple voltages, or even a single contiguous electrode of nonuniform areal density (e.g., a spiral, or an asterisk-like "star" where the arms taper in width with radial distance [Kuznetsova et al., 2010a]). Given sufficient acumen with photo- or electron-beam lithography, arbitrary potential energy landscapes can be implemented and controlled dynamically *in situ*.

Given suitable electronics, the electrodes can be manipulated on very fast timescales, much faster than the indirect exciton lifetime [Winbow et al., 2007; Winbow et al., 2008; Winbow et al., 2010]. Pulsed or sinusoidal waveforms may be supplied to the sample via transmission lines from outside the cryostat. The frequencies attainable may be limited by the sample (semiconductor heterostructure) intrinsic capacitance, which can be minimized by choice of sample geometry, or by the sample carrier package parasitic inductance and capacitance. Considerable care needs be taken with thermal packaging and electrical geometry, parasitics, and termination, but GHz frequencies are certainly achievable, perhaps ultimately even several tens of GHz. It may be possible to implement active driving electron-

ics directly adjacent the sample, if cryogenic-compatible integrated circuits can be obtained. Alternatively, electrodes on the sample surface may be modulated *optically* [Kuznetsova et al., 2010b], and in principle this might also be performed on fast timescales [Hammack et al., 2007, 2009].

2.3.4 Spin

Excitons are composite bosons made from spin-1/2 fermions, and can occur in different varieties with different total angular momentum. The experiments in this dissertation do not measure polarization, and are thus largely spin-insensitive, however it is appropriate to briefly catalog the different species of fermions and bosons present in GaAs. The electron, once excited into the conduction band, is in an s-wave state, with quantum numbers $l = 0$ and $s = \frac{1}{2}$, giving $j_e = l + s = \frac{1}{2}$. The hole is in a p-wave state[5] with quantum numbers $l = 1$ and $s = \frac{1}{2}$, giving $j_h \in \{\frac{1}{2}, \frac{3}{2}\}$. Thus, there are three possible (j_h, j_h^z) spin states and three species of holes.

Spin-orbit coupling $E_{\text{so}} \propto \vec{l} \cdot \vec{s} = j^2 - (s^2 + l^2)$ causes the $j = \frac{1}{2}$ holes to be lower in energy, by about 360 meV in our samples; these "split-off band" holes do not contribute to our results. The holes of total angular momentum $j = \frac{3}{2}$ can have $j^z \in \{\pm\frac{3}{2}, \pm\frac{1}{2}\}$; the different spin projections have different effective mass (differing curvature of the dispersion relation), and are named, respectively "heavy holes" and "light holes". In bulk GaAs, the energy of the two species is degenerate at $k = 0$ momentum, but in quantum wells the broken symmetry in the z-direction leads to an exciton energy difference of about 20 meV. For these experiments, we deal only with excitons formed from heavy holes.

Having simplified the hole species down to $(j_h = \frac{3}{2}, j_h^z = \pm\frac{3}{2})$, we form "heavy hole" excitons with $s = \frac{1}{2}$ electrons. This gives two subspecies: excitons with $j_z^{\text{ex}} = \pm 2$, and those with $j_z^{\text{ex}} = \pm 1$. The excitons with two units of angular momentum cannot satisfy conservation by decay and emission of a single spin-1 photon; they can decay only by two photons or by photon + phonon (and phonons

[5] In zincblende crystal lattice semiconductors like GaAs, the structure of the valance band at the top, ie near zero momentum, stems mainly from p-bonding orbitals [Rössler, 2004].

are rare at our cryogenic temperatures), thus this rate is very low, and these excitons are termed "optically dark". We observe only the optically-active $j_z = \pm 1$ excitons. Optically-dark excitons can, however, become optically-active by electron or hole spin flip, and spin coherence and spin-flip processes are the subject of other experiments [Leonard et al., 2009].

2.4 Studied GaAs/AlGaAs CQW heterostructures

The experiments described in this dissertation were performed with three related variants of coupled quantum well nanostructures. They all use a pair of GaAs quantum wells separated by a thin layer of $Al_{0.33}Ga_{0.67}As$, surrounded by much thicker layers of $Al_{0.33}Ga_{0.67}As$. The bottom gate is heavily doped for conductivity as a ground electrode, and sits upon a further substrate for support. The direct exciton has lifetime of tens or hundreds of picoseconds, while the indirect exciton lifetime varies with the sample geometry and gate voltage, from tens of nanoseconds to several microseconds.

Photonic storage "narrow sample" The pair of GaAs QW are each 8 nm wide, separated by a 4 nm layer of $Al_{0.33}Ga_{0.67}As$. The CQWs are positioned midway in a 400 nm-thick layer of $Al_{0.33}Ga_{0.67}As$ (200 nm above and below). V_g for indirect excitons ranges 1–1.4 V. The top gate is Si-doped GaAs, a single homogeneous electrode. Employed in the first and second photonic storage experiments (Chapter 3 and Chapter 5).

Photonic storage "wide sample" The pair of GaAs QW are each 15 nm wide, separated by a 4 nm layer of $Al_{0.33}Ga_{0.67}As$. The CQWs are positioned midway in a 400 nm-thick layer of $Al_{0.33}Ga_{0.67}As$ (200 nm above and below). V_g for indirect excitons ranges 1–1.4 V. The top gate is Si-doped GaAs, a single uniform electrode. The wider quantum wells increase the electron-hole separation, reducing overlap and leading to a longer lifetime. Employed in the first photonic storage experiment (Chapter 3).

Conveyer sample The pair of GaAs QW are each 8 nm wide, separated by a 4 nm

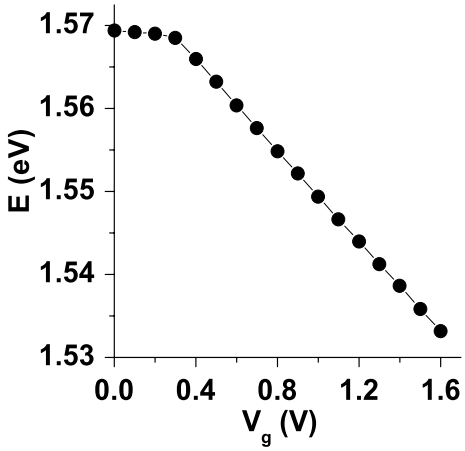

Figure 2.6: Plot of exciton energy as a function of gate voltage. The excitons have energies around 1.5 eV, corresponding to photoluminescence in the vicinity of 800 nm. The direct excitons (at V_g=0) have highest energies (around 1.57 eV $\sim$ 790 nm), while the indirect excitons emit at longer wavelengths with increasing gate voltage (towards 1.53 eV $\sim$ 810 nm). These particular gate voltages are applicable to the CQW samples used in the photonic storage experiments; for the sample used in the exciton conveyer experiment, see Figure 2.7. (The voltages are actually negative as applied to the top gate relative to the bottom ground plane.)

layer of $Al_{0.33}Ga_{0.67}As$. The CQWs are positioned 10% from the bottom of a 1000 nm-thick layer of $Al_{0.33}Ga_{0.67}As$(800 nm above and 200 nm below). A larger V_g of 2.5-4 V is needed to obtain electric field strengths (and hence indirect excitons) similar to those in the photonic storage samples, but the CQW proximity to the bottom ground plane has a key advantage: undesired *in-plane* electric fields arising from inhomogeneous top electrodes are screened. The top surface is a mix of layers of transparent ITO (indium titanium oxide) conductor and SiO_2 insulation. Employed in the conveyer experiments (Part IV), and shown in detail in Figure 2.8.

2.5 Controllable, versatile experimental system

Indirect excitons in GaAs CQW nanostructures are thus a controllable and versatile system for studying neutral cold bosonic gases. Indirect exciton lifetimes range from nanoseconds to microseconds, vastly longer than the cooling time. Tem-

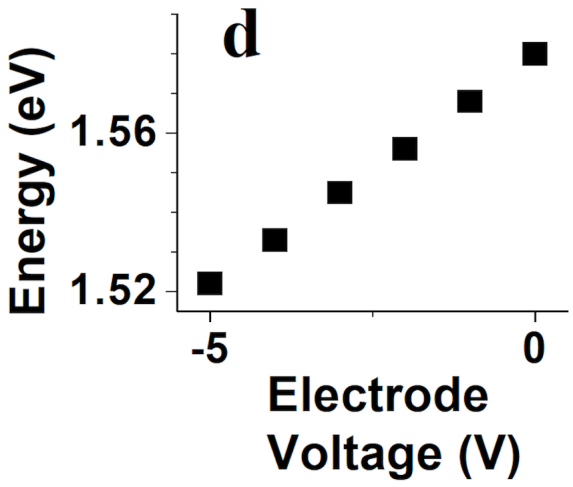

Figure 2.7: Plot of exciton energy as a function of gate voltage for the CQW sample used in the conveyer experiment. Analogous to Figure 2.6, but in this sample the wider separation between top electrodes and ground plane call for greater voltages. From High et al. [2007].

peratures are readily accessed with ordinary liquid-helium cryostats. Stimulation and photoluminescence emission wavelengths are in the red or very-near-IR, conveniently accessible by CW and pulsed lasers and detectors offering high spectral, spatial, and temporal resolution. GaAs nanostructures can be grown with high purity, yielding narrow emission linewidth. Electrode structures can be patterned photo- or electro-lithographically, yielding almost arbitrary potential energy landscapes. Both the lifetime and energy landscapes can be controlled very rapidly, on timescales much shorter than the lifetimes themselves. These flexible combinations of spatial and temporal *in situ* control of both energy and lifetime permit fabrication of a wide variety of devices, for both investigation into the fundamental properties of bosonic gases, and for demonstration of novel optical- and electro-optical devices operating at the GHz speeds essential to modern industrial application. Once demonstrated, devices may later be fabricated in other semiconductor materials for operation at higher temperature.

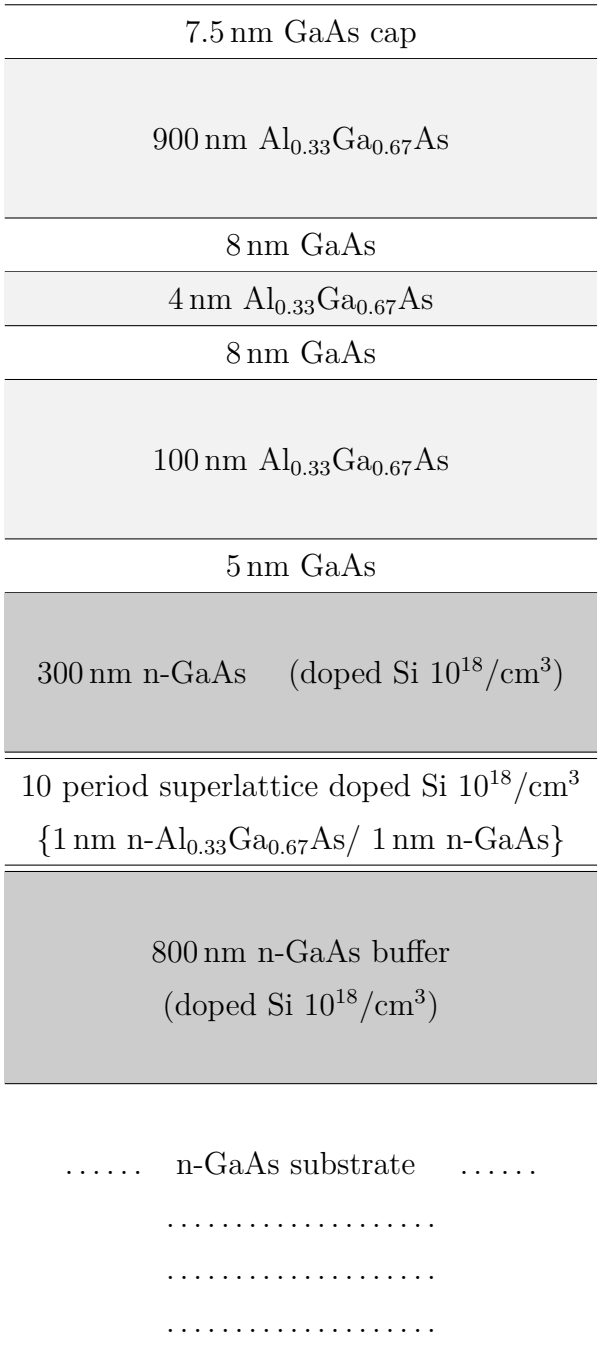

Figure 2.8: Diagram of the heterostructure layers grown by MBE for the CQW structure used in the exciton conveyer experiments. The 8-4-8 GaAs/AlGaAs CQW are positioned about $\frac{9}{10}$ of the way towards the bottom of the ∼1000 nm region between upper electrodes and ground plane / back electrode (doped GaAs layers.)

2.6 Quick reference to typical numerical parameters

Table 2.1: Typical numerical parameters.

Direct exciton PL emission wavelength	790 nm
Indirect exciton PL emission wavelength	near 800 nm
(depending on density and V_g)	(795 - 810 nm)
Direct and indirect exciton PL linewidth	1-2 nm
Excitation laser wavelength	
HeNe cw or pulsed diode	635 nm
diode conveniently below ITO bandgap	690 nm
Ti:Sp for resonant excitation	790 nm
Working gate voltage V_g for indirect excitons	
Photonic storage samples	1.0 or 1.4 V
Conveyer samples	3-5 V nom 4.0 V
Exciton effective mass m_x	$0.22\, m_e$
Exciton binding energy	
direct exciton E_D^{binding}	10 meV
indirect exciton E_I^{binding}	5 meV
E_I^{binding}/k_B	60 K
Cryostat sample bath temperature	
Photon storage experiments	5 K
Exciton conveyer experiments	1.5 K

Part II

Photonic storage

Chapter 3

Excitonic photonic storage: Proof of principle

3.1 Introduction

Photon storage is one of the major parts of optical signal processing in optical networks. Effective photon storage in semiconductor nanostructures was demonstrated recently. In particular, photons were stored in the form of separated electrons and holes in the acoustically [Rocke et al., 1997; Santos et al., 1999] and electrostatically [Zimmermann et al., 1999; Zhang et al., 2000; Krauß et al., 2004] induced lateral superlattices and in quantum dot pairs [Lundstrom et al., 1999]. A switching time shorter than 20 ns has been demonstrated [Zimmermann et al., 1999]. The storage dynamics in the electrostatically induced lateral superlattices were also studied at 200 MHz ac voltage [Zhang et al., 2000]. Each oscillation period of the voltage resulted in recombination of a fraction of the separated electrons and holes, with the total readout of the storage device within about 20 ns.

Here we report on photon storage with nanosecond switching time in semiconductor nanostructures. The GHz switching speed meets the requirement for optical networks. Moreover, the switching speed is not fundamentally limited by the device design and can be further increased to meet the demand of ever faster networks.

3.1.1 Principle of operation

The storage device employs spatially separated electrons and holes in coupled quantum well semiconductor nanostructures (CQW), Fig. 1a. The demonstration of the storage is presented for low temperatures where the spatially separated electrons and holes are bound, forming indirect excitons, Fig. 1a (for a review on indirect excitons see Butov [2004]), however the operation principle of the device is the same at high temperatures for the unbound electrons and holes. We note also that both our photon storage devices and the devices studied in earlier works [Rocke et al., 1997; Santos et al., 1999; Zimmermann et al., 1999; Zhang et al., 2000; Krauß et al., 2004] employ a spatial separation of electrons and holes in QW structures. However, the operation principle of our devices is based on separation of electrons and holes in the sample growth direction (in different QWs a few

nanometers apart), while the operation principle of the devices studied in [Rocke et al., 1997; Santos et al., 1999; Zimmermann et al., 1999; Zhang et al., 2000; Krauß et al., 2004] is based on separation of electrons and holes in the QW plane.

The emission rate of the indirect excitons (or unbound electrons and holes) is determined by the overlap between the electron and hole wave functions and controlled by the applied gate voltage within several orders of magnitude [Butov, 2004]. This opportunity of electronic control of the emission rate constitutes the basis for the device operation. The schematic of the photon storage is presented in Figs. 1b-e. Photons generated by a laser pulse (Fig. 1b) are absorbed in the CQW device. Writing is performed by the gate voltage pulse (Fig. 1c), which reduces the exciton emission rate and stores the absorbed photons in the form of indirect excitons. Emission of the indirect excitons during the storage occurs at lower energy and is weak due to their long lifetimes [Butov, 2004] (shown schematically in Fig. 1e). Readout of the stored photons is provided by termination of the gate voltage pulse, which increases the emission rate and results in fast conversion of excitons back to photons (Fig. 1d).

3.1.2 Other Applications

Rapid control of the indirect exciton energy and lifetime is also required for manipulating excitons in electrostatic traps. Such traps are based on the quantum confined Stark effect [Miller et al., 1985]: the laterally modulated gate voltage $V_g(x, y)$ creates a laterally modulated electric field in the sample growth direction, $F_z(x, y)$, and, in turn, a lateral relief of the exciton energy $\delta E(x, y) = eF_z(x, y)d$, where d is the exciton dipole moment [Zimmermann et al., 1999; Zhang et al., 2000; Krauß et al., 2004; Hagn et al., 1995; Zimmermann et al., 1997; Huber et al., 1998; Hammack et al., 2006; Gärtner et al., 2006; Chen et al., 2006]. A suitable design of $V_g(x, y)$ allows creating a variety of in-plane potential reliefs for the excitons. Particular cases for the potential relief, considered in the recent studies, include potential gradients [Hagn et al., 1995; Gärtner et al., 2006], 1D [Zimmermann et al., 1999; Krauß et al., 2004; Zhang et al., 2000; Zimmermann et al., 1997] and 2D [Hammack et al., 2006] lateral superlattices, and traps [Huber et al., 1998;

Hammack et al., 2006; Chen et al., 2006]. The gate voltage control should allow manipulating the relief in-situ, opening an opportunity for studying excitons in controlled potentials. Note that the drastic progress in studies of ultracold atoms originated from an opportunity of studying atoms in controlled potentials [Cornell and Wieman, 2002; Ketterle, 2002]. For studies of excitons in the controlled electrostatic traps and other potential reliefs, the operation speed for varying the potential must be faster than the exciton recombination rate. The studies presented in this work show that the switching rate is orders of magnitude faster than the exciton recombination rate. This demonstrates the feasibility of studying excitons in *in situ* controlled potentials.

3.2 Experimental setup

n^+-i-n^+ GaAs/AlGaAs CQW samples were grown by molecular beam epitaxy (Fig. 1a). The i region consists of a single pair of 8 nm (15 nm) QWs separated by a 4 nm $Al_{0.33}Ga_{0.67}As$ barrier and surrounded by 200 nm $Al_{0.33}Ga_{0.67}As$ barrier layers for sample A (B). The n^+ layers are Si-doped GaAs with $N_{Si} = 5\times10^{17}$ cm^{-3}. The electric field in the sample growth direction F_z is controlled by the gate voltage V_g applied between n^+ layers. At $V_g = 0$ the lowest energy state in the CQW is the direct exciton with a short lifetime, below 0.1 ns, while at $V_g \sim 1V$ the lowest energy state is the indirect exciton with a long lifetime, which is determined by the QW and barrier width and varies from tens of nanoseconds to several microseconds for the studied gate voltages and samples.

The carriers were photoexcited by a 635 nm laser diode. The 200 ns laser excitation pulse (Fig. 1f) has a rectangular shape with edge sharpness ~ 0.6 ns and repetition frequency 500 (100) kHz for the experiments with sample A (B). The average excitation power was 80 μW and the excitation spot diameter was $\sim 100\,\mu$m. The emitted light was diffracted by a single-grating spectrometer and detected by a Peltier-cooled photomultiplier tube and time correlated photon counting system. The direct exciton emission was at 1.569 eV ($\lambda = 790$ nm) for sample A and 1.534 eV ($\lambda = 808$ nm) for sample B, and the indirect excitons were lower

in energy by 20-50 meV for the studied gate voltages and samples. The exciton energy and emission intensity oscillated in the transient periods near the edges of the gate voltage pulses; these transient oscillations are not essential for the device operation principle, and therefore are not considered here but in Chapter 5. The experiments were performed in a He cryostat at $T = 5$ K.

3.3 Results

The experimental data (Fig. 1f) demonstrate proof of principle for the device operation, which is schematically presented in Fig. 1b-e and described above. The storage time $\tau_{storage}$ reaches $\sim 2\mu$s for the 8-4-8 nm CQW sample and $\sim 8\mu$s for the 15-4-15 nm CQW sample (Fig. 2a,b). (A larger $\tau_{storage}$ for a smaller V_g is possibly due to an additional in-plane separation of electrons and holes, which takes place in the vicinity of $V_g = 1$ V and, for instance, leads to formation of spatial patterns in the emission [Butov, 2004; Rapaport et al., 2004]. In-plane spatial separation can also be explored for the memory devices with CQWs as was done in the memory devices with lateral superlattices [Rocke et al., 1997; Santos et al., 1999; Zimmermann et al., 1999; Zhang et al., 2000; Krauß et al., 2004]. This issue will be considered in future studies.) Figure 2c presents a readout pulse on an extended timescale. The exponential fit (line) gives the rise time $\tau_{readout} \sim 0.9$ns and the full width at half maximum of the pulse is 3 ns. This switching time of the photon storage devices is smaller by an order of magnitude than the previously established record of about 20 ns [Zimmermann et al., 1999; Zhang et al., 2000].

3.4 Conclusion

While the chapter reports on the proof of principle for the photon storage in CQW nanostructures, in this paragraph we address briefly the issues of the device operation at high temperatures and carrier loss, which are essential for practical applications. The switching of the device is based on the tunneling of the electrons and holes through the potential barrier which separates the quantum

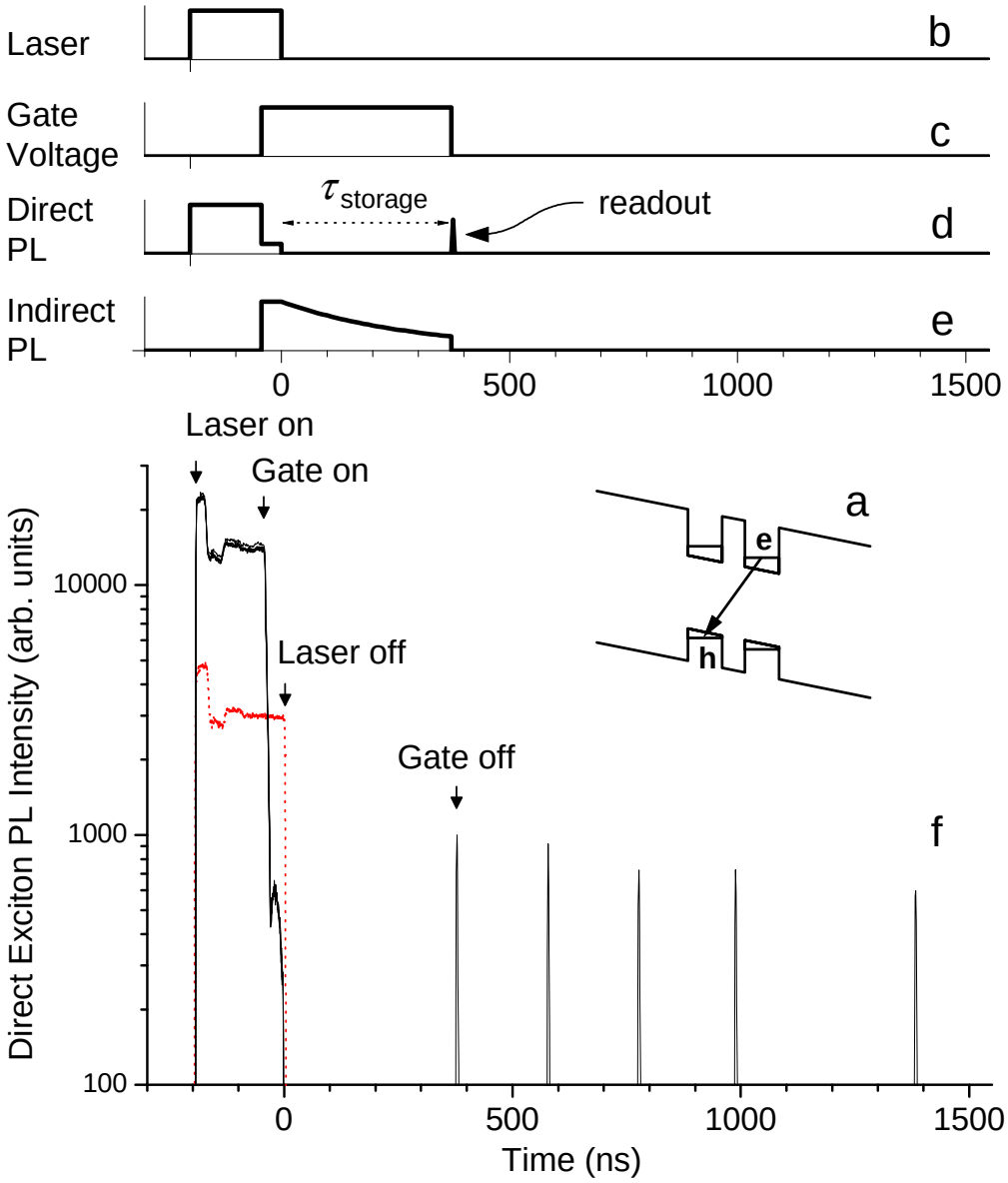

Figure 3.1: (a) GaAs/AlGaAs CQW band diagram. (b)-(e) Schematic of the photon storage and readout in the CQW device showing the sequence of the laser (b) and gate voltage (c) pulses as well as the direct (d) and indirect (e) exciton emission. The operation principle of the device is described in the text. (f) Experimental implementation of the photon storage and readout in the GaAs/AlGaAs CQW device with 8 nm QWs and 4 nm barrier (sample A). The gate voltage pulse $V_g = 1$ V. The solid lines present the kinetics of the direct exciton emission for five different storage times. The timescale on the schematic (b-e) corresponds to the experimental data (f) with the shortest storage time. The laser pulse shape is shown by the dashed line. From Winbow et al. [2007].

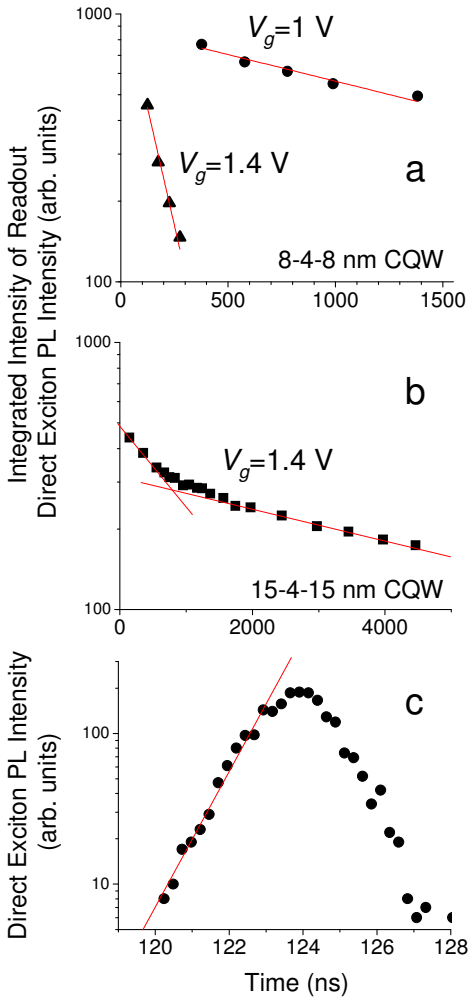

Figure 3.2: Integrated intensity of the photon readout as a function of the storage time, which is given by the duration of the gate voltage pulse after the laser pulse, for (a) CQW sample A with 8 nm QWs and 4 nm barrier and (b) CQW sample B with 15 nm QWs and 4 nm barrier. Circles in (a) correspond to gate voltage pulse $V_g = 1\,\mathrm{V}$ and triangles to $V_g = 1.4\,\mathrm{V}$. The exponential fits (lines) give the storage decay time for both samples. In (a), $\tau_{storage} \sim 2\,\mu\mathrm{s}$ for $V_g = 1\,\mathrm{V}$ and $\sim 0.1\,\mu\mathrm{s}$ for $V_g = 1.4\,\mathrm{V}$, while in (b), $\tau_{storage}$ increases with increasing time delay from $\sim 1.6\,\mu\mathrm{s}$ to $\sim 8\,\mu\mathrm{s}$. (c) A readout pulse. The exponential fit (line) gives the rise time $\tau_{readout} \sim 0.9\,\mathrm{ns}$. From Winbow et al. [2007].

wells, see above. While demonstration of the photon storage is presented at low temperatures where the spatially separated electrons and holes are bound, forming excitons, at high temperatures the electrons and holes are unbound. However, since the height of the barrier, which separates the QWs, is much higher than the exciton binding energy [Butov, 2004], the tunneling rate of unbound electrons and holes is essentially the same as the tunneling rate of electrons and holes bound as excitons. Furthermore, the tunneling rate is practically independent of temperature, which makes development of the photon storage in CQW nanostructures with a short switching time feasible. The issue of carrier loss during the storage is also important: it is essential for the long storage time and for lateral scalability in memory applications. The carrier loss can be minimized by suppressing the recombination of electrons and holes (e.g. by reducing the overlap between the electron and hole wave functions [Butov, 2004]), by suppressing the lateral escape of the electrons and holes from the photon storage cell (e.g. by lateral confinement of the carriers [Hammack et al., 2006]), and by optimization of the collection of the absorbed and emitted photons (e.g. by using multiple CQW pairs, distributed Bragg reflector mirrors below the CQW, and ridge waveguide structures on the top of the device [Caulfield and Tocci, 1994]). The optimization of the device parameters is a subject of future work.

In conclusion, we presented experimental proof of principle for the photon storage devices with indirect excitons (or unbound electrons and holes) in coupled quantum well nanostructures with nanosecond switching time and microsecond storage time. Optimization of the device parameters including particularly the storage and switching times is a subject of future work. Furthermore, the presented exciton control on a time scale much shorter than the exciton lifetime demonstrates the feasibility of studying excitons in *in situ* controlled electrostatic traps and other potentials.

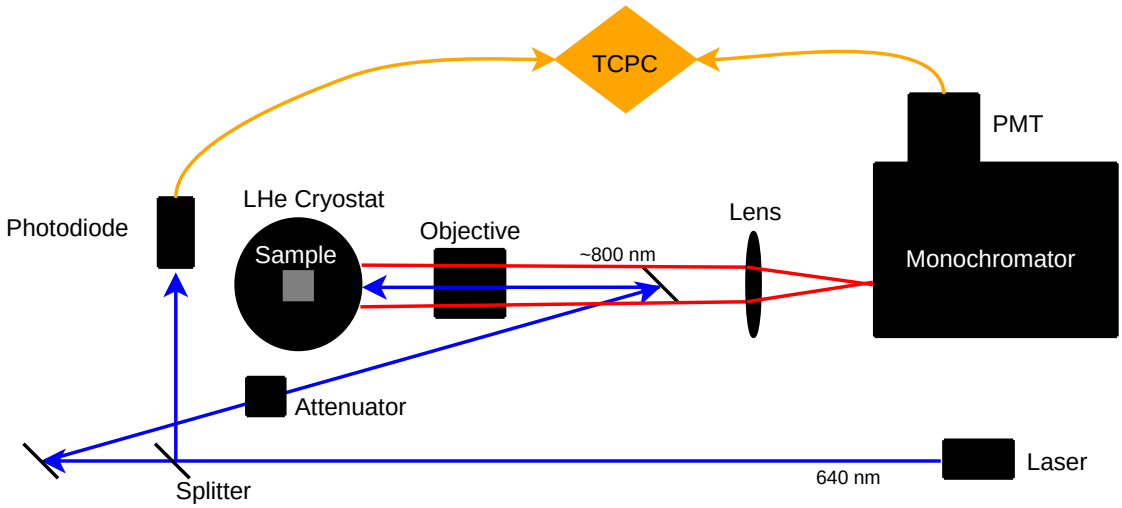

Figure 3.3: Schematic of the optical layout used in these experiments. The 640 nm pulsed diode laser illuminates the sample; the exciton photoluminescence, near 800 nm, is imaged through a scanning monochromator onto a fast photomultiplier. A portion of the original laser is split and detected by a photodiode as a timing reference. The time correlated photon counting system (TCPC), histogramming over many repetitive cycles, reconstructs the temporal evolution of the PL signals with resolution into the tens of picoseconds.

3.5 Acknowledgements

This work is supported by ARO grant W911NF-05-1-0527 and NSF grant DMR-0606543. We thank K. L. Campman for growing the high quality samples.

The text of Chapter 3, in part, is a reprint of the material as it appears in A.G. Winbow, A.T. Hammack, L.V. Butov, & A.C. Gossard, *Photon Storage with Nanosecond Switching in Coupled Quantum Well Nanostructures.* Nanoletters, **7**, 1349-1351. © 2007 American Chemical Society, where the dissertation author was the first author.

Chapter 4

First-generation high-speed cryostat sample insert

4.1 Introduction

The first generation high-speed sample insert might warrant a detailed account of its design and construction, but it was largely superseded by the much more ambitious Octopus described in Part III; much of the technical description here should be read in the context of those chapters.

This sample insert is derived from the Janis SVT-300 factory insert, and designed to accommodate a pair of 0.141″ semi-rigid cryogenic coaxial cables. It is also, in principle, capable of accommodating two smaller 0.085″ cables. Only one 0.141″ cable was mounted, used to provide a single GHz–class channel for the photonic storage experiment described in Chapter 5. The Micro-Coax 141B-SS cable has 10 GHz (3 dB) bandwidth, chosen to remove the cable entirely as a performance limitation. The insert was designed by hand on paper[1], and machined entirely by hand by the author. The principal design elements are an entirely new crown, where the cryostat seals from the outside, and the sample holder, which mounts a 16-pin DIP socket and provides a minimalist method for terminating the transmission line at the sample.

4.2 Design elements

4.2.1 Crown

The crown was the principal design challenge. The original drawings of pencil and ink and protractor on paper would appear inscrutable, but the successful crown design was subsequently drawn in CAD for adaptation to the Octopus; see Section A.1 for diagrams.

The crown is intended to mimic the (much smaller and simpler) Janis crown by mounting to the cryostat sample bore with a ladish flange seal, and providing a 1/4-inch cylindrical vacuum feedthrough for the main shaft and side plates with vacuum feedthroughs for DC wiring.[2] The vacuum flange is a “ladish” or “sanitary”

[1] Having not yet seen the light of SolidWorks 3D CAD!

[2] The very first iteration was in aluminum, and slipped in the milling machine at the final machining steps, destroying the o-ring groove.

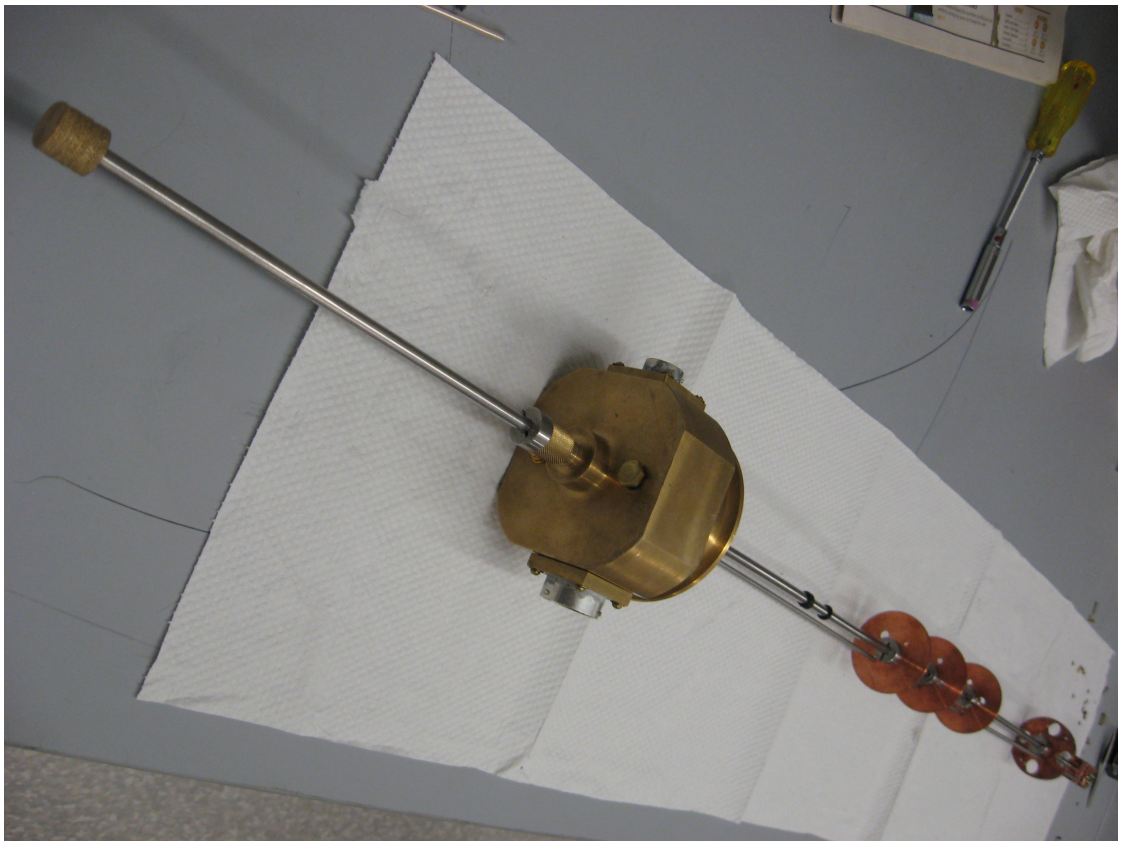

Figure 4.1: Photograph of the first-generation custom cryostat insert, top view.

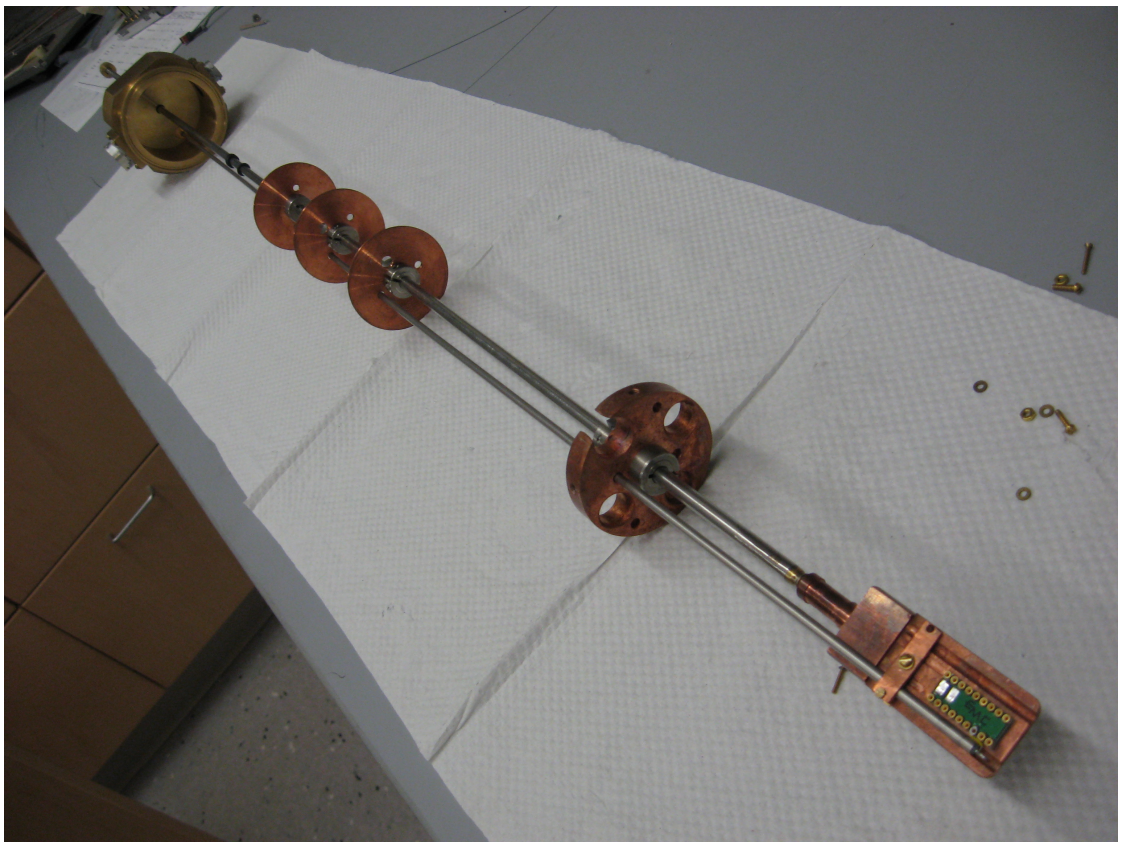

Figure 4.2: Photograph of the first-generation custom cryostat insert, bottom view.

flange, employed by Janis for historical reasons (the basic Janis cryostat design may be decades old, and the flange is purportedly found in e.g. brewpubs), and is based on an o-ring gland of circular cross section; o-rings and the ladish clamp were sourced from Janis. The main shaft feedthrough is half-integral to the crown: the threads are 1/2-20, and the cap (i.e., nut) is from an A&N #B-25-K.

The coaxial cable terminates at the top of the crown in a soldered bulkhead vacuum SMA feedthrough (from Pasternack). The bulkhead feedthrough seals in the clear-drilled hole in the crown via a nut and compression against a Viton o-ring. See Section B.1 for details on cutting and soldering the cable.

Machining details

The crown began as a single lump of brass, turned first on the lathe to make the 1 in stub, and then reversed and the interior bored out; the part was held by four-jaw chuck after being thus sufficiently lightened, and then mounted by the 1 in colleting stub and turned between centers with a large live center in the lower opening. Finishing work was done on the mill. The peculiar mix of round and square in the outer diameters was designed to accommodate several goals: lightening the part as much as possible, boring out the interior diameter as widely as possible to give maximum room for the coaxial cables, maintaining sufficient wall thickness, and providing square flats to securely clamp the part for milling (the aluminum prototype was lost at this stage). Particular attention was given to planning the exact order of machining steps (since clamping is difficult), and the overall design was partly driven by the desire to make the the part in a single piece to reduce the number of vacuum joints.

4.2.2 Sample holder

The sample holder proper was intended as the simplest part that would reliably serve a single channel on the experiment. The piece that screws to the mainshaft is quite similar to the original Janis component, and attached to that is an L-bracket of OFHC copper. The 16-pin DIP socket[3] pins pass through holes

[3]Not a typo; the lab had both 8x2 and 9x2 DIP sockets on hand, unbeknownst at the time.

drilled in the L-bracket; four of the holes are press-fit as both mechanical attachment points and electrical grounds, and the remainder clear-drilled as floating signal pins.

The bracket has shallow semi-circular channels, milled by ball endmill[4], that countersink the semi-rigid coaxial cable as it runs straight down from the top. The center conductor thus exits the cut end of the cable close to the ground plane, in order to reduce the size of the inductive loop[5] The cable clamps to the sample holder via a clamping bar with semi-circular cutouts. Copper was chosen so that the bar would mold slightly to the shape of the hard stainless-steel cable, rather than risk damaging the cable internal reactive geometry by point pressure; however, the copper is too soft and did not easily obtain adequate clamping force to hold the cable against the sample holder by friction.

The cable attaches to the relevant pin on the DIP socket by a simple soldered wire. The signal pin on the socket (and hence the cable) need to be terminated to ground via $50\,\Omega$. This was achieved by using a signal pin adjacent to one of the four ground (press-fit) pins, and bridging the two pins with a metal-film surface mount resistor, all on the back side of the L-bracket.

4.2.3 Other components

The heatshields and concentric spacer are similar to that described in the Octopus, though machining them by hand was difficult. The heatshields were crudely cut out with a saw, then turned on a dedicated clamp jig. Obtaining the necessary clamping pressure to turn the edges without spinning the disk using the small 1/4" bolt hole worked barely adequately. The concentric spacer visibly suffered damage in the mill. The sideplates used in the Octopus are actually the ones that were made by hand for this insert. The center shaft and end parts are as in the Janis design, although small holes were drilled in the center shaft to permit any helium (perhaps superfluid liquid helium) that entered the tube to escape easily during warming-up. The shaft bottom-cap was silver-soldered, and the top

[4] 5/32" if memory serves; oversize for the cable.

[5] Unfortunately, the cable was not cut to quite the correct length for the single pin ultimately used, and the connection wire is too long.

cap welded by CRMS.

4.3 Pulsed RF performance

The RF performance is simply demonstrated by the oscilloscope traces in Figure 4.3 and Figure 4.4[6], and by the results achieved (measured optically, indirectly) in Chapter 5.

4.4 Future use

Although the Octopus is a very much more advanced apparatus, this sample insert may still be useful for undertaking experiments requiring one or perhaps two high-speed signals, without needing to make changes to the Octopus.

Second channel

To add a second channel, disassemble the insert and bore a new hole in the crown as in the existing one. (The dimensions may be obtained from the bulkhead feedthrough specifications.) The principle obstacle will be satisfactorily mastering the techniques to cut another cryogenic coaxial cable to length and then to solder it to the feedthrough. Choice of signal pins at the bottom may remain limited, given the simple mechanics available for the termination scheme.

Vertical travel

The original design intention was that the cable would have sufficient springiness to permit a small amount of vertical travel by drawing up the center shaft. This was erroneously based on the behavior of several test pieces of cryogenic coaxial cable that *did not* have the stainless steel outer conductor of the 141B-SS cable actually used. Attempts to draw the center shaft up and thus adjust the height of the sample holder require tremendous force, which will soon exceed the capacity of the cable clamp. The height should not be adjusted, unless the coaxial cable is cut

[6]Being ignorant, at the time, of vector network analyzers.

back and travel obtained via a flexible wire (the unshielded length of which will degrade the RF performance). A small length of flexible cryogenic coaxial cable might be added here; the poor bandwidth common to such cables per unit length may not be an obstacle if only a couple of inches is used.

Figure 4.3: Oscilloscope trace of pulsed gate voltage $V_{\rm g}$ for original (Janis factory) cryostat sample insert. After switching on, ($t = 2350$), considerable ringing and voltage overshoot due to impedance mismatch is evident. The ringing has has barely damped even $\sim$150 ns later when $V_{\rm g}$ is switched off, and new ringing and overshoot are again induced. The impedance mismatch slows the transition edge (ie, reduces the rise/fall times), and the ringing causes the indirect excitons to oscillate in energy. Vertical scale in volts.

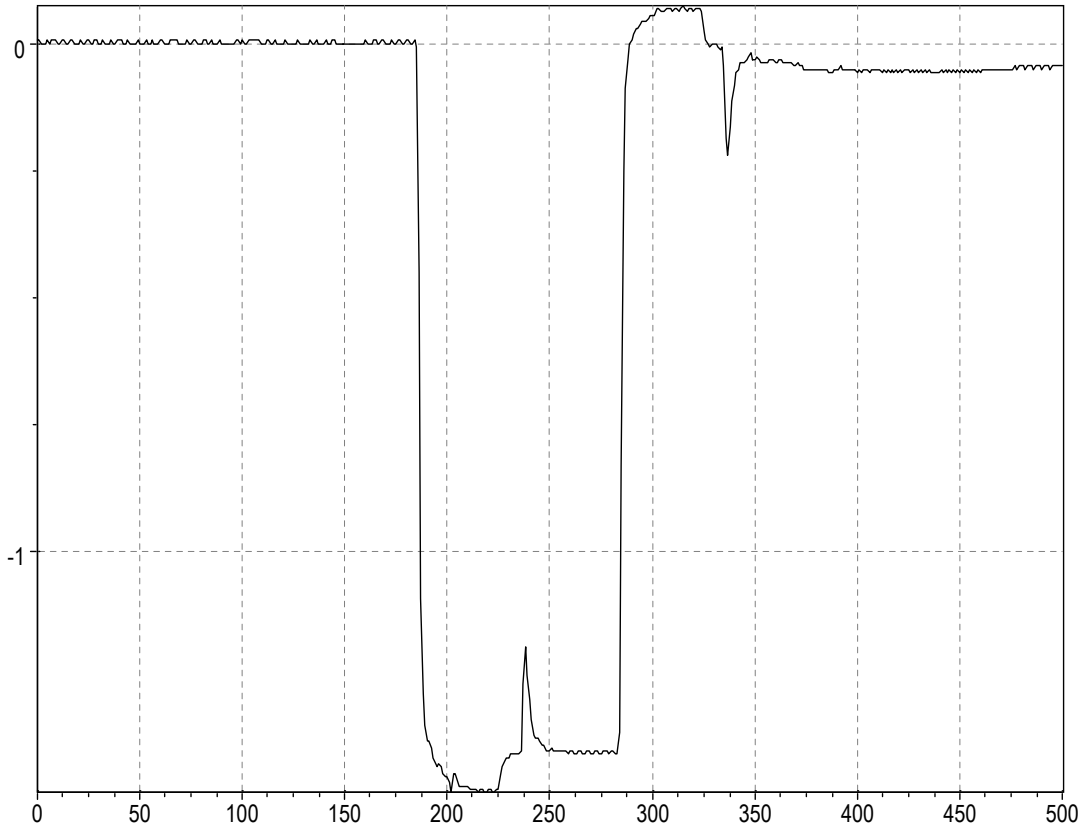

Figure 4.4: Oscilloscope trace of pulsed gate voltage V_g for the custom cryostat sample insert. The switch on and switch off transitions (rise and fall times) are sharper, and exhibit much reduced overshoot and little to no ringing. Reflections of the switch on and switch off transitions are evident near $t = 240$ and $t = 340$ ns, indicating that there is still some impedance mismatch at the end of the transmission line (due to the capacitive sample load in parallel with the matched termination resistor). The $\sim$50 ns delay between the switching transition and reflection corresponds to the round trip signal propagation time between the signal tap/oscilloscope and the bottom of the cryostat, including intermediary external cabling. Vertical scale in volts.

Chapter 5

Excitonic photonic storage with subnanosecond switching

5.1 Introduction

Photon storage is an essential part of optical signal processing in optical networks. Efficient photon storage in semiconductor nanostructures has been recently demonstrated. Photons were stored in the form of separated electrons and holes in acoustically [Rocke et al., 1997; Santos et al., 1999] and electrostatically [Zimmermann et al., 1999; Zhang et al., 2000; Krauß et al., 2004] induced lateral superlattices, quantum dot pairs [Lundstrom et al., 1999; Kroutvar et al., 2003, 2004; Young et al., 2007; Krenner et al., 2008], and coupled quantum wells (CQW) [Winbow et al., 2007]. The fastest demonstrated rise time of the readout optical signal in these devices was about one nanosecond [Young et al., 2007; Winbow et al., 2007]. Here, we report on refining the photon storage in CQW and achieving a 250 ps rise time of the readout optical signal. The refining also has led to an effective elimination of transient oscillations after the storage pulse.[1]

5.2 Principle of operation

The storage device employs spatially separated electrons and holes in CQW, Fig. 1a. The same device was employed in the proof of principle photon storage in CQW [Winbow et al., 2007]. The storage is presented for low temperatures where the spatially separated electrons and holes are bound, forming indirect excitons (for a review on indirect excitons see Butov [2004]); however, the operation principle of the device is the same at high temperatures for unbound electrons and holes. The same device and temperature as in Winbow et al. [2007] and Chapter 3 are studied in this chapter so that the refined photon storage can be compared with the earlier one.

The principle of the photon storage with CQW is as follows: The emission rate of the indirect excitons (or unbound electrons and holes) is determined by the overlap between the electron and hole wave functions and can be controlled by the applied gate voltage, typically within several orders of magnitude. The energy of

[1]The term photon storage is used in a general sense and the issue of the carrier or phase information loss is not addressed here.

the indirect excitons (or unbound pair of electron and hole) is also controlled by the applied gate voltage V_g, which results in the exciton energy shift $\delta E = edF_z$, [Miller et al., 1985] where d is the separation between the electron and hole layers (close to the distance between the QW centers), $F_z = V_g/D$ is an electric field perpendicular to the QW plane, and D is the width of the intrinsic layer in the $n^+ - i - n^+$ CQW sample. The energy can be typically controlled within several tens of meV in CQW samples. Figs. 2a-d present the schematic of the photon storage. Photons generated by a laser pulse (Fig. 2a) are absorbed in the CQW device. Writing is performed by the gate voltage pulse V_g (Fig. 2b), which reduces the exciton emission rate and stores the absorbed photons in the form of indirect excitons. Emission of the indirect excitons during storage occurs at energy lower by approximately edV_g/D (for corrections due to the interaction see Butov [2004]) and is weak due to their long lifetimes. This emission is shown schematically in Fig. 2d. Readout of the stored photons is provided by termination of the gate voltage pulse, which increases the emission rate and results in conversion of excitons back to photons (Fig. 2c). The earlier implementation of this scheme [Winbow et al., 2007] (Chapter 3) demonstrated photon storage with microsecond storage time and nanosecond rise time of the optical readout.

5.3 Need for improved electrical control

A principal limitation of the proof-of-principle experimental setup [Winbow et al., 2007] was that the gate voltage pulse from the pulse generator was delivered to the CQW sample via ordinary wires over $\sim$1 m from the top of the He cryostat to the sample at the bottom. Such a circuit segment is suited for dc signals. However, for the nanosecond switching time of the applied gate voltage, i.e. GHz switching speed, the characteristic wavelength $\sim c/f$ is smaller than the $\sim$1 m length of the wire. An impedance-matched broadband transmission line is required in such regime for optimal device performance. This is briefly discussed below.

The characteristic impedance of the pulse generator and external cabling is $Z = 50\,\Omega$, while the CQW sample has resistance between the top and bot-

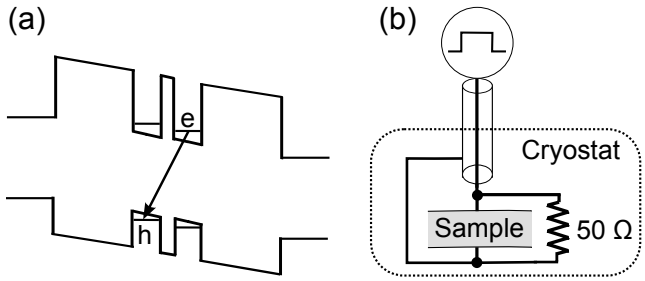

Figure 5.1: (a) GaAs/AlGaAs CQW band diagram. (b) Schematic of the photon storage circuit with an impedance-matched broadband transmission line. From Winbow et al. [2008].

tom planes in the range of MΩ - GΩ depending on the laser excitation and acts approximately as a parallel plate capacitor with $C \sim \epsilon S/4\pi D \sim 60\,\mathrm{pF}$, where $S \sim 0.5 \times 0.5\,\mathrm{mm}^2$ is the sample area. (Note that such circuit also acts as an RC low-pass filter, which slows the switching time.) The apparent impedance mismatch between the ordinary wire and the sample results in reflection of the voltage pulse at the sample and oscillation of the applied voltage V_g and electric field $F_z = V_\mathrm{g}/D$ in the sample. We detected these oscillations by analysis of the evolution of the emission spectra, as described below. (The voltage oscillations were also observed on an oscilloscope.) These oscillations hinder the storage in two ways: First, each swing of the oscillating electric field reduces the exciton lifetime and, therefore, reduces the photon storage efficiency. Second, the oscillations complicate the readout process, while waiting for their damping (as in the proof-of-principle experiment [Winbow et al., 2007]) sets a minimum storage time.

Furthermore, an ordinary wire also acts as an antenna. In the case when multiple gate voltages are applied to the CQW sample via different wires, the radiation emitted by such an antenna can lead to crosstalk among the wires. Multiple wires are used for creating potential landscapes for excitons, as discussed below, and thus eliminating crosstalk is required for improving the control of potential landscapes for excitons.

Therefore, improving the device performance requires gating the CQW via an impedance-matched broadband transmission line appropriate for the demanded

switching speed. In this chapter, we exploit gating the CQW sample via a broadband coaxial cable with a 50 Ω termination resistor, see Fig. 1b. This method can be applied to a variety of semiconductor structures of diverse layer designs. The achieved performance improvement of our device is described below.

5.4 Experimental setup

n^+-i-n^+ GaAs/AlGaAs CQW samples were grown by molecular beam epitaxy. The i region consists of a single pair of 8 nm GaAs QWs separated by a 4 nm $Al_{0.33}Ga_{0.67}As$ barrier and surrounded by 200 nm $Al_{0.33}Ga_{0.67}As$ barrier layers. The n^+ layers are Si-doped GaAs with $N_{Si} = 5 \times 10^{17}\,cm^{-3}$. The electric field in the sample growth direction F_z is controlled by the gate voltage V_g applied between n^+ layers. At $V_g = 0$, the lowest energy state in the CQW is the direct exciton with a short lifetime, while at $V_g \sim 1.4$ V, the lowest energy state is the indirect exciton with a long lifetime, about 0.1 μs for the studied sample.

The carriers were photoexcited by a 635 nm laser diode. The 200 ns laser excitation pulse (Fig. 2a) has a rectangular shape with edge sharpness $\sim$ 0.6 ns and repetition frequency 500 kHz. The average excitation power was 80 μW and the excitation spot diameter was $\sim 100\,\mu$m. The emitted light was diffracted by a single-grating spectrometer and detected by a Peltier-cooled photomultiplier tube and time correlated photon counting system. The experiments were performed in a He cryostat at $T \approx 5$ K.

The step-like voltage pulses for the storage and read-out were provided by a pulse generator with 0.5 ns exponential rise/fall time. (Note that the rise time of the readout signal was shorter than 0.5 ns; after termination of the gate voltage pulse, the emission line moves to higher energies to reach the energy at zero electric field and the rise time of the readout optical signal measured at this energy depends on the spectral shape of the emission line and is faster for the lines with a sharp high-energy edge.) The pulse was transmitted within the cryostat over a semi-rigid coaxial cable UT-141B-SS with silver-plated beryllium-copper inner conductor, PTFE teflon dielectric, and stainless-steel outer shell of diameter 3.6 mm,

having room-temperature attenuation of 3 dB/m at 10 GHz. The cable bandwidth complies with the requirement for fast control while the cable composition reduces heat conductance to the sample, thus facilitating future measurements with several such cables at low temperatures (Part IV). The cable was routed vertically straight from the sample through the exterior vacuum SMA feedthrough and countersunk in a channel in the sample plane for good electrical ground. The 5 mm contact pin from the sample socket passed through a hole in the ground plane and terminated on the back side with a metal-film surface-mount resistor having 50 Ω at 4.2 K.

5.5 Results

Figure 2f shows that the rise time of the readout optical signal in the refined system was 250 ps, which is an improvement compared to the nanosecond rise time achieved in Chapter 3.

We also analyzed the transient processes in the CQW after the storage pulse by measuring the kinetics of the exciton emission spectra. Figures 3c,d show the presence of strong oscillations of the exciton emission wavelength in the transient regime for the CQW gated via dc-suited wiring. The oscillation of the emission energy E reveals the oscillation of the electric field in the sample F_z, with the relation given by $\delta E = ed\delta F_z$. After the voltage pulse, the emission wavelength of the indirect excitons varies from about 810 nm ($E \approx 1.530$ eV) to 793 nm ($E \approx 1.563$ eV), close to the wavelength of the spatially direct emission at 791 nm ($E \approx 1.567$ eV). The emission intensity rises strongly as the wavelength reaches a minimum, caused by the increased recombination rate at smaller F_z; this causes losses of stored photons.

Figures 3a,b show these oscillations are effectively suppressed when the CQW is gated via an impedance-matched broadband transmission line. After application of the gate voltage pulse, the exciton energy changes without oscillations to the value determined by the applied voltage. The following slow fall in energy observed in Figs. 3a,b is consistent with the reduction of the indirect exciton density with decay, which results in the reduction of the repulsive interaction between

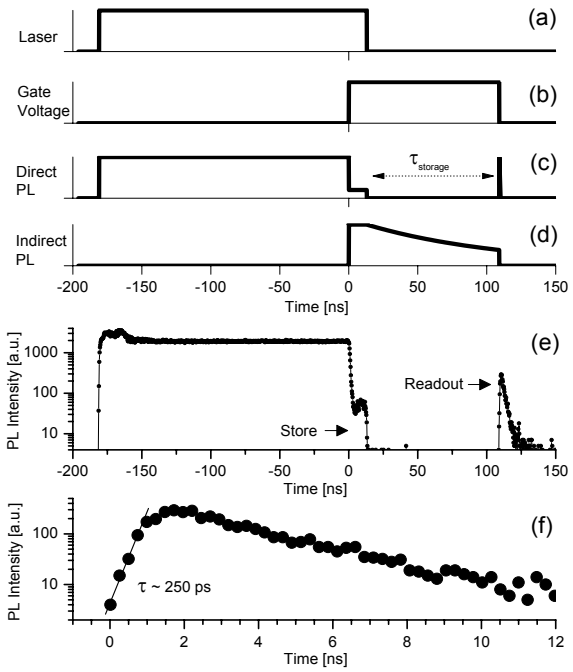

Figure 5.2: (a)–(d) Schematic of the photon storage and readout in the CQW device showing the sequence of the laser (a) and gate voltage (b) pulses as well as the emission of direct (c) and indirect (d) excitons. The operation principle of the device is described in the text. (e,f) Experimental implementation of the photon storage in the CQW device. The gate voltage pulse $V_{\rm g} = 1.4\,{\rm V}$. (e) Kinetics of the direct exciton emission of the refined system with an impedance-matched broadband transmission line, demonstrating photon storage followed by readout. The timescale on the schematic (a-d) corresponds to the experimental data. (f) The readout pulse on an extended time scale. The exponential fit (line) gives the rise time $\tau_{\rm readout} \sim 250\,{\rm ps}$. The fall time and FWHM of the readout signal are both 2.5 ns. From Winbow et al. [2008].

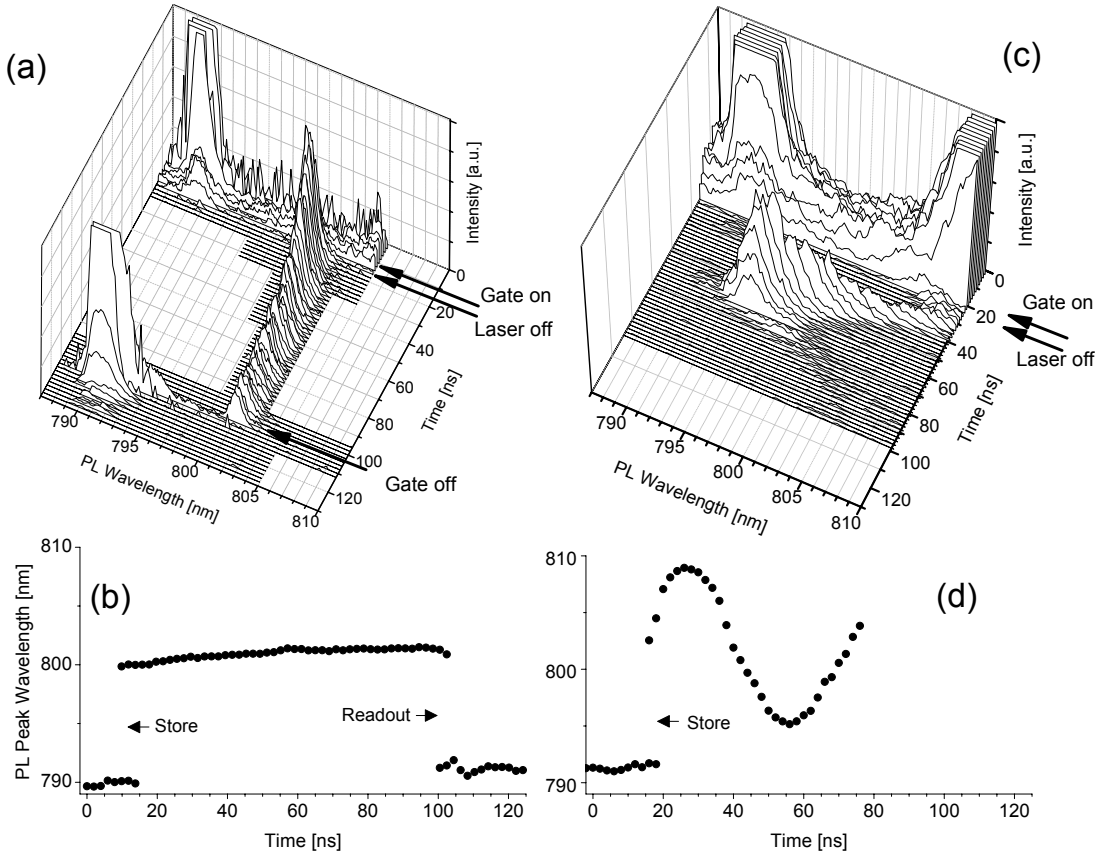

Figure 5.3: Evolution of emission spectra during storage and readout for (a,b) the refined system employing an impedance-matched broadband transmission line and (c,d) the proof-of-principle system employing dc-suited wiring. The applied voltage is $V_{\mathrm{g}} = 1.4\,\mathrm{V}$. Each spectrum is stepped 2 ns apart in time and is measured within a 2.3 ns window. The emission peaks while the laser is on (a,c) and at readout (a) are clipped in the plots to show small scale details. In the proof-of-principle system, the readout PL pulse occurs later in time and is not shown. Bulk n^+ PL is seen at $\lambda \gtrsim 805\,\mathrm{nm}$ during the laser pulse in (c). (b,d) The mean emission peak wavelength $\bar{\lambda}_{\mathrm{peak}} = \int \lambda I(\lambda)\mathrm{d}\lambda \,/\, \int I(\lambda)\mathrm{d}\lambda$ for the spectra presented in (a,c). The refined system eliminates the emission oscillations suffered by the proof-of-principle system after the voltage pulse. From Winbow et al. [2008].

the excitons [Butov, 2004]. The absence of oscillations demonstrates expedient switching at storage. As mentioned above, the oscillations cause losses of stored photons and complicate the readout processes; their elimination improves the device performance. Note that the data reported here demonstrate proof of principle for refining the device performance. The issues essential for practical applications, such as device operation at high temperatures, are briefly discussed in Section 3.4.

5.6 Conclusion

We would like to emphasize an important application of the rapid control of the indirect exciton energy and lifetime. A laterally modulated gate voltage $V_g(x, y)$ created by a pattern of electrodes on a sample surface can form a variety of in-plane potential landscapes for indirect excitons in CQW. Particular cases for such potential landscapes include potential gradients [Hagn et al., 1995; Gärtner et al., 2006], 1D [Zimmermann et al., 1999; Krauß et al., 2004; Zhang et al., 2000; Zimmermann et al., 1997] and 2D [Hammack et al., 2006] lateral superlattices, traps [Huber et al., 1998; Hammack et al., 2006; Chen et al., 2006; High et al., 2009a], and excitonic circuits [High et al., 2007]. The switching of the exciton energy to a required value without oscillations and within a short time, much shorter than the exciton lifetime, Figs. 3a,b, demonstrates an improvement for the control of such potential landscapes, which can be exploited in studying the physics of excitons.

Note also that the storage scheme can be used to realize a cold gas of *direct* excitons. Due to their short lifetime, direct excitons are typically hotter than the lattice, while indirect excitons live long enough to cool down essentially to the lattice temperature. [Butov, 2004] In the storage scheme, initially hot direct excitons transform to indirect excitons by the voltage pulse, cool down toward the lattice temperature during the long storage time, and then transform to direct excitons at the pulse termination. This method uses the long lifetime of indirect excitons to realize a cold gas of direct excitons after the last step, provided that essentially no heating occurs then. Note that indirect excitons have a built-in dipole mo-

ment and, therefore, interact relatively strongly [Yoshioka and Macdonald, 1990; Zhu et al., 1995; Lozovik and Berman, 1996; Ivanov, 2002; Schindler and Zimmermann, 2008]. However, direct excitons have no built-in dipole moment and interact weakly. Therefore, this method may permit extending the studies of cold exciton gases to a new system of weakly interacting cold direct excitons.

In conclusion, gating the CQW via an impedance-matched broadband transmission line has lead to an effective elimination of the transient oscillations in the electric field across the sample and to expedient switching of the exciton energy to a required value within a short time, much shorter than the exciton lifetime. A rise time of the readout optical signal as short as 250 ps was achieved.

5.7 Acknowledgements

This work is supported by ARO, DOE, and NSF. We thank K.L. Campman for growing the high quality samples, and R. Heron, G. Kassabian, B. Naberhuis, and R. Parker for help in preparing the experiment.

The text of Chapter 5, in part, is a reprint of the material as it appears in A.G. Winbow, L.V. Butov, & A.C. Gossard, *Photon storage with subnanosecond readout rise time in coupled quantum wells.* J. Appl. Phys., **104**, 063515. © 2008 American Institute of Physics, where the dissertation author was the first author.

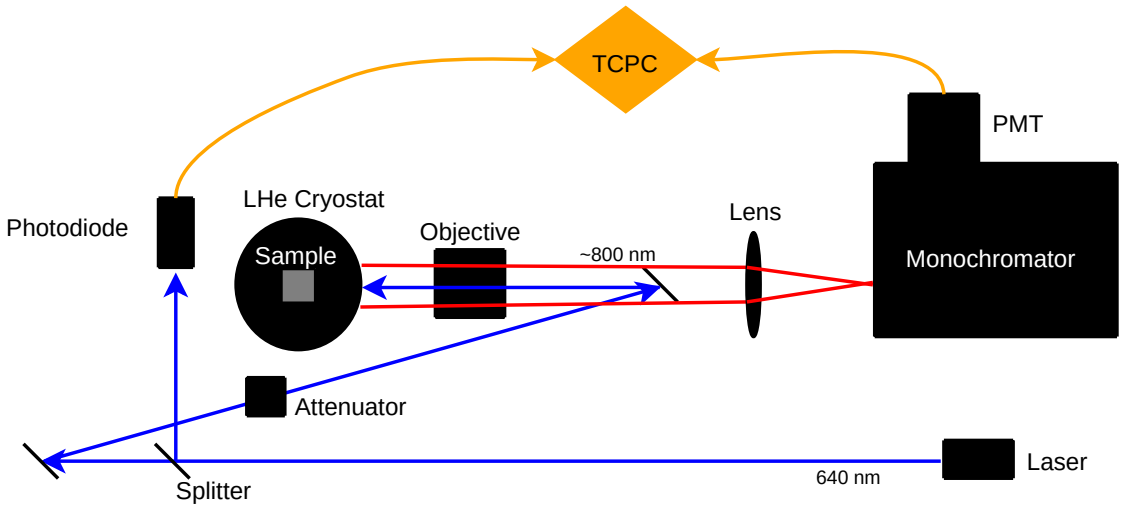

Figure 5.4: Schematic of the optical layout used in these experiments. The 640 nm pulsed diode laser illuminates the sample; the exciton photoluminescence, near 800 nm, is imaged through a scanning monochromator onto a fast photomultiplier. A portion of the original laser is split and detected by a photodiode as a timing reference. The time correlated photon counting system (TCPC), histogramming over many repetitive cycles, reconstructs the temporal evolution of the PL signals with resolution into the tens of picoseconds.
This is a similar setup to that of Chapter 3, but the TCPC is employed in two different modes: rather than holding the monochromator at a particular wavelength (e.g., the indirect exciton PL) while reconstructing the complete temporal signal (as in Figure 5.2), the TCPC can also be gated to examine only a particular point in time while scanning the monochromator to collect a spectrum. Stepping the time-gating window permits reconstruction of the complete temporal spectra, as in Figure 5.3.

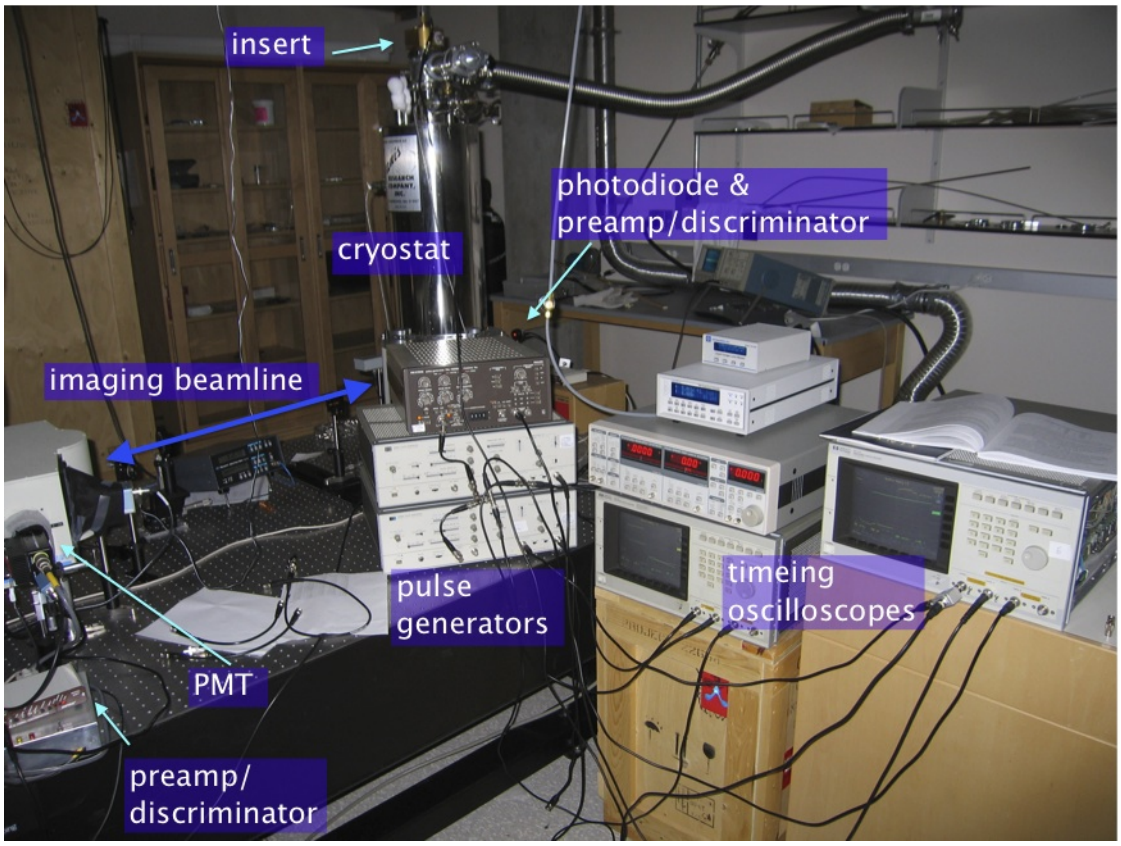

Figure 5.5: Photograph of portions of the experimental setup. The cryostat and optical beamline lead to the scanning monochromator at left, and photomultiplier at extreme left. The subnanosecond pulse generators, center, drive the laser diode and the sample gate voltage, and the pulse timing is monitored on several oscilloscope. The TCPC electronics are off-screen left. The brass crown of the custom sample insert is visible at the top of the cryostat.

Part III

The Octopus: a multichannel RF optical cryostat sample insert

Chapter 6

Octopus design overview

Contents

6.1 Introduction

The Octopus is a complete sample insert for a Janis SVT-300 optical liquid helium variable-temperature cryostat, from outside crown to sample holder. It places a physics sample very close to a cryostat window, and provides up to eight channels for RF signals, plus DC wiring, two temperature sensors, provision for heater, limited sample vertical positioning movement, and sample guard armor.

The Janis SVT-300 cryostat interior has a circular cross section of about 2.5 in interior diameter for most of its length, a 1 in interior rectangular cross section at the bottom where the sample area and cryostat windows are located, and is about 1 m tall. The Octopus is designed to suspend freely from the top, and contact the cryostat only at the top "ladish" joint, at the concentric spacer about 3/4 of the way down, and at the teflon alignment nosepiece in the sample area.

The Octopus incorporates 22 vacuum joints, all but two sealed by o-rings: one main "ladish" clamped seal between the crown and cryostat, eight axial seals between the cable vacuum feedthroughs and the crown, eight face seals between the vacuum feedthroughs and the cables, two face seals between the DC sideplates and the crown, and two solder joints between the DC feedthroughs and the sideplates. Considerable care was taken with the design and machining of the vacuum joints, and at original construction and after nine months of use, no Octopus seals appear to have leaked at all.

Directional nomenclature

A word on directional nomenclature: with the Octopus laying horizontally "face up" on a lab bench for inserting samples, the sample socket naturally defines a *top face*, and the back of the socket the *bottom face*. With the Octopus mounted vertically in the cryostat, rather than confusingly overload those adjectives, these documents refer to the *upper* and *lower* ends of the Octopus (and cryostat). The Octopus top face then faces the optical beamline.

6.2 Principal design constraints

The Octopus design is driven by several awkward mechanical constraints: the need to match the (two) cryostat bore cross-sectional shapes, the need to route up to eight 0.141 in-diameter semirigid coaxial cables over ∼1 m between 1.4 K and 300 K, and the need to fit those eight cables into the ∼ 1 in square sample space bore, the need to mount a sample in a 14-pin DIP chip packaging close to the cryostat window but absolutely without contact, and the need to connect the signals from the cables to the sample through a printed circuit board. These mechanical constraints drove the design of the Octopus geometry, which is unfortunately complex and manufactured to small (and hence expensive) tolerances.

1. The need to match the (two) cryostat bore cross-sectional shapes:
   Round and comparatively spacious for most of its length, the bottom section is square and exceedingly cramped; the square peg must fit in a square hole

with clearance of order 10 thou at the end of a meter-long flexible shaft, and negotiate the alignment into the square hole completely blind while the user is suspending a heavy, delicate, expensive object into the expensive borehole while standing atop a ladder. The cryostat bore has several weld discontinuities along its length and especially at the square-round junction.

2. The need to route up to eight 0.141 in-diameter semirigid coaxial cables over $\sim$ 1 m between 1.4 K and 300 K, and the need to fit those eight cables into the $\sim$1 in square sample space bore:

   The coaxial cables occupy in cross-section a considerable fraction of the square bore, not counting the obvious need for some sort of structural support as well (which necessarily must attach to the main shaft coming down the round bore above.) The cables need to end in a geometry partially countersunk into metal, so that heat conducted down the cables from 300 K does not wick to the sample, and so that the cable shield is electrically grounded. The cables need to be sturdily mechanically secured both to make that thermal and electrical joint and to be strong enough to withstand the considerable mechanical force applied to overcome friction in order to provide some vertical travel to adjust the final sample position in front of the cryostat window. Finally, the ends of the cables need to be within millimeters of the circuit board or sample mount pins to minimize the signal travel outside the coaxial cable shielded impedance to accommodate GHz frequencies. For only four or even six cables, several simpler, cheaper, easier Octopus geometries may be possible, but for seven cables (and hence eight by symmetry) only a single final geometric arrangement seemed possible: the highly compressed two layer planer arrangement, where the two lower-inner cables are unavoidably close to the main shaft.

3. The need to mount a sample in a 14-pin DIP chip packaging close to the cryostat window but absolutely without contact, and

4. The need to connect the signals from the cables to the sample through a printed circuit board, to accommodate both resistive and capacitive termi-

nation.

6.3 Present configuration

Transmission lines

Only seven of the eight mechanical channels for 0.141 in coaxial cables (UT-141B-SS) are occupied. All holes, feedthroughs, and clamps are fully ready for an eighth cable.

RF bandwidth

The cables have 3 dB bandwidth of 10 GHz, but the DIP socket and associated wiring is limiting factor. The 7 lines were tested at the individual DIP socket pins with fairly flat performance out to $\sim$ 700 MHz, with phase-skew difference among the lines of order one or two degrees.

Temperature sensors

At present, only one true temperature sensor is mounted, a fully-calibrated Lakeshore Si diode thermometer in the upper sensor mount position. A second sensor, a Lakeshore CX-1030 Cernox, has also been fully calibrated by the author for mounting in the lower sensor position, below and somewhat closer to the sample; four-wire measurements should be run through the 32-pin feedthrough. This sensor was intended to more closely measure the sample temperature, using a copper braid and thermal clamp, but the schema (discussed below) is not installed at present. An auxiliary carbon resistor has been fitted above the tailstock; it will exceed $\sim$MΩ[1] when the liquid helium level in the cryostat sample bore rises to the top of the tailstock, covering the sensor.

[1] Check calibration by dipping in a helium storage dewar if necessary, or by distantly observing the helium level in the cryostat with a flashlight.

Design changes

Several changes were made to the Octopus and particularly the sample holder after completion of the original design and manufacturing. The nosepiece was added and adopted the threaded holes intended for lateral ball rollers; the soft nosepiece required two thin stainless steel screwcaps; brass sample armor was added and adopted the holes intended for the thermal clamp (and shares a third hole with a temperature sensor mount); and the printed circuit board was added, obviating the eighteen 0.037″ holes, requiring the addition of three more on the sample holder, the grounding plate, and the machining of the sample socket.

6.4 Semirigid coaxial cables

The coaxial cable transmission lines are the same as employed in the earlier sample holder of Chapter 4: Micro-coax type "UT-141B-SS" (sourced from Amawave). The cables are termed *semi rigid* because the outer shield is a uniform stainless-steel tube ('UT') 0.141 in in diameter. The center conductor is beryllium-copper alloy; BeCu has electrical conductivity inferior to pure electrical-grade copper, but considerably lower thermal conductivity. The conductor is plated in a thin layer of silver. High-frequency electrical signals travel principally along the outer surface of the conductor (the "skin effect"), where the silver affords very low resistivity, but the thin layer amounts to minimal cross-sectional area and thus carries little heat despite the conductivity. The insulation in between the shield and center conductor is PTFE (Teflon). [2]

At about 1 m in length, the cables have a bandwidth of about 10 GHz (that is, a 10 GHz signal coupled perfectly into one end will transmit to the other with 3 dB attenuation, ie about 50% of the original power or 70% of the original voltage amplitude). These type of cables have been used for microwave and RF work since

[2]Semirigid cables are also available in other materials. Pure copper center conductors or shields are, naturally, heat pipes. Stainless steel conductors, especially in smaller diameters, have poor conductivity. Storm Products "Maximizer" cables are another option, using an expanded dielectric that may not suffer from thermal creep; they may not be hermetic and hence not intended for cryogenic use. CMR CobraFlex may also be a quite different option.

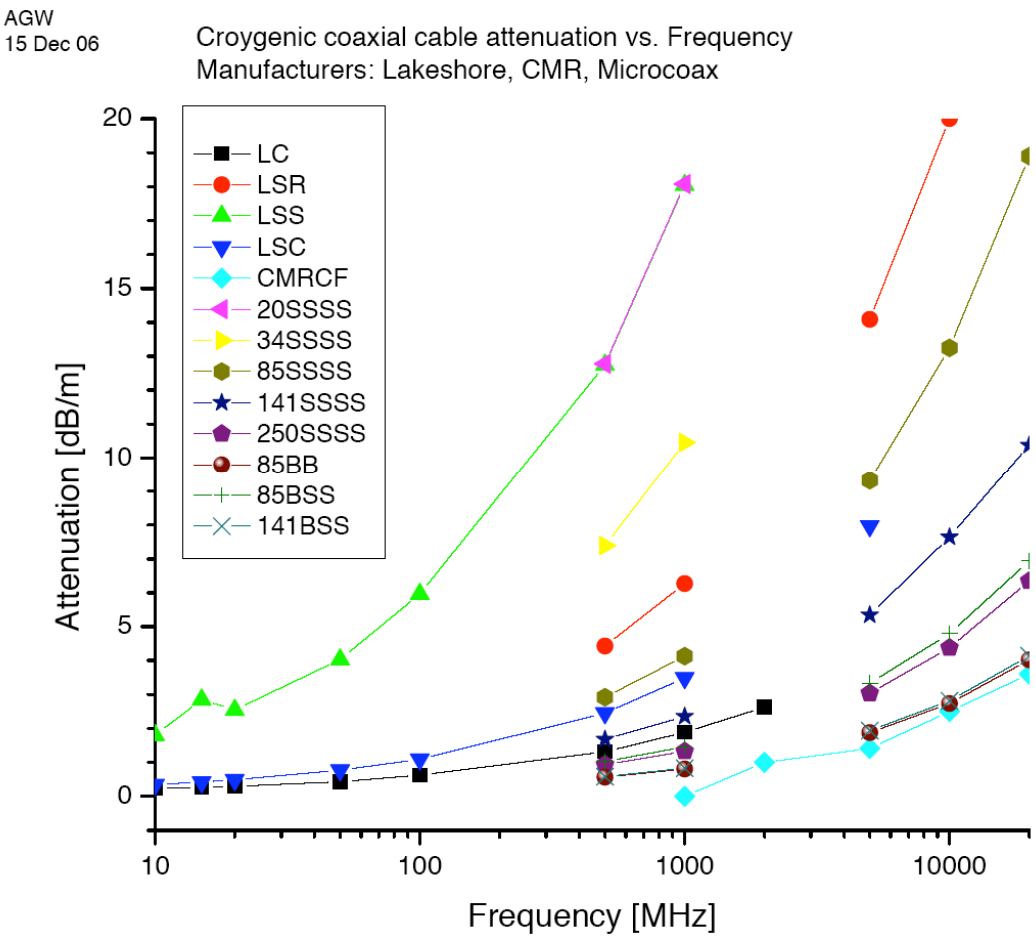

Figure 6.1: Cryogenic semi-rigid coaxial cable attenuation curves. The cables whose legend names begin with the numerical size are manufactured by Micro-coax; 'B' refers to beryllium-copper, 'SS' to stainless steel, used for inner or outer conductors. The cables used in these custom cryostat inserts are about 1 m long; UT-141B-SS was selected (whose plot symbols are barely visible and overlay the 85-B-B).

at least the 1960s, originally specified by a MIL-STD (military standard) undoubtedly for radar, and are available in variety of diameters and metals. Other common sizes are 250, 85, 34, and 20, fabricated using plain steel, plain copper, or stainless steel for either conductor, and with a variety of bandwidths and DC resistances. The 141B-SS cable selected here is among the highest performance in frequency yet with remarkably low thermal conductivity, suitable for liquid-helium cryogenics. (For comparison, in cryogenics it is customary for even simple DC wiring to be made not from ordinary copper but special low thermal-transmissibility alloys like Manganin or Phosphor Bronze.)

Safety caution

> **Caution**: the center conductor is *beryllium* copper. Beryllium dust is highly toxic to breathe, causing berylliosis.[3] **Exercise caution if it should appear at all necessary to smooth the beryllium-copper center conductor by sanding or abrasion. Do not generate toxic dust. Do not use a belt sander or file.** One might try an approach such as using sandpaper soaked in machining oil, discarding the sandpaper as toxic waste.

141B-SS and related high-performance cables may be difficult to source, and relatively expensive, for example $35/ft in five-foot lengths from a distributor.[4] Unfortunately, center conductors of stainless steel have poor electrical performance (silver-plating may improve the RF transmission carried by skin effect, but low frequencies will still be attenuated), and those of pure copper are heat pipes.

Impedence

Coaxial cables have a characteristic impedence determined by their radial geometry, $Z = 50\,\Omega$ for these as in most cables and applications; that is, the inner and outer diameters and materials have been selected such that the inductance

[4]The author recalls a conversation with the manufacturer where they stated that production runs are infrequent, perhaps several years apart, and the use of beryllium-copper adds to the manufacturing safety obstacles.

MICRO-COAX
Leading the way in transmission line solutions.

UT-141B-SS

206 Jones Blvd. Pottstown, PA 19464 USA
Phone: 610-495-0110 : 800-223-2629
www.micro-coax.com

Semi-Rigid Coaxial Cable

MECHANICAL CHARACTERISTICS

Outer Conductor Diameter, inch (mm)	0.141+/-0.001 (3.581+/-0.0254)
Dielectric Diameter, inch (mm)	0.1175 (2.985)
Center Conductor Diameter, inch (mm)	0.0359+/-0.001 (0.912+/-0.0254)
Maximum Length, feet (meters)	20 (6.1)
Minimum Inside Bend Radius, inch (mm)	0.25 (6.35)
Weight, pounds/100 ft. (kg/100 meters)	2.94 (4.37)

ELECTRICAL CHARACTERISTICS

Impedance, ohms	50+/-1.0		
Frequency Range GHz	DC-34		
Velocity of Propagation %	70		
Capacitance, pF/ft. (pF/meter)	29 (95.1)		
Typical Insertion Loss, dB/ft. (dB/meter) and Average Power Handling, Watts CW at 20 degrees Celsius and Sea level	**Frequency**	**Insertion Loss**	**Power**
	0.5 GHz	0.18 (0.58)	347.5
	1.0 GHz	0.25 (0.83)	243.9
	5.0 GHz	0.59 (1.94)	105.8
	10.0 GHz	0.86 (2.82)	73.2
	20.0 GHz	1.26 (4.14)	50.2
Corona Extinction Voltage, VRMS @ 60 Hz	1900		
Voltage Withstand, VRMS @ 60 Hz	5000		

ENVIRONMENTAL CHARACTERISTICS

Outer Conductor Integrity Temperature, Deg Celsius	250
Maximum Operating Temperature, Deg Celsius	200

MATERIALS

Outer Conductor	304 Stainless Steel
Dielectric	PTFE
Center Conductor	SPBeCu

CUTAWAY

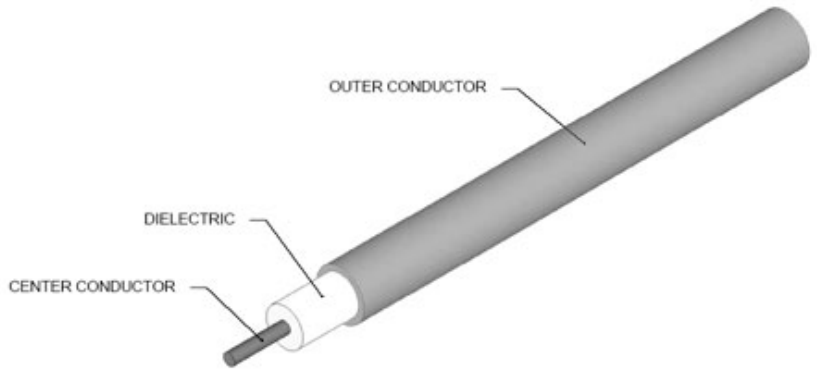

Figure 6.2: Specifications of Micro-coax semi-rigid cryogenic coaxial cable type UT-141B-SS. From [Micro-coax, Inc.]

and capacitance per unit length give an impedance independent of frequency and length. However, *attenuation* will increase with both frequency and cable length. (Also, the conductance of the insulator must be essentially zero (Teflon is excellent), and the conductance of the conductors must be very high (copper alloys and silver are excellent), and the stainless steel shield has sufficient cross-sectional area to keep the resistance low provided the cable is not too long.) Distortion or damage to the cable will cause a frequency-dependent impedance at the damage site different from the characteristic impedance, and hence signals in the transmission line will partially reflect at that site. Nonetheless, satisfactory performance may be obtained even with a slightly crimped outer shield, as may be necessary [Isaacson et al., 1980].

Procedures

Some procedures used to assemble the cryogenic coaxial cables are given in Appendix B.

6.5 Fabrication services and parts sourcing

The Octopus comprises a large number of parts, designed almost entirely in Solidworks 3D CAD, machined by UCSD MSDC (both hand and CAM milling) and personally by the author, and some welding at CRMC.

Stock material, particular components, and services were sourced from a number of vendors. Abbreviations used here:

MMC McMaster-Carr

MSC MSC Industrial Supply

Thyssenkrupp Copper and Brass Sales (of ThyssenKrupp Materials NA). Carries Hitachi "OFE-HIT" grade of oxygen-free high-purity copper C10100, 99.995% pure.

A&N A&N Corporation

Janis Janis Research Company

Lakeshore LakeShore Cryotronics

SIO MSDC UCSD Scripp Institute of Oceanography Marine Science Development Center; Ken Duff, foreman.

CRMC UCSD Campus Research Machine Shop; Don Johnson, foreman

6.6 Design practices for cryogenic mechanics

The design and construction of apparatus for cryogenics (especially liquid-helium temperatures) is a somewhat arcane branch of experimental science and engineering. A well-known reference is White and Meeson [2002], but a recent and impressively comprehensive book is Ekin [2006].[5] It only lacks a detailed description of the mechanical techniques for deploying cryogenic semi-rigid coaxial cables, for which there seem to be unfortunately few references.

This section is not intended as a broad reference to the art, but as context for some of principles that underlay the Octopus (and the first generation high speed sample insert) in particular.

6.6.1 Structural materials

The Octopus is constructed of a wide variety of materials, for cryogenic compatibility, high thermal conductivity, low thermal conductivity, corrosion resistance in a wet environment (from condensation), and sufficient hardiness to accommodate repeated scientific use, insertion and removal from the cryostat, and thermal cycling from 325 K to 1.4 K.

Thermal conductivity — deliberately high and deliberately low — is naturally of great importance in cryogenic fabrication. Thermal conductivity *among metals alone* varies by nearly four orders of magnitude at helium temperatures, and varies notably with temperature. Nonmetals are even more diverse. See Ekin [2006] for discussion, Figure 6.3, and the remarks below on copper.

[5] Recommended it in the strongest possible terms.

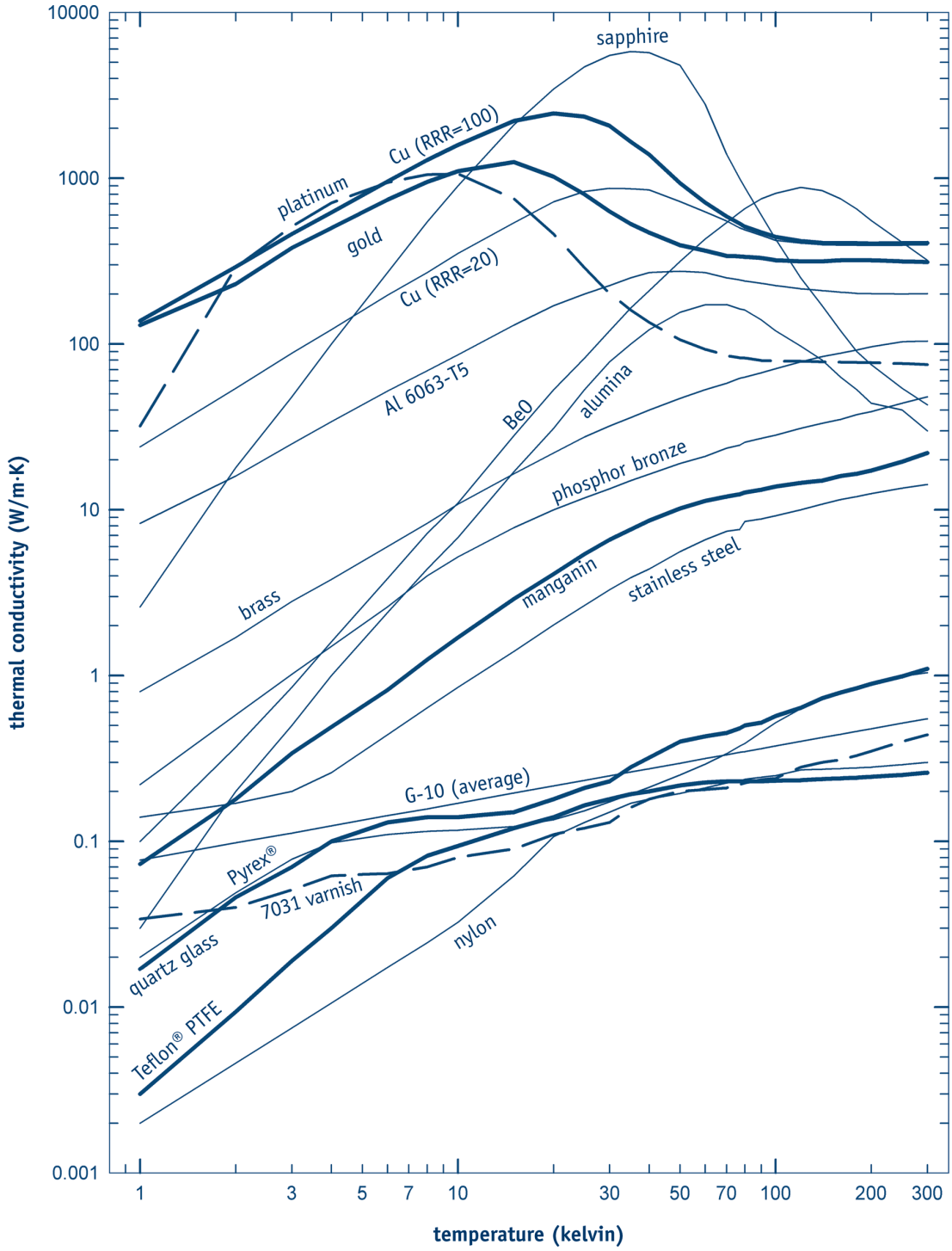

Figure 6.3: Plot of thermal conductivity of materials suitable for cryogenic use. From [Lakeshore Cryotronics, Inc.]. See also Ekin [2006].

Stainless steel Used for strength, especially when a part must be thin due to mechanical constraints; very low thermal conductivity; and is comparatively light for its strength. More expensive to machine.

Brass The easiest and hence cheapest material to machine, brass is heavy, comparatively weak, does not corrode in ordinary application, and used where its weight permits. Cleaned (deoxidized) in mineral acid solution.

Copper , oxygen-free high purity electronic-grade, alloy C10100. This form of OFHC copper has by far the highest thermal conductivity of the machinable metals, and is indispensable for that reason. It is melted in a nonoxygen atmosphere, and can be difficult to source. For this work we obtained Hitachi "OFE-HIT", discussed briefly in Section 6.5.

At very low temperatures, in the absence of phonons, thermal conductivity is governed mainly by electron mean free path; very slight impurities cause scattering. In such regimes, copper purity is measured mainly by "RRR" *Residual Resistance Ratio*, the ratio of electrical resistance at $T = 4\,\mathrm{K}$ to that at $T = 300\,\mathrm{K}$. (Sometimes $T = 77\,\mathrm{K}$ is used, perhaps if the supplier does not have access to liquid helium cryogenics.) The thermal conductivity is strongly dependent on impurities, and may not be specified by the vendor, perhaps because the main commercial use is not cryogenics but ultra-low electrical resistance for electrical power applications.

It is soft, lacks strength, and is difficult and somewhat costly to machine on account of its "stickiness" and the probability of machining failure (usually fatal to the part), a contingency which a shop must reserve against in bidding. Best machined with very sharp tooling and extensive lubrication. Tapped threads are avoided whenever possible, both because of the cost and because the threads are weak and may fail during use.

The surface of high-purity copper oxidizes easily, especially when heated; this, plus the high thermal conductivity, makes soldering very difficult. Before final assembly, and especially before assembling a thermal joint, all high-purity copper was cleaned (in addition to acetone and alcohol) with mineral

acids, to remove the oxide layers.

Teflon PTFE Teflon is a machineable plastic, occasionally useful as a contact material because its thermal conductivity is extremely low, and its slippery smooth surface will avoid damage to other materials on contact. It is very nearly inert, and machining oils and residue — embedded during the maching process — can be removed by cleaning in strong mineral acids. Has a very large coefficient of thermal expansion.

Aluminum Conspicuously *not* used anywhere on the Octopus. Although the default metal for many purposes because it is inexpensive, light, and relatively easy to machine, unanodized aluminum tends to corrode when placed in contact with other metals in the presence of damp (as with condensation on cryogenic equipment). Its thermal conductivity is undesirably high or low for many cryogenic structural uses. Similar remarks apply to plain (non-stainless) steel.

6.6.2 Soft materials for thermal or electrical joints

Various soft materials can be used when joining cryogenic components.

Indium foil Good thermal and electrical conductivity, but thermal conductivity at cryogenic temperatures requires sufficient clamping pressure to effect a cold weld. See Ekin [2006].

Apiezon-N grease Good thermal conductivity, comparable to indium; electrically insulating.

Colloidal silver paste Thermally and electrically conductive, also adhesive and may be difficult to remove without solvents. Thermal conductivity at a joint probably much poorer than cold-welded indium.

Stycast epoxy Strongly adhesive and insulating.

GE (IMI) 7031 varnish Adhesive and insulating. Sourced from Lakeshore.

6.6.3 Solvents and surface preparation

Metal parts can be cleaned effectively by soaking in acetone, followed by deionized water. Any of the alcohols can be used afterwards to remove remaining water.

Brass and copper can be effectively cleaned and their surface deoxidized by immersing in a solution of 25% nitric acid and 25% sulfuric acid, with the balance distilled water. Immersion may need to be brief to avoid surface pitting, or the acid mixture further diluted. Different strengths may be needed for raw metal stock vs. freshly deoxidizing an already-prepared surface.

6.6.4 Mechanical connections

Cryogenic equipment is subject to repeated thermal cycling from 300 K to 1.4 K. Differential thermal expansion and contraction works joints loose, e.g. screw threads, and either loosens or tightens machine screws by changing the relative length of the screw and the material it traverses.

Choice of metals

For metals, increasing thermal coefficient of expansion runs A-B-C-S-SS:

1. Aluminum
2. Brass
3. Copper
4. Steel
5. Stainless Steel

When choosing material for a screwed joint, the key is to use a machine screw made from a material which will shrink *more* than the material it joins. Since aluminum is rarely used at all, copper is too weak for screw applications, and plain steel is subject to rust, the preference is to use *brass* screws. (In the case of joining purely brass parts, it might be advisable to use aluminum screws, and replace them regularly.)

Threading

When bolting or screwing parts together, female threaded (tapped) holes are avoided where possible in favor of through-bolted connections with a machine nut. Threaded holes in stainless steel would be acceptable, but there are none in the Octopus (except the shaft collars); where threaded holes have unavoidably had to be used due to geometry or clearance constraints, the threads are, unfortunately, in extremely soft pure copper. Generally, brass screws are used (satisfying the differential thermal shrinkage constraint) and the soft brass — although stronger than soft copper — somewhat retards the onset of thread damage. Great care should be taken not to over-torque the fastener; regrettably, no torque wrench was used, so torque will have to be judged by long mechanical experience. Nuts are generally brass or stainless steel, and use a lock washer (generally split-ring, although the conical type would be preferable) to reduce the loosening of the fastener by rotation, especially as induced by thermal cycling. The lockwashers will likely not be springy at all at 1.4 K, however, so whenever the Octopus is removed from the cryostat and accessible for servicing, all the threaded joints should be checked for tightness. Split-ring lockwashers are usually available only in stainless steel, and the sharp edge swiftly damages a copper or brass surface, so the lockwashers are backed by flat washers (generally brass) in all cases (except possibly a few where total fastener stack length is constrained and the washer thickness must be avoided).

6.7 Coping with coaxial cable shrinkage

An unexpected challenge was continued mechanical migration within the cryogenic coaxial cables over dozens of thermal cycles. Differential expansion and contraction of the dielectric caused the center conductors to retract from within the top (outer) SMA female connector, and extrusion of the dielectric and conductor at the bottom. The center conductor retraction alters the SMA geometry, degrading the RF conductivity or disconnecting entirely. (It is possible that this problem could be avoided by judicious crimping of the semirigid coax, according to Isaacson

et al. [1980].)

Conductivity was restored by fabricating semicustom SMA "adapters" to match the cable shrinkage. Length of brass hex stock were drilled and tapped with the SMA thread, and screwed onto the semirigid cable's terminating bulkhead female bulkhead connector. The conductor retraction at each time was precisely measured using depth micrometers, and compensating lengths of appropriate diameter wire cut; the diameters and tips require careful sanding to ensure a smooth fit into both SMA sockets. An additional SMA female–female barrel connector was then threaded into the brass stock. Although the compensating pins are not encapsulated in dielectric, at least much of the SMA geometry is preserved.

6.8 Network analyzer S_{11} reflection measurements

Since RF conductivity is not a simple matter of open/closed circuit or DC conductivity, the connector can be diagnosed and the performance of the repair measured by using a vector network analyzer (VNA), especially using simulated time-delay reflectometry (TDR). A measure of the results can be seen in Figure 6.4.

Many other measurements were made with several different vector network analyzers, spanning the frequency range of KHz to several GHz. VNA calibration quality is essential for accurate measurements, as well as attention to the sweep properties when measuring over wide frequency spans and several meters of cabling. A portion of this data is illustrated in Figure 6.5. The vector network analyzer is an essential tool for RF systems fabrication, diagnosis, test, and characterization.

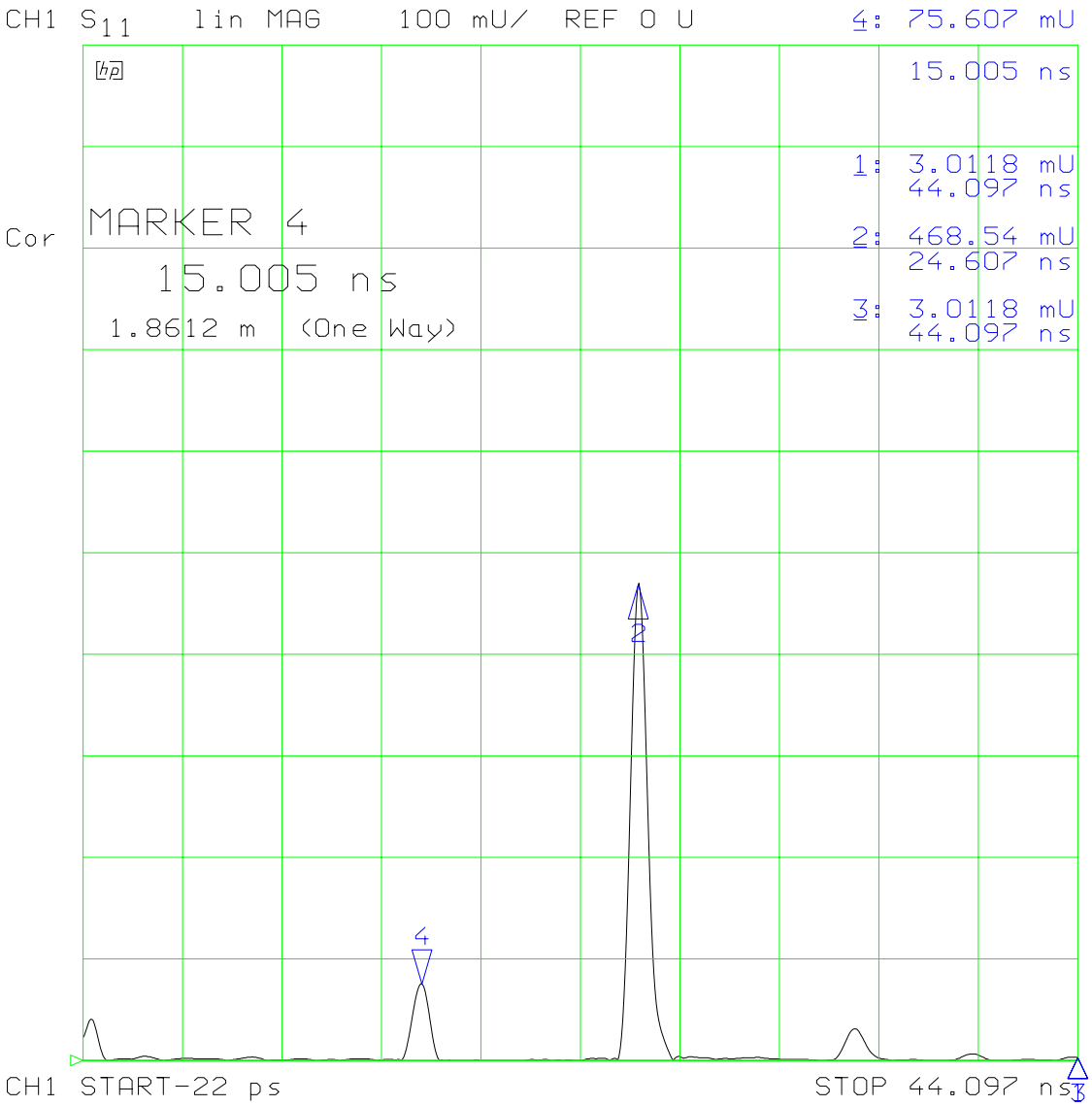

Figure 6.4: VNA S_{11} measurements as a synthetic Time-Delayed Reflectometry (TDR), looking into the Octopus wiring to a single channel, with a sample in place. The horizontal axis is time, about 4.4 ns per graticule square, and the vertical axis is S_{11} reflections in linear magnitude (%). Visible at point #4, about 15 ns from the VNA input (and 1.86 m, away, with the VNA calibrated to the $0.86c$ velocity of the LMR-240UF), is a small reflection of about 7.5%; this corresponds to the semicustom SMA connectors described in the text. At point #2, about 24.6 ns away, is a larger reflection of about 47%; this corresponds to the end of the cryogenic coaxial cabling at the sample, and illustrates how the sample capacitive loading (plus other parasitic effects) have altered the $Z = (50 + 0j)\,\Omega$ termination at the sample.

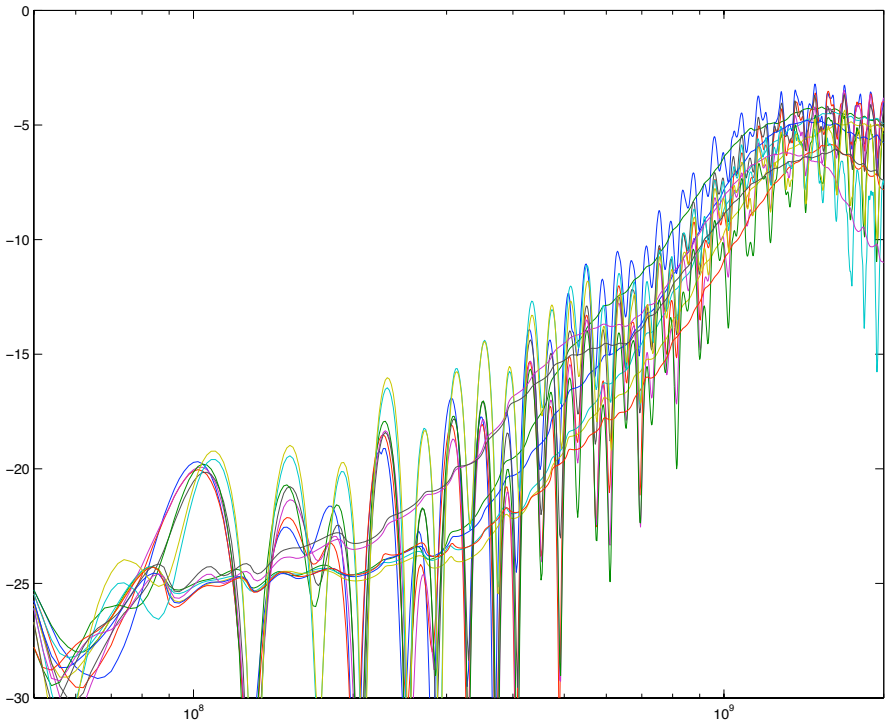

Figure 6.5: VNA S_{11} curves, looking into all seven Octopus channels, with a sample in place (at cryogenic temperatures). The horizontal axis is frequency in Hz (from 50 MHz to 2 GHz), and the vertical is S_{11} magnitude of reflection in dB. The seven channels are plotted simultaneously, first as raw data (large periodic oscillations), and again with strong smoothing to remove much of the visual effect of phase–looping. Reflections remain below -20 dB until ∼300 MHz, and below -10 dB until closer to 1 GHz. (The VNA calibration is questionable above 2 GHz, given the calibration standards available.)
The plot illustrates the rich complexity of the sensitive VNA measurements, which can be used to measure the total loading impedance at the end of each channel, and, in principle, to gain insight into the effective circuit components present at the end of the cryogenic coaxial cables (both parasitic reactances in the Octopus wiring and the capacitive effect of the sample itself.)

Chapter 7

Octopus components

Contents

Screw sizes

A variety of small screw sizes were used throughout the Octopus. The correct screw for a given hole can be deduced from the diameter of the hole given on the relevant machine drawing and consulting a table of standard hole diameters for small machine screws. Typically, coarse thread was used, and typically the even screw numbers. #4-40 is particularly common, but sizes down to #0-80 were used.

Janis machine drawings

Janis proprietary machine drawings are not reproduced in this work, but Table 7.1 lists a number of Janis drawings that may be useful for illustrating how the Octopus fits into the cryostat.

Table 7.1: Selected relevant Janis machine drawing numbers and description. Note that Janis's title may not be identical to the Octopus's part's names.

Drawing #	*Janis title*	Description
A28-0024	"3.0 nom ladish (16AMP)"	Illustrates a ladish blank plate
A11-0034	"3.0 nom crown for 2.50 sample tube"	Ladish flange cross-section
A44-0019	"Universal header"	Typical Janis crown design; specifically illustrates feedthrough-plate mounting dimensions
	Specifically intended for the SVT-300, job #8705	
Drawing #	*Janis title*	Description
D02-05-04		Overall cross-section of SVT-300
14885	"Sample tube"	Lower square-bore cross-section
Sub-assembly #S-8705-B		Sample rod assembly, showing heat-shield and concentric spacer vertical locations
A55-V3	"Control knob"	
A55-V4	"Control rod"	Seals the upper end of the sample rod and mounts the control knob
A05-0006	"Concentricity spacer"	
A02-0007	"Baffle"	Copper heat shields
A47-0007	"Sample rod end screw"	Seals lower end of the sample rod
A39-0014	"Sample mount"	Original, minimalist mounting point

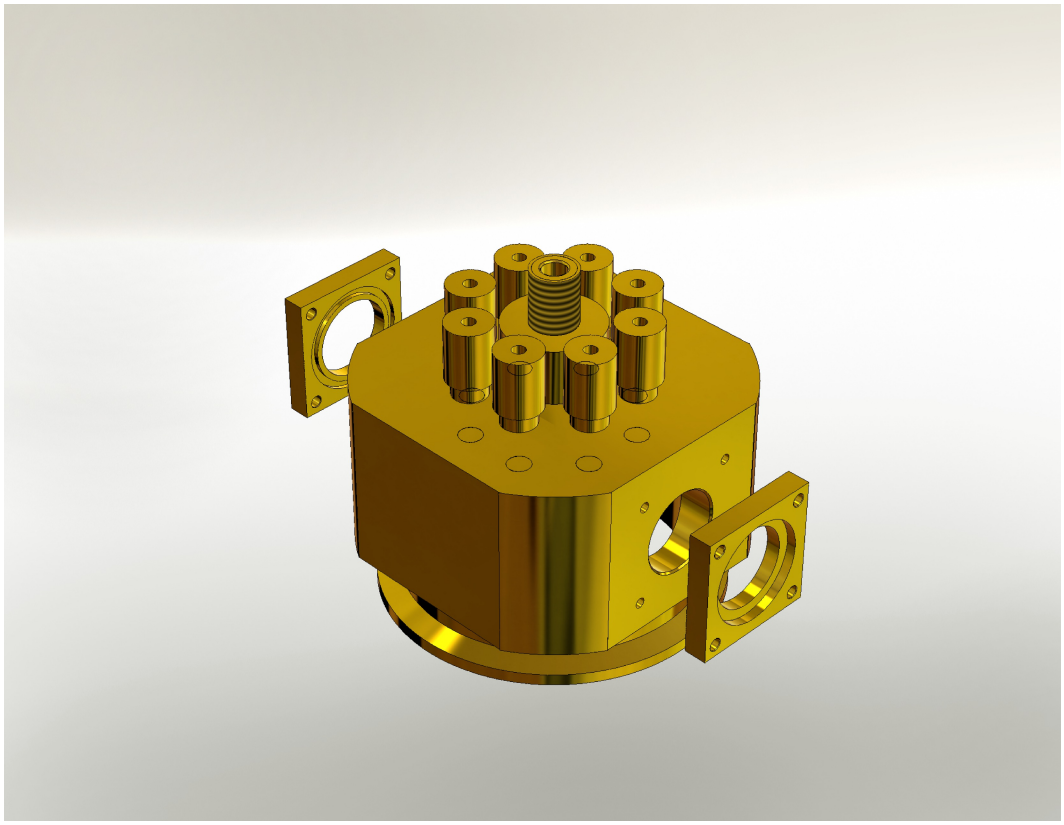

Figure 7.1: assembledcrown

7.1 Crown/Head section

The head of the Octopus, built around the crown proper, sits at the top of the cryostat bore and provides the external vacuum seals and feedthroughs to the outside world.

Crown Machined from a single large lump of brass, the heavy crown is the second-most expensive component of the Octopus by machining time. It is intended to mimic the (much smaller and simpler) Janis crown by mounting to the cryostat sample bore with a ladish flange seal, and providing a 1/4-inch cylindrical vacuum feedthrough for the main shaft and side plates with vacuum feedthroughs for DC wiring.

The crown is a near duplicate of the crown built for the first generation high-speed sample insert, which the author designed on paper and entirely

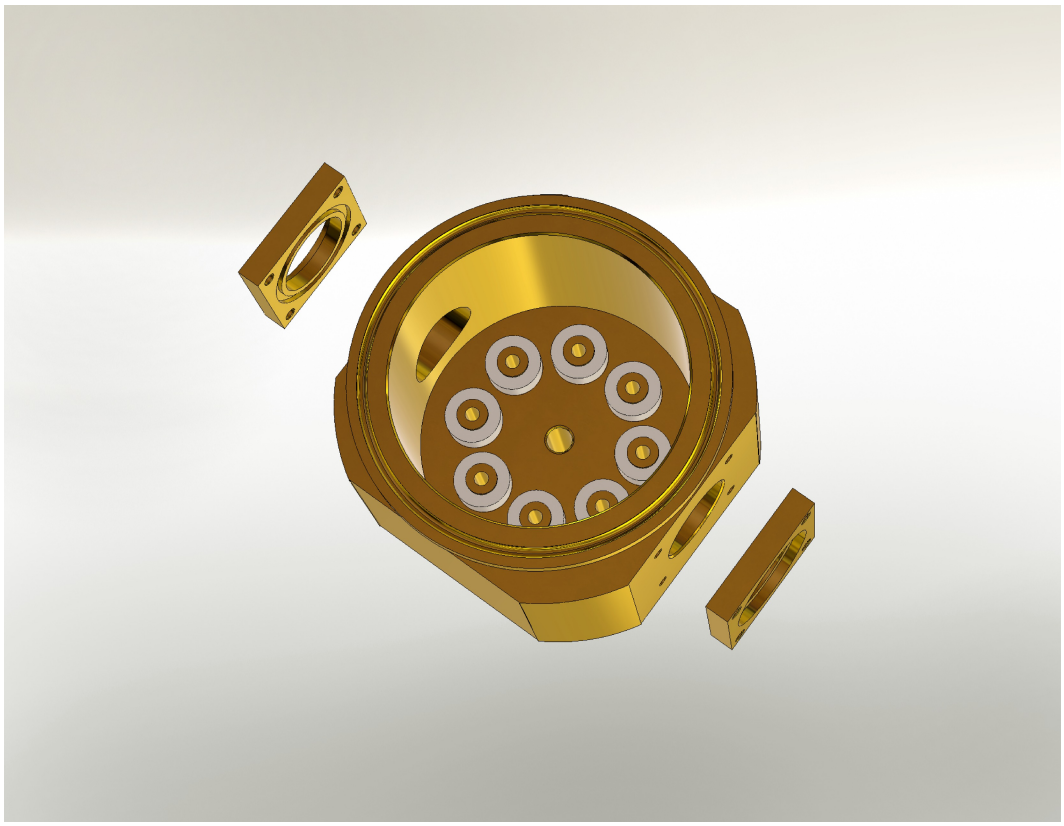

Figure 7.2: assembledcrown-reverse

personally machined over the course of two weeks. (The first iteration was in aluminum, and suffered damage before completion.) The crown on the Octopus was rendered into SolidWorks CAD for external fabrication, and differs from the first generation version mainly in the eight holes provided at the top for the semi-rigid coaxial cable feedthroughs.

The vacuum flange is a "ladish" or "sanitary" flange, employed by Janis for historical reasons (the basic Janis cryostat design may be decades old, and the flange is purportedly found in e.g. brewpubs), and is based on an o-ring gland of circular cross section (although trapezoidal approximation with steep 20° walls, 55 thou deep, 100 thou wide was used successfully in the first generation insert); o-rings and the ladish clamp were sourced from Janis. (Janis drawing #A11-0034 illustrates the groove design; it specifies a 105 thou thick edge, but that was slightly loose in the clamp, and indeed Janis's actual part was closer to 115 thou; 120 thou was used on the first generation insert crown, with superior sealing, and the Octopus crown drawings specify 126 thou.)

The main shaft feedthrough is half-integral to the crown: the external threads are 1/2-20, and the cap (i.e., nut) is from A&N #B-25-K.

Machining details: the crown (the one hand-machined by the author) begins as a single lump of brass, turned first on the lathe to make the 1 in stub, and then reversed and the interior bored out; the part is held by four-jaw chuck after it is thus sufficiently lightened, and then can be mounted by the 1 in colleting stub and turned between centers with a large live center in the lower opening. Finishing work is done on the mill. The peculiar mix of round and square in the outer diameters was designed to accommodate several goals: lightening the part as much as possible, boring out the interior diameter as widely as possible to give maximum room for the coaxial cables, maintaining sufficient wall thickness, and providing square flats to securely clamp the part for milling (the aluminum prototype was lost at this stage). Particular attention was given to planning the exact order of machining steps (since clamping is difficult), and the overall design was partly driven by the desire

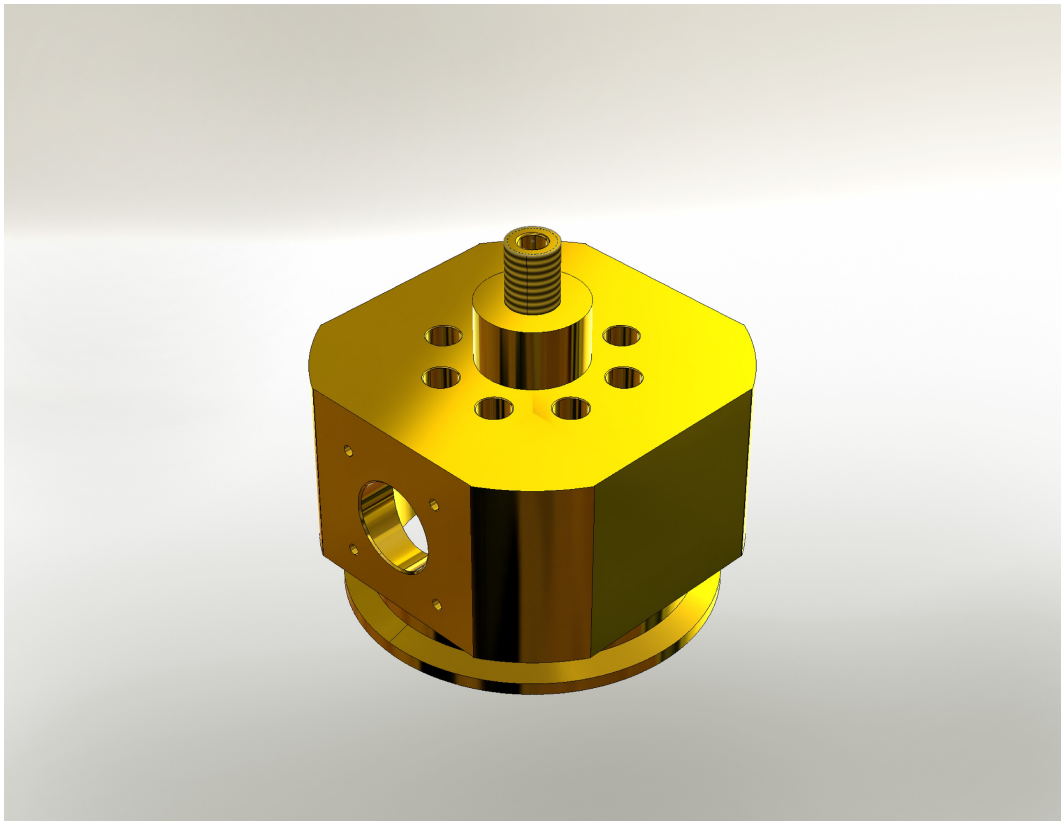

Figure 7.3: fullcrown

to make the the part in a single piece to reduce the number of vacuum joints.

Side feedthrough plates The side plates mount vacuum-sealed multi-pin DC wiring feedthroughs. This is an old type of Amphenol vacuum wiring feedthough (probably a MIL-STD from the 1960s), but is preserved for compatibility with our lab's existing electronics accessories. The 8-pin is dedicated for four-wire measurements of the diode temperature sensor, and the 32-pin for all other uses. (Detoronics #DT1H-12-8 and #DT1H-18-32, sourceable from Janis or Connector Technology, Inc.) The plates have the same outer dimensions and bolt pattern as the original Janis plates, but are not compatible in that the interior o-ring gland is placed on the plates, not the crown; this was done to reduce the number of critical machining steps on the crown (thus vulnerability).

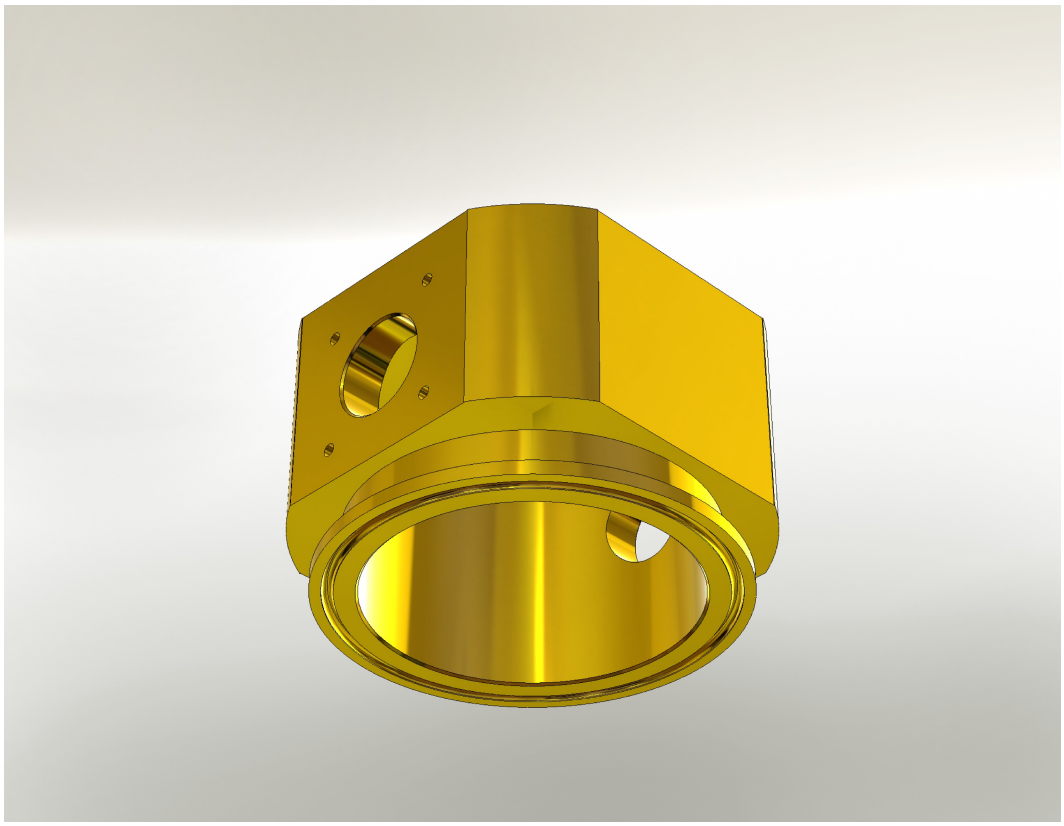

Figure 7.4: fullcrown-reverse

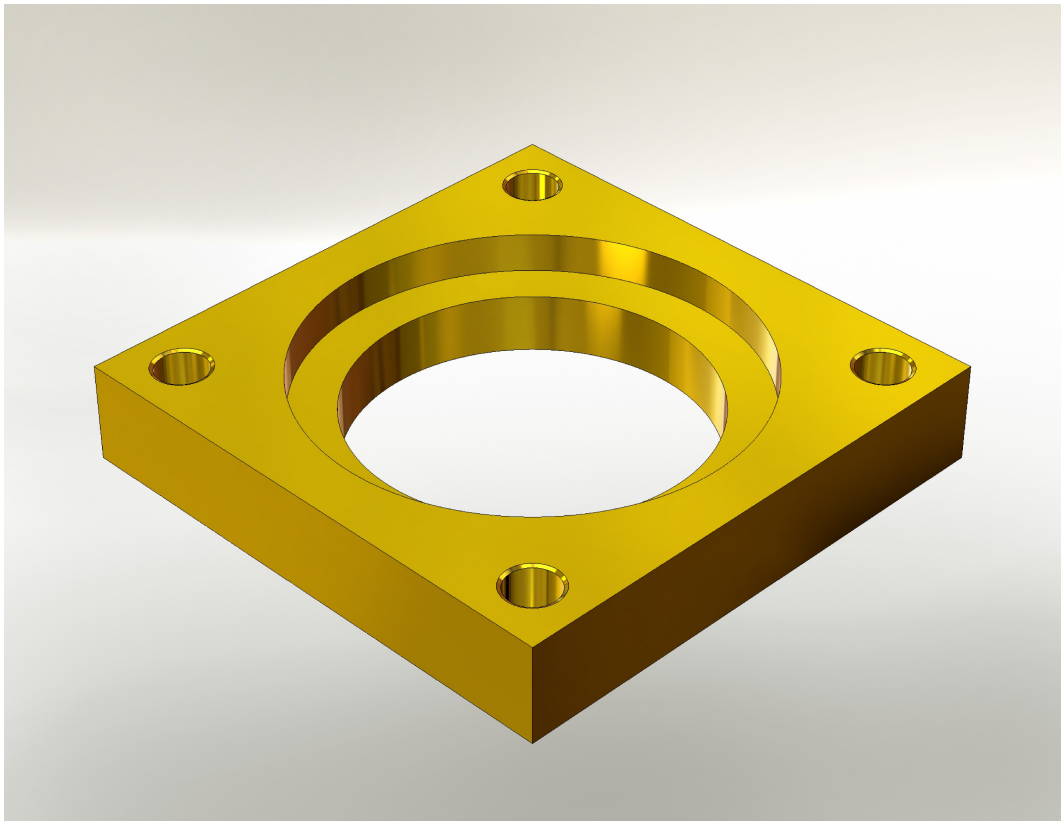

Figure 7.5: sideplate-bigfeedthrough

Machining details: milled from solid brass, the o-ring grooves were made with a ball endmill, and the stepped feedthrough openings by trepanning. The Amphenol feedthroughs were soldered to the plates on a hotplate.

Coaxial cable vacuum feedthroughs The feedthroughs for the 0.141″ semi-rigid coaxial cable were made from an A&N B-12-KM2, heavily modified. The interior is bored wider to accommodate the 0.141″ coax instead of the designed 1/8 tube. The feedthroughs mount through the clear-drilled holes in the top of the crown, and are held in place by compression with a heavy 5/16-24 brass nut and stainless-steel split-ring washers (backed by flat washers, so as not to damage the interior surface of the brass crown); the nuts tighten on external die-cut threads. The feedthroughs vacuum seal to the crown via a *radial* o-ring gland (for 1/16″-diameter o-ring), milled in the feedthrough wall, whose compression should be largely unaffected by the

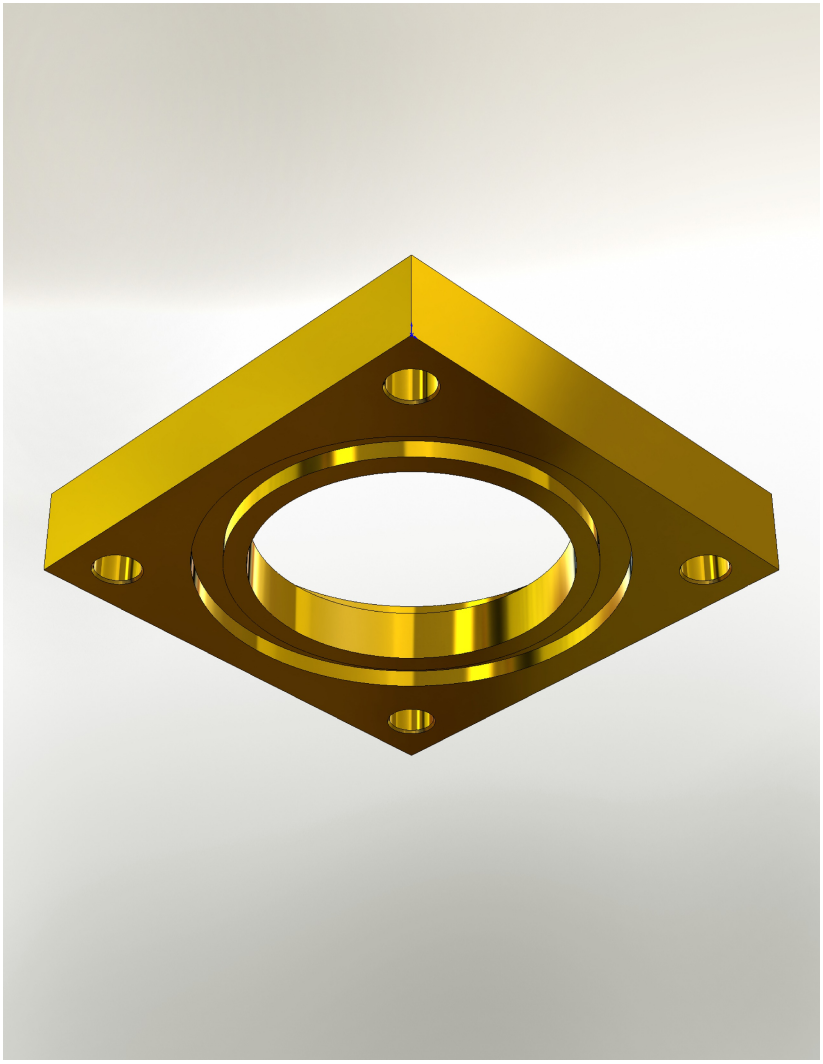

Figure 7.6: sideplate-bigfeedthrough-reversed

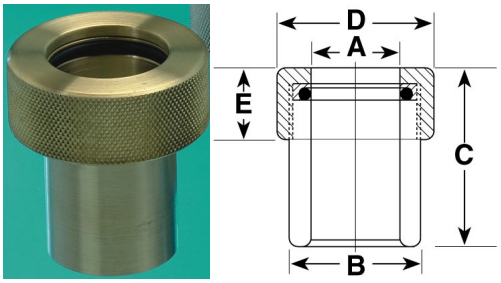

(a) (b)

Figure 7.7: A&N vacuum quickdisconnect #B-12-KM2 before modification (photograph (a) may not correspond to this precise part number). Interior dimension $\mathbf{A} = 0.136''$, intended for $1/8''$ tubing.

nut+lockwasher+thread force. The coaxial cables vacuum seal at the top of the feedthroughs by an o-ring face seal, as stock, with the o-ring inner diameter stretching slightly to accommodate the larger ($0.141''$) cable.

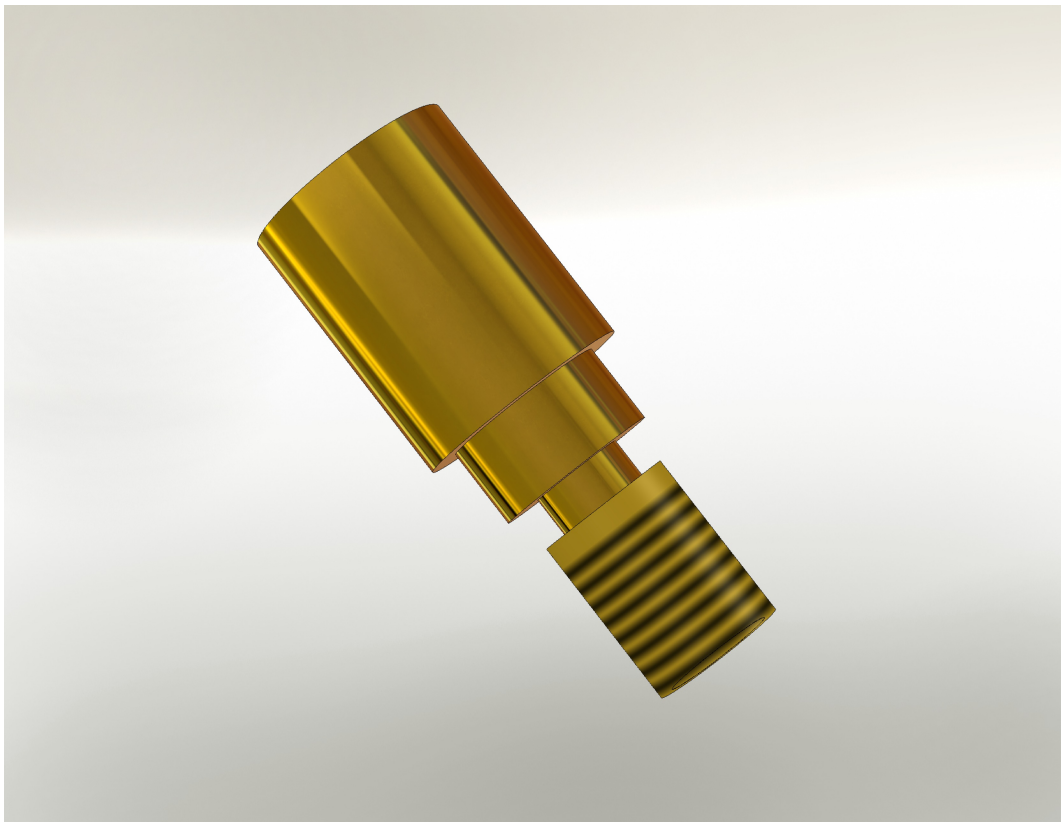

Figure 7.8: quickdisconnect-improved

7.2 Shaft

The shaft assembly is those components between the crown assembly at the top of the cryostat, at 300 K, and the tail assembly at the bottom of the cryostat at 1.4 K. It comprises the central support shaft with endpieces, heat shields, and several concentric metal spacers that serve to route the semi-rigid coaxial cables between their bunched rectangular alignment at the tail and a circular, spaced-apart alignment at the crown. This change in alignment occurs over about 1 m of travel, to minimize the cable bend angles, and to make it possible to move the entire sample insert assembly, below the crown, up or down vertically by approximately half an inch. This vertical travel is necessary to permit aligning different portions of physics samples with the approximate center of the cryostat window.

Main shaft The main shaft is stainless steel structural tubing, 1/4-inch outer diameter, thin wall (0.020″), providing the structural centerpiece and minimizing heat flow from the 300 K section to the 1.4 K section. McMaster #9773T113 (Extra-Hard Type 304 SS Seamless Tubing, 6 ft, cut to length).

Upper shaft tip The upper shaft tip vacuum seals the main shaft outside the cryostat, and provides the mount point for the rotator knob. Turned from stainless steel, and the setscrew flat milled, the tip was welded to the main shaft. The welding was done by CRMC, and the bead sanded flat afterwards, so that the various concentric parts later tightly mounted to the mainshaft can clear the tip-shaft joint.

Lower shaft tip The lower shaft tip follows Janis's original equivalent part. It is turned from a stainless steel machine screw, and welded to the mainshaft by CRMC, with the same attention given to the weld bead.

Adjusting knob A simple knob on the mainshaft for manual rotation of the entire Octopus below the crown assembly, the knob is turned from brass, knurled on the outside for grip, drilled with a blind hole to fit the upper shaft tip and shaft, and drilled for a setscrew to secure the knob against the upper shat tip.

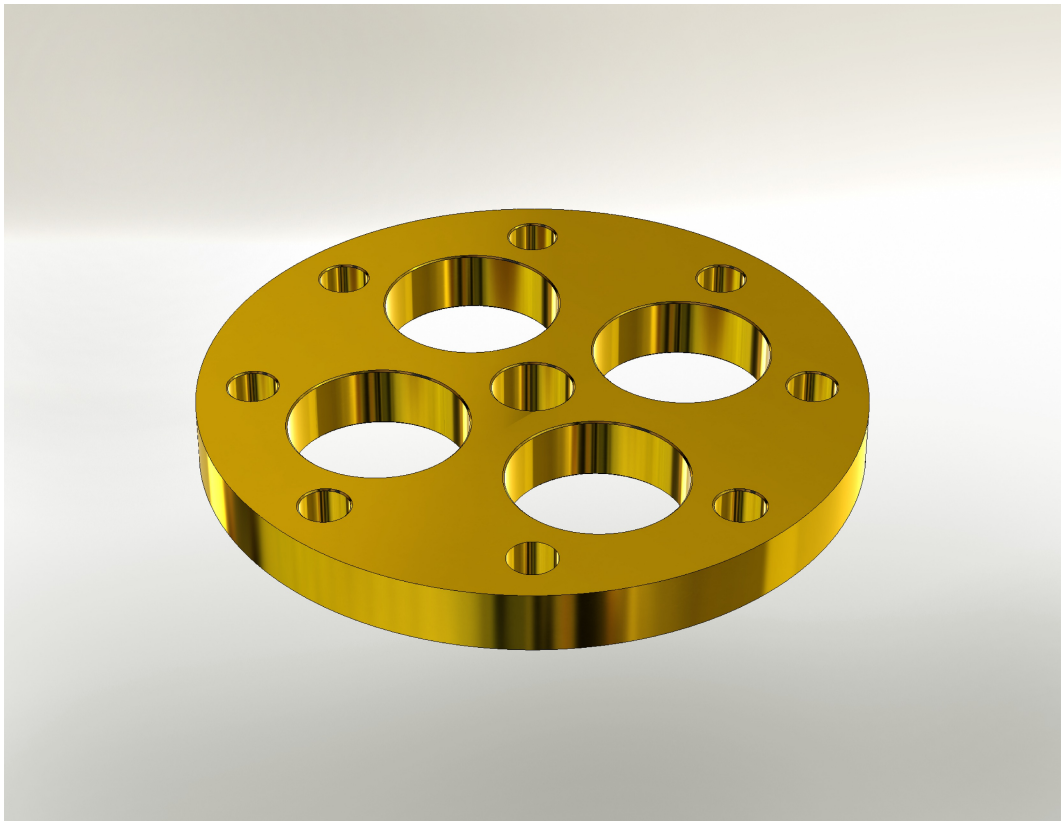

Figure 7.9: uppercablespacer

Upper cable spacer Milled from solid brass, the upper cable spacer forces the coaxial cables from their intermediate skewed orientation into their final circular orientation into the crown assembly; it insures that the cables travel straight through the cable feedthroughs, keeping lateral pressure off the feedthrough nuts and o-rings. This reduces the opportunity for leaks at the vacuum feedthroughs. It permits a small amount of vertical travel (perhaps 1/4 in at this bend before excessive side-loading.

Lower cable spacer The lower cable spacer is similar to the upper cable spacer, but is drilled for the compressed-rectangular (rather than wide-circular) cable pattern. It forces the coaxial cables form their intermediate skewed orientation into the compressed rectangular pattern. It permits a small amount of vertical travel (perhaps 1/4 in at this bend before excessive side-loading. The spacer is held to the main shaft by two setscrews spaced 120 ° apart; the

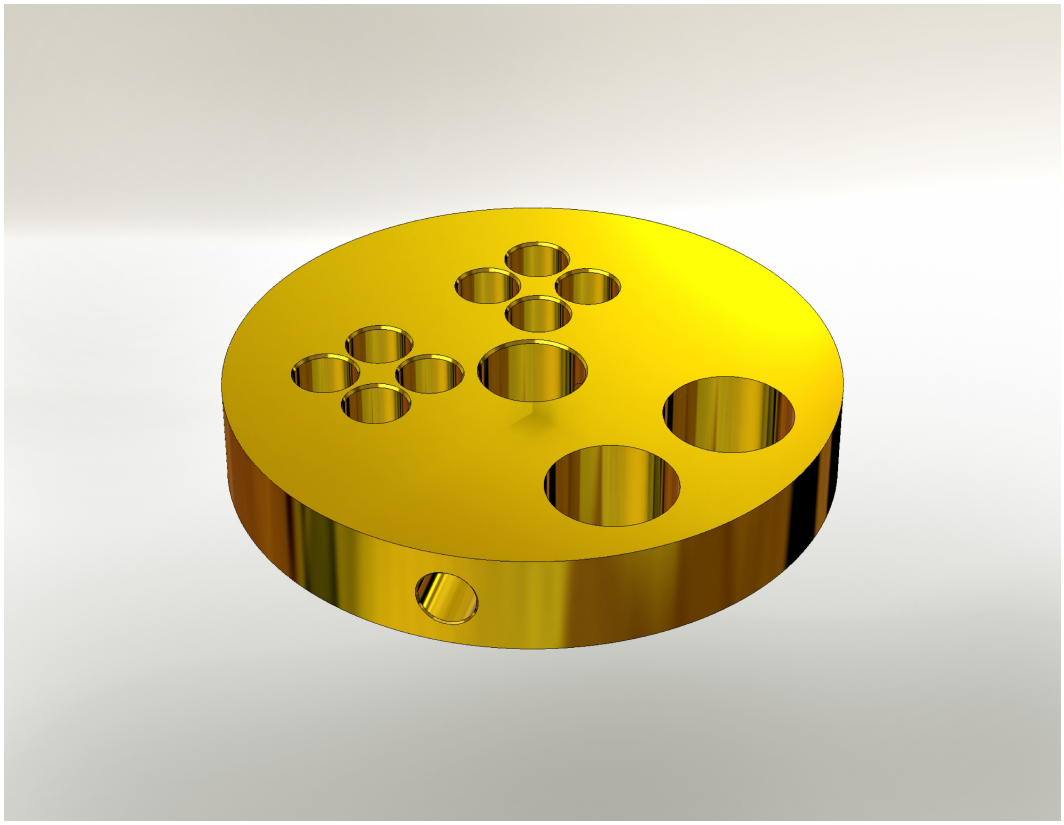

Figure 7.10: lowercablespacer

stainless-steel setscrews are nylon-tipped to prevent scarring the main shaft.

Concentric spacer The concentric spacer's chief role is to ensure that the entire sample insert assembly is concentric with the circular cryostat bore, so that the tail assembly, which is approximately square in cross section, is aligned to successfully insert into the lower nearly-square cryostat sample area bore. This part is derived from an analogous Janis part, but quite different. The original Janis concentric spacer used a set of flexible springy beryllium-copper "fingers", braised to the copper spacer, to make somewhat elastic contact with the inner cryostat bore. It was preferable to not to need to machine beryllium copper springs, so an alternative is employed: the spacer has four radial tapped holes, 90° apart, in which are threaded ball spring plungers. Originally, Janis suggested using stainless steel plungers, but

we found in operation that the stainless steel balls (MSC #85508224) tended to gall the stainless steel interior of the cryostat bore. Neither brass- nor Teflon-balled plungers were readily available (possibly only with (unacceptable) carbon steel bodies), so nylon-balled, stainless-steel bodied plungers (MSC #06694327) are employed. The nylon balls wear rather quickly (the balls develop flats, and evidently begin to slide rather than roll), and the plungers ought to be replaced. The plunger depth is adjusted by screwing the threaded body within the threaded hole, using a special wrench (MSC #65218935), and the exact depth is critical to obtain the correct spacing of the plunger (and hence concentric spacer) to the cryostat bore. Although the plungers were sized to obtain the largest travel possible, the total travel is only 35 thou; if the design nominal compression is 50%, there is only 17 thou of travel in each direction, and it is evident that even 10 thou mis-adjustment depth is a significant error. If screwed in too deeply to the spacer, a plunger may not make contact with the cryostat bore causing the whole Octopus to be misaligned in the upper bore and thus fail to enter the lower bore. If screwed in too little, as the Octopus is lowered into the cryostat there is excessive resistance to inserting the spacer into either the top of the cryostat bore tube or past the weld joints of the bore tube some distance down. The correct depth is obtained by considerable trial and error, and measured with a depth gage against the spacer, however as the nylon balls wear the plungers need to be screwed out to restore adequate contact. All four plungers should be set and measured uniformly, and "eyeballed" in side profile to observe geometry. Satisfactory performance was obtained after considerable experimentation. Careless usage, if the Octopus can be inserted successfully at all, will result in nylon dust being deposited on the bottom of the cryostat, possibly on the windows or carried there by the liquid helium.

The concentric spacer also has drilled through-holes for the coaxial cables in the compressed rectangular pattern, plus additional large diameter holes to lighten the mass. The spacer is made from OFHC 101 Copper, and in operation liquid helium may fill the cryostat sample space as high as the

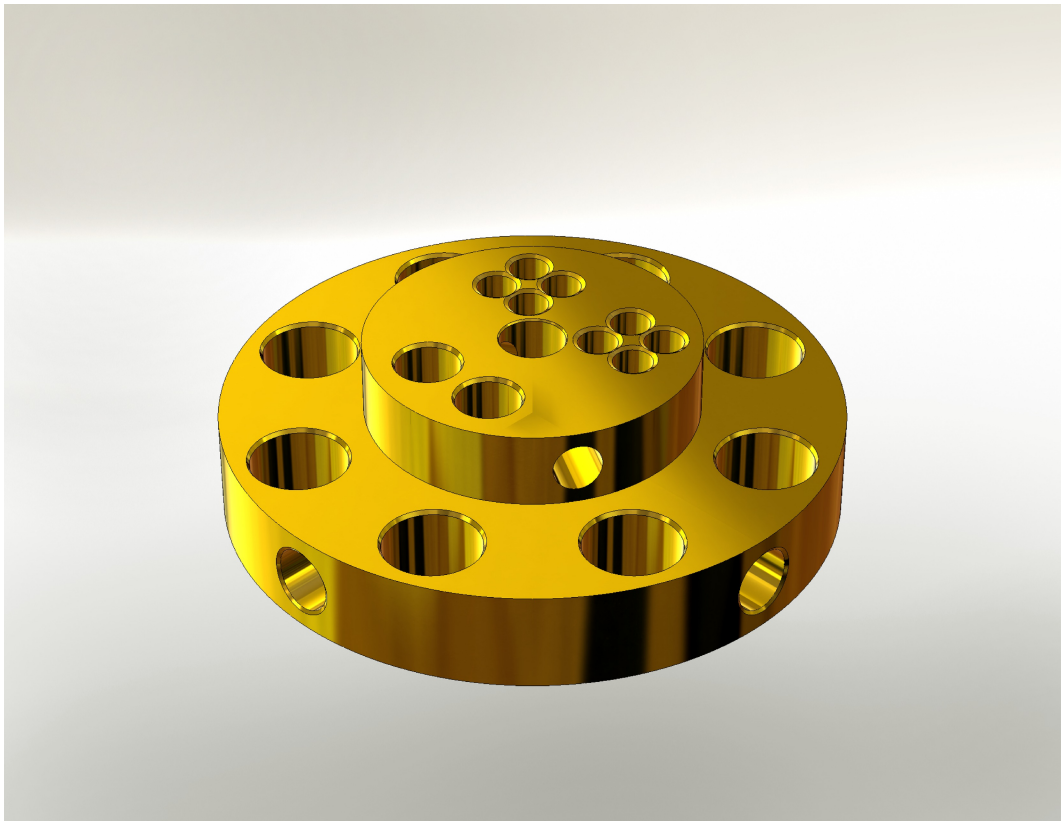

Figure 7.11: concentricity-spacer

level of the spacer. The spacer is held to the main shaft by two setscrews spaced 120° apart; the stainless-steel setscrews are nylon-tipped to prevent scarring the main shaft.

Heat shields The heat shields reduce the flow of heat down the cryostat bore, by blocking the optical path from the ≈300 K crown to the 1.4 K liquid helium bath. They are made from OFHC 101 Copper sheet (McMaster #2545T51, 0.062″), and are slightly smaller in diameter than the cryostat spacer. Helium vapor evaporates from the sample space into near vacuum, but its free upward rise is blocked by the heat shields, and so the vapor is constrained to flow along the surfaces of the heat shields before slipping over the edges or through the holes, cooling the shield en route. This reduces the cryostat helium consumption rate.

There are several heat shields in operation, drilled with through-holes for the coaxial cables in either the compressed-rectangular or wide-circular hole patterns, plus several small holes to accommodate DC wiring. The upper heat shields are held in position by shaft collars, but for the lower shield the compressed-rectangular pattern of the coaxial cables overlaps the relevant diameter, so those shields are held, loosely, by Viton rubber o-rings. Care should be taken not to nick them, but several duplicate o-rings are slipped onto the shaft above and below the spacer, so that if one breaks, the entire shaft assembly need not be disassembled.

The original Janis shields are nickel-plated[1] When the Octopus underwent final assembly before moving into the cryostat, the heat shields were briefly acid-bathed to remove the copper oxidation and present fresh, shiny surfaces.[2]

Shaft collars The upper heat shields and upper cable spacer are held in position on the main shaft by stainless-steel shaft collars (MSC #87991030). Originally, single-piece split-round collars that clamp with a single screw were tried (and used on the first insert), but they needed to be mechanically forced open at the workbench to loosen the central bore enough to slide them over the main shaft, and then required considerable torque on the screw to clamp the bore sufficiently tightly. After thermally cycling the Octopus, the collars tended to work loose. The original collars were replaced with double-horseshoe shaped collars that clamp via two screws. Care should be taken to tighten the screws symmetrically, otherwise an apparently-tight clamp during assembly room temperature tends to work loose after thermal cycling.

[1] Possibly more out of tradition than thermal necessity.

[2] It might be advisable to deoxidize these surfaces again whenever the Octopus is disassembled and the shields accessible on the shaft.

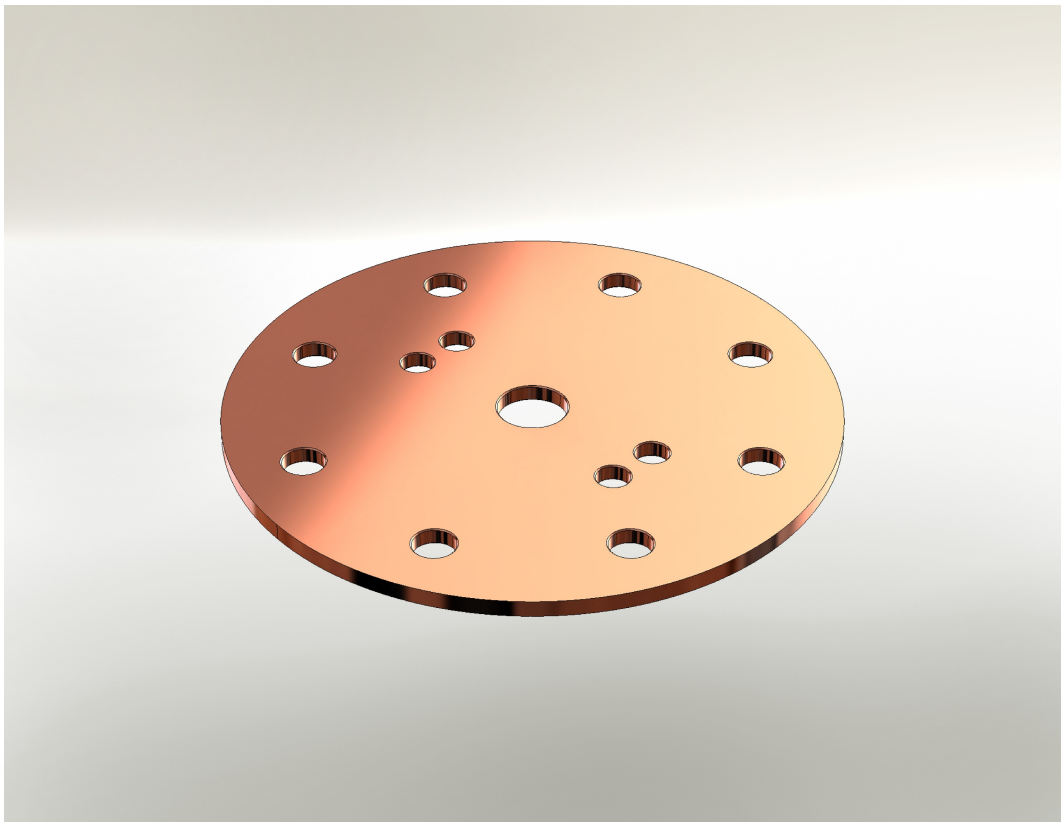

Figure 7.12: heatshield-upper

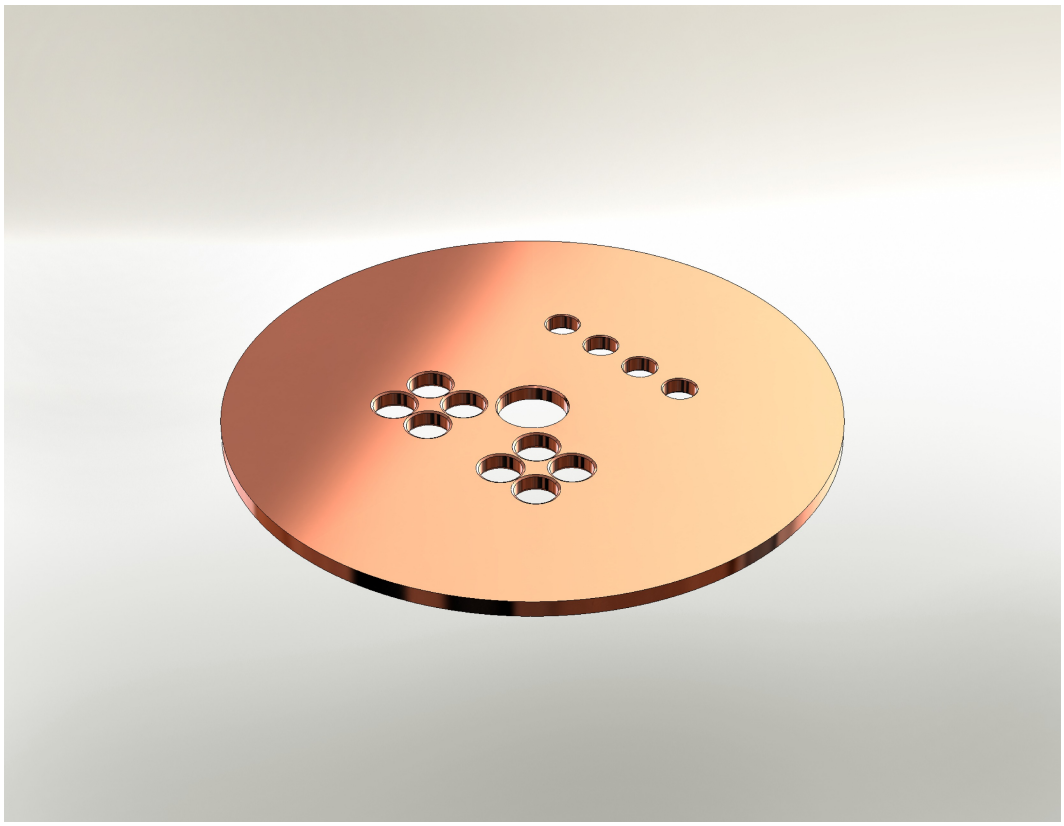

Figure 7.13: heatshield-lower

7.3 Tail

The tail section comprises the tailstock, heater holder, screwcap, upper and lower clamp plates, and the sample holder; the sample holder itself has several other attaching components and is discussed further in its own section.

Tailstock The tailstock is the principal structural component of this section, and the third most difficult part of the Octopus to machine. It attaches to the main shaft by screwing to the lower shaft tip and provides the mount for the sample holder plate and the heater holder. It is intended to serve as a large (massive) thermal reservoir for heat generated at the sample or circuit board, and so is made of special high-purity certified OFE-HIT copper C10100 for maximum thermal conductivity. Alternatively, if the sample heater is employed, heat must flow a distance of several inches from the heater to the sample, again calling for excellent thermal conductivity. The mechanical junction to the sample holder plate (or to the heater holder) need to be good *thermal* joints. A considerable amount of clamping pressure is available via the triple through bolts, but it is difficult to manufacture an indium gasket of the required shape. Since electrical conduction is unnecessary, a thin layer of Apiezon-N grease is applied between the freshly acid-deoxidized surfaces of the tailstock and sample holder and clamped together shortly thereafter. The three through-bolts should be tightened uniformly in several stages, with the heavy brass 1/4-20 nuts backed by both flat and split-ring lock washers and held in an allen socket. Should the tailstock-sample-holder joint need to be disassembled, the machine screws should be replaced anew since the countersunk flat-heads mar from the screwdriver.

The threaded joint between the tailstock and the lower shaft tip is a vulnerability. The soft copper threads are quite weak, even using a 1/4-20 screw (the largest diameter that can be accommodated given the geometry of the nearby coaxial cable channels). The joint needs to be screwed fairly tightly during assembly, otherwise counterclockwise rotation of the adjusting knob outside the cryostat will merely unscrew this joint rather than rotate the

sample assembly.

The tailstock has channels for the four lower coaxial cables. The critical diameter channels in the sample holder and the top and bottom clamp plates are described in detail below, but these are merely pass-through channels, and milled oversize with a $5/32''$ (≈ 0.156) ball endmill. The "meat" of soft copper between adjacent channels is only 20 thou – the rectangular cable pattern is compressed as far as possible!

Four pairs of milled slots are provided on the tailstock bottom faces, so that DC wiring runs can be countersunk into the metal. The countersinking on the upper bottom face is necessary to provide clearance for the wiring against the cryostat bore, and on both faces the the long area of surface contact provides a thermal joint to sink heat carried by the wires down from above before it would reach the sample. The lower ends are chamfered to provide a fair lead without chafing for the wires, which will generally be under some tension, from the tailstock to the backside of the sample area.

Heater holder The heater holder is intended to accommodate a nichrome wire resistive heater, for operation of the Octopus at stable temperatures above 1.4 K. There is very little available room to wrap a heater, so the holder takes a shape that is more difficult to machine than its simplicity would suggest. It is made from OFE-HIT copper, and clamps to the tailstock in a similar manner as the sample holder (with thermal grease between freshly acid-deoxidized surfaces), however through-bolts could not be accommodated. The clamping screws are #4-40 brass machine screws that thread into tapped holes in the tailstock, and considerable care should be taken when torquing these screws to obtain adequate clamping force for good thermal conduction without stripping the soft threads. The screws are soft brass to render thread damage less probable, and the tapped holes in the tailstock are deliberately quite deep to try to distribute the force insofar as possible.

The heater holder is not mounted at this time, since the present experiments intended operation at only 1.4 K. The rounded surface for wrapping

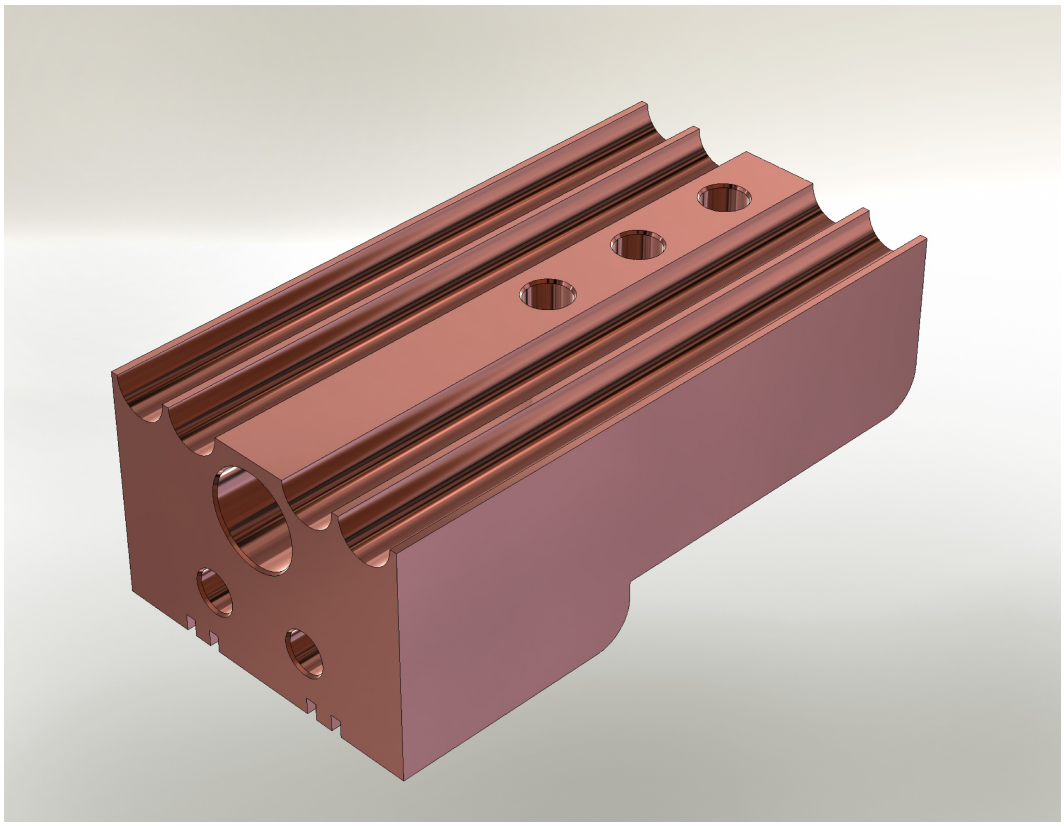

Figure 7.14: tailstock

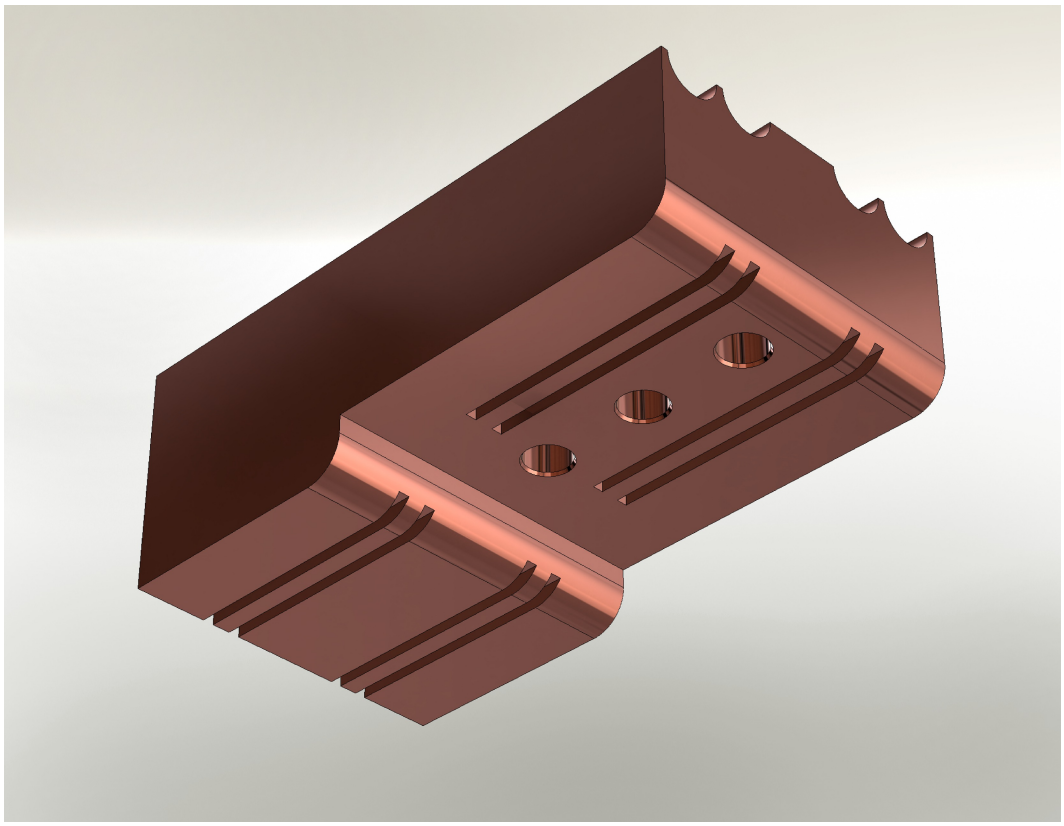

Figure 7.15: tailstock-reversed

the heater wire has been calculated as indented sufficiently to just accommodate the full length of the Janis heater wire kit (#HK/325) in about two layers of wrapping. The available wrapping indentation and surface area was severely (and surprisingly) constrained by the available outer clearance dimensions and the need for adequately sized through-holes for the clamping bolts (#4-40) to give some hope for not stripping out the tapped holes in the tailstock. To install the heating wire, test the fitting geometry by wrapping the somewhat stiff but fragile (in its outer fabric-like coating) wire about the holder and design a method for securing one end of the wire while wrapping successive turns as tightly as possible, so that the wraps in a single layer butt up against one another compactly. GE varnish should be applied to the wrapping surface before winding the wire, and again across the wraps after wrapping the first then second layer of wire. The varnish is deliberately fairly nonconductive, but take care not to damage the fabric-like insulating coat of the wire. The end of the wire will need to be tied securely via some appropriate knots (test this beforehand on a test piece of wire). It is best that the entire length of wire[3] be used without cut or damage, because the temperature controller (Lakeshore model 331 or 332) requires an adequate resistive load in order to source adequate heater power at the available current. Care will also need to be taken when acid-deoxidizing the heater holder clamping surface not to get acid on the heater wires nor leave any in the through-holes. If the heater wire is completely encased in epoxy, the wire-assembled holder can probably be washed judiciously.

Sample holder plate The sample holder plate (something of a misnomer) is the most complicated and expensive to machine component, and manufactured to the closest tolerances, of 2 thou or better. The sample holder clamps to the tailstock as described above, and serves several roles:

1. as the structural support for all components below the tailstock
2. as a thermal conduit for wicking heat away from the sample area, es-

[3] probably 25 Ω

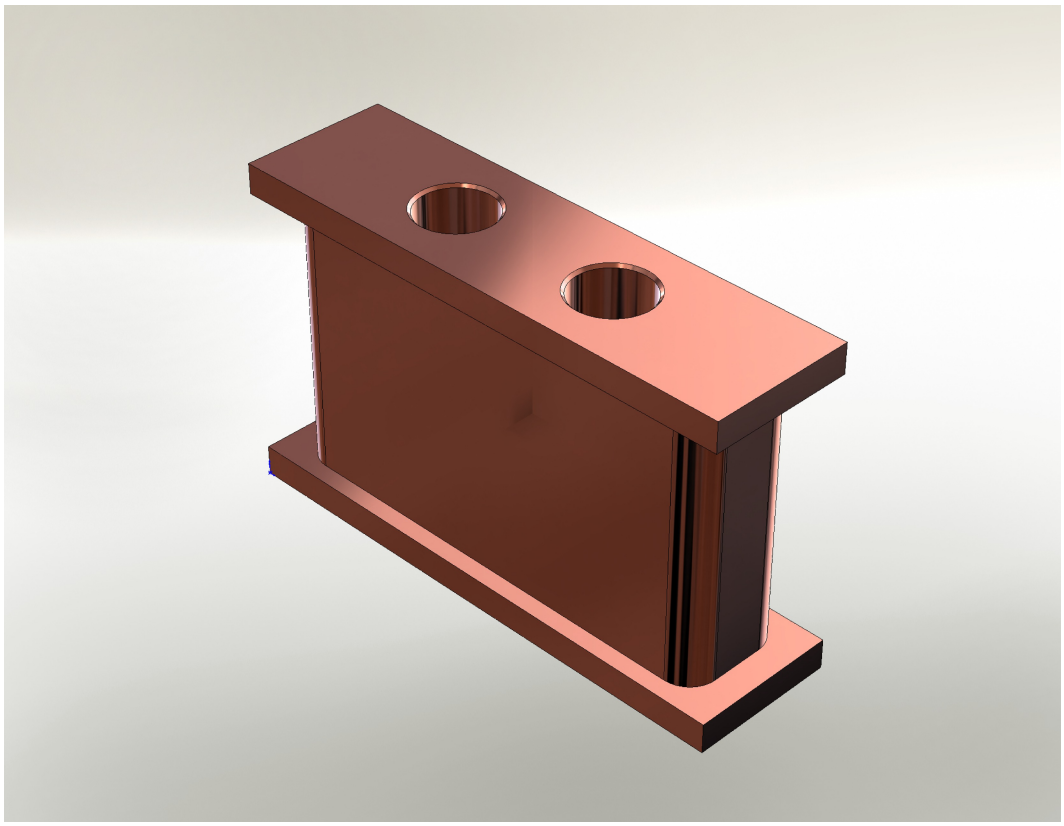

Figure 7.16: heaterholder

pecially the termination resistors (or alternatively for conducting heat down from the heater holder)

3. as the set of channels into which the coaxial cables are countersunk, providing a good thermal and electrical ground and support for the cable clamping forces
4. as a mounting place for all the lower accessory pieces, not least the sample socket

The second role dictates the sample holder be made of soft OFE-HIT copper, and the third and fourth cause it to be honeycombed (or "Swiss-cheesed") with channels and holes; as a result, the structural design was compelled to be extraordinarily complicated, barely permitting adequate "meat" between adjacent holes, and had to be machined throughout to tolerances of better than 2 thou (80 microns). An an illustration of the complexity of the part, when it became necessary to modify the original expensively-machined version, several days were expended in 3D CAD design looking for a single place where it might be possible to add a single tiny screw hole. No such place could be found. The author even seriously investigated the possibility of *tapping a threaded hole* ***inside*** *another screw!*

The coaxial cables lie in semi-circular channels of barely larger diameter and positioned below the surface to a depth of half the diameter; the copper thus envelops and supports the cable over most of 180 ° and permits the application of considerable clamping force (since the matching clamps have similar design) without crushing or distorting the cable shell and impairing the high-frequency geometry. The large (long) surface area of contact should afford good thermal conductivity between the cable shield and the copper, sinking any heat conducted by the cable shield down from above before the heat can flow to the sample area; it also electrically grounds the cable shield. No grease or paste need be used, and the channels extend far enough to place the cable end within millimeters of the relevant sample pin. The channels are machined by the happy coincidence that a 9/64″ ball endmill (≈ 0.1406) has

a diameter very nearly that of the 0.141″ nominal (closer to 0.143″ actual) coaxial cables, and the ball endmill is traversed laterally "a few thou"[4] on the final machining passes to obtain the last little bit of lateral clearance. The cables clamp to the top and bottom faces via the top clamp plate and bottom clamp plate, discussed in the next section, using two machine screws that pass through clear-drilled holes, since obviously such copper, if threaded, would not hold the required force.

The center area of the sample holder, with the 4x18 matrix of holes, is for mounting the chip socket holding the sample proper. The outer columns are for the 18 pins of the DIP socket; the middle seven holes are clearance holes so that the socket pins do not contact the copper, while the upper and lower holes are sized to press-fit their pins to the copper as electrical grounds and thermal sinks. The two inner columns of tiny (0.037") holes were originally intended to press-fit brass pins, to be used as mounting points for termination resistors, analogous to the scheme employed on the first-generation high speed sample holder. Subsequently, it became necessary to modify the sample holder to accommodate a full printed circuit board, and these holes were unnecessary. The PCB, however, mounts on the bottom side of the sample holder, and needed a mechanical fastener to press it against the copper for good thermal joint. The only remaining place possible to fit machine screws was through the area occupied by these inner columns of holes, and indeed the screws run all the way through the DIP package itself (this design is discussed in the next section).

The sample holder also provides mounts for several accessories. One temperature sensor mounts to the flat on the bottom face, middle, immediately above ("upwards") of the sample socket. The area is designed to accommodate a Lakeshore "SD" package sensor mounting in Lakeshore's "CO" sensor clamp (#SN-CO-C1). The gold-plated sensor is compressed between the clamp face and the copper by spring pressure; the spring rides on a

[4] I did not specify the exact width of traverse, but explained the goal to the machinist and left it to their judgment.

#4-40 screw that threads into the tapped hole provided immediately above the flat (the lowest of the six in-line holes). Originally, this tapped hole was intended only for Lakeshore's custom screw (a component of the clamp package), threaded in from the bottom with the spring pressed against the screw head. Unfortunately, the hole has had to be repurposed to also fasten the sample plate (described in the next section), so the spring rides on an *ordinary* #4-40 screw threaded in from the *top* face, which is overlength to serve double-duty, and presses against a washer and nut.

Another temperature sensor mount is provided at the lower bottom edge of the sample holder, with a milled flat and tapped hole for the "CO" package clamp. The area is slightly countersunk to reduce the copper thickness for measuring temperature closer to the sample, although this proved fortuitous for clearance when the nosepiece was added later. The upper temperature sensor is intended to be a Lakeshore silicon diode, principally measuring the temperature of the *sample holder*, and the sensor for feedback loop regulation of the heater coil mounted on the heater holder above. The lower temperature sensor was originally intended to measure better the temperature of the *sample*, to be used in concert with a braided lead and the *thermal clamp*, discussed below. The two second-lowest holes (#4 clearance) were intended for bolting that thermal clamp, and have been repurposed to attach the sample armor.

The two tapped holes (of three lowest on the sample holder) with the peculiar #4-48 (fine thread) were originally intended to mount a pair of ball plungers. The concern was that the sample holder, at the end of a long moment arm and despite the concentric spacer, might move out of position if the optical table, cryostat, and hence Octopus were bumped, and that as a result the sample holder – or worse yet, the sample – might contact the cryostat bore; this could be fatal for the sample. The ball plungers would stick up from the sample face and act as bumpers or shock absorbers. Since the plungers mount via external threads, and the sample holder copper is fairly thin (about $0.200''$), plungers with especially fine thread were selected. Subsequently, in

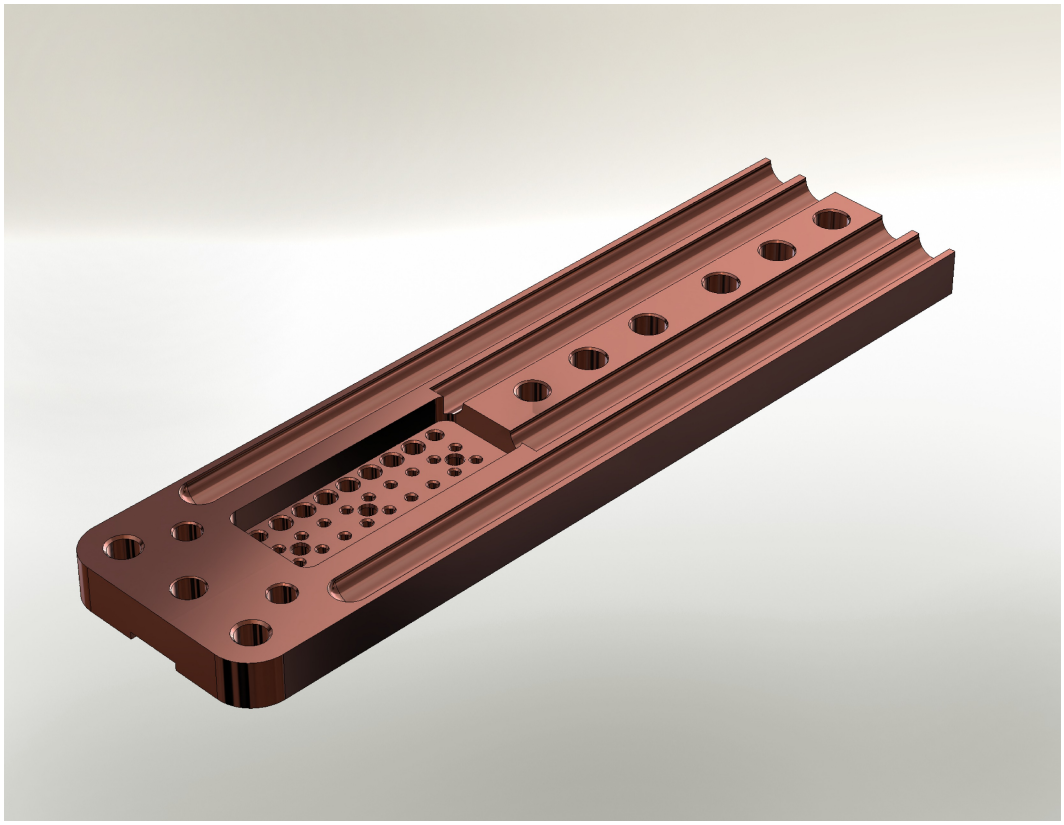

Figure 7.17: sample-holder

attempted operation, it was discovered that getting the sample holder to align into the square cryostat bore was serious difficulty, and an entirely new component, the *nosepiece*, was added and adopted these tapped holes as clearance holes for larger screws.

Screwcap As described above, the sample holder fastens to the tailstock via three machine screws passing through the triple through-holes on the tailstock and sample holder. There is very little clearance between the top of the sample holder and the cryostat wall, insufficient clearance to accommodate a round-head screw (or nut, if the fastener was reversed) and flat washer; the clamping force is considerable for the structural and thermal joint (especially since the fasteners may tend to loosen under thermal cycling), and washers would be necessary to avoid stripping the soft copper. Instead, a metal cap is provided that takes countersunk flat-head screws, and distributes the clamping force

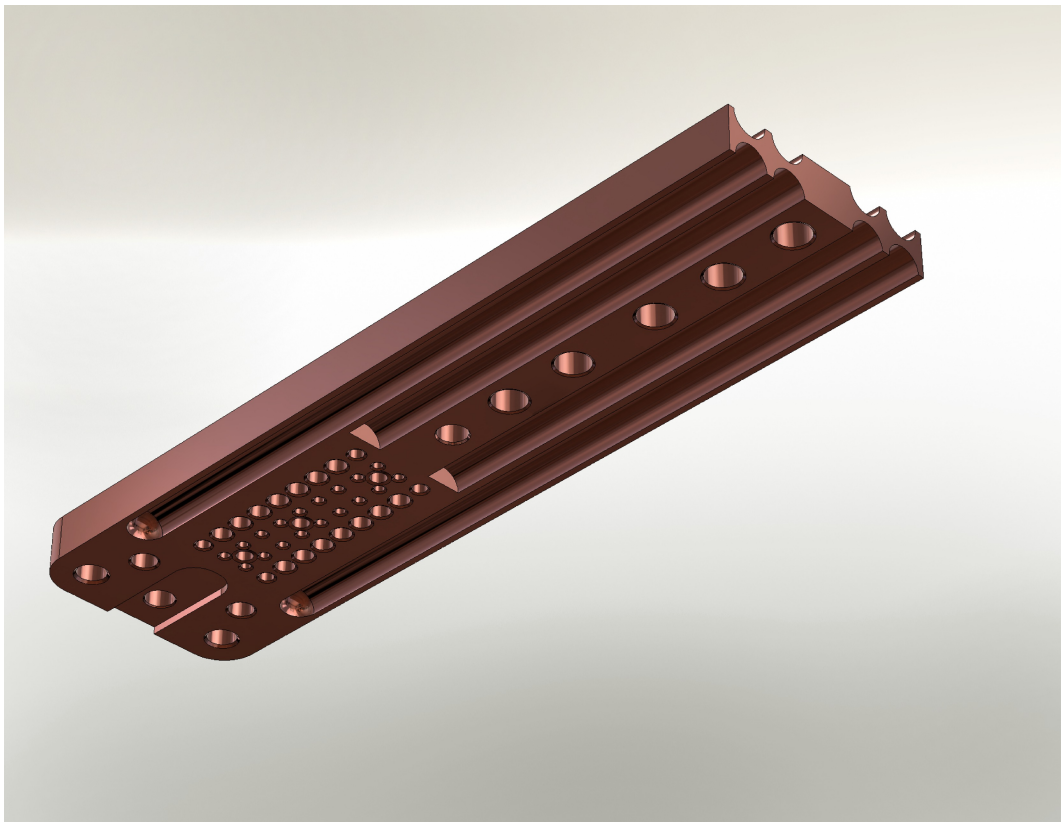

Figure 7.18: sample-holder-reversed

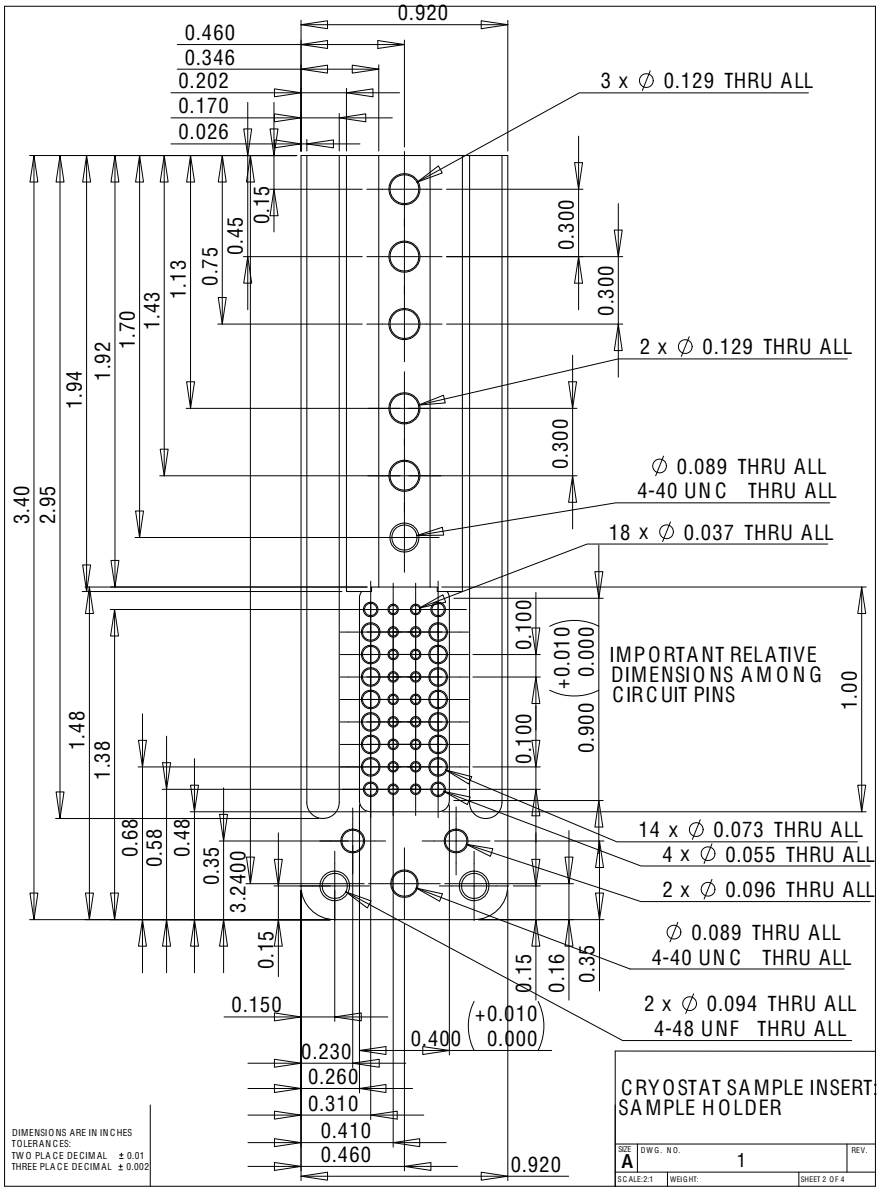

Figure 7.19: Example machine drawing sheet for the sample holder plate, one of several for that particular machine part, illustrating the degree of design detail and tolerances required to fit the required features into the space constraints. Complete machine drawings for all parts are in Appendix A.

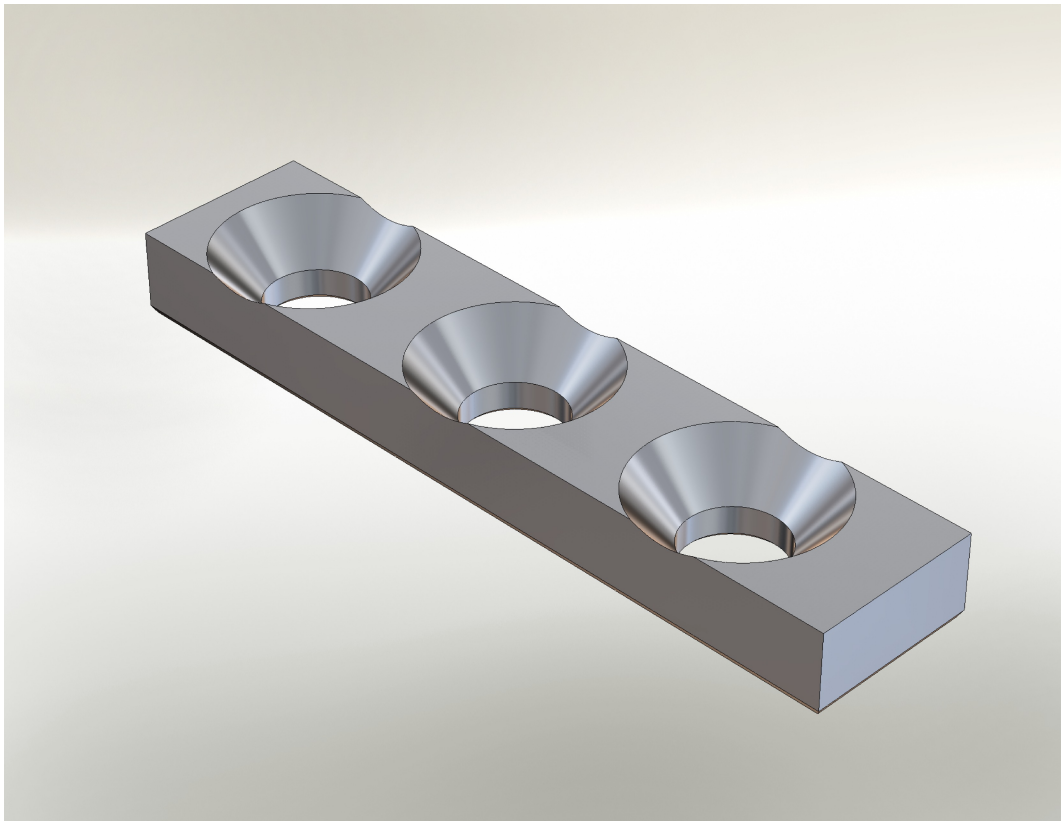

Figure 7.20: screwcap

over a larger area of copper. This screwcap is made of stainless steel because it is critically thin, especially in the countersinking, and needs to be both strong and hard.

Top cable clamp The coaxial cables fit closely in the countersunk channels of the sample holder (and the four lower cables pass through the oversize channels in the tailstock), but the cables need be pressed against the sample holder with considerable force, both for the thermal and electrical (ground) joint but also to provide considerable friction to clamp the cable ends in place. (If the Octopus is adjusted vertically in height via the small travel provided for, a great deal of pulling or pushing force will be placed on the cables as a side effect, and if they break loose for the clamping will immediately break most any electrical solder joint at the sample holder.) The upper and lower clamp plate work in concert; the upper plate must be thin because

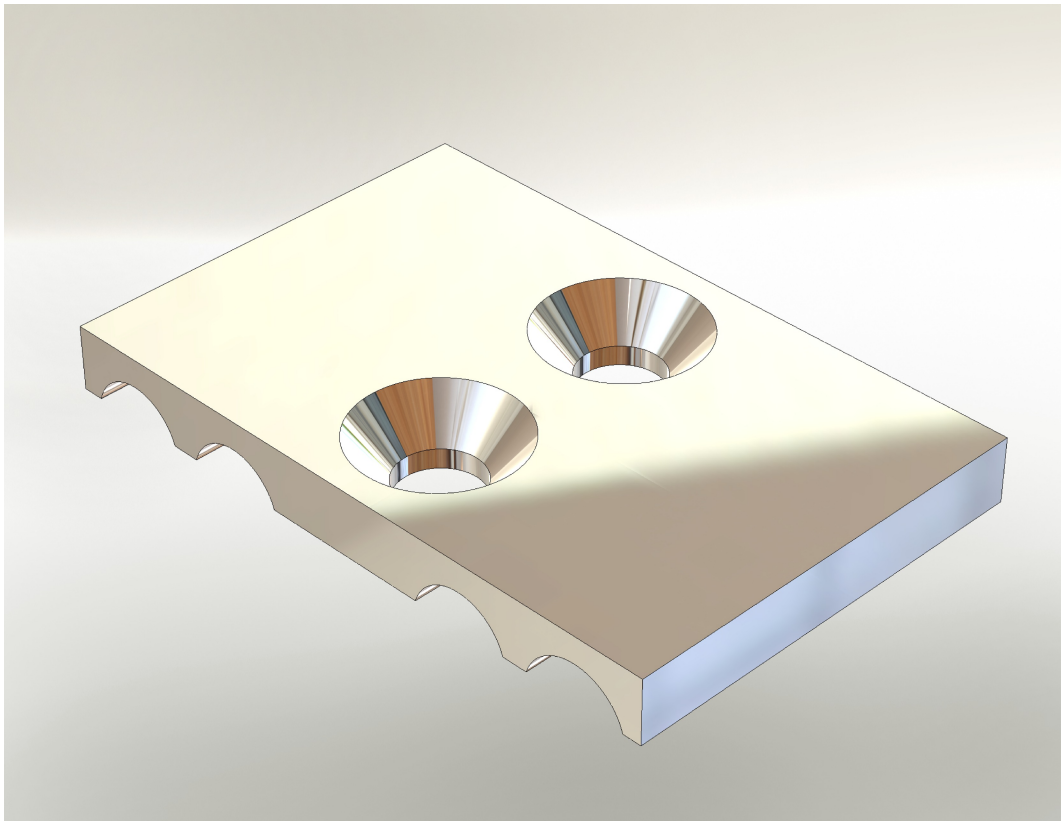

Figure 7.21: topcablecap

of the little clearance between the sample holder and cryostat wall, and is made of stainless steel for strength and rigidity. It would be preferable for multiple screws to be used *transversely* to clamp the four rows of cables adequately and uniformly, but there was simply no room. Thus, the upper clamp plate has been made as thick as could be dimensionally spared against the cryostat wall to give enough rigidity to keep the clamping force on the outer cables adequate if not uniform. In practice, the fasteners need to be extremely tight to prevent the outer cables from slipping, but the design is adequately robust in operation. The very close matching of the countersunk cable channel profiles/diameters to the cables themselves was necessary not least to prevent the inner cables from being crushed by the force required to keep the outer cables from slipping. The upper clamp plate has countersunk holes for the machine screws.

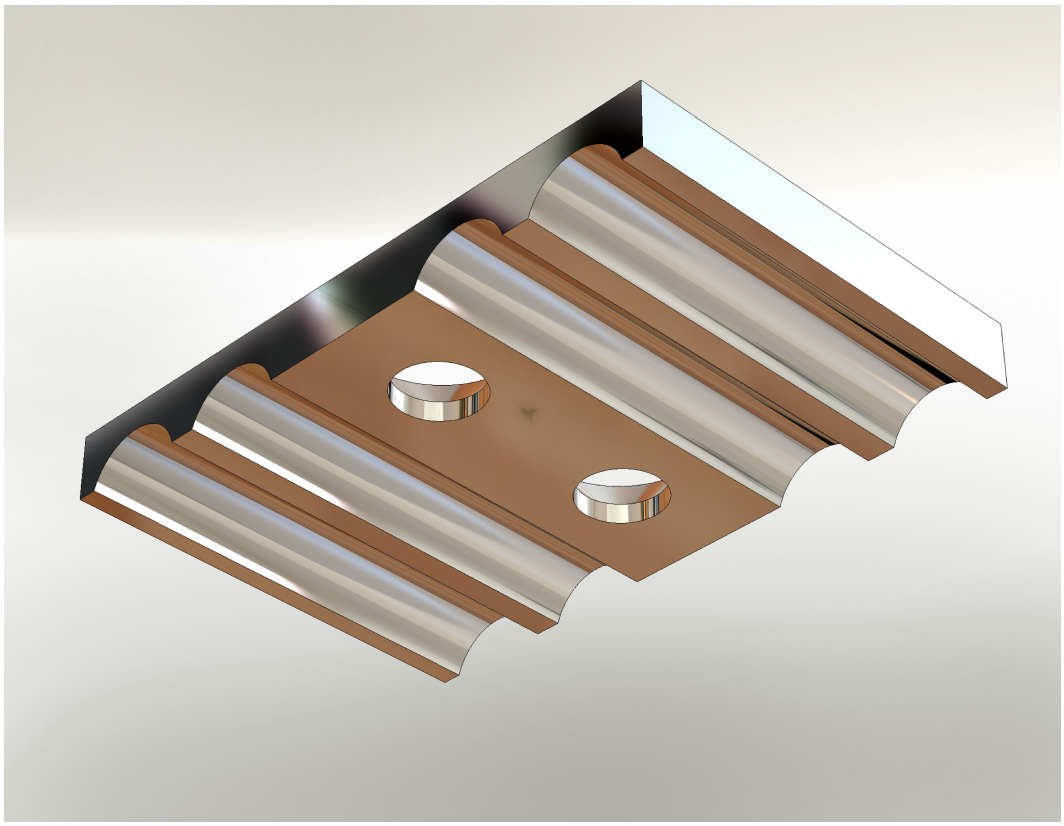

Figure 7.22: topcablecap-reversed

Bottom cable clamp The lower clamp plate has much more room than the upper plate, and can be made much thicker and of brass. The cable clamp machine screws secure with nuts, washers, and lockwashers. It is essential that the two screws be tightened progressively and uniformly, to keep the upper and lower clamp plates from rotating about an axis transverse to the sample holder plate, which would not distribute the clamping force over a large enough area.

The bottom clamp plate also serves an additional roles. DC wiring soldered from the pins of the sample socket on the bottom of the sample holder need to be held in slight tension while running up the cryostat, otherwise the loose wire will inevitably snag in the tight confines and then rip out during Octopus insertion or removal. Solder joints to the socket pins (or the printed circuit board) cannot withstand such (fairly small) force. Therefore, structural pins have been placed in the lower clamp plate which the DC wires wrap about. The wires can then be held under tension from the structural pins up to the concentric spacer (where they wrap again), and need only the slightest tension to keep the slack out from the structural pin to the socket pin. These four structural pins are brass, and have been both press-fitted and soldered to the four holes in the lower clamp plate. The soldering was carried out by hot plate, and oxides the brass badly despite using a dry-nitrogen bath and mask.

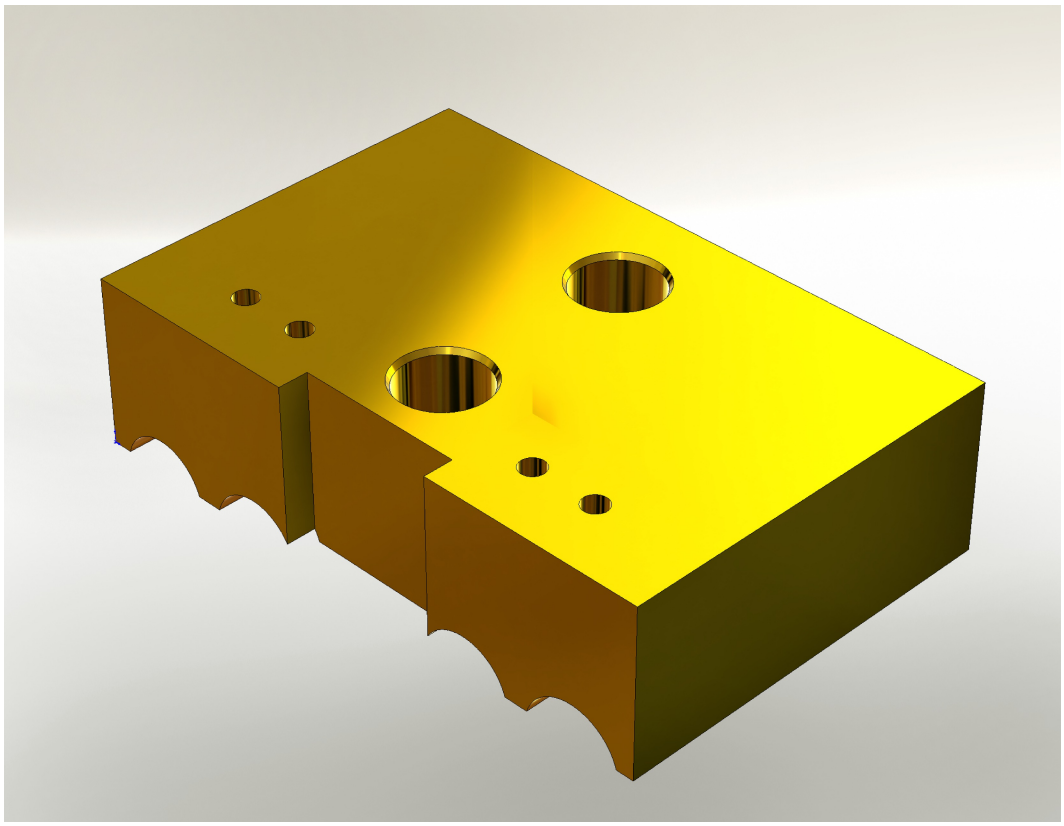

Figure 7.23: bottomcablecap

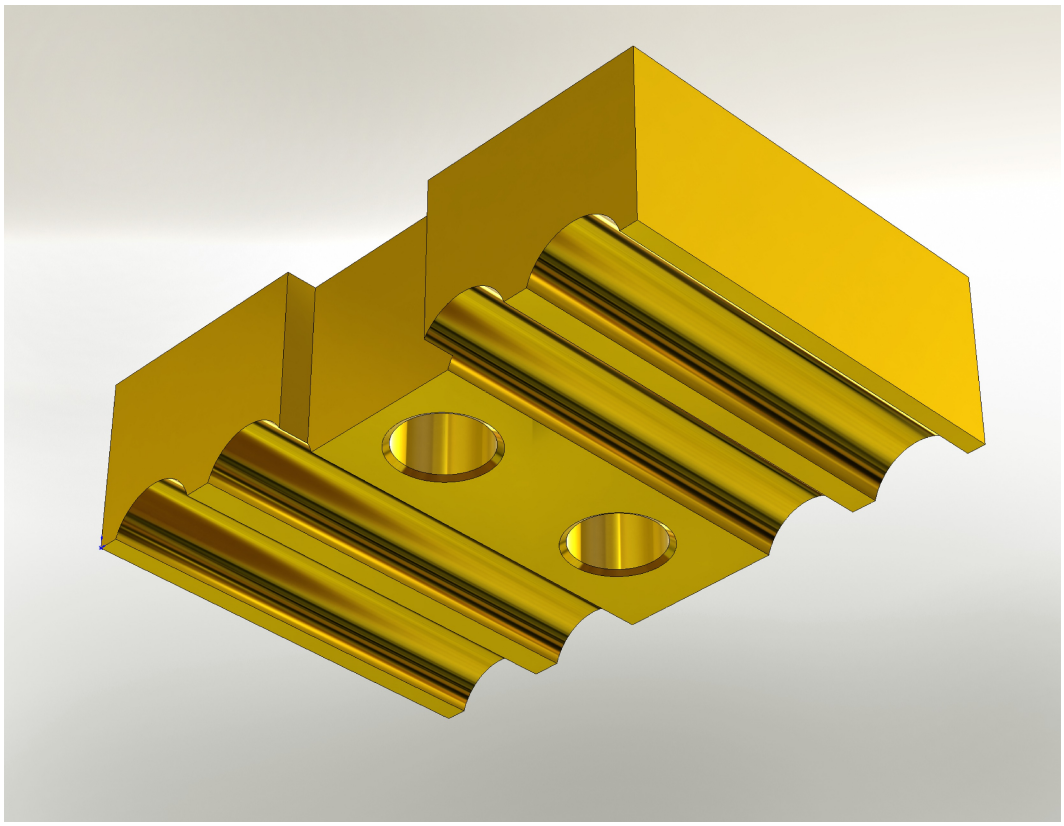

Figure 7.24: bottomcablecap-reversed

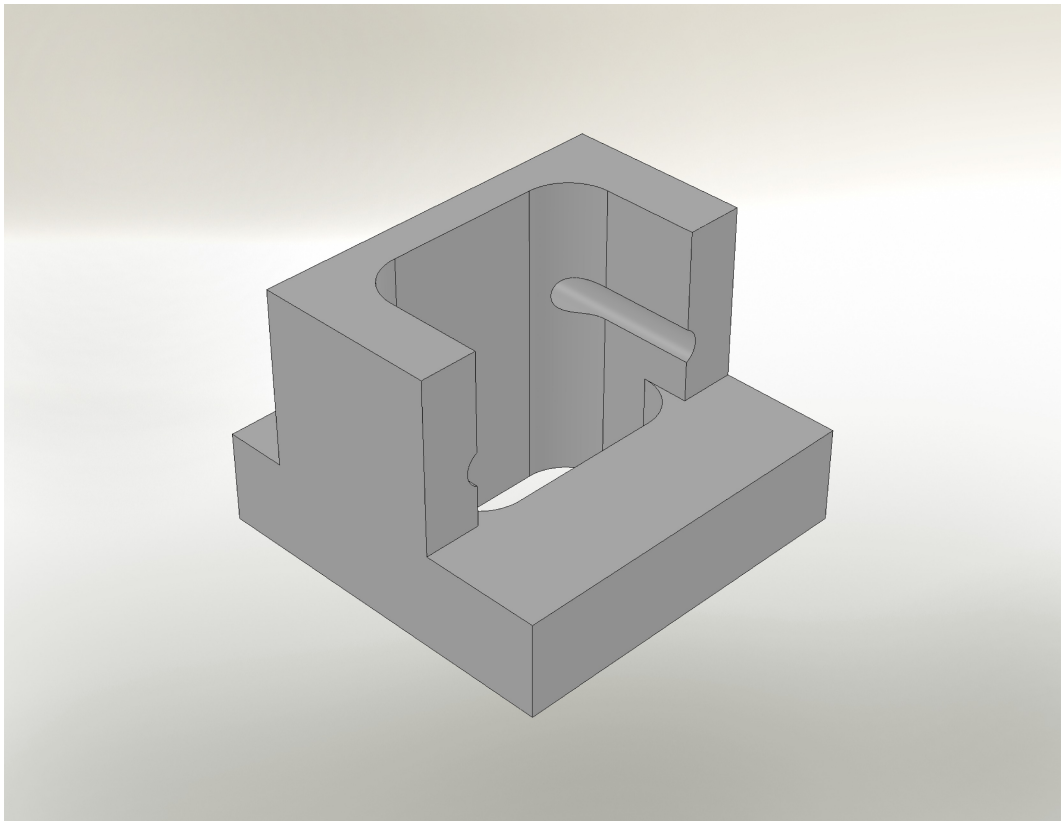

Figure 7.25: pyramidaligner

7.4 Sample holder assembly

A number of pieces mount to the sample holder plate. The modified sample DIP socket, sample holder plate, printed circuit board, and grounding plate comprise a "sandwich" secured by #0-80 screws. The Teflon alignment nosepiece, aka pyramid aligner, guides the entire lower assembly into the square cryostat bore. The physics sample itself, mounted in a DIP chip package and placed into the DIP socket, is surrounded and protected on its upper face (ie, towards the window) by the sample armor.

Alignment nosepiece aka "pyramid aligner".

Alignment nosepiece top screwcap

Alignment bottom screwcap

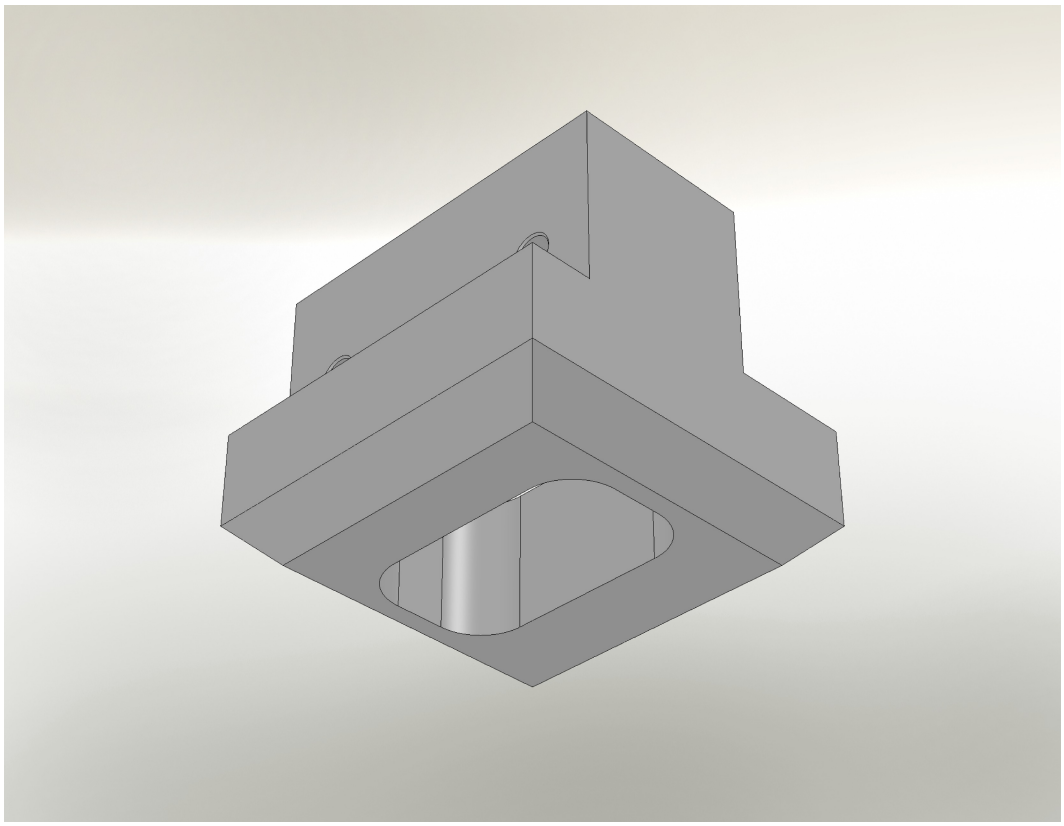

Figure 7.26: pyramidaligner-reversed

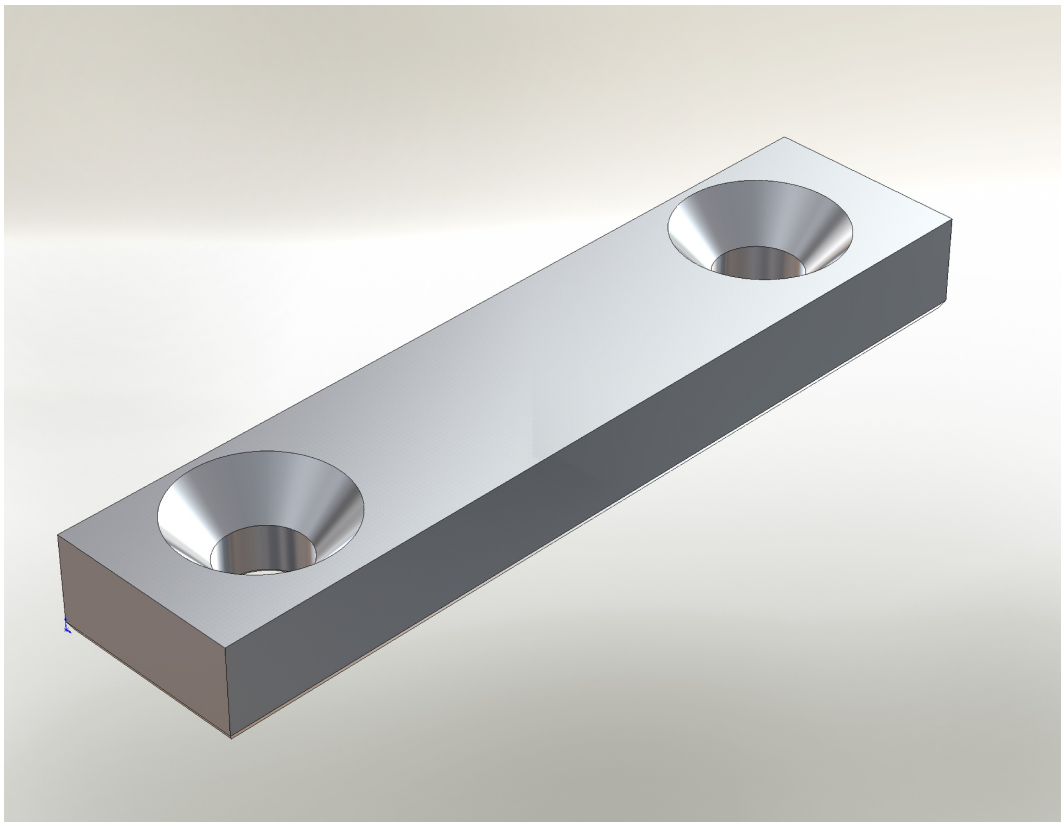

Figure 7.27: alignerscrewcaptop

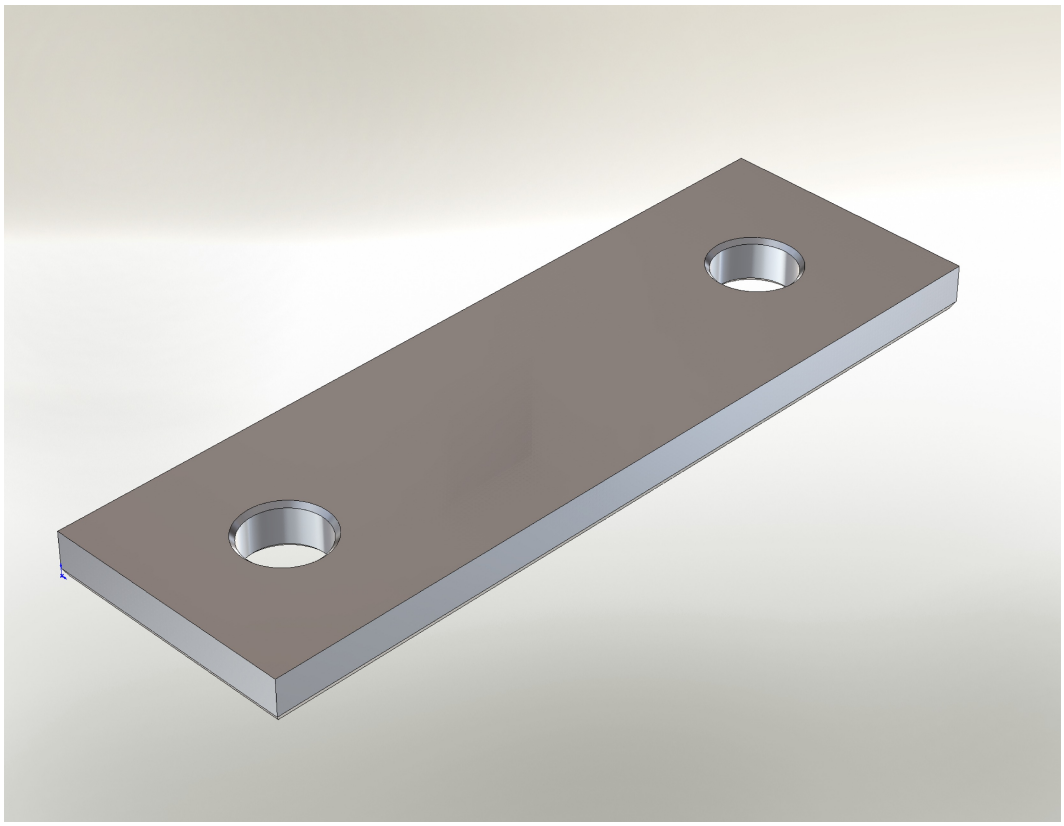

Figure 7.28: alignerscrewcapbottom

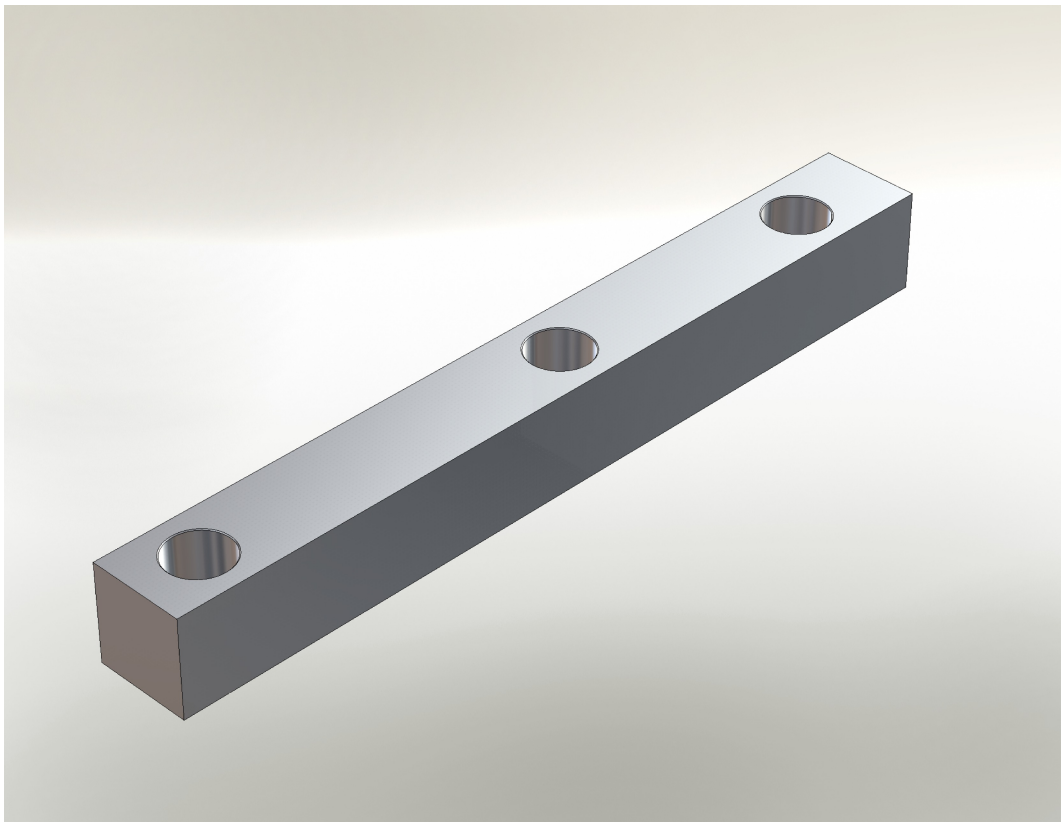

Figure 7.29: groundingplate

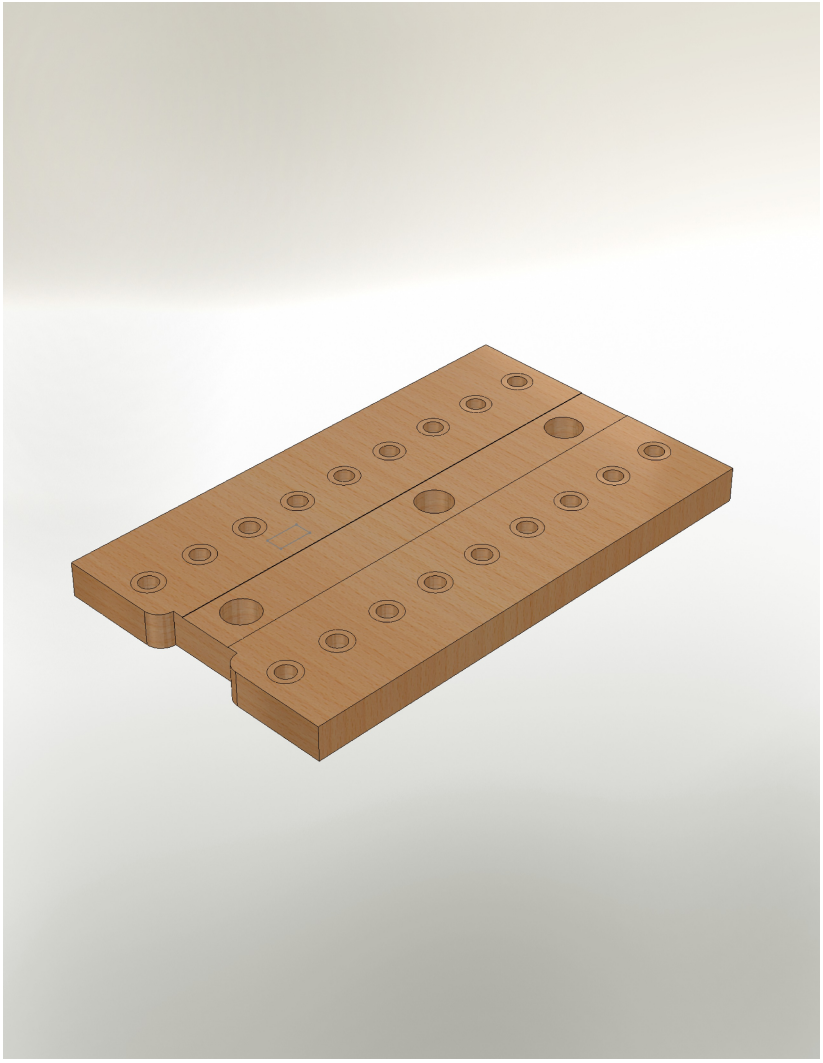

Figure 7.30: pcb

Grounding plate

Printed circuit board

Sample DIP socket

Sample armor

Thermal clamp The idea contributed within the research group was that a flexible copper braid might be soldered directly to the sample chip package itself, and led to the flat area on the upper face.

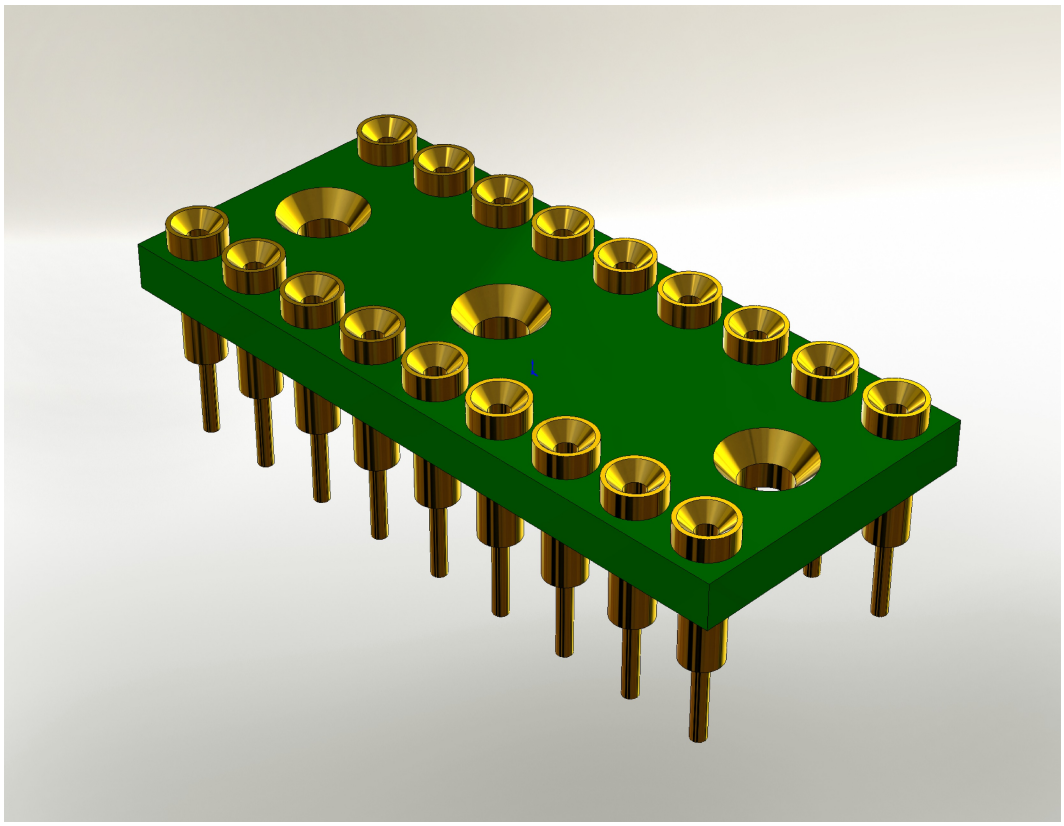

Figure 7.31: Sample DIP socket, modified. Derived from a CAD model by ATH [Hammack, 2009]

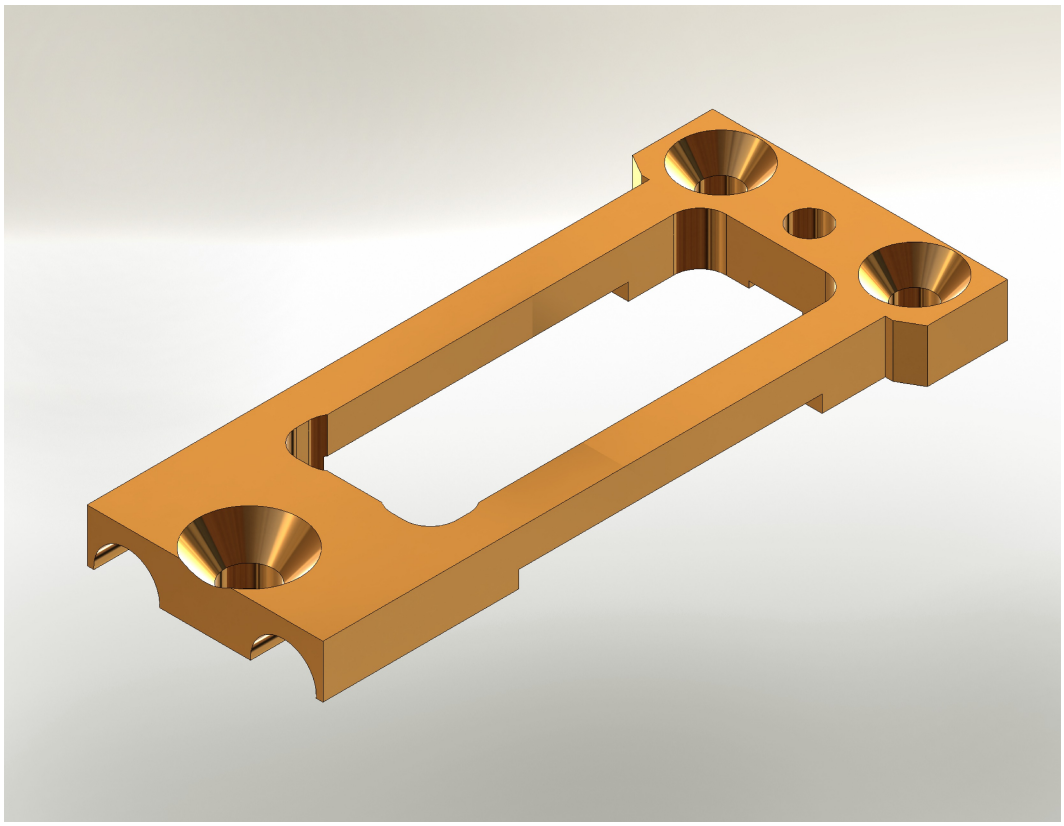

Figure 7.32: toparmor

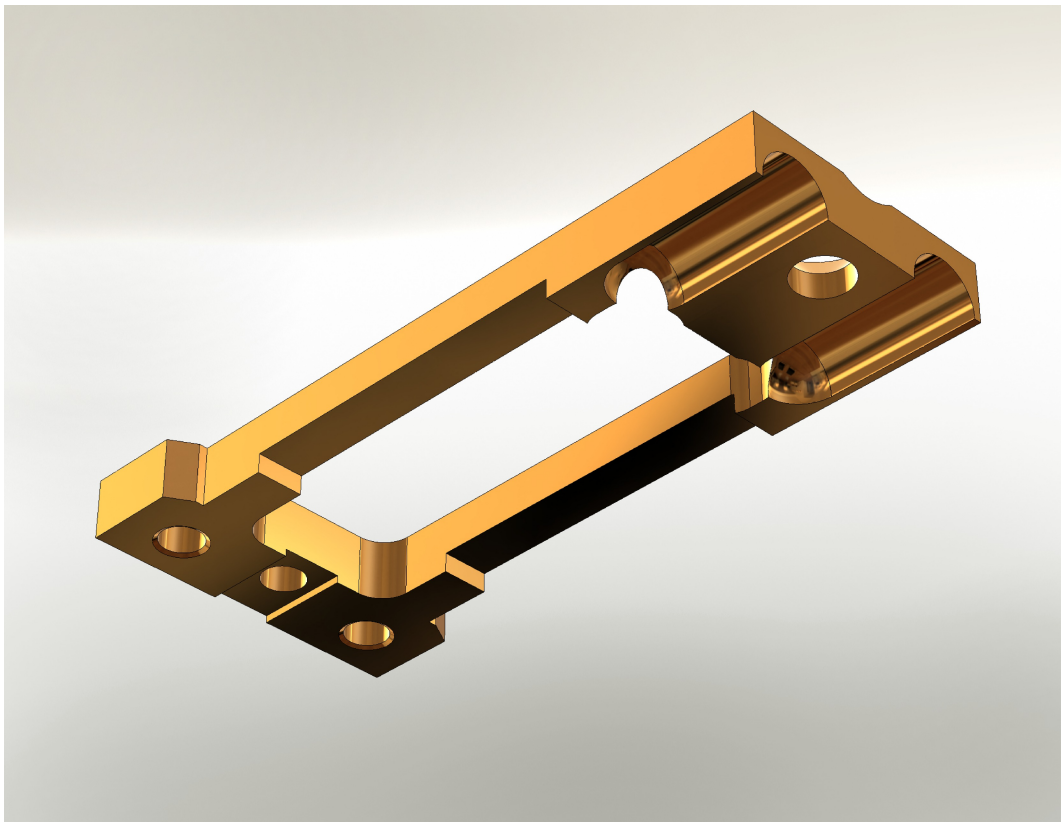

Figure 7.33: toparmor-reversed

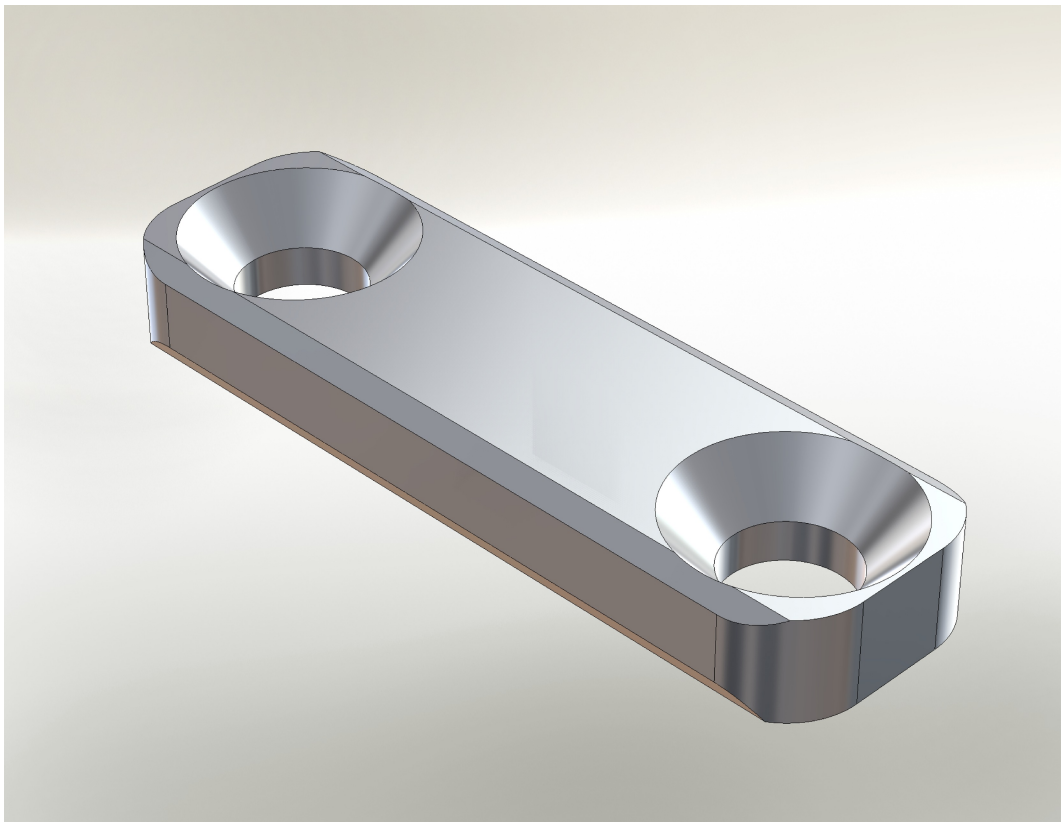

Figure 7.34: thermal-clamp

7.5 Printed circuit board and SMT components

7.5.1 Overview

The PCB mounts to the back side of the sample holder plate, while the socket mounts to the plate front side. The socket pins pass through holes in the plate and through the PCB and solder to pin lands on the PCB. The outer four pins fit tightly in the sample plate holes as grounding pins, while the other 14 pins pass through without contacting the plate. The back (ie, inner) side of the PCB is plated uniformly with copper, except for annual insulating rings around the 14 signal pins so that they do not short to the plate. The socket+plate+PCB are sandwiched against each other by machine screws. Unfortunately, there was almost no room to fit the necessary holes; the geometry adopted was that tiny #0-80 screws pass directly through the miniature PCB integral to the sample socket itself, with the screw heads countersunk flush against that miniature PCB providing the minimal clearance needed under the DIP package casing of the sample.

The termination resistors on the PCB dissipate considerable heat, and it is better that that heat sink to the sample holder plate (and be cooled by helium vapour or liquid) than travel up the signal pins into the sample. The copper sample holder plate and copper PCB require some inter-medium to make a good thermal joint. Indium foil is an obvious choice, but indium joints are actually a species of cold weld, and require far more clamping *pressure* than could be supported by three #0-80 screws to cause the indium to flow [Ekin, 2006]. Adhesive agents like Apiezon-N grease and GE varnish are electrically insulating, and the PCB ground plane need to be grounded to the sample holder plate.

The agent selected was colloidal silver paste, Pelco #16032 [Ted Pella, Inc.]. Originally intended for bonding samples in electron microscopy, the nitrocellulose lacquer base is fully vacuum compatible when dried, and leaves a thin layer of 40% close-packed silver [Armigoda, 2009]. The manufacturer was aware of it having been used in liquid nitrogen temperatures, but not liquid helium. The silver paste dissolves in acetone, but the solvent may not penetrate from the periphery into the center, so it is likely that removal of the PCB will require mechanical destruction.

7.5.2 PCBs and SMT components in cryogenics

Electronic components are scarcely designed for use in liquid helium. Operation at such extreme temperatures is problematic for printed circuit boards and especially surface-mount components, because of the differential thermal contraction. At the least, this can alter component values or destroy them entirely. Naturally, there is no manufacturer literature for such extraordinary conditions, but some guidance can be found in Hammoud et al. [1998]; Patterson et al. [1998]; Pan [2005]; Li et al. [1992] on components that have been tested to work satisfactorily under such conditions.

Additionally, the design was intended for use at GHz frequencies. Capacitor equivalent series resistance (ESR) can strongly adversely affect capacitor performance at high frequency, and depends of the type of capacitor; see [Murata Manufacturing Co., Ltd.; Boser and Newsome, 1987] for discussion.

The capacitors selected were TDK Corporation #C1608C0G1E562J, which are type 'C0G, NP0' multilayer ceramic, high precision, low ESR even into the GHz; at 5600 pF they were the largest size available in an 0603 (1608 Metric) package. The 25 V breakdown rating is adequate for the voltages intended to be employed.

Several types of precision metal thin film chip resistors were used: Susumu #RR0816Q-49R9-D-68R (49.9 Ω) for termination, Susumu #RR0816P-4992-D-68C (49.9 kΩ) for bias rail isolation, and Yageo #RC0603JR-070RL (0.0 Ω) to bridge SMT pads.

All components seemed to maintain their values well even at 1.5 K, and worked undamaged through dozens of complete thermal cycles.

7.5.3 PCB layout and wiring pinout

The PCB trace and pad layout is illustrated in Figure 7.35.

The wirebonding pinout choices for DIP chips to be used in the Octopus (given by the geometry for the eight coaxial cables) is illustrated in Figure 7.36.

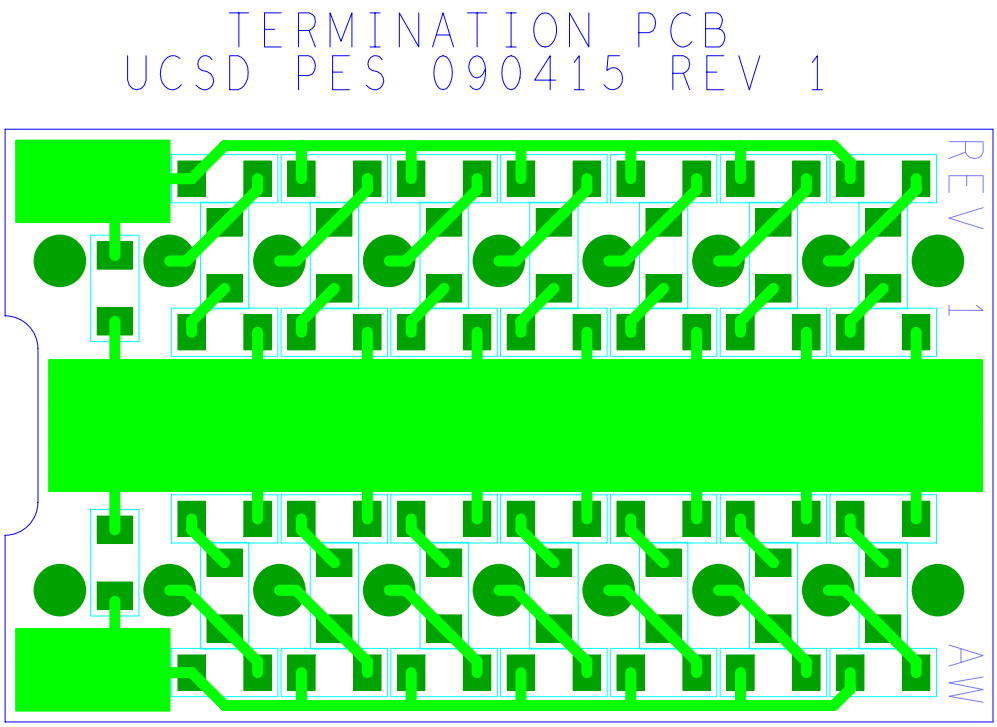

Figure 7.35: PCB trace and SMT pad layout

Pinout configuration suggestions for samples to be used in the "Octopus" high-speed sample insert

Alex Winbow, May 2009. Rev. June 2009

Rationale: the coaxial cables cannot be positioned directly adject to pins 7, 8, 11, and 12. Cables for those pins end near the north end, and the pins connect via jumper wires that add stray inductance; the wires for pins 7 & 12 will be longest. These four pins are, ordinarily, permanently connected to coaxial cables. Additionally, the DIP chip package has long *internal* runs for pins 2, 8, 11, and 17, though degradation due to that may not be so bad since the internal runs appear to be close to the DIP chip's internal ground plane.

Among pins 2-6 and 13-17, only two cables are available per side, but they can be re-positioned as desired. (n.b. only 3 of 4 cables available as of May '09)

Pins 1, 9, 10, and 18 are permanently grounded via the holes in the copper sample holder. Any pins except the permanent grounds (including 7, 8, 11, and 12 if necessary), not connected to coaxial cables, can be used for DC signals or temporary ground points, depending on wiring and configuration of the termination PCB.

Suggestion: separate high-speed pins apart if possible to reduce crosstalk issues among the wiring once it exits the coaxial cables; ie, use non-adjacent pins if available.

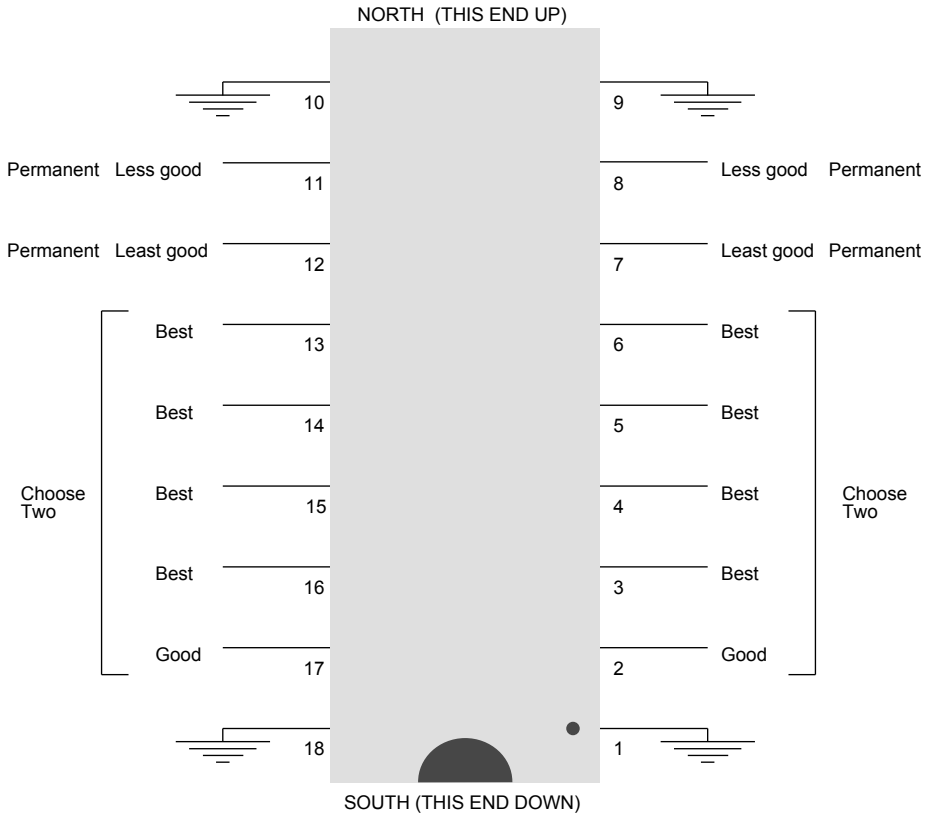

Figure 7.36: Pinout diagram for Octopus DIP chip socket, as guide to wirebonding

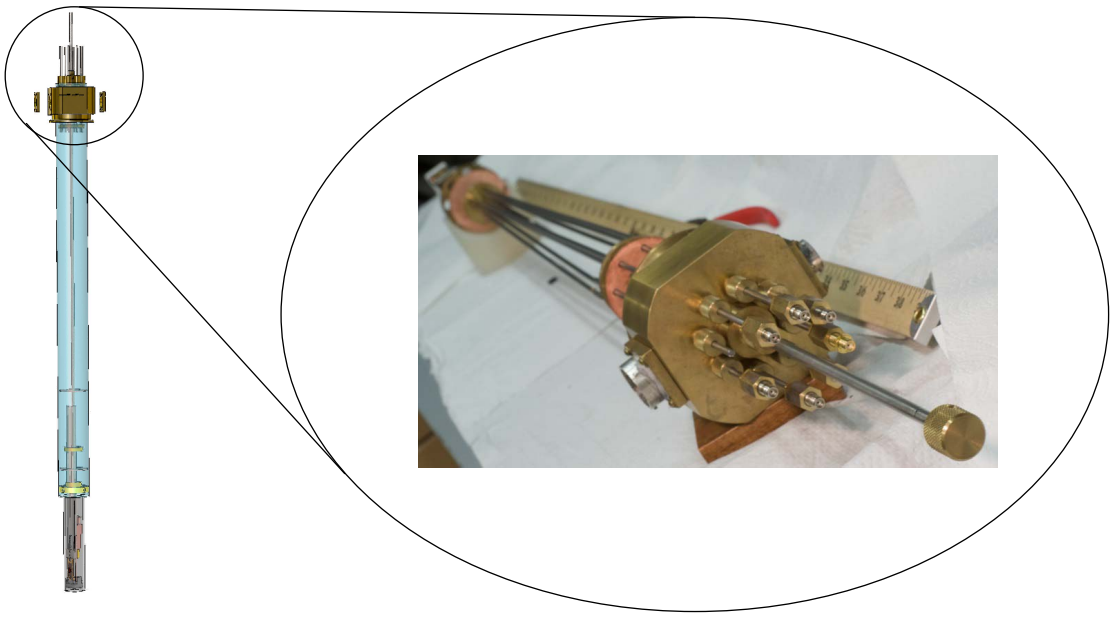

Figure 7.37: Photographs of the Octopus upper end

7.6 Additional renderings

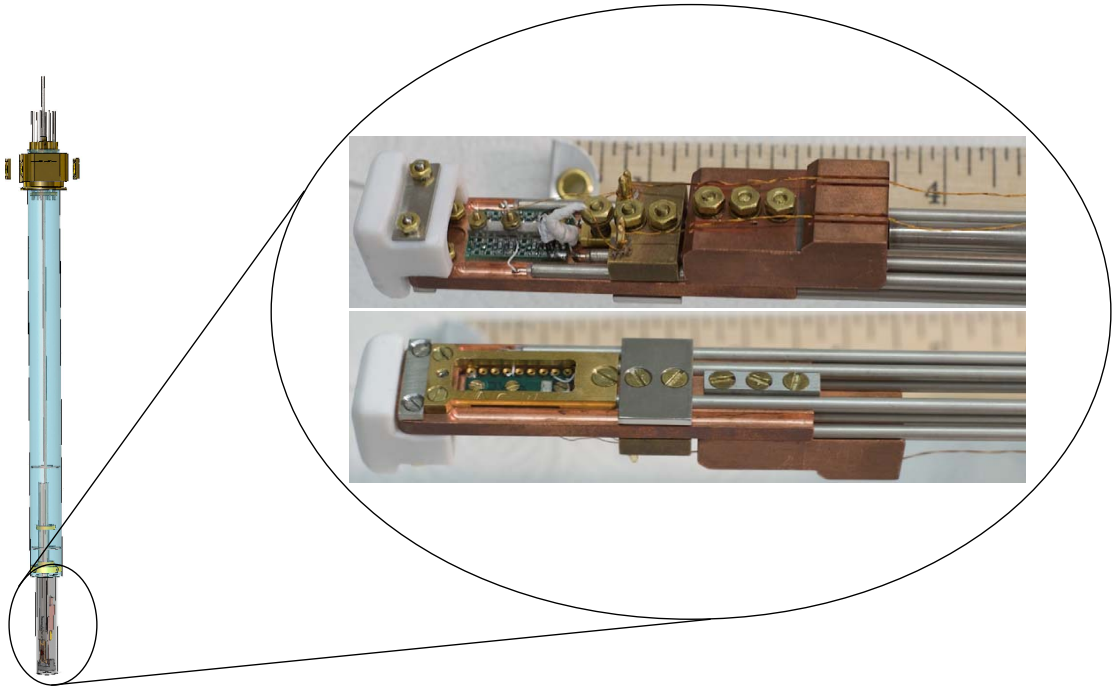

Figure 7.38: Photographs of the Octopus lower end

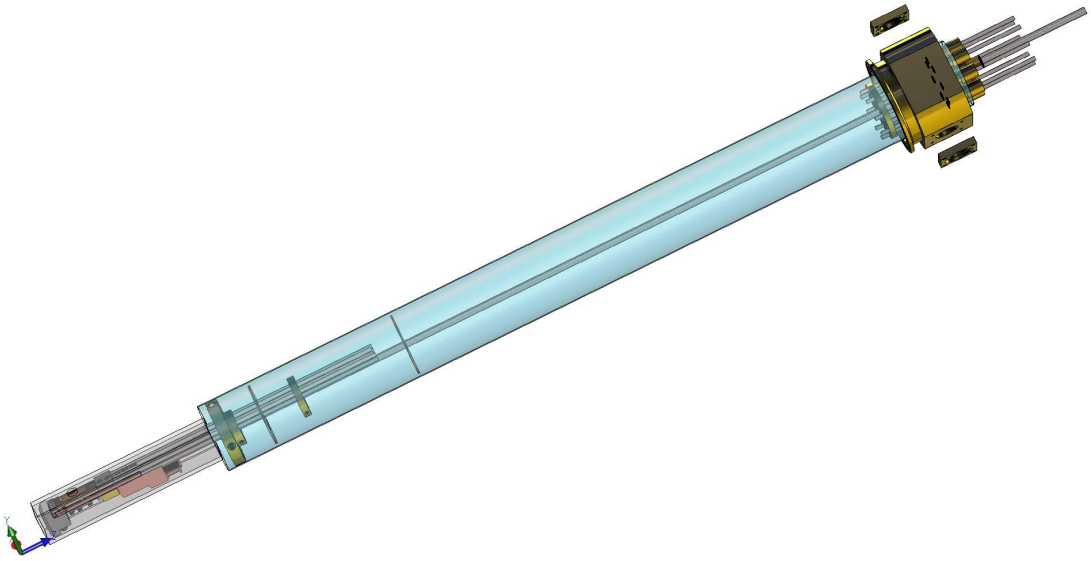

Figure 7.39: 3D CAD rendering of the assembled Octopus machine components.

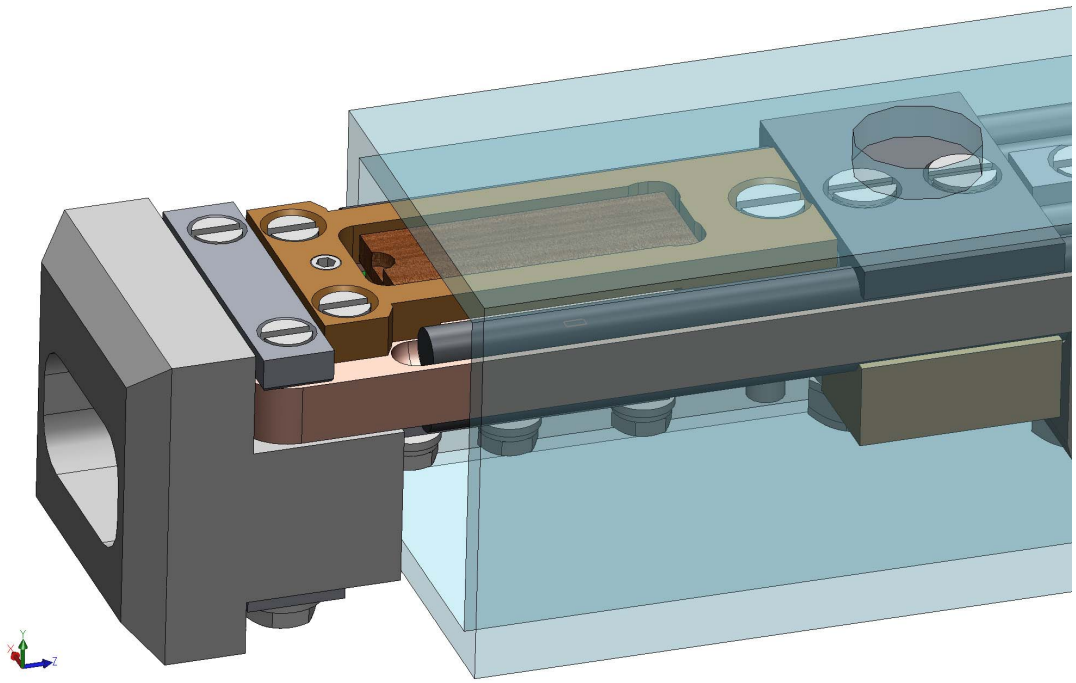

Figure 7.40: 3D CAD rendering of the Octopus lower end, top face. The blue rectangular prism represents the cryostat bottom bore, and the sample itself (represented by the piece of wood) would be aligned under the cryostat window hole.

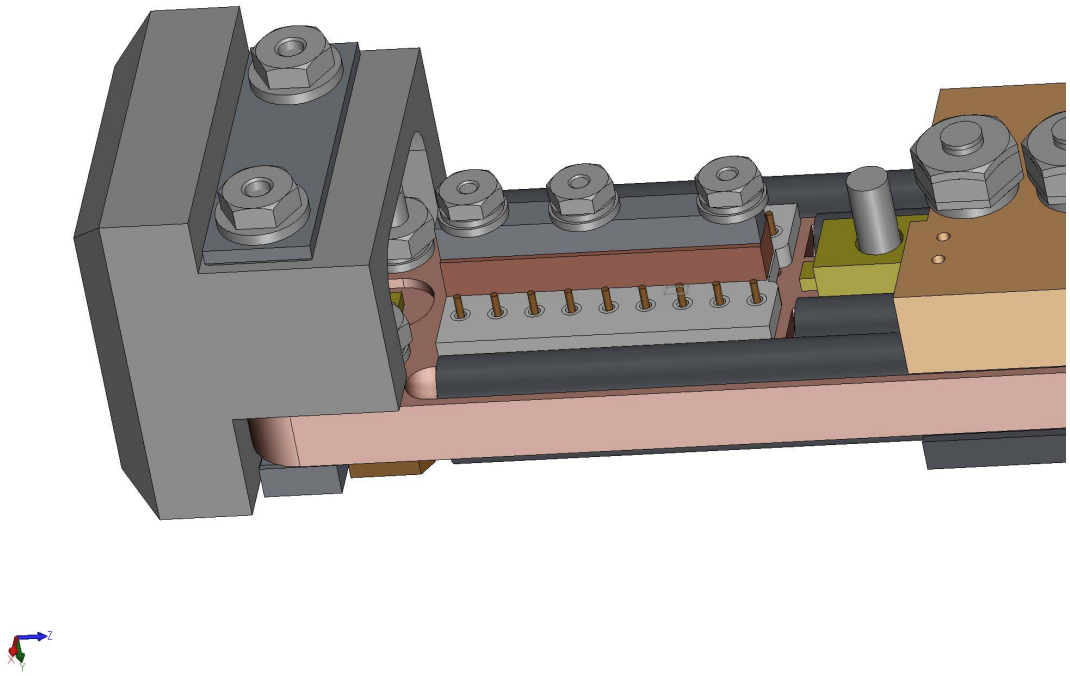

Figure 7.41: 3D CAD rendering of the Octopus lower end, bottom face.

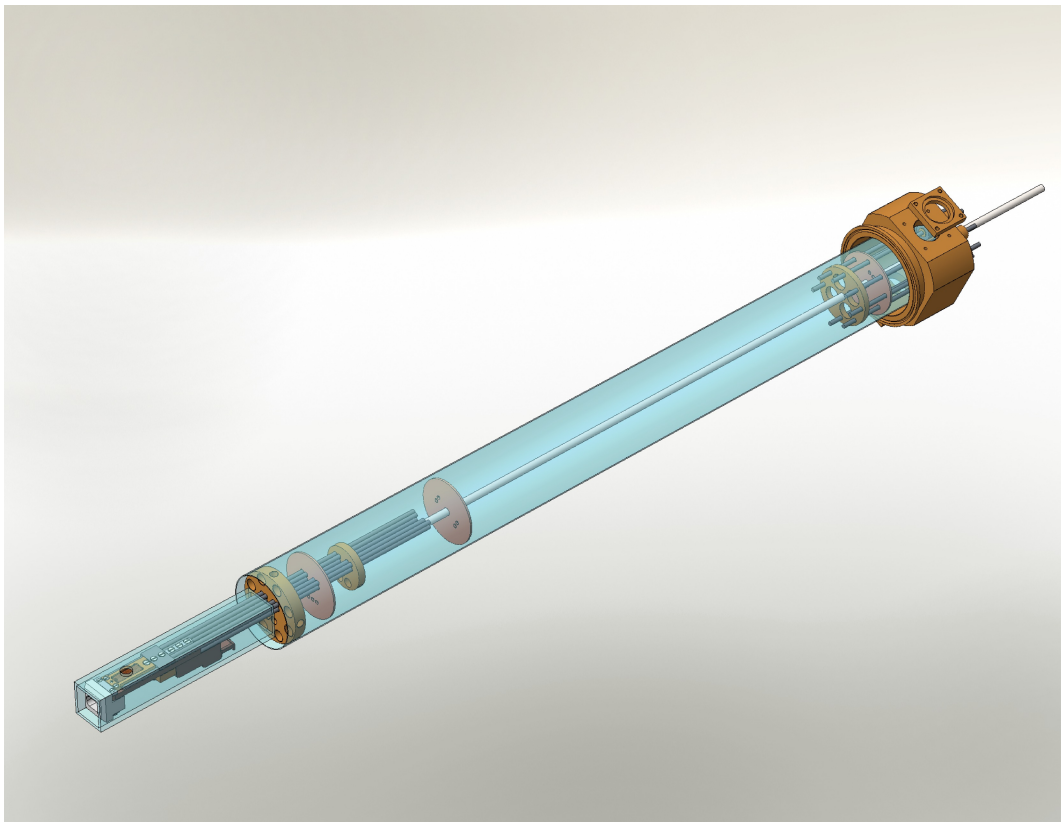

Figure 7.42: wholething-bore

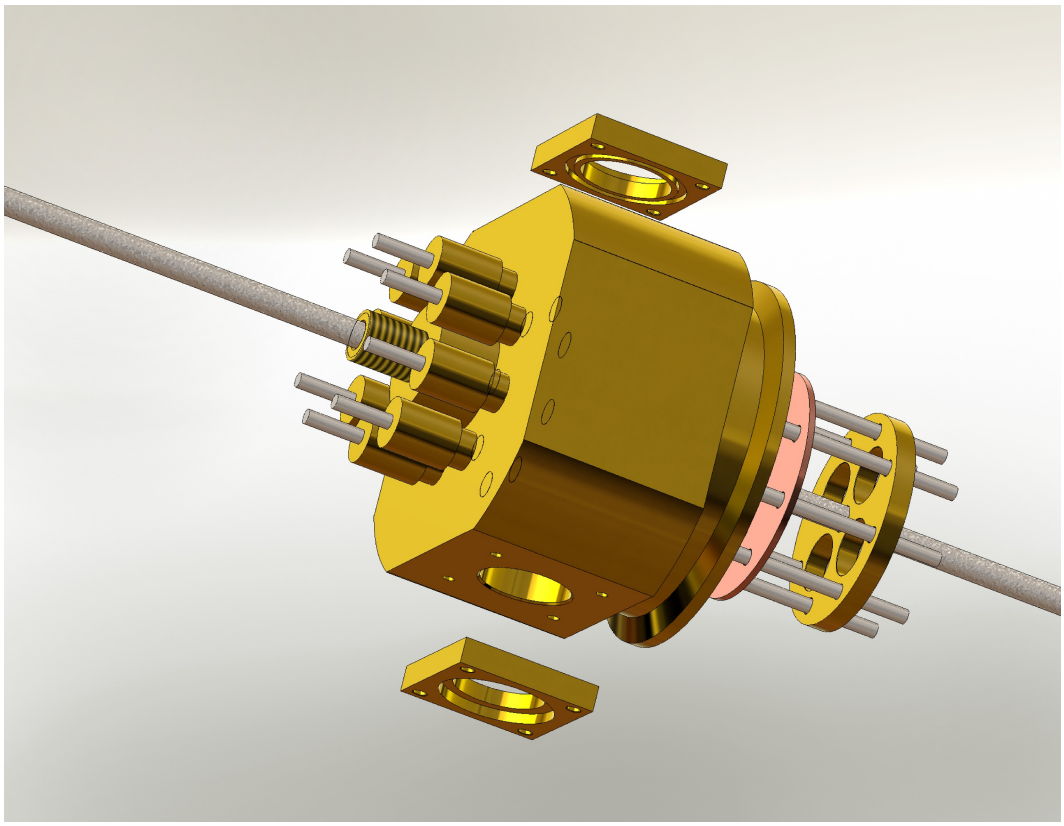

Figure 7.43: wholething-crown

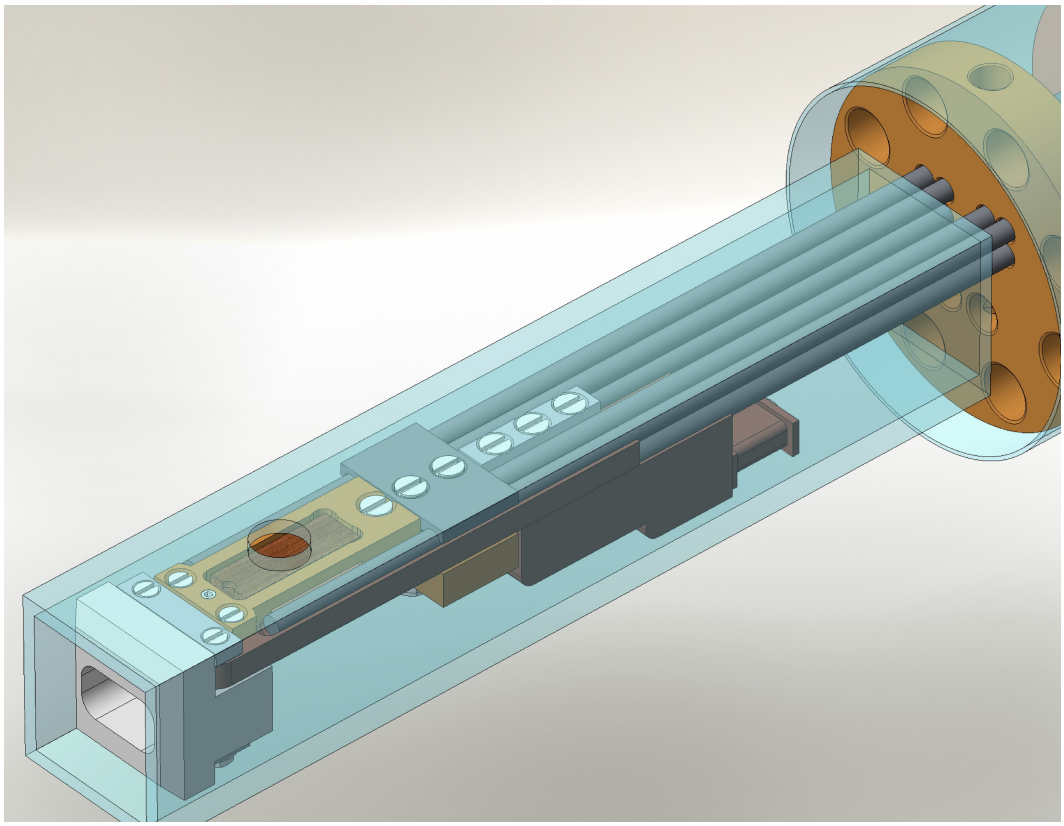

Figure 7.44: wholething-tail-bore

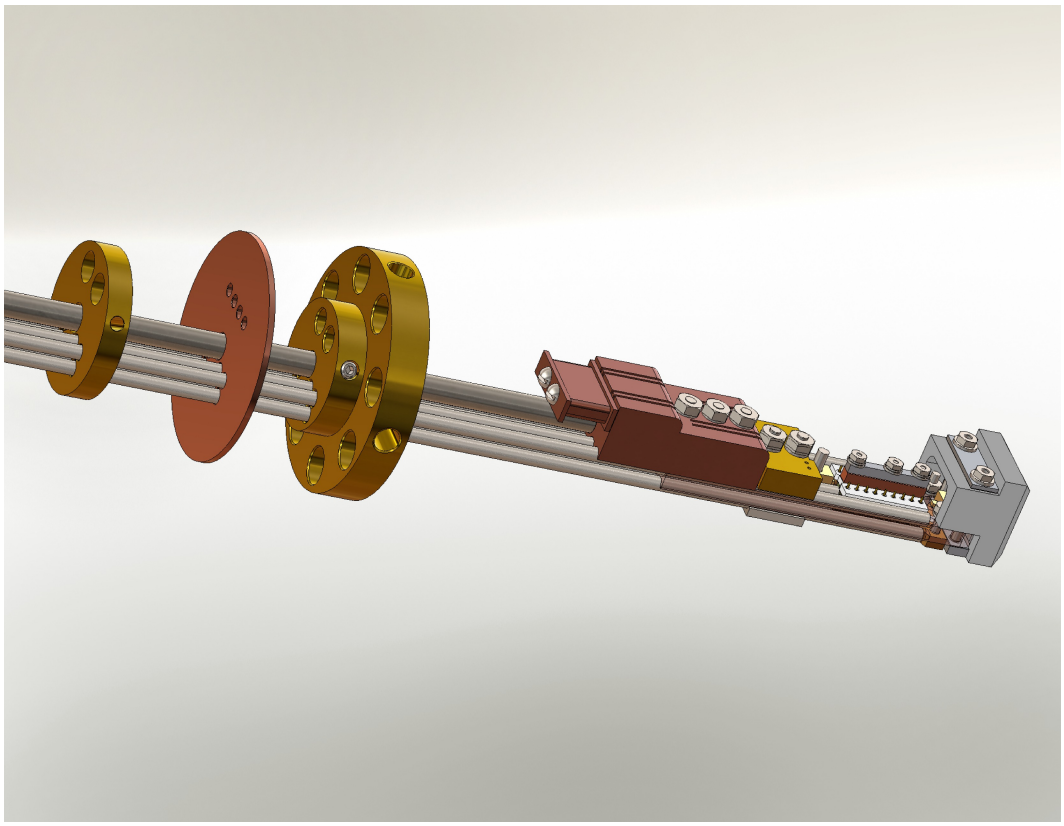

Figure 7.45: wholething-tail1

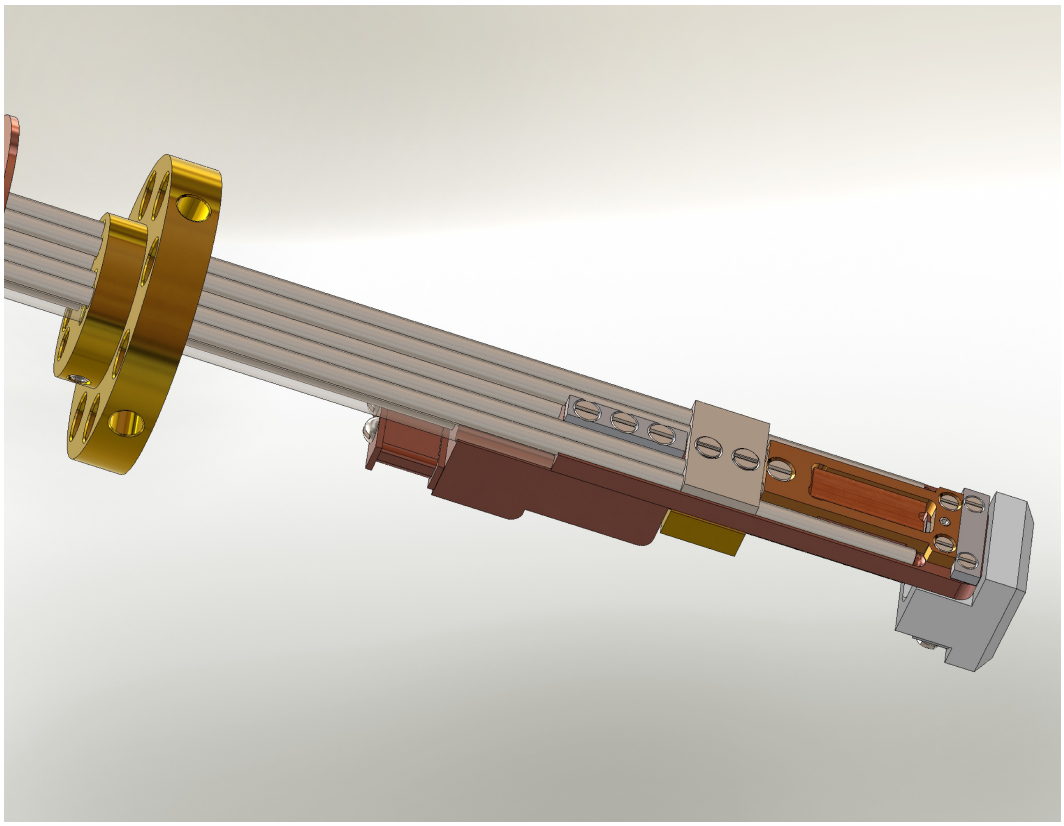

Figure 7.46: wholething-tail2

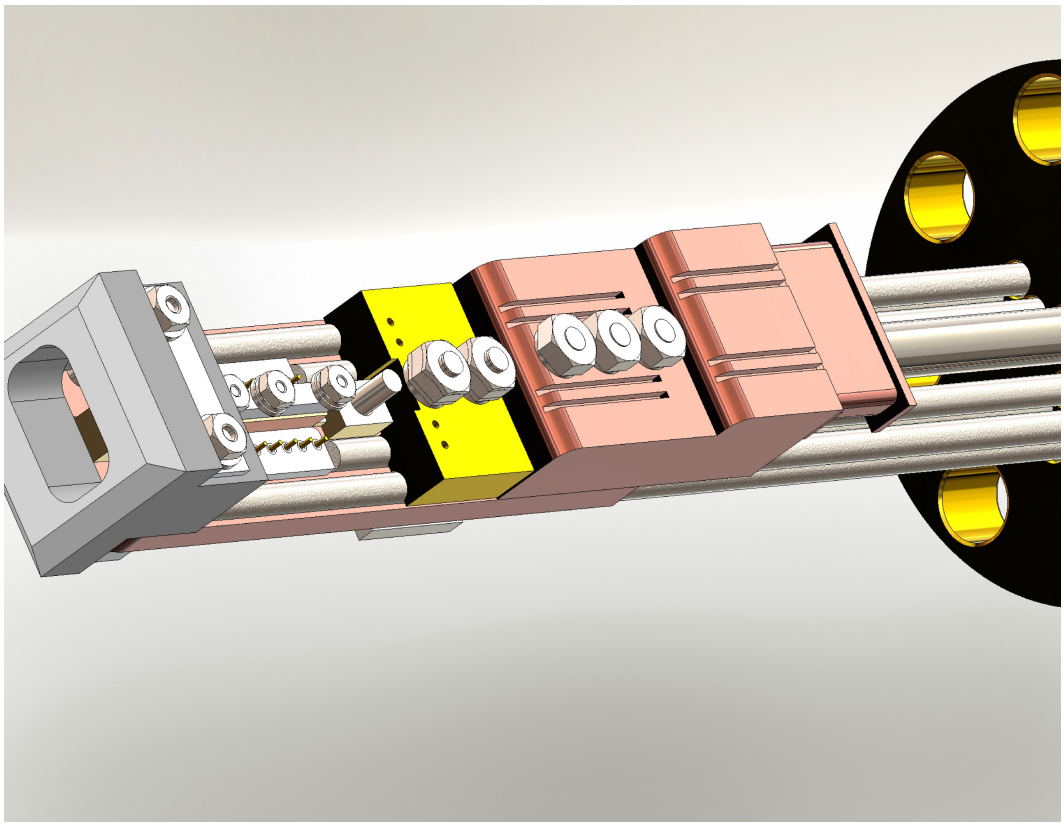

Figure 7.47: wholething-tail3

Part IV

Exciton conveyer

Chapter 8

Exciton conveyer: theory of operation and semiconductor device

8.1 Introduction

The ability to control exciton energy via gate voltage means that, in principle, it is possible to create arbitrary potential landscapes for excitons. *Electronic* devices (e.g., the FET) generally manipulate the in-plane movement of electrons by using electrode structures to create in-plane electric fields. For excitonic devices, large in-plane electric fields may lead to exciton disassociation. However, electrode structures creating spatially-varying out-of-plane electric fields create in-plane variations of indirect exciton energy — and such in-plane energy landscapes make certain *excitonic* devices possible. Landscape devices already demonstrated include:

Traps Diamond trap [High et al., 2009b], and the elevated trap [High et al., 2009a].

Transistors Electronically-controlled exciton transistor [High et al., 2007], exciton integrated circuit [High et al., 2008], and the optically-controlled exciton transistor [Kuznetsova et al., 2010b].

Static lattice [Remeika et al., 2009].

The demonstrated ability to create static in-plane energy landscapes is distinct from the demonstrated ability to manipulate the indirect exciton energy and lifetime very rapidly (ie, on timescales much faster than the indirect exciton's own lifetime), which led to the photonic storage device in Part II. These abilities can be combined to realize new exciton devices.

Excitons already move in the plane of a CQW structure by drift and by diffusion. The exciton conveyer is a device for *actively* transporting excitons.

8.1.1 Avoiding a side-effect: disassociation due to in-plane fields

Surface electrodes for creating out-of-plane electric field landscapes $F_z(x, y, z)$ can also create in-plane electric fields $F_r(x, y, z)$, and large in-plane electric fields are undesirable for excitonic devices because they can lead to exciton disassociation. However, these in-plane fields vary strongly with height z: at the top surface

they can be large (driven by adjacent electrode voltages and the distances between surface electrodes), but at the homogeneous ground plane they must necessarily be zero; thus, in-plane fields are progressively suppressed as one approaches the ground plane. Positioning the quantum wells near the bottom ground plane does not hinder the ability to control exciton lifetime or energy, and permits spatially-varying electrode designs on the top while avoiding exciton disassociation [Hammack et al., 2006].

8.1.2 Lateral fixed electrostatic lattice

Recently, Remeika et al. [2009] reported the realization of lateral electrostatic lattices for indirect excitons. Some of the main elements can be seen in Figure 8.1. A pair of interdigitated electrodes A and B are lithographically deposited on the surface of the sample, and connected to DC voltages $V_a = V_0 + \Delta V$ and $V_b = V_0 - \Delta V$, where V_0 is the gate voltage required to create indirect excitons and ΔV a perturbation. This leads to an oscillatory voltage potential at the sample surface and a nearly sinusoidal energy potential $E(x) = E_0 \cos^2(qx/2)$ (where the amplitude $E_0 = 3\,\mathrm{meV}$ for $\Delta V = 0.5\,V$ and lattice period $2\pi/q = 2\,\mu\mathrm{m}$ in the experiment), and hence a one-dimensional lattice potential for excitons.

The lattice period is set by the lithographically-deposited electrode pattern, but the lattice depth is controlled *in situ* by ΔV. Increasing the lattice depth causes the indirect excitons to localize in the lattice minima. Increasing the laser excitation increases the density of indirect excitons, and eventually their dipole-dipole repulsion energy can exceed the lattice depth (alternatively, the excitons become sufficiently numerous to fill in the lattice minima), causing the excitons to no longer be localized in the lattice minima. Thus, control of ΔV or laser excitation causes a localization-delocalization transition.

8.1.3 A traveling electrostatic lattice

We would like to combine this demonstrated ability to create a lateral electrostatic lattice with the demonstrated ability of rapid *in situ* control, to make a

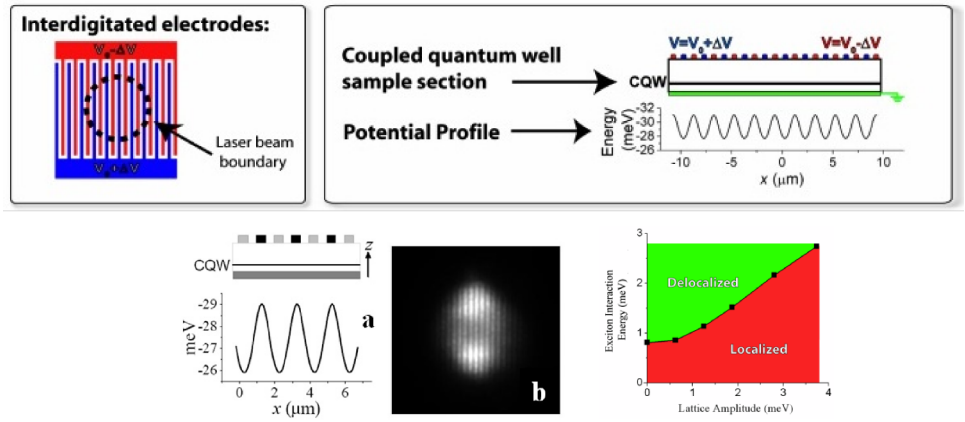

Figure 8.1: Features of a fixed lateral electrostatic lattice for excitons. Top left, a view of the interdigitated electrode structure; top right, a side profile of the device (lithographed lattice overlaying quantum wells), and a plot of exciton energy in the potential profile (for $\Delta V = 0.5\,\mathrm{V}$). Bottom center, a PL spatial (X-Y) image of indirect excitons in the lattice. From [Remeika, 2009; Remeika et al., 2009].

moving lattice. If such a moving lattice potential could be created and controlled in speed over a sufficiently broad range, several physical phenomena of interest would be open for exploration:

1. If the excitons' ability to follow a moving lattice (collect to the lattice minima) depends on the lattice velocity, there would be a *dynamic* localization-delocalization transition.

2. From the perspective of an exciton localized ("riding along") in a moving lattice, one might envision seeing an oncoming "phonon wind".

3. If the accessible velocity range is broad enough to span the phonon velocity, it might be be possible to study the behavior through a supersonic transition.

8.1.4 Electron/hole and exciton transport via surface acoustic waves

An alternative approach to transporting electrons and holes in a traveling lattice is by using surface acoustic waves. A pair of interdigitated electrodes de-

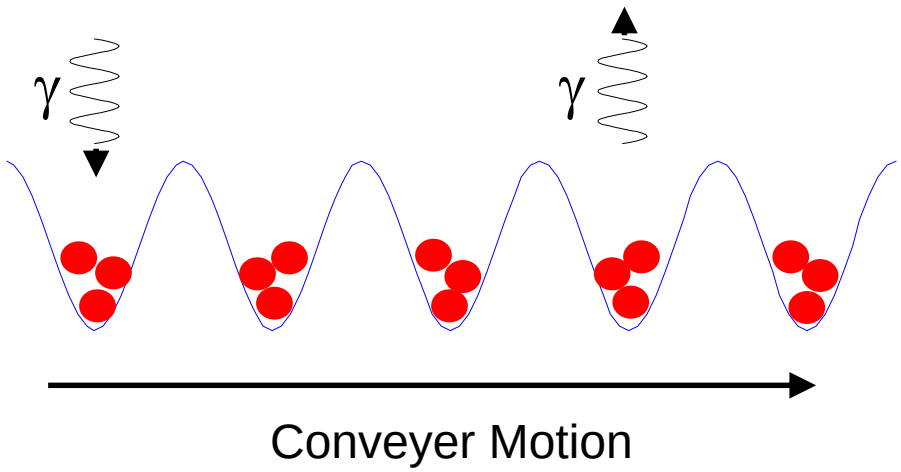

Figure 8.2: Cartoon illustrating the moving conveyer lattice potential carrying photoluminescent excitons.

posited lithographically on the sample surface can be driven with an AC sinewave (e.g., of order 500 MHz), acting as a transducer and exciting surface acoustic waves that travel across the sample surface. The SAW distorts the underlying semiconductor lattice piezoelectrically, and for quantum wells positioned near the surface (relative to the SAW wavelength), instantaneous potential minima and maxima are created at the wave peaks and troughs (electrons and holes regarding the amplitude peaks or troughs oppositely as energy potential minima or maxima). Photoexcited electrons and holes (excitons are disassociated by the lateral electric field) can collect to those moving minima and travel along at the wave phase velocity, the electrons and holes separated by half a wavelength [Rocke et al., 1997; Santos et al., 1999; Streibl et al., 1999]. More recently, transport has been demonstrated for excitons, by directing the SAW along a non-piezoelectrically-active axis of the semiconductor heterostructure, where the SAW strain field creates a lateral modulation of the band gap without large in-plane electric fields [Rudolph et al., 2007].

The depth of the potential wells is controlled by the strength of the RF signal supplied to the transducer (of order as large as $^{+}25$ dBm), and the resonant RF frequency determined by the choice of transducer geometry (spacing of the

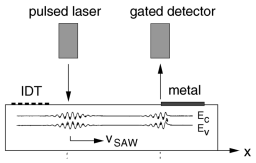

Figure 8.3: Schematic of a surface acoustic wave PL experiment. From Rocke et al. [1997]

interdigitated electrodes), itself determined by the desired SAW wavelength that sets the width of the potential minima.

A key limitation of this method is that the transport can only occur at the SAW sound velocity, which is essentially fixed characteristic of a given semiconductor material, and for which there is not a terribly wide range of choices. Being able to vary the velocity over a wide range, especially both above and below the sound velocity(ies), may lead to more optoelectronic device opportunities and permit exploration of new physics.

8.2 Conveyer device

8.2.1 Lithographic structure

The exciton conveyer is a laterally moving lattice potential for excitons, generated by electrode voltages laterally modulated in both space and time. The device begins with the CQW semiconductor heterostructure in Figure 2.8, with lithographic patterning atop the structure as illustrated in Figure 8.4. First, we lay down a set of (conveyer) lattice stripes; for this device, the stripes are 1 μm wide and 2 μm apart center-to-center, and there are hundreds of such stripes. Next, we lay down a layer of transparent indium titanium oxide (ITO) insulation. The lattice stripes will need to be periodically interconnected, which is done by laying down a set of access electrodes, which connect to the lattice electrodes through holes (1 μm-wide slits) in the transparent insulation.

The number of access electrodes determines the number of independent voltages that can be applied to the stripes, determining the periodicity of the resulting lattice. For the conveyer, it was determined by simulation that it would

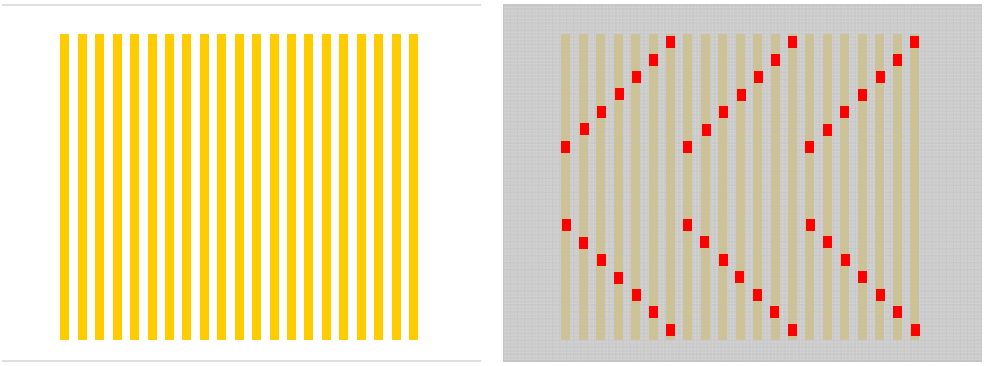

(a)

(b)

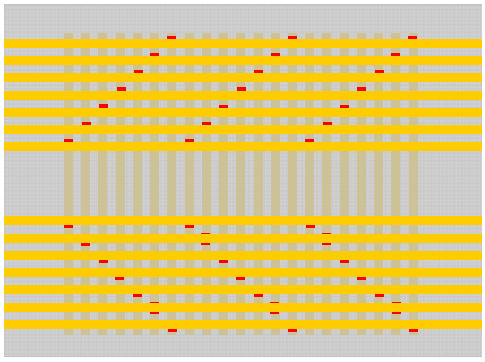

(c)

Figure 8.4: Cartoon of the conveyer device 3D photolithography structure, illustrating fabrication layers.
(a) First, hundreds of conveyer lattice stripes (1 μm-wide, 2 μm center-to-center) are laid down.
(b) Lattice stripes overlaid with a layer of transparent ITO insulator (light gray), incorporating a periodic array of holes (red, 1 μm-wide slits).
(c) Seven access electrodes overlay the insulation, interconnecting through the slits to the lattice stripes, so that the stripes form a 1-D lattice of period 14 μm with seven degrees of (voltage) freedom. The access electrodes are duplicated for redundancy.

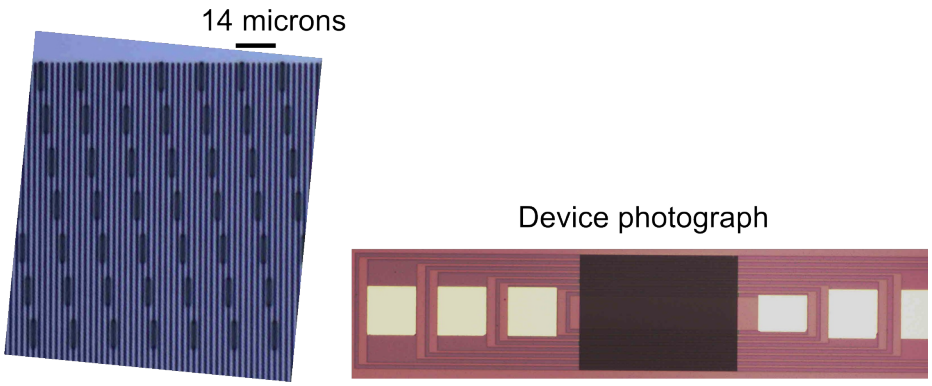

Figure 8.5: Left, photograph of a test sample at an intermediary fabrication step showing the 1 μm-wide slits. Right, photograph of a complete fabricated conveyer device with wirebond pads and conveyer region proper.

be desirable to have at least seven such degrees of freedom, to be able to piecewise-discretize a spatial sinewave with sufficient fidelity. (The earlier work described in Section 8.1.2, may be regarded as a two-degree-of-freedom version, albeit exploiting simpler, purely-planer geometry without the 3D-interconnect.) Thus, there are seven access electrodes, resulting in a periodic electrode lattice of period $\lambda = 7 * 2\mu\text{m} = 14\,\mu\text{m}$. The access electrodes are deposited in duplicate sets (above and below the lattice stripes) for redundancy in case of photolithographic imperfections, and run out to wirebond pads beyond the edges of the conveyer device region. Figure 8.5 are photographs illustrating fabrication geometries of both a test device showing the holes in the insulation and of the wider geometry of a completed device. Figure 8.6 is a schematic view of the wider device geometry.

8.2.2 Voltage and potential profile

This lithographic device structure creates a 1-D periodic lattice with 7 discretization degrees of freedom; by applying a set of DC voltages, one can design a semi-arbitrary purely static potential profile. The exciton conveyer is generated by driving this device by a set of 7 AC sinewaves, all of the same frequency f but successively phase-delayed by $1/7^{th}$ of a (temporal) period ($\Delta\phi = 2\pi/7$), i.e. the

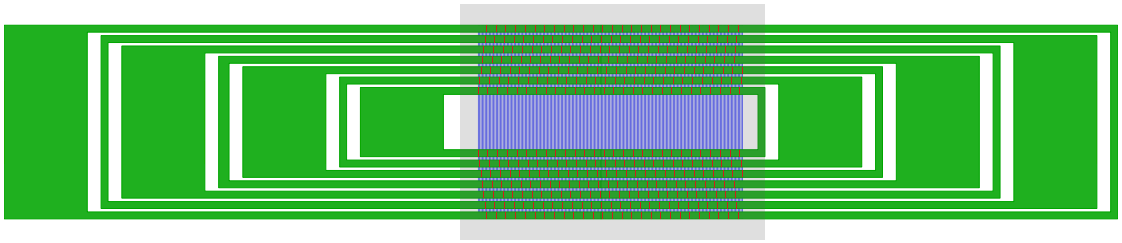

Figure 8.6: Photolithography pattern of the wider conveyer device structure. The conveyer region proper is in the center (under the transparent insulator, light grey rectangle), and the access electrodes run out to wire bonding pads (large green rectangles). The access electrodes are duplicated top and bottom for redundancy.

voltage on each access electrode $m \in \{1 \ldots 7\}$ is

$$V_m(t) = V_0 \cos(2\pi f t + m\frac{2\pi}{7}) + V_{\text{bias}}$$

The result is a (pseudo)sinusoidal[1] electrostatic wave of spatial wavelength λ oscillating in both space and time and traveling at $v = \lambda f$. The lattice depth and the conveyer velocity are controlled *in situ* respectively by the voltage V_0 and the frequency f. The DC voltage offset V_{bias} keeps the excitons in the indirect regime (and ordinarily $V_0 < V_{\text{bias}}$).

In order to drive the conveyer at velocities near the sound velocities in GaAs, ie several μm/ns, the lithographically-set wavelength $\lambda = 14\,\mu$m calls for frequencies of order a few hundred MHz, varying over a wide range of frequencies to provide a variety of velocities. The desired amplitude is of order a few volts. This necessitates a broadband multichannel RF system of fair power and variable phase delays, an additional engineering development described in the next chapter.

[1]Sharp variations in the potential profiles formed by a set of discrete voltages might be smoothed out by surface currents between the electrodes, given (real) nonzero inter-electrode conductivity.

Chapter 9

Conveyer RF system

Contents

9.1 Introduction

The conveyer device is driven by a set of seven differentially phase-delayed sine waves of amplitude of up to several volts and frequencies of order hundreds of MHz, where the operation frequency (controlling the conveyer velocity) needs to be varied over a wide range. Phase delays of $\frac{1}{7}(2\pi)\ldots\frac{6}{7}(2\pi)$ are needed for each particular frequency. The conveyer sample is installed in the Octopus multichannel cryogenic sample holder, and it is the task of the conveyer RF system to provide the broadband source signals.

Obtaining the requisite phase delays presented design challenges and a degree of precision in manufacturing and calibration.

To provide large enough voltage amplitude at the conveyer sample sites, the design total power before splitting was of order $^{+}27\,\mathrm{dBm}$ and a frequency range of at least 50–500 MHz and preferably capable of 1 GHz. Subsequently this was extended towards $^{+}33\,\mathrm{dBm}$ and down to 10 MHz. Such power levels of 1–2 W,

although apparently quite modest for e.g. DC electronics, are high for RF *instrumentation* (where a typical power level may be e.g., 1 mW). The frequency range — one to two decades — is extremely broadband for most RF *power* applications (where a typical frequency range might be more like 10 MHz modulation on a 500 MHz carrier, and "broadband" often means closer to a single octave!) Satisfying both the frequency and power requirements within a limited budget meant even versatile components would necessarily be used up to or even beyond their specified ratings, thus their "non-idealness" (secondary characteristics) became relevant as well as the interactions between each component. The system required meticulous design as an interacting whole, not merely as a sum of independent pieces hooked together.

This chapter is a complete description of the *what*, but only provides some of the *why* and some of the *how*.

9.2 Conceptual design

9.2.1 Single channel

The circuit schematic for a single channel (to a single access electrode on the conveyer device) is shown in Figure 9.1. A source sinewave provided outside the cryostat travels over a transmission line to the sample at the bottom of the cryostat, where the transmission line terminates with a $R = Z_0 = 50\,\Omega$ resistor to ground. The conveyer sample site is modeled as a capacitor (preferably of small capacitance) in parallel with the termination load. The source sinewave is AC-coupled, ie enters through a DC-block, and DC bias on the sample is provided separately at the bottom of the cryostat from an external voltage. The bias voltage ($V_{\text{bias}} \approx 4\,V$) would continuously dissipate $V_{\text{bias}}^2/Z_0 \approx 320\,\text{mW}$ of power for each channel, creating in aggregate a considerable heat load at the sample.

Such heating is undesirable because, at the least, it wastes liquid helium, and worse, leads to sample heating, possibly nonuniform sample temperature, and thermal movement of the sample holder. Helium boiling adds vibrations, and while operating in superfluid helium rather than vapor greatly improves the thermal

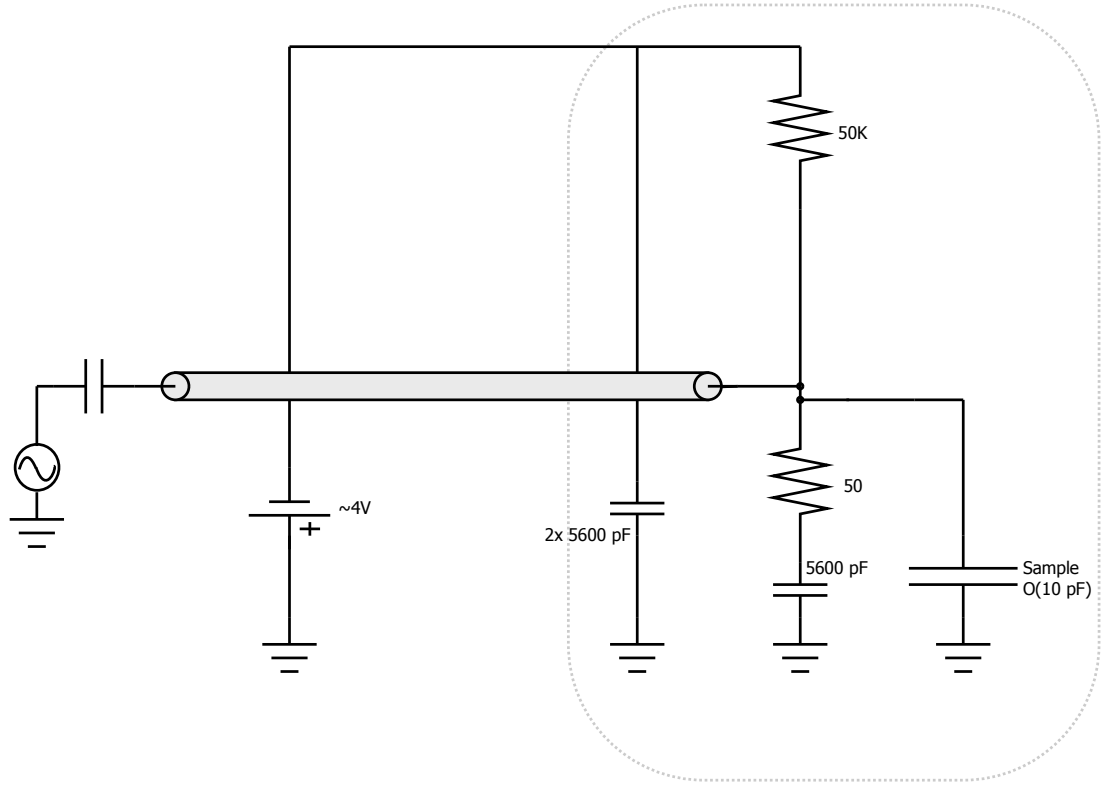

Figure 9.1: Circuit schematic for a single channel. After being generated, amplified, and split (not shown), a sinewave is AC-coupled into a transmission line down the cryostat. DC bias and resistive and capacitive termination are handled at the sample.

uniformity, the consumption rate is high. Therefore, the DC current is blocked by terminating with an additional (large) capacitor. Since the DC current is now negligible, RF leakage onto the DC voltage rail can be blocked by a large resistance (50 kΩ) rather than the conventional RF choke. (Finding inductors of adequate size in the small packaging available appear to be problematic, especially for cryogenic operation.) The DC rail is buffered (and remaining RF leakage shunted to ground) by large capacitors. The design and construction of the sample holder and PCB is described in Chapter 6 and Chapter 7.

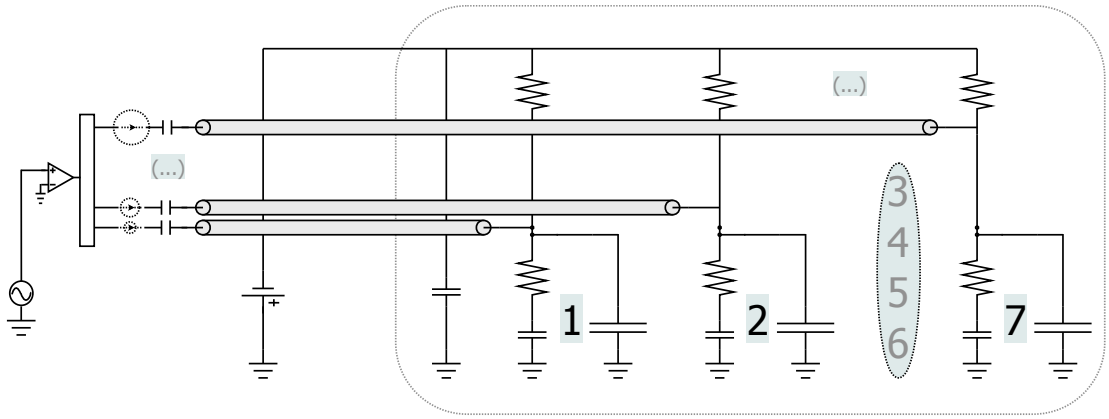

Figure 9.2: Circuit schematic for the multi-channel conveyer RF system, Octopus sample holder, and conveyer sample, as idealized without parasitic elements. The dotted rounded rectangle represents the cryostat. Sinewaves from a signal generator are amplified by the power RF amplifier, split by a combination of RF power splitters, individually phase-delayed by delay cables, and capacitively coupled to the Octopus coaxial transmission lines. External DC bias is applied to each channel at the sample through coupling resistors; the resistors block RF leakage into the bias rail, and leakage is shunted to ground through the buffer capacitor. The transmission lines terminate resistively for impedance matching and capacitively to block DC bias current to ground. Three of seven channels are shown for clarity.

9.2.2 Multi-channel block design

The conveyer RF system needs to provide (at least) seven such channels. The circuit schematic block diagram is shown in Figure 9.2. The source sinewave is supplied by a signal generator, amplified by an RF power amplifier, and then divided into nine channels by an RF splitter chain (two-level cascade of three-way splitters). Each channel passes through lengths of phase delay cable, and then DC blocks and into the Octopus's transmission lines.

9.2.3 Design alternatives

Custom PCB

The design actually used — monolithic block modules interconnected by coaxial cable and SMA couplings — was actually the second design. The more

obvious initial path would have been to build a dedicated printed circuit board with conventional surface-mount components, where the PCB would have used correct RF trace geometry. The design would have used nine separate amplifiers, one per channel; disparities in gain might be controlled by precision adjustment of each amplifier's power supply voltage, but individual variable attenuators might be needed. The key advantage, naturally, is that each channel of amplifier and signal splitter need handle much less power, opening a wider range of component choices. This approach was rejected because the up-front cost appeared greater, and the time to design the large PCB, send out for fabrication, populate, and test appeared unattractive; it would also have been somewhat less amenable to reconfiguration.

Directional couplers

Another option would have been that, rather than have nine channels including two duplicates for monitoring the seven needed, use only seven channels but add a directional coupler to "sniff" each channel. The great advantage would be in-situ monitoring of each conveyer channel in both amplitude and phase, rather than only two channels. In monolithic form, seven broadband directional couplers with sufficient power-handling would have added considerable expense; that approach may have worked better in the dedicated PCB design. Directional couplers have frequency-variable phase shift from the input to the coupled channels, and skew among the separate couplers would need to be calibrated out when measuring overall channel-channel relative phase.[1]

Phase delay

Phase delays can be supplied by many means other than lengths of delay cable, which have the disadvantages of needing to be cut precisely, non-adjustable (tunable), and suffering differential attenuation when the required lengths vary greatly. Superconducting delay lines remove the attenuation problem. NIM time-

[1]It was interesting to note that the phase shift data for one directional coupler appeared to be linear with frequency over most of the operation range, as if it were like a *negative* length of delay line, and could possibly be removed entirely with a precision *positive* (real) length of delay line.

delay modules (as used in e.g. the Ortec time-correlated photon counting system employed in Chapter 3 and Chapter 5) appear to have too large a stepping for the frequency range needed. LRC filter phase-delay is tunable, but over a narrow range near the resonant frequency and with strong attenuation off-resonance. Specialty time-delay modules are available for PCBs, but intended for pulses (ie, correcting clock skew), not CW.

Phase measurement

Signal phase different was actually measured between two channels of an oscilloscope (whose channels were checked for relative timing accuracy). This time-digitization method is not terribly accurate by itself, though an accuracy of better than a couple of degrees seemed obtainable with very long averaging. It may be sensitive to amplitude differences among the channels (which occurs, for example, if a longer delay line accumulates an attenuation difference versus the other reference line.) Another approach would have been dedicated phase detectors, or, instead of an oscilloscope (which is basically poorly suited for working in the *Fourier* domain), an RF vector voltmeter.[2] A vector network analyzer might work well for this role (since it is in some sense the combination of an RF vector voltmeter and an RF lock-in amplifier), but would need large external attenuators to avoid destroying the sensitive inputs.

9.2.4 Choosing operation frequencies

The choices of operation frequency and phase-delay methods are illustrated in Table 9.1, an early design document. Operation well above and below $\sim 350\,\mathrm{MHz}$ was desired to access conveyer velocities above and below the sound velocity. Frequencies of a few tens of MHz correspond to transport velocities where the excitons would expect to be barely carried beyond the laser excitation spot.[3]

[2] If I had known about such a creature and been able to borrow one!

[3] At this stage, the means of signal source generation were less clear; the natural choice of a dedicated RF signal generator was unavailable within budget limits, and methods were explored that included such tactics as subverting a pulse generator for sinusoidal operation. This explains some of the peculiar entries in Table 9.1. Fortunately, such measures became unnecessary when we were luckily able to borrow the correct equipment.

Table 9.1: A design document illustrating frequency goals and options, including different methods of obtaining phase delays, and the impact of different choices on phase delay lines.

Exciton Conveyor Electrical Time and Distance Scales

Alex Winbow, 25 Mar 09
6 Apr 09, 14 Jul 09

Assumptions:

wavelength	= 14 um	
v_signal [cm/ns]	25.18	(NOTE: This is 83% of c0 for LMR-series cable, ***not*** the 66% in regular RG-58 coax)
indirect lifetime	= 100 ns	(@ 3.6V, decreasing to 30ns)
v_phonon	= 4800 m/s = 4.8 um/ns	(varies weakly with temp, strongly with crystal direction; this is for <100>)
v_gas	= 1000 m/s = 1 um/ns	?? Assertion
Diffusion length	= 30 um	?? Assertion

Comment	Frequency [MHz]	Wave velocity [um / ns]	Distance travel in lifetime: long life [um]	short life [um]	Period [ns]	Delay step time [ns]	Delay step length [cm]	Delay step length [ft]	Longest delay line **[ft]**	Attenuation over [ft] 14.2: LMR195 **[dB]**	LMR240UF **[dB]**
~3x sound	1000	14.00	1400	420	1.0	0.14	3.6	0.1	0.7	1.7	1.4
200% sound	680	9.52	952	286	1.5	0.21	5.3	0.2	1.0	1.4	1.1
125% sound	430	6.02	602	181	2.3	0.33	8.4	0.3	1.6	1.1	0.9
100% sound	**340**	**4.76**	**476**	143	**2.9**	**0.42**	10.6	0.3	2.1	1.0	0.8
pulser-II max freq. (302)	300	4.20	420	126	3.3	0.48	12.0	0.4	2.4	0.9	0.7
pulser-I max freq.	285	3.99	399	120	3.5	0.50	12.6	0.4	2.5	0.9	0.7
0.5 ns delay step	285	3.99	399	120	3.5	0.50	12.6	0.4	2.5	0.9	0.7
6 inch cable length step	233	3.26	326	98	4.3	0.61	15.4	0.5	3.0	0.8	0.6
1 ns delay step	143	2.00	200	60	7.0	1.00	25.2	0.8	5.0	0.6	0.5
1 ft. cable length step	117	1.63	163	49	8.6	1.23	30.9	1.0	6.1	0.6	0.5
v_gas?	**75**	**1.05**	**105**	**32**	**13.3**	**1.90**	**48.0**	1.6	9.4	0.4	0.4
2 ft. cable length step	58	0.82	82	24	17.2	2.45	61.8	2.0	12.2	0.4	0.3
1/6th pulser; lowest VCC	***50***	***0.70***	***70***	***21***	***20.0***	***2.86***	***72.0***	***2.4***	***14.2***	***0.4***	0.3
4 ft. cable length step	29	0.41	41	12	34.3	4.90	123.5	4.1	24.3	0.3	0.2
transport = diffusion	22	0.30	30	9	46.5	6.64	167.3	5.5	32.9		
	1	0.01	1.40	0.42	1000.0	142.86	3597.5	118.0	708.2		

Delay line methods:

Type	Comments
NIM modules (Ortec etc.)	some not HF (timesteps!)
coax cables	attenuation at LF
specialty delay lines	prob. same as cables
supercon delay lines	need LN2
LRC phase delay	dispersive, narrow bandwidt
delay mod. circuit pieces	not sure work for CW

Phase Angles:

channel	theta (deg)
1	0
2	51
3	103
4	154
5	206
6	257
7	309

Accessible frequencies

Harmonic of 29 [MHz]	Harmonic of 50 [MHz]	Harmonic of 58 [MHz]	[MHz]	Harmonic of 233 [MHz]
			87	
3			146	
5				
		3	175	
9			262	
		5	291	
	6		300	
11			320	
	8		400	
	13		650	
			699	3
			1165	5

The key issue with phase delay cables is that it is possible to obtain the correct relative delays at multiple frequencies of operation, not just a single set of cables for a single frequency — but the useable frequencies are quantized. Choice of the fundamental and accessible harmonics (set by the delay length stepping) defines what velocities are experimentally accessible. The phase delay calculations are explained in greater detail in Section 9.4, but it became clear that choosing the fundamental frequency to be near 50 MHz would provide a number of accessible transport velocities between minimally-measurable (minimal transport distance) and the sound velocity, and that supersonic transport would probably be achievable at useable harmonics before channel-skew (both phase and amplitude) became excessively destructive. The anticipated range of operation is illustrated in Table 9.2.

Table 9.2: Chosen operation frequencies and velocities; numbers are *approximate*, based on a fundamental of 50.0 MHz.

Alex Winbow, July 2009

Assumptions:

wavelength	= 14 um	
v_signal [cm/ns]	25.18	(NOTE: This is 84% of c0 for LMR-series cable, ***not*** the 66% in regular RG-58 coax)
indirect lifetime	= 100 ns	(@ 3.6V, decreasing to 30ns)
v_phonon	= 4800 m/s = 4.8 um/ns	(varies weakly with temp, strongly with crystal direction; this is for <100>)
v_gas	= 1000 m/s = 1 um/ns	?? Assertion
Diffusion length	= 30 um	?? Assertion

Comment	Mode [#]	Frequency [MHz]	Wave velocity [um / ns]	Distance travel in lifetime: long life [um]	Distance travel in lifetime: short life [um]	Period [ns]	Delay step time [ns]	Delay step length [cm]	Delay step length [ft]	Longest delay line **[ft]**	Attenuation over [ft] 14.2: LMR195 **[dB]**	Attenuation over [ft] 14.2: LMR240UF **[dB]**
α-forward	22	1100	15.40	1540	462	0.9	0.13	3.3	0.11	0.6	1.7	1.4
standing wave, phase indt.	21	1050	14.70	1470	441	1.0	0.14	3.4	0.11	0.7	1.7	1.4
α-backward	20	1000	14.00	1400	420	1.0	0.14	3.6	0.12	0.7	1.7	1.4
β-backward?	19	950	13.30	1330	399	1.1	0.15	3.8	0.12	0.7	1.6	1.3
γ-backward?	18	900	12.60	1260	378	1.1	0.16	4.0	0.13	0.8	1.6	1.3
γ-forward	17	850	11.90	1190	357	1.2	0.17	4.2	0.14	0.8	1.5	1.2
β-forward	16	800	11.20	1120	336	1.3	0.18	4.5	0.15	0.9	1.5	1.2
α-forward	15	750	10.50	1050	315	1.3	0.19	4.8	0.16	0.9	1.4	1.2
standing wave, phase indt.	14	700	9.80	980	294	1.4	0.20	5.1	0.17	1.0	1.4	1.1
α-backward	13	650	9.10	910	273	1.5	0.22	5.5	0.18	1.1	1.3	1.1
β-backward?	12	600	8.40	840	252	1.7	0.24	6.0	0.20	1.2	1.3	1.0
γ-backward?	11	550	7.70	770	231	1.8	0.26	6.5	0.21	1.3	1.2	1.0
γ-forward	10	500	7.00	700	210	2.0	0.29	7.2	0.24	1.4	1.2	0.9
β-forward	9	450	6.30	630	189	2.2	0.32	8.0	0.26	1.6	1.1	0.9
α-forward	8	400	5.60	560	168	2.5	0.36	9.0	0.30	1.8	1.0	0.8
standing wave, phase indt.	7	350				2.9	0.41	10.3	0.34	2.0	1.0	0.8
100% sound		**340**	**4.76**	**476**	143	**2.9**	**0.42**	10.6	0.35	2.1	1.0	0.8
α-backward	6	300	4.20	420	126	3.3	0.48	12.0	0.39	2.4	0.9	0.7
β-backward?	5	250	3.50	350	105	4.0	0.57	14.4	0.47	2.8	0.8	0.7
γ-backward?	4	200	2.80	280	84	5.0	0.71	18.0	0.59	3.5	0.7	0.6
γ-forward	3	150	2.10	210	63	6.7	0.95	24.0	0.79	4.7	0.6	0.5
β-forward	2	100	1.40	140	42	10.0	1.43	36.0	1.18	7.1	0.5	0.4
v_gas?		**75**	**1.05**	**105**	**32**	**13.3**	**1.90**	**48.0**	1.57	9.4	0.4	0.4
α-forward (baseline)	***1***	***50***	***0.70***	***70***	***21***	***20.0***	***2.86***	***72.0***	***2.36***	***14.2***	***0.4***	0.3
transport = diffusion		22	0.30	30	9	46.5	6.64	167.3	5.49	32.9	0.2	0.2

9.2.5 Amplitude/power/attenuation budget

Early on, it become clear that satisfying the required voltage amplitudes at the conveyer across the required frequency range would be difficult using affordable amplifiers. The feasibility of the overall system became quite sensitive to the precise specifications of *each* component — not merely the *nominal* specifications but the real-world actual performance. (Ie, manufacturer's spec tolerance and manufacturing variation became critical). Beyond insertion losses and flatness, account needed to be taken (and possible components rejected in the design) due to e.g. poor VSWR matching. Table 9.3 is a design document showing the design amplitude/power/attenuation budget for the principal components used in the first stage of the experiment. Subsequently, during the course of successful experiments it become possible to purchase a second, more powerful amplifier, although that thereby necessitated replacement of one of the power splitters and both reduced the available frequency range of operation.

9.3 RF components and cabling

The key components used are listed in Table 9.4.

Cabling

For the lengths of cable required in the system, including cumulative interconnect cables but especially the differential lengths of delay line, standard RG-58 coax would not be adequate. Crosstalk among many parallel runs at identical frequency and constant phase-shift was a concern. RG-6 would be troublesome to use given the high probability of wiring "spaghetti", need to dynamically rewire the system, and restrictions on physical flexibility and minimal bend radius. LMR-240UF cable proved attractive. The outer shield includes a multi-ply bonded foil element with continuous outer coverage rather than a fractional braid, affording enormous inter-cable isolation. The cable attenuation characteristics are superb, providing RG-6 performance in an ultra-flexible RG-58-size diameter. Due to the

Table 9.3: Amplitude/power/attenuation budget as initially designed

Alex Winbow | Conveyor Attenuation Budget | July 2009

	Typical	***Worst-case***
Starting peak-to-peak amplitude [V]	17	11.3
Starting RMS amplitude [V]	6.01	4.00
Starting power (for ZHL-2010+) [dBm]	28.6	25.0
Segment	*Loss [dB]*	*Loss [dB]*
RF power amplifier VSWR insertion loss (in)	0.3	0.5
RF power amplifier VSWR insertion loss (out)	0.3	0.5
Attenuator nominal attenuation	1	1
Attenuator insertion loss	0.3	0.3
Splitter nominal attentuation (cascade 3-way)	9.6	9.6
Splitter insertion loss (combined)	1.4	3
Cable interconnects, cumulative (not opt)	0.6	1.2
Cable: delay line	0.8	1.4
Octopus semi-rigid cable	0.6	0.8
Semi-rigid SMA connector loss		
Octopus lower assembly losses?????		
individual SMA connector loss	0.016	0.030
Total SMA connector losses	0.23	0.42
(losses typical/worst @ usually 350MHz / 1GHz)		
Total losses [dB]	*15.1*	*18.8*
Remaining power [dBm]	13.4	6.3
Remaining RMS amplitude [V]	1.1	0.5
Remaining peak-to-peak amplitude [V]	3.0	1.3
Remaining semi-amplitude [V]	***1.49***	0.65
Margin above minimal (1V p-t-p) [dbM]	9.4	2.3
Margin above preferred (2V p-t-p) [dbM]	3.4	-3.7

conductor geometry and dielectric, the signal phase velocity is $0.84c$ rather than the $\sim 0.66c$ more typical among coaxial cables.

9.4 Phase delay lines

The simplest approach to using delay cables to obtain a set of phase delays at multiple frequencies is to use a complete set of cables for each desired operating frequency. However, considerable economy is possible, because a particular set of

Table 9.4: Principal Conveyer RF system components. All use SMA connectors.

Component	p/n	Sel. parameters	Qty
Amplifier, broadband	Minicircuits ZHL-2010+	1 W	1
Amplifier, broadband	Minicircuits ZHL-1-2W-S	2 W	1
Power splitter	Minicircuits ZFSC-3-4B-S+	3-way, 1 W	4
Power splitter	Minicircuits ZA3CS-400-3W-S	3-way, 3 W	1
DC Block	Minicircuits BLK-89-S+		9
Coaxial cabling	Tessco 40260	LMR-240UF	$\sim$ 200 ft

Table 9.5: Properties of LMR-240UF coaxial cable

Times Microwave LMR-240UF
Inner conductor: stranded bc
Outer conductors: braided tinned copper, aluminum tape bonded foil
Bend radius: 2.5 in (for repeated bends)
Velocity: 0.84 c
Capacitance: 24.2 pf/ft Inductance: 0.060 uH/ft
Isolation: $>$ 90 dBm (ie, 180 dBm between two cables)
Attenuation: 2.1 dB/100 ft @ 50MHz, 9.1 db @ 900 MHz

cable lengths can be used at multiple frequencies – not merely one octave above the fundamental, but at intermediate quantized frequencies. This is illustrated in Table 9.6. However, if the cables are being used at harmonics above the fundamental, the precision with which the cables are cut to specified lengths becomes essential. The phase delay cables used for all modes except #7 are given in the design document Table 9.7 and for #7 in Table 9.8.

In this case, the cable lengths are specified to sixteenths of an inch. The reason is simply that the commercial manufacturer measures cables on the fabrication cable using a measure whose finest graduations are sixteenths of an inch. Excellent results can be obtained by careful explanation and request.

Table 9.6: Accessible phase delays at multiple frequency modes (in normalized units), illustrating how correct delays can also be obtained not merely at mode #8 (directly conjugate to mode #1), but at modes #2-#6 if the cables are rearranged in three different permutations and forward or reversed-order.

Abstract phase delay w/o inversion

Velocity = 1 Frequency	Period	Wavelength	Length:	Cable A 0/7	Cable B 1/7	Cable C 2/7	Cable D 3/7	Cable E 4/7	Cable F 5/7	Cable G 6/7	Comment
1	1	1	Incremental shift:		1/7	2/7	3/7	4/7	5/7	6/7	α–forward (baseline)
			Total phase shift:		**1/7**	**2/7**	**3/7**	**4/7**	**5/7**	**6/7**	
2	1/2	1/2	Incremental shift:		2/7	4/7	6/7	1 1/7	1 3/7	1 5/7	β–forward
			Total phase shift:		2/7	4/7	6/7	1/7	3/7	5/7	
3	1/3	1/3	Incremental shift:		3/7	6/7	1 2/7	1 5/7	2 1/7	2 4/7	γ–forward
			Total phase shift:		3/7	6/7	2/7	5/7	1/7	4/7	
4	1/4	1/4	Incremental shift:		4/7	1 1/7	1 5/7	2 2/7	2 6/7	3 3/7	γ–backward?
			Total phase shift:		4/7	1/7	5/7	2/7	6/7	3/7	
5	1/5	1/5	Incremental shift:		5/7	1 3/7	2 1/7	2 6/7	3 4/7	4 2/7	β–backward?
			Total phase shift:		5/7	3/7	1/7	6/7	4/7	2/7	
6	1/6	1/6	Incremental shift:		6/7	1 5/7	2 4/7	3 3/7	4 2/7	5 1/7	α–backward
			Total phase shift:		**6/7**	**5/7**	**4/7**	**3/7**	**2/7**	**1/7**	
7	1/7	1/7	Incremental shift:		1	2	3	4	5	6	
			Total phase shift:	0	0	0	0	0	0	0	
8	1/8	1/8	Incremental shift:		1 1/7	2 2/7	3 3/7	4 4/7	5 5/7	6 6/7	α–forward
			Total phase shift:		**1/7**	**2/7**	**3/7**	**4/7**	**5/7**	**6/7**	
9	1/9	1/9	Incremental shift:		1 2/7	2 4/7	3 6/7	5 1/7	6 3/7	7 5/7	β–forward
			Total phase shift:		2/7	4/7	6/7	1/7	3/7	5/7	
10	1/10	1/10	Incremental shift:		1 3/7	2 6/7	4 2/7	5 5/7	7 1/7	8 4/7	γ–forward
			Total phase shift:		3/7	6/7	2/7	5/7	1/7	4/7	
11	1/11	1/11	Incremental shift:		1 4/7	3 1/7	4 5/7	6 2/7	7 6/7	9 3/7	γ–backward?
			Total phase shift:		4/7	1/7	5/7	2/7	6/7	3/7	
12	1/12	1/12	Incremental shift:		1 5/7	3 3/7	5 1/7	6 6/7	8 4/7	10 2/7	β–backward?
			Total phase shift:		5/7	3/7	1/7	6/7	4/7	2/7	

Table 9.7: Design document for phase delay cables

Custom cable assemblies for Alex Winbow <awinbow@physics.ucsd.edu> **Revision: 27 Aug 09**

All cable assemblies made from LMR-240UF, with SMA male connectors on both ends

LMR-240UF	Tessco# 40260	
SMA plug for 240 cable	Tessco# 315399	(two per assembly)

Description for cable assemblers:

Measurement: Measure and cut lengths as raw cables.
Assemblies will be slightly longer tip-to-tip after adding connectors, but that will be identical for all.
It is important that cables are *consistent.*
Precision: here 1/16 inch
(Application: Precision subnanosecond timing delays for scientific electronics)

Cable Name	Billing Length [ea] [ft]	Cut length [ft]	Cut length [in]	**Cut length [in]**	Cut length [cm]	Quantity [#]	Extended Billing Length [ft]	Length as Received [cm]
(Note that these cables are all stepped in lengths increasing consecutively by 28 5/16 inches)								
A	1	1.000	12.0000	**12**	30.5	2	2	32.0 & 32.1
B	4	3.359	40.3125	**40.31**	102.4	1	4	123.0
C	6	5.719	68.6250	**68.63**	174.3	1	6	183.0
D	9	8.078	96.9375	**96.94**	246.2	1	9	274.9
E	11	10.438	125.2500	**125.25**	318.1	1	11	335.6
F	13	12.797	153.5625	**153.56**	390.0	1	13	395.5
G	16	15.156	181.8750	**181.88**	462.0	2	32	487.4 & 487.9
(These are interconnect cables, at even lengths in feet for convenience, but they also need to be measured consistently.)								
H	1	1				4	4	
I	2	2				4	8	
J	3	3				2	6	
K	6	6				9	54	

Total number of assembled cables	Total billing length
28	149 [ft]

Table 9.8: Phase-delay cable lengths for mode#7

Cable id	Length [in]
A, A′	12 0/16
B	20 4/16
C	28 8/16
D	36 12/16
E	45 0/16
F	53 4/16
G, G′	61 8/16
Length stepping: 8.25 in	

Table 9.9: Design document for mode #7 phase delay cables

Custom cable assemblies for Alex Winbow <awinbow@physics.ucsd.edu> **Version: 11 May 2010**

All cable assemblies made from LMR-240UF, with SMA male connectors on both ends

LMR-240UF	Tessco# 40260	
SMA plug for 240 cable	Tessco# 315399	(two per assembly)

Description for cable assemblers:

Measurement: Measure and cut lengths as raw cables.
Assemblies will be slightly longer tip-to-tip after adding connectors, but that will be identical for all.
It is important that cables are *consistent.*
Precision: here 1/16 inch
(Application: Precision subnanosecond timing delays for scientific electronics)

Cable Name	Billing Length [ea] [ft]	Cut length [ft]	Cut length [in]	**Cut length [in]**	Quantity [#]	Extended Billing Length [ft]
(Note that these cables are all stepped in lengths increasing consecutively by 8.500 inches)						
A	1	1.000	12.000	**12**	2	2
B	2	1.708	20.500	**20 8/16**	1	2
C	3	2.417	29.000	**29**	1	3
D	4	3.125	37.500	**37 8/16**	1	4
E	4	3.833	46.000	**46**	1	4
F	5	4.542	54.500	**54 8/16**	1	5
G	6	5.250	63.000	**63**	2	12

Total number of assembled cables	Total billing length
9	32 [ft]

9.5 Frequency calibration

Although the phase-delay cables are carefully specified in length for operation at particular frequencies, even correctly-manufactured cables turn out to operate differently than designed. A cable's physical and electrical length may not be the same, due to e.g. the effects of end connectors or variation in propagation velocity with manufacturing batch or even cable bend angles (altering the coaxial geometry). The actual frequencies of operation differ from the design frequencies, and it was necessary to calibrate the actual performance. It is important to emphasize that at the higher operation modes, the longer delay cables are "looping" by many whole periods: for example, what might be an tolerable 5° phase error at mode #1 becomes a 45° error at mode #9, almost as large as and hence utterly invalidating the 51° shift the cable exists to create!

In principal, this could be done simply by e.g. time-delay reflectometry measurement of the actual (electrical) end-to-end cable length, but picosecond TDR is not trivially available. (Even later on, with access to vector network analyzers, we could not accurately calibrate their performance beyond a few GHz;

that is rather insufficient length resolution when simulating TDR via Fourier-transform.) Furthermore, cable lengths alone do not take account of differential phase skew among the multiple terminals of the splitter cascade. Thus, phase delay performance was actually calibrated by measuring end-to-end phase "zeros" at many frequencies, using that to extract corrections to the cable lengths (or, alternatively, propagation velocities), using that to predict the corrected operation frequencies, and then tuning those frequencies by hand to minimize the deviations across all channels on some average basis for each operation mode. (Clearly, perfect delay could be obtained for any one channel at a time, but not the other channels simultaneously.)

The phase calibration measurements and calculations are too cumbersome to present in detail here; see Appendix D for tabulations.

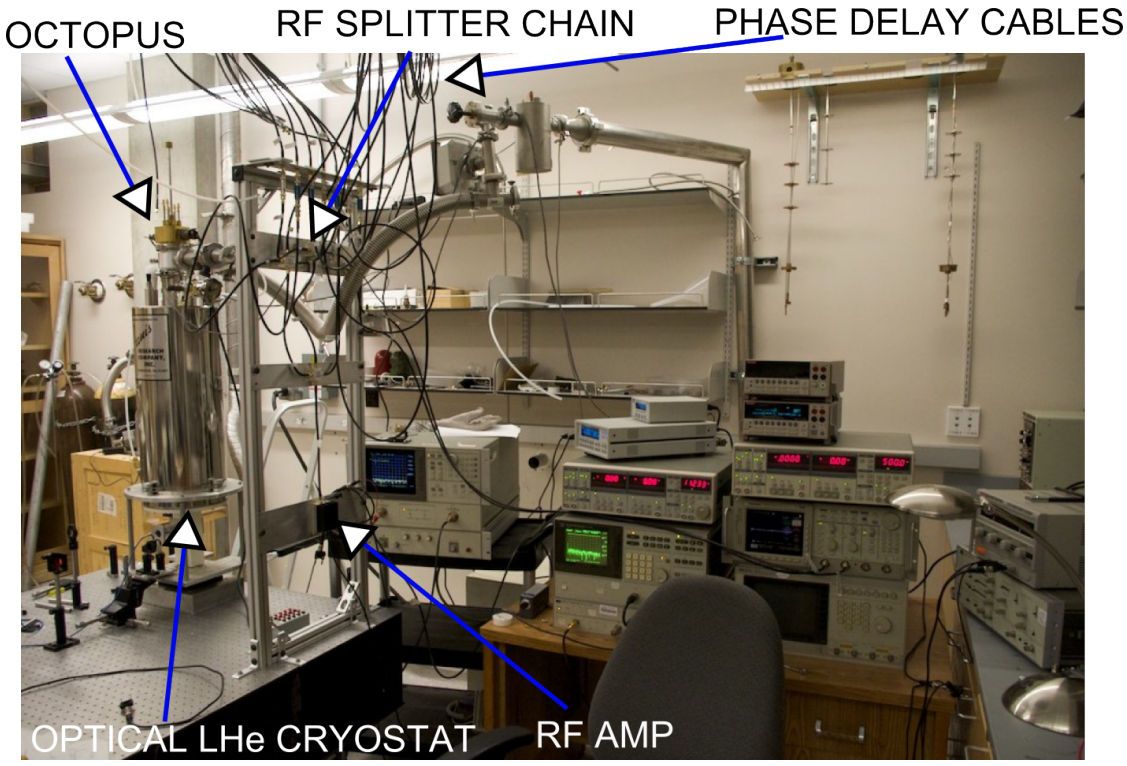

Figure 9.3: Photograph of portions of the conveyer experimental setup, showing the conveyer RF system. Signal generator (not shown) supplies RF sinewaves to the RF power amplifier, which are split into nine copies by the two-level (4x 3-way) splitter cascade, and then pass through various lengths of phase delay cable (suspended overhead) followed by DC blocks. Seven channels run to the Octopus insert in the optical liquid helium cryostat, and two monitoring channels route to an oscilloscope.

Chapter 10

Exciton conveyer experiment

Contents

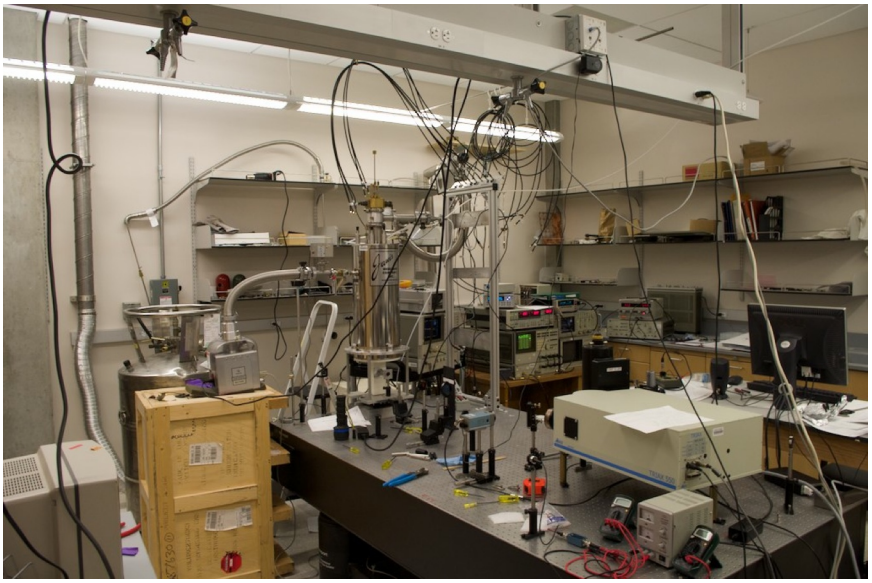

Figure 10.1: Photograph of the conveyer experiment. The Octopus is mounted in the Janis LHe cryostat, whose optical window is visible at the bottom. The beamline extends through the spectrometer; the LN_2 CCD is behind it. The Conveyer RF system labeled in Figure 10.2 is visible in the background, and the Ti:sapphire excitation laser is piped from the adjacent room. Visible in the foreground are the NIR-sensitive security camera and diode lasers used during alignment and navigation. (Naturally, the vacuum turbopump is dismounted during experiments.)

With the operating principle of the exciton conveyer device, fabrication of the conveyer sample, its mounting in the Octopus cryogenic optical RF sample holder, and the driving conveyer RF system all in hand, this chapter describes the conveyer experiments, raw data, elements of data calibration, and some preliminary comments on the results.

10.1 Experimental setup

Figure 10.2 and Figure 10.1 are photographs of the experimental setup.

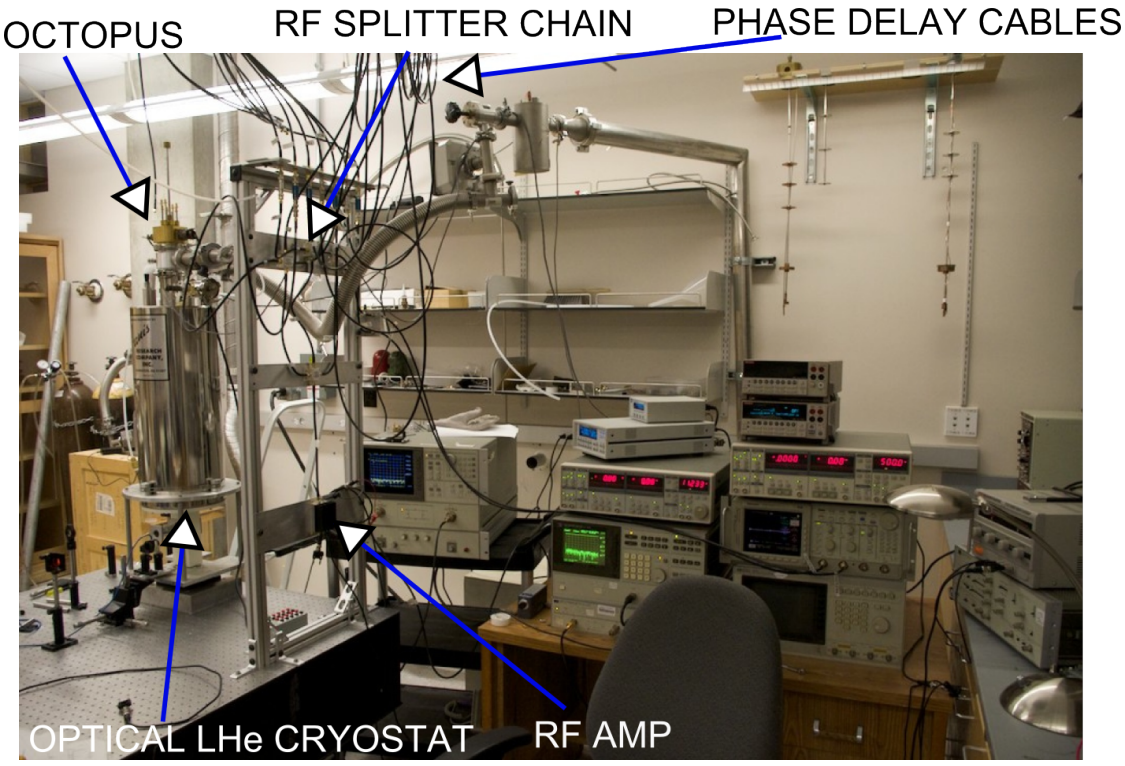

Figure 10.2: Photograph of portions of the conveyer experimental setup, showing the conveyer RF system. Signal generator (not shown) supplies RF sinewaves to the RF power amplifier, which are split into nine copies by the two-level (4x 3-way) splitter cascade, and then pass through various lengths of phase delay cable (suspended overhead) followed by DC blocks. Seven channels run to the Octopus insert in the optical liquid helium cryostat, and two monitoring channels route to an oscilloscope.

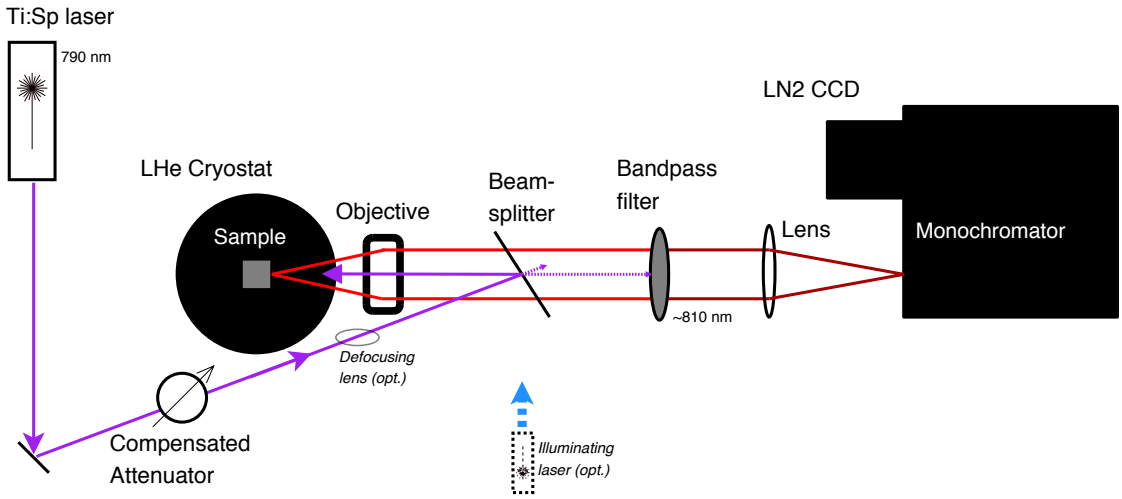

Figure 10.3: Schematic diagram of the optical setup. The collimated Ti:sapphire photoexcitation laser beam focuses through the long working-distance objective (f=20 mm, NA=0.28, positioned at 1-f) onto the sample surface. The laser is resonantly tuned to the direct exciton PL energy near 790 nm, and the compensated attenuator varies pump power without disturbing laser focus. Sample photoluminescence, collected by the objective, passes in the collimated regime through a bandpass filter and images onto a scanning monochromator and liquid nitrogen-cooled CCD. Either spatial (x–y) or spectral (x–Energy) images may be taken by adjusting the monochromator entrance slit and grating incidence angle. The angle-tuned bandpass filter (FWHM=10 nm) is centered about the indirect exciton PL emission near 810 nm to block laser and direct exciton light below and extraneous sample bulk emission above the indirect exciton spectral region of interest. Two optional components aid experiments: A weak defocusing lens (actually, detuning of a beam-collimating telescope) is used to obtain (pseudo)diffuse photoexcitation employed in Section 10.4. (See also Section C.4.5.) An additional 690 nm diode laser serves as a convenient bright illumination source while navigating about and aligning the sample; the method is described in the text.

10.1.1 Optics

The conveyer experiments were performed in the optical beamline illustrated schematically in Figure 10.3. In simplest form, the sample is illuminated with a CW laser in the red or near infra-red, and the NIR photoluminescence observed with an liquid nitrogen-cooled CCD to obtain both spatial and spectral images.

The imaging is essentially diffraction-limited, through an objective lens placed 1-f from the sample; it focuses a collimated laser beam to a point on the sample, and collimates light emitted (or diffusely reflected) from the sample; the collimated output beam is imaged downstream by a large lens onto the entrance slit of the spectrometer. A flip mirror diverts the beam to an inexpensive CMOS camera (with NIR sensitivity) for navigation and setup, and a variety of filters are placed in the collimated beam regime.

For spectral (x–Energy) images, the vertically-oriented spectrometer slit observes a swath in the direction of transport (ie, perpendicular to the horizontal conveyer stripes), relative to the frame of the optical table. For spatial (x–y) images, the CCD actually sits behind the spectrometer (as before) but the entrance slit is opened wide and the diffraction grating is tuned to zero incidence as a mirror. Accumulation times are typically 1–10 s for best quality.

Excitation laser

For the data presented in this chapter, the excitation laser was a Ti:sapphire[1] tuned to the direct exciton resonance near 790 nm. The indirect exciton photoluminescence is 795–815 nm, depending on the gate voltage (DC, or AC with DC bias). Undesirable "bulk" (termed "n^+") emission also occurs in a broad spectral band beginning roughly around 815 nm, limited spatially to the laser spot, but sufficiently bright even near 815 nm to overlap with the indirect exciton emission (especially at higher voltages). The uncomfortably-close excitation laser on one side and the parasitic bulk emission on the other bracket the indirect exciton spectral region of interest. The camera is protected and the signal-to-noise ratio improved by

[1] actually piped in some distance from another room

interposing a 810 nm bandpass filter angle-tuned to 805 nm, with FWHM about 10 nm. See Figure 10.5 for illustrative spectra. (Measurements can also be greatly improved by exploiting polarization, commented on in Section C.4.3.)

Although excitation at the direct exciton resonance provides best results (the excitons are created with minimal kinetic energy, ie "colder", and the absorption efficiency is good), the exciton conveyer also works with higher-energy excitation; indeed, the very first results were obtained with a 690 nm diode laser.

Accessory laser

An additional diode laser serves as a convenient bright illumination source while inspecting the sample. At 690 nm, it is above the bandgap energy of GaAs but below that of $Al_{0.33}Ga_{0.67}As$, causing the GaAa portions of the sample surface to photoluminesce broadly while metallic electrodes appear dark. Bandpass filters at the direct exciton (790 nm), indirect exciton (800 or 810 nm), and bulk n^+ (820 nm) energies, combined with selective application of gate voltage, further distinguish the active/inactive regions and form recognizable patterns that aid both gross "navigation" and precise alignment. A HeNe laser, above the bandgap of $Al_{0.33}Ga_{0.67}As$, generally creates excessive photocurrent and endangers the sample by the point at which it is bright enough for good visibility.

10.1.2 Electrical and cryogenic setup

The electrical setup comprises the combination of the Octopus multi-channel RF optical cryogenic sample holder (Chapter 6 and Chapter 7) installed in the cryostat and driven by the Conveyer RF system (Chapter 9), illustrated schematically in Figure 10.4. Of the seven channels driving the Conveyer, two are duplicated (those corresponding to the longest and shortest phase delay cables) and connected to an oscilloscope, for monitoring amplitude and relative phase at each operating frequency.

The experiments described in this chapter were conducted in liquid helium, where the lower portion of the Octopus and cryostat are flooded entirely and pumped on in near-vacuum to a temperature of about 1.5–1.6 K. The surrounding

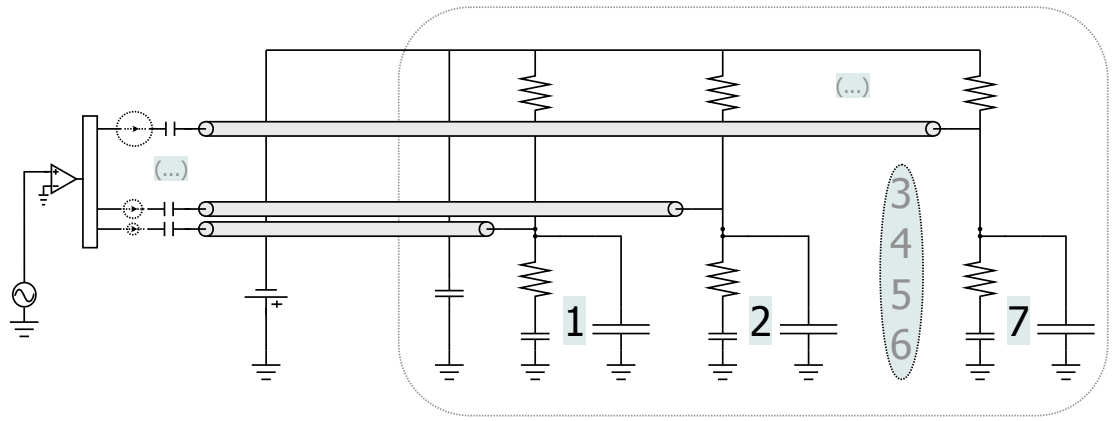

Figure 10.4: Circuit schematic for the multi-channel conveyer RF system, Octopus sample holder, and conveyer sample, as idealized without parasitic elements. The dotted rounded rectangle represents the cryostat. Sinewaves from a signal generator are amplified by the power RF amplifier, split by a combination of RF power splitters, individually phase-delayed by delay cables, and capacitively coupled to the Octopus coaxial transmission lines. External DC bias is applied to each channel at the sample through coupling resistors; the resistors block RF leakage into the bias rail, and leakage is shunted to ground through the buffer capacitor. The transmission lines terminate resistively for impedance matching and capacitively to block DC bias current to ground. Three of seven channels are shown for clarity.

Table 10.1: Studied conveyer (approximate) frequencies and velocities. See also Table 10.3 for additional detail. $1\,\mu\text{m/ns} = 10^5\,\text{cm/s}$

Mode		#1	#2	#3	#4	#5	#6	#7	#8	#9
Frequency	[MHz]	48.5	97	145.5	194	243	291	337	388	437
Velocity	[μm/ns]	0.67	1.3	2.0	2.7	3.4	4.0	4.7	5.4	6.1

superfluid helps to make the sample holder temperatures more uniform despite the localized heating, and removes the fluid boiling interface to a level some inches above the sample (which would otherwise add local vibration or disturb the optical path). The conveyer was also demonstrated to operate in helium vapour, although depending on conveyer amplitude the temperature (as measured locally at the sensors) climbs rapidly by tenths or whole Kelvins in a few seconds.

Studied conveyer velocities

The conveyer was studied over a range of frequencies and velocities for modes #1-#9, corresponding approximately to 50–450 MHz, listed in Table 10.1. The relationship of these velocities to the phonon sound velocity(ies) is subsequently discussed in Table 10.3 and Section 10.6.1. The earliest demonstrations of conveyer operation, below, is at mode #1.

10.2 Conveyer operation demonstrated

Conveyer off

Figure 10.5 demonstrates operation of the exciton conveyer. First, with the conveyer off (AC voltage set to zero on all electrodes, but with $V_{\text{bias}} = 4.0\,\text{V}$), a cloud of indirect excitons is observed surrounding the focused laser spot. The finite spacing between the conveyer stripes, comparable in distance to the ground plane, means that, although the same voltage is applied to all electrodes, the potential $V(x, y)$ is not quite uniform; in the real-space image, Indirect excitons visibly diffuse more easily *along* the lattice stripes (y-axis) than *between* the lattice stripes (x-axis). In the spectral image, the majority of the emission can be seen around

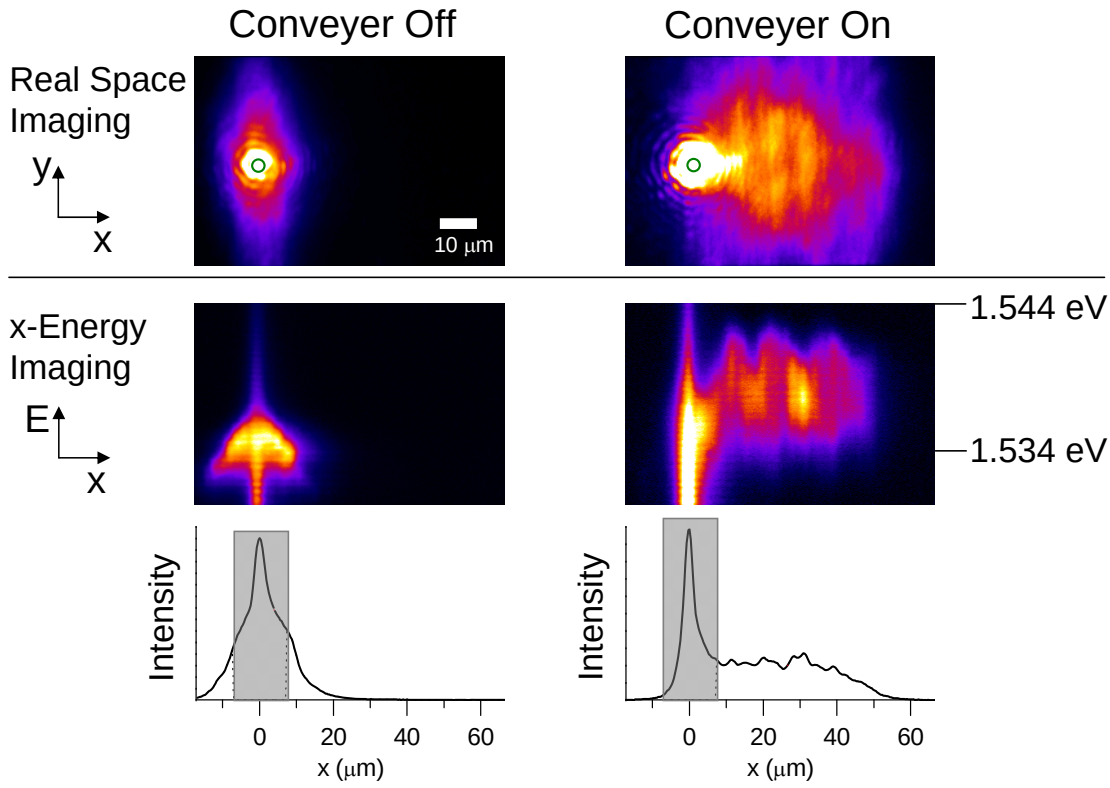

Figure 10.5: PL images and spectra illustrating the conveyer operation. Top row: real space (x-y) images showing the exciton cloud being transported many tens of microns when the conveyer is switched on (the small green circle indicates the exciton laser spot). Middle row: spectra (x-energy) images, showing the indirect excitons (about 805 nm) being transported laterally down the sample. (Stray bulk emission at longer wavelengths is visible below 1.53 eV, while the laser resonantly excites the shorter direct exciton emission line near 790 nm $\equiv$ 1.57 eV, offscale). Bottom row: Photoluminescence intensity as a function of x-distance from the laser spot, integrated over the indirect exciton spectral range (ie, approximately cutting off the bulk emission). Subsequently, transport distance will be characterized by the first moment of this distribution. The shaded grey rectangle denotes the spatial region deemed to be "laser spot" that will be discarded for calculating distribution moments.

1.54 eV $\approx$ 805 nm, signifying the indirect excitons which are long-lived and able to diffuse away from the laser spot. Direct exciton emission at shorter wavelength is deliberately cut off by choice of the spectrometer position (as well as the bandpass filter), to avoid sending resonantly-tuned laser reflection straight into the detector. Bulk n^+emission is visible at higher energies, but only spatially-located at the laser spot.

Conveyer on

With the conveyer on, indirect excitons are observed to travel many tens of microns away from the sample, several times farther than the mere diffusion distance seen with the conveyer off. In the spatial picture, the excitons are seen to be transported much more in the conveyer (x) direction than diffusing along the (y) conveyer stripes; the exciton emission intensity drops off towards the farthest transport distance. (This could be due to a sample defect located 50–60 μm from the laser spot.) In the spectral image, it is clearly seen from the spectral range that it is the *indirect* excitons that are transported down the sample. The peak indirect emission wavelength is also seen to shift with transport distance, possibly periodically, suggesting that the electrode spacing or sample photolithography leads to some kind of nonuniformity in the "average" voltage amplitude at a given x-position.

10.3 Exploring transport as a function of parameter space

10.3.1 Characterizing "transport" distance

We explore the conveyer transport as a function of tunable parameters: exciton density, controlled by the excitation laser power; conveyer velocity, controlled by frequency; and conveyer amplitude. Although excitons are plainly visible in Figure 10.5 nearly 60 μm from the laser spot, and in raw images small amounts of exciton photoluminescence can be seen even $\sim$100 μm away, we need some quan-

titative measure of the transport distance. A simple approach is to integrate the exciton PL emission intensity, visible in the spectral images over the indirect exciton spectral range, and plot as a function of distance from the laser spot. The transport distance is some measure of the width of this distribution, which we can characterize by the first distribution moment. (The second moment works as well, giving similar results.) In other words, we characterize transport distance as the "center of mass" of the indirect exciton cloud.

Distinguishing the indirect-exciton PL emission

Measuring the indirect exciton PL luminescence distribution *only* is made difficult by spectrally-nearby bulk emission. Although bandpass filtered, the bulk emission peak is very bright near the laser spot; the bulk emission tail on the short-wavelength side overlaps with the indirect exciton emission linewidth, both modulated (especially in the spectral overlap region) by the tailoff on the long-wavelength side of the bandpass filter passband. The spectrum is additionally affected by laser power (which directly controls both bulk emission intensity and indirect exciton density and hence intensity) and exciton density (which shifts the indirect exciton emission energy). It is difficult to deconvolve these elements purely spectrally, and it is necessary to do so to avoid the distribution moment being dominated by the peak around zero distance. However, the indirect exciton PL emission is clearly separated *spatially*, because only indirect excitons can diffuse or be transported far from the laser spot. Therefore, a straightforward way to proceed is to simply cut out the distribution "near" the laser spot, illustrated by the shaded box in Figure 10.5. We choose to cut out the 20 pixels $\sim 7\,\mu$m near the laser spot. As a result, transport distances comparable to 10 microns or so feel some artifacting effects of this spatial filter, and characterization of shorter transport distances is affected by the choice of filter width, but the side effects do not much affect the data especially towards the larger transport distances of greatest interest.

An *average* measure

This is a particular choice of measure, quantifying some kind of *average* transport. In the simplest model, one might expect that the transport distance $d \sim v_{\text{conveyer}} * \tau^{\text{x}}_{\text{lifetime}}$, giving a PL intensity curve maximum close to the laser spot and diminishing smoothly with distance. However, excitons may be less willing to localize into the moving conveyer potential at higher conveyer velocities, ie the collection efficiency to the conveyer minima is an unknown function of velocity, convolving the PL emission distributions. In other words, at higher conveyer velocities, excitons that *do* ride in the conveyer may transport farther, but many excitons may not be transported much at all. The notion of "transport distance" and choice of measure thus may depend very much on the precise question that one is asking. Indeed, preliminary measurements with the conveyer at low velocities observed a few excitons at least 100 μm from the sample. Measurements are probably also constrained by the observed, regrettably unfortunate presence of one or more photolithography defects 50–60 μmdownstream from the sample.

10.3.2 Transport as a function of amplitude for small velocities

Figure 10.6 illustrates exciton transport at the lowest velocities v_1–v_3 measured as a function of applied conveyer amplitude — actually, conveyer voltage amplitude as measured outside the cryostat (which will shortly be an important distinction). At sufficiently large amplitudes, the excitons are clearly transported several tens of μm from the origin, and thus have been localized in the moving conveyer potential. At small amplitudes, the excitons do not follow the moving conveyer potential. This localization–delocalization transition is dynamically-controllable, and a counterpart to that observed in static lattices [Remeika et al., 2009].

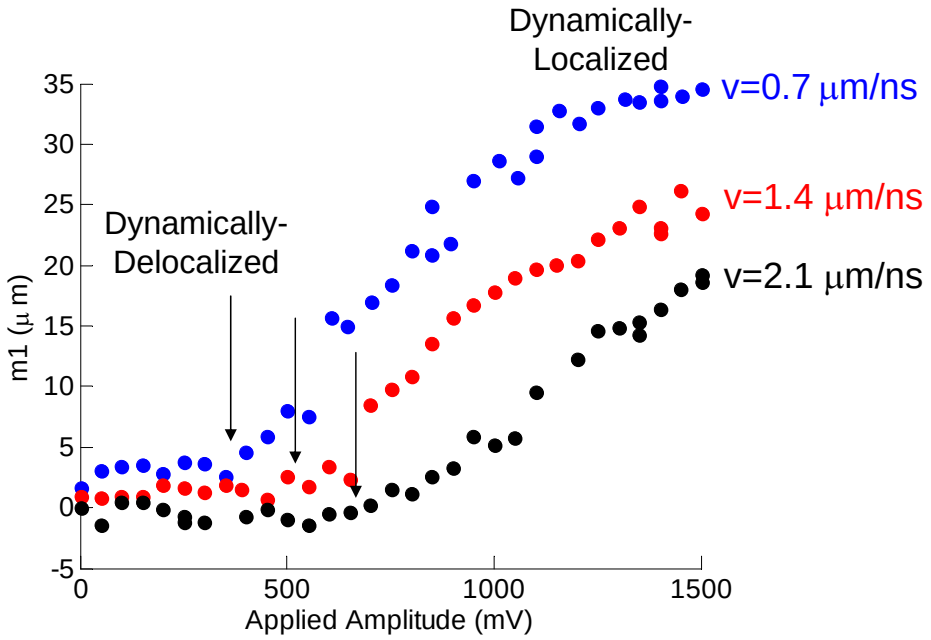

Figure 10.6: Exciton transport distance (as characterized by m_1) as a function of applied (unrescaled) conveyer voltage amplitude, for conveyer velocities #1–#3. At large conveyer amplitudes excitons are dynamically localized in the moving conveyer lattice, while at small amplitudes they do not follow the lattice.

10.3.3 Transport as a function of density

Figure 10.7 illustrates exciton transport for velocities v_1 and v_2 as a function of applied laser power, controlling the exciton density; the amplitude set is the maximum amplitude used in Figure 10.6. At moderate densities, excitons are transported several tens of μm from the origin, and thus have been localized in the moving conveyer potential. At very large and small densities they are not localized in the moving lattice; we may speculate why: At large exciton density, the exciton-exciton dipole-dipole repulsion energy may become superior to the conveyer lattice depth; ie, excitons are sufficiently numerous to screen ("fill in") the conveyer minima. At small exciton densities an additional effect may come into play. The CQW semiconductor sample is not perfectly homogeneous, but includes defects (e.g., impurities, or non-uniform number of monoatomic layers for the quantum wells, or crystal defects at the composition interfaces). Although excellent-quality samples, these unavoidable defects leads to scattered potential minima that confine indirect excitons (see, for example, High et al. [2009a]). For low exciton densities, the relatively few indirect excitons may be localized by the disorder potential instead of the conveyer, but as density increases the disorder is screened ("filling in the cracks"), leaving the excitons able to follow the conveyer.

10.3.4 Transport distance for many velocities

Figure 10.8 plots exciton transport distance (as characterized by m_1) as a function of conveyer amplitude for all studied conveyer velocities v_1–v_9. These conveyer velocities span most of the set of phonon velocities in GaAs (see Table 10.3). Several features are evident: generally, transport distance is shorter for higher velocities, except possibly for v_2 eventually overtaking v_1. For the highest velocities, transport distance falls off appreciably. Transport as large as 40 μm (to emphasize, an *average* measure) is observed. The minimum conveyer amplitude at the onset of transport appears to increase for higher velocities. Lastly, there is some suggestion of transport distance saturating with increasing amplitude for some of the studied velocities. However, this plot is studied as a function of *applied* voltage amplitude, as observed after the RF conveyer system before the signals en-

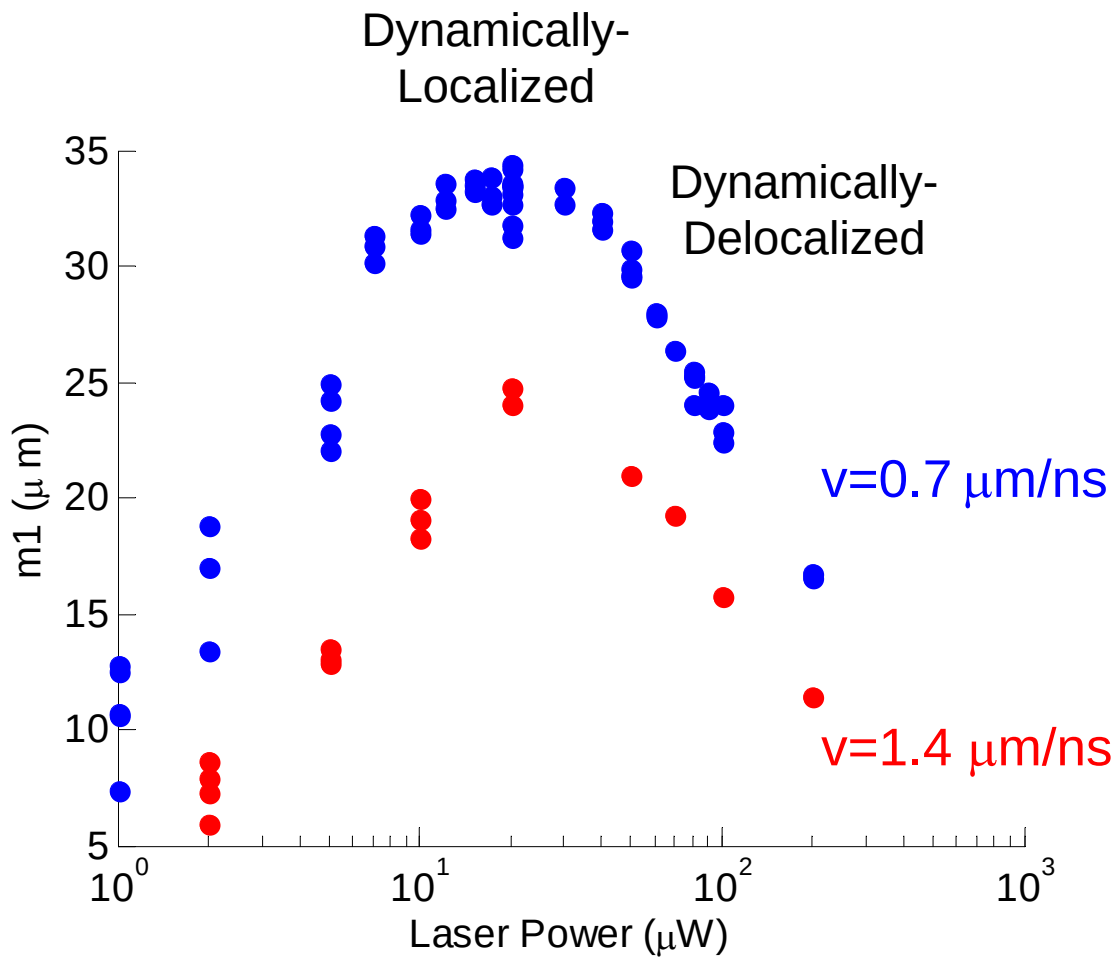

Figure 10.7: Exciton transport distance (as characterized by m_1) as a function of laser power (exciton density), for two different conveyer velocities. At moderate exciton power excitons are dynamically localized in and transported by the conveyer, while at much lower and higher densities they do not follow the moving lattice.

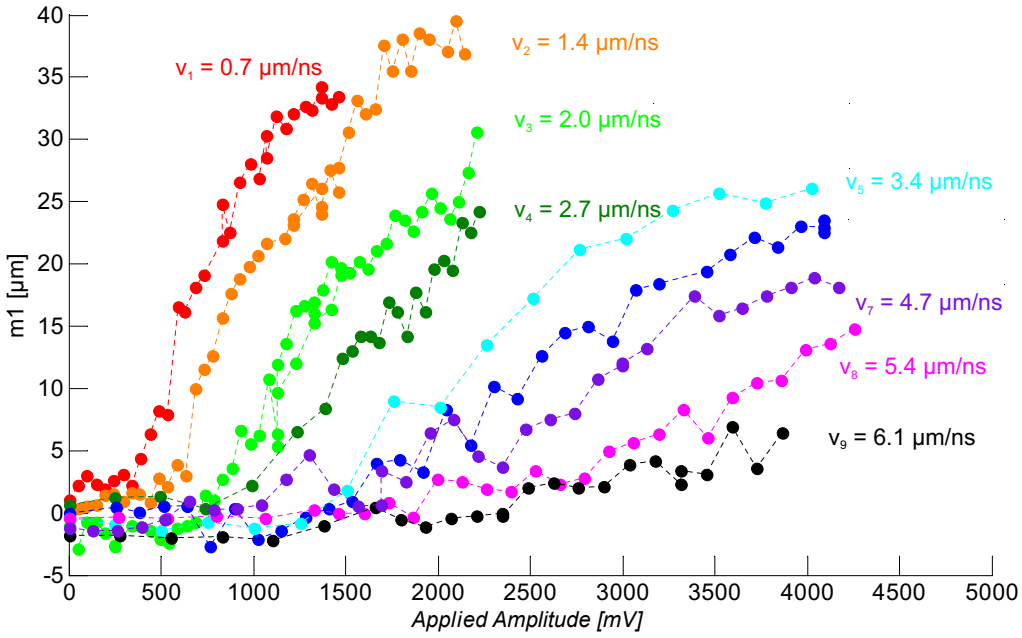

Figure 10.8: Exciton transport distance (as characterized by m_1) as a function of applied (unrescaled) conveyer amplitude, for all measured conveyer velocities from modes #1-#9 (0.68 - 6.1 μm/ns.)

ter the cryostat. The measure of greater physical interest is the energy depth of the conveyer potential at the sample, determined by the voltage actually applied at the sample. This could be (and is) quite different, and it is necessary to find some method of calibrating to physical amplitude.

10.4 Device frequency response and amplitude calibration

In principle, the (energy) depth of the conveyer potential could be calculated entirely from knowing the actual voltage present on the conveyer electrodes, essentially $\mathcal{E} = eF_z d$ (d nearly the distance between the quantum well centers, leading to the dipole moment of the indirect exciton), where the electric field

$$F_z(x,z) = F_z(z, V_{\text{electrode}}(x, z = \text{top}))$$

is a function of the electrode voltages determined by solving Poisson's equation (for the simplest homogeneous geometry $F_z = V/D$, D the thickness between top and ground electrodes, but see Section 10.5). A difficulty is that the actual electrode voltages $V(x)$ cannot readily be measured directly.[2]

10.4.1 Capacitive sample load and circuit parasitics

For a given voltage applied to the Octopus transmission lines, the actual voltage present on the conveyer electrodes is a complicated and difficult to predict *a priori* function of frequency, due to the many reactive elements necessarily and actually present in the circuit (and alluded to in Section 6.8). Figure 10.9 illustrates some of the elements.

Sample capacitive loading

The single largest contribution is that the conveyer sample itself acts approximately as a parallel plate capacitor, imposing a capacitive load at the end of the transmission line. For low frequencies, the sample impedance $Z = j/(2\pi f C)$ ($j \equiv \sqrt{-1}$) is approximately infinite (and imaginary), and the current from the transmission line signal dissipates entirely through the termination resistor to ground. (For very low frequencies, the AC termination capacitors are also open circuit, but these have deliberately been selected as large as possible (5600 pF) to become effectively dead shorts by ∼10 MHz.) Thus, in the low frequency regime, the full voltage applied externally to the transmission lines is present across the sample electrodes.

At higher frequencies, the sample impedance becomes finite, and some portion of the signal current begins to flow through the sample and the wiring leading to it. The key parameter, then, is the sample capacitance C; unfortunately, it is not directly known. A trivial parallel-plate estimate yields figures of order 10–50 pF, placing an RC low-pass filter knee $\sim (2\pi \cdot 50\,\Omega \cdot C)^{-1}$ in the vicinity of 100 MHz

[2]It does appear possible, after protracted effort, to obtain some form of calibration across different frequencies, and this section goes into some detail about how this is accomplished; the reader primarily interested in the resulting physics may wish to skip ahead to Section 10.6.

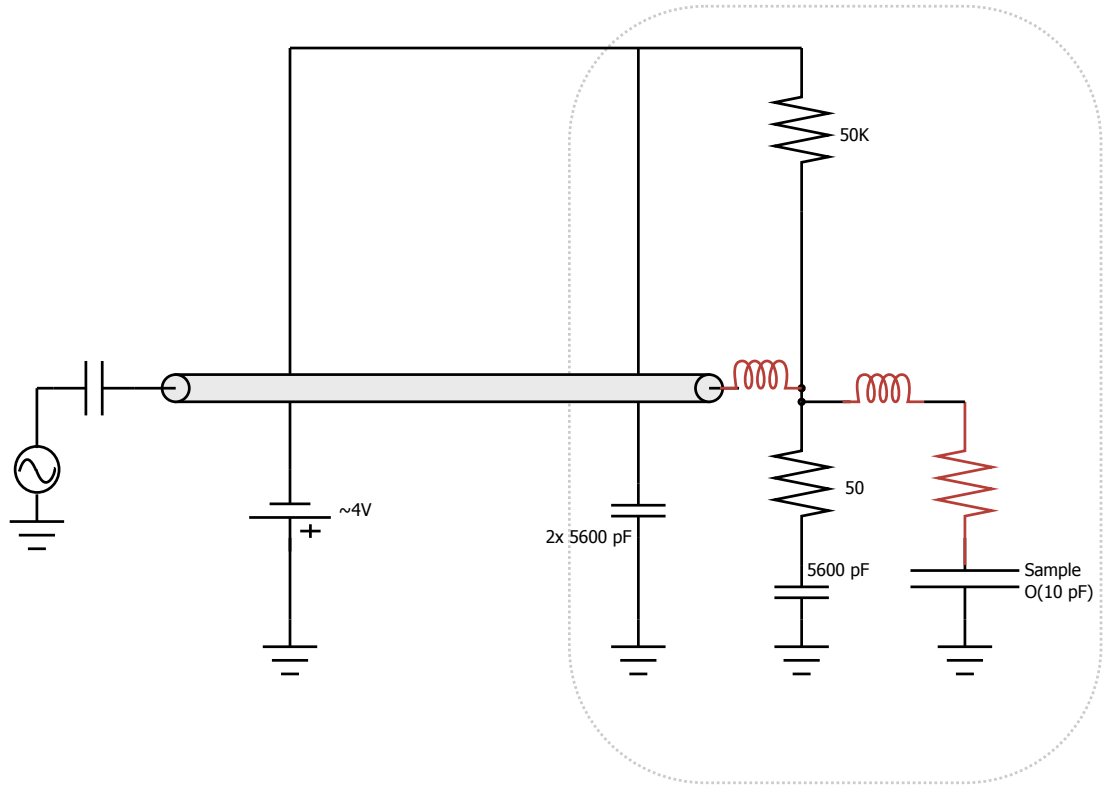

Figure 10.9: Circuit schematic of a single channel shown with three parasitic elements that alter the RF amplitude seen at the sample, which is itself idealized as a capacitive load: series inductance from end of the cryogenic coaxial cable to the printed circuit board, series inductance within the PCB and along the DIP socket and package pins, and series resistance in the sample. Not shown is parallel capacitance formed where the DIP socket pins pass narrowly through the copper sample holder plate (ground plane).

— ie, the filter fall-off is strongly frequency dependent right in the operating frequency (conveyer velocity) regime of interest! The actual capacitance cannot be simply predicted, because it is not a parallel plate: there are actually hundreds of top electrodes stripes tied into seven sets, the stripe widths are approximately 1 μm but photolithography is imperfect and optical microscopy of the sample surface is diffraction-limited, there is finite surface conductivity between the stripes, and the access electrodes overlaying the stripes complicate the geometry still more.

Direct measurements

Direct measurement of the capacitances (or inter-electrode conductivity) cannot easily be made by microprobing, because voltage ought not to be applied to the sample at room temperature (the DC resistance of thin layers of GaAs being too much *conductor* and not enough *semi*). In situ measurements in the Octopus at LHe temperature can be made, but (a) an AC capacitance meter operating at 1 kHz may not be much guide to the capacitance at hundreds of MHz, and (b) the sample is in parallel with much larger capacitance (the 5600 pF termination caps, plus additional effects of the buffer caps on the DC bias rail). (Other possible approaches are briefly discussed in Section C.2.2.)

Other parasitics

At least four other parasitic elements beyond the sample capacitive loading also enter into the circuit diagram, some of which are indicated in Figure 10.9:

1. Series inductance, from where the signal wire (center conductor) extends from the cut face of the semirigid coaxial transmission line to the DIP socket pin and into the PCB, through to the termination elements. This was minimized by taking pains to make the exposed wire as short as possible, placed as close to the copper ground plane as possible, and by the small size of the PCB and traces itself.

2. Series inductance of the length of the DIP socket pin extending into the socket itself, into the sample DIP package pin and along the wirebonding

wire.

3. Parallel capacitance between the DIP socket pin and the copper ground plane, where the pin passes through the thickness of the sample holder plate through a narrow hole with a small pin-wall gap. (Not shown in the figure.)

4. DC series resistance along the sample electrodes, either the access electrodes or the stripes, made of thin ITO.

For all four of these parasitics only crude estimates can be placed on the values, and they are difficult to measure *in situ* for same reasons as above. Optimization of these undesirable elements is briefly discussed in Section C.2.1. Incidentally, sample *parallel* (DC) resistance is of course easily measured, and known to be fairly high, of order 10MΩ–GΩ, though dependent on laser illumination which photoexcites free carriers in the semiconductor (which are not thermally excited into the conduction band at liquid helium temperatures); such parasitic parallel resistance is likely unimportant — it is quite different from the sample capacitive *ESR* (equivalent series resistance) which *does* appear to play a role.

10.4.2 Predicting the RF filter response

A circuit model was made incorporating estimates of the combination of these reactive and resistance elements as a lumped-element model distinguishing the total loading at the end of the transmission line, losses due to reflection, and the remaining (complex) amplitude on the optically active portion of the sample. Unfortunately, the algebra rapidly becomes too unwieldy to include here.

Figure 10.10 are a set of Bode plots of predicted amplitude at a conveyer electrode for inputs into the transmission line.

Tuning of the input parameters makes clear that the sample capacitive loading is the dominant effect in the frequency range of interest, but the parasitic inductances and capacitances and the possible sample DC series resistance alter the shape of the response curve once the *RC* falloff is underway.

Figure 10.10: Bode plots of sample RF response from predicted circuit model

10.4.3 Optical characterization of AC voltage amplitude

Predicting the actual electrode voltages from circuit theory is clearly difficult, especially given the lack of direct measurements of *in situ* component values. However, we do possess the capability of high-resolution spatially-resolved *in situ* measurements of photoluminescence emission wavelength. Is it possible to extract the effective calibration optically?

Direct observation

At the operating frequencies, the voltage and hence emission wavelength of a point on the sample is oscillating with a period of order nanoseconds, while our camera exposures times are of order seconds. If it were possible to measure the PL spectra at subnanosecond windows, one could observe the emission wavelength sinusoidal oscillation nearly instantaneously and note the extreme values, giving the amplitude (energy) depth directly. This may be feasible using a TCPC system (as employed in the photonic storage experiments of Part II) plus a spatial pinhole, or by using a time-gated intensifier with the CCD camera; the latter is discussed briefly in Section C.1.1.

Indirect observation

Consider a conveyer electrode operating at RF frequencies: the instantaneous PL emission wavelength is oscillating between extreme values, but as observed on a camera with long (seconds) exposure time, a sharp instantaneous PL emission line will "blur" out into a wide emission band, where the width of that band corresponds in some manner to the extreme wavelengths. The blurred band (plot of PL intensity vs. wavelength) may not be rectangular. For emission $\lambda(t) \propto V(t) \propto \sin(\omega t)$, the spectral velocity $\partial\lambda/\partial t$ is maximum at the oscillation center and minimum at the extrema; a constant emission intensity (photon pro-

duction rate) will yield a greater integrated emission intensity at the *turning points* of the oscillator (assuming the emission intensity under DC-bias only conditions is the same for differing V_{bias}— which it is *not*, due to changes in exciton lifetime; see Figure 10.12 for illustration). If the *instantaneous* emission spectrum is perfectly sharp (δ-function), the observed PL intensity spectrum will peak at the extreme wavelengths and dip about the center — and the observed (time-averaged) spectrum extrema will correspond exactly to the instantaneous emission wavelength extrema. For real emission lineshape of finite width, the observed emission spectrum will be a convolution of the instantaneous lineshape with the temporal-averaging effect of the oscillator turning points. For sufficiently broad instantaneous emission lineshape, the observed emission spectrum may degenerate to a very broad peak, from which the instantaneous behavior cannot be determined.

To extract optical calibration, we remove the phase delay lines and drive all electrodes identically. This would be equivalent to a homogeneous top electrode if the lattice stripe spacings were infinitesimal. A focused excitation laser spot on the sample leads to additional spatial inhomogeneity of exciton density as excitons diffuse away from the laser spot, and exciton density itself shifts the emission wavelength by dipole-dipole interaction, so we illuminate using a diffuse laser spot. (This is actually experimentally nontrivial to achieve, requiring the input laser beam to the imaging objective to be sensitively converging/diverging in order to exit collimated and avoid imposing Airy (diffraction) rings; see Section C.4.4 and Section C.4.5 for brief discussion.) The actual illumination used was a poorly diffuse spot with Airy rings, but the centermost region is very approximately uniform.

Figure 10.11 is an example PL spectrum under these conditions. With the oscillation off (ie, zero AC voltage but with V_{bias}), the emission lineshape is approximately uniform in the centermost region, where the pseudodiffuse excitation leads to approximately constant (and low) exciton density for a distance of many lattice sites. With the AC amplitude on, the lineshape broadens (blurs) out into the larger pattern.

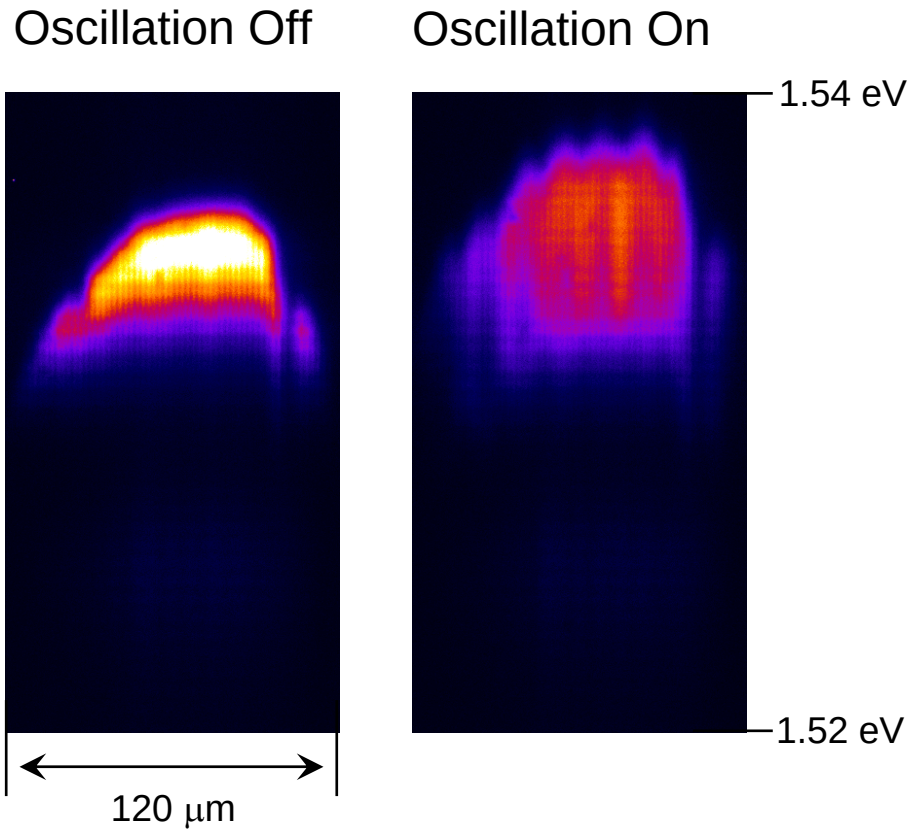

Figure 10.11: PL spectra (x-energy) images of the conveyer device with zero phase delays under pseudodiffuse laser illumination, showing the spectral broadening. Left, with no RF amplitude applied, the indirect exciton cloud has a minimal spectral width; right, with RF power applied, the indirect exciton PL emission oscillates many orders of magnitude faster than the camera exposure time, creating a broad PL emission cloud. (DC bias voltage is present in both cases to create the indirect excitons.) The spectral broadening can be measured as a function of RF amplitude to attempt to calibrate the effective RF voltage amplitude actually present on the device surface after circuit attenuations.

Complications in measuring broadening

The zero-amplitude lineshape is indeed sufficiently narrow to permit extracting useful information from the broadening. We then measure these broadened lineshapes as a function of frequency. Since the cumulative *RLC* filter transmission curve to the sample is strongly frequency-dependent, measurements over the wide range of operating frequencies (modes #1–#9) require using different absolute AC voltage amplitudes to maintain the emission broadening sufficiently large to adequately distinguish the AC-broadened lineshape from the DC lineshape. We assume (and there is experimental evidence) that these piecewise-different input AC amplitudes can be normalized and that narrowband results can be patched together over a wide frequency range. A constant large amplitude cannot be used for all frequencies, because at low frequencies a large effective voltage risks damaging the sample device, and short of that pushes the spectral lineshape out of the flat region of the optical bandpass filter. In fact, it is also necessary to remove the effects of the bandpass filter, by measuring and dividing out its response function; because the optical filter is fairly narrow (3-cavity design, FWHM 10 nm), the intensity attenuation is quite steep just outside the flat region, and in but a few spectral nanometers the response function is difficult to measure given achievable signal/noise ratios for the optical measurement. In fact, the non-flatness of the the blackbody spectrum of the lightbulb used to illuminate and characterize the filter is also removed, and the optical filter induces spectral ripples (not due to rolloff steepness per se, but from the Fabry-Pérot cavities used at off-normal incidence) that are smoothed out but not properly removed.

Additionally, one can question whether the broadening measured with zero phase delay and diffuse excitation (the "calibration" regime) is an accurate measure of the response with phase delays included and using focused excitation (the conveyer transport regime). One issue concerns whether inter-electrode currents due to finite inter-electrode conductivity alter the voltage distribution on the electrodes in the transport regime, when the instantaneous electrode voltages are not the same; the DC resistances *in aggregate* as seen between access electrodes $n, m \in \{1 \ldots 7\}$ have been measured and are roughly 1–10 kΩ, apparently much larger than than

the impedance to ground *through* the sample. Another issue concerns whether the spectral lineshifts used for calibration vs. transport are being strongly affected not merely by voltage but by exciton density due to laser power; the calibration measurements attempted to use a sufficiently low pseudodiffuse laser power to keep the exciton emission energies in the non-density-driven regimes.[3]

Calibration by normalizing conveyer amplitudes

The simplest method to process the numerous accumulated spectral broadening calibration PL images is to extract the broadened spectral width at some "good" spatial position. We find the "center" of the pseudodiffuse laser spot (position of maximum intensity), move 20 pixels ($\sim$7 μm) away to measure mostly indirect excitons (and not bulk n^+ emission, yet remaining within the spatially-pseudohomogenous area), and take a spectral cut along that x-position. The width of that spectrum[4] (FWHM, although other measures can be used) is calculated, for both the case of the AC oscillation on ($\Delta\lambda_{\text{on}}$) and AC oscillation off ($\Delta\lambda_{\text{off}}$). The spectral width with oscillation off functions as an effective zero reference, so it is subtracted in quadrature: $\Delta\lambda_{\text{broadening}} = \sqrt{(\Delta\lambda_{\text{on}})^2 - (\Delta\lambda_{\text{off}})^2}$.

For a single sufficiently-large excitation amplitude across a range of frequencies, this $\Delta\lambda_{\text{broadening}}(\text{f})$ is a measure of effective oscillation amplitude, ie the sample electrode (aggregate RLC filter) response function. For a small excitation amplitude, the measure can fail imaginary (the effective zero is also a noise floor), but sufficiently large amplitudes can be used over different frequency-response regions for usable signal/noise, and these are patched together linearly.

10.4.4 Frequency response curves

Figure 10.13 and Figure 10.14 are plots of this spectral broadening vs. linear and logarithmic frequency scales over the range of 1–1000 MHz. Immediately visible on the logarithmic plot is the *RC* falloff due principally to sample capacitance in the vicinity of 100 MHz, becoming less important by 10 MHz when the sample

[3]This should be checked more carefully in future measurements.

[4]Spectral energy-width is often used in calculation instead of spectral wavelength-width.

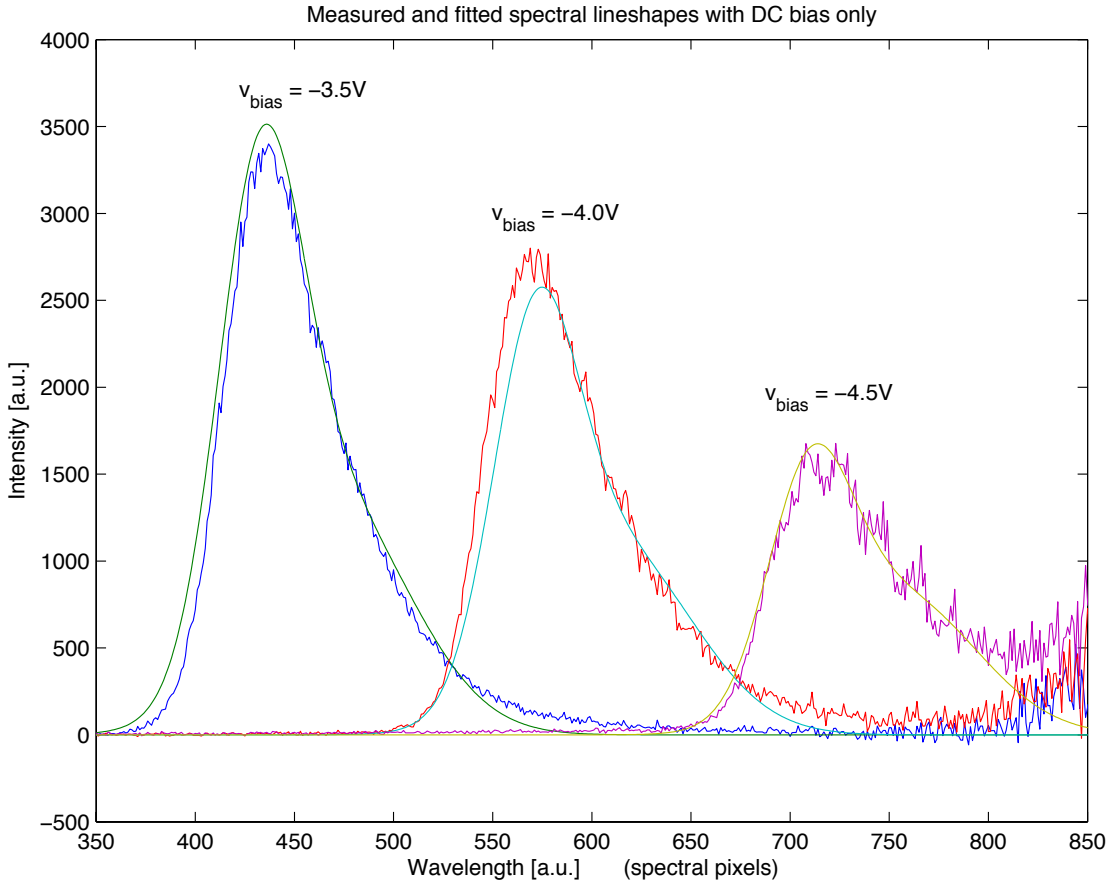

Figure 10.12: Plot of the spectral lineshapes under DC bias only (conveyer off) with pseudodiffuse laser excitation for $V_{\rm bias}$= -3.5, -4.0, and -4.5 V. The rolloff of the optical bandpass filter has been removed (and the filter ripple is smoothed but not removed). Larger $V_{\rm bias}$ shifts the spectral center to longer wavelengths, and (in general) lengthens the exciton lifetime. (Here, the larger values of $V_{\rm bias}$ may sufficiently tilt the energy band structure to begin *shortening* the exciton lifetime, leading to the lower emission intensity.) At the right edge, the onset of bulk n^+ emission is apparent, as well as noise from removal of the filter rolloff curves.

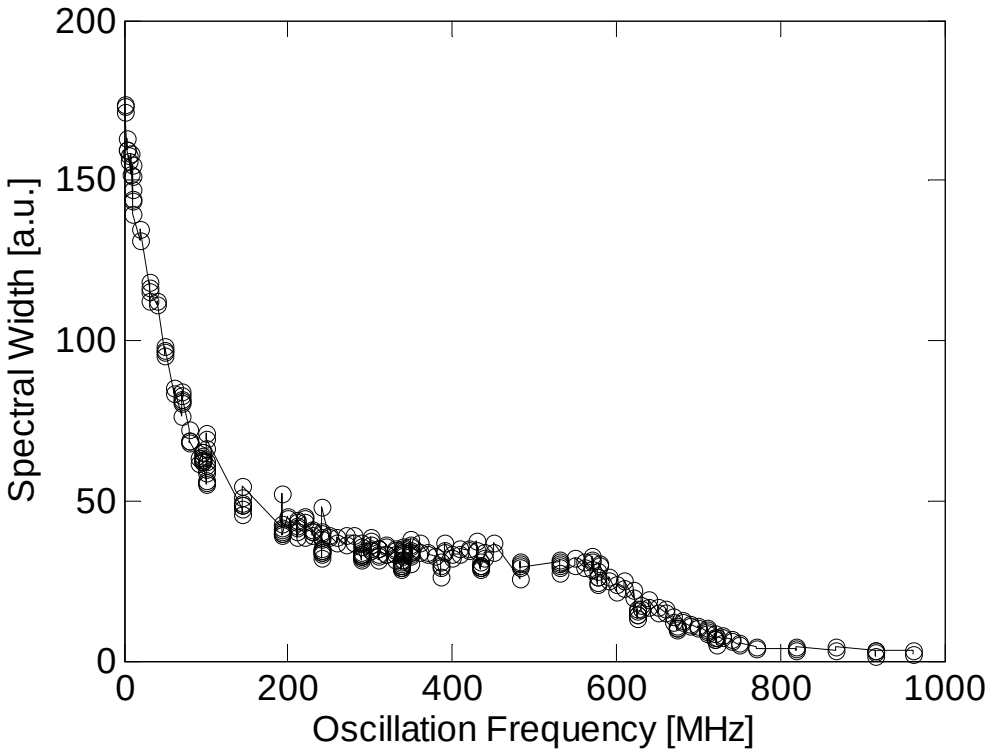

Figure 10.13: Frequency response of the combined Octopus+conveyer device system plotted on a linear scale; the transmitted RF amplitude has been measured by optical spectral broadening.

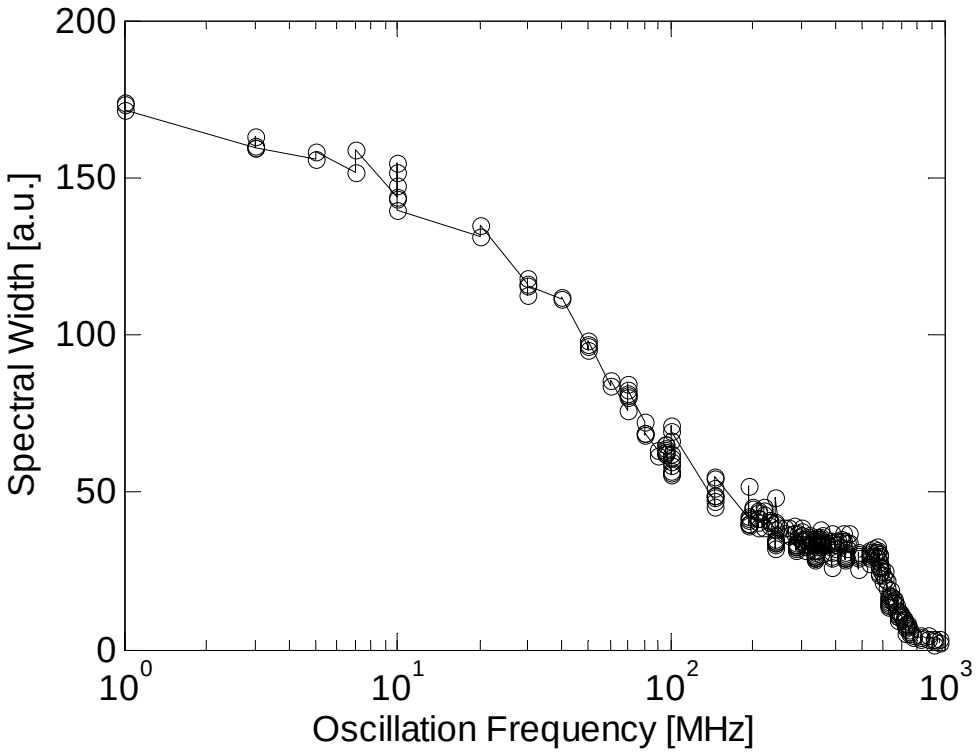

Figure 10.14: Frequency response of the combined Octopus+conveyer device system plotted on a logarithmic scale; the transmitted RF amplitude has been measured by optical spectral broadening.

is approximately open-circuit. (The curve shape below 10 MHz is questionable, with the amplifier being pushed well beyond its operating range.) Interestingly, the response appears to temporarily stabilize over some region 250–550 MHz, suggesting that some form of DC resistance in the photoactive region of the sample is flattening the response. Around 600 MHz and above there is again response falloff, suggesting that parasitic series inductances ($Z = 2\pi f L$) or the parallel pin package capacitances are switching on. The sharp transition near 600 MHz is peculiar: it appears too sharp a single-pole RC or RL filter response. It might be caused by the combined effects of multiple single-pole filters with (entirely accidentally) closely-aligned knee frequencies; it might also be a measurement artifact due to the poorer signal/noise ratio under (non-optimal) measurement parameters for those datasets.

The overall conclusion is that the device frequency response is quite definitely nonlinear over appreciable frequency ranges of interest, due to the combination of multiple reactive and resistive circuit elements, and that the different elements' responses overlap sufficiently in frequency (lack of clearly asymptotic regions) to render accurate disentanglement difficult.

These response curves are not complete; they extend only as low as 10 MHz, and although there are signs of the response asymptoting below that, that particular data is unreliable and cannot be extrapolated down to DC ($f = 0$). (Actually, of course, both the termination capacitors and then the DC blocking capacitors come into play.)[5] Thus, these curves are only a measure of relative amplitude response, and cannot be used to extract absolute voltage, but they can be used to normalize conveyer transport data at different velocities (frequencies) to each other (ie, v_1).[6]

[5] An attempt was made to make measurements at very low frequency (Hz to kHz), necessarily using a quite different electrical configuration of driving the DC bias rail with V_{bias}+ AC, but that data unfortunately turned out not to be usable.

[6] It may also be possible to extract estimates of the the absolute *energy* amplitude of the conveyer potential, but such analysis is not discussed here.

10.5 Effects of actual electrode geometry

10.5.1 The need to consider inter-electrode spacing

At the outset of Section 10.4 it was noted that, if the electrode voltages were actually known and directly measurable, the energy depth of the conveyer potential could be calculated, essentially $\mathcal{E} = eF_z d$ (d nearly the distance between the quantum well centers, leading to the dipole moment of the indirect exciton). The electric field

$$F_z(x, z) = F_z(x, z, V_{\text{electrode}}(x, z = \text{top}))$$

is a function of the electrode voltages and determined by solving Poisson's equation, given the boundary conditions of the top electrode voltages, ground plane at $z = 0$, and periodic boundary conditions in the $+x$ and $-x$ directions beyond a single lattice period of $7 * 2 = 14\,\mu$m. For a uniform top electrode at potential V (ie, the ideal parallel-plate capacitor), the electric field $F_z(x, z)$ is uniform *everywhere*, trivially $F_z(x, z) = V/D$, where D is the thickness between top electrode and ground.

Intuitive picture

For the conveyer device geometry, with its multiple electrodes spaced apart, this is not a good model even in the case where all electrodes are set to the same voltage. A key aspect of the device geometry, easily overlooked, is that the $1\,\mu$m spacing between electrodes is comparable (indeed, identical) to the $1\,\mu$m thickness of the sample between electrodes and ground plane. Put differently, the (x, z) geometry is *square*. The electrode voltage can be calculated everywhere given Poisson's equation and the boundary conditions, but the key effect is easily intuitively understood: with all top electrodes set to the same voltage V_0, consider a point at the top surface midway between two electrodes. The $\frac{1}{2}$-μm-equidistant electrodes will tend (by symmetry) to bring to the voltage *up* towards V_0, but the infinite ground plane only $1\,\mu$m away will exert a strong influence *down* to $0\,$V. The result will be somewhere in between. Consider, now, the voltage midway

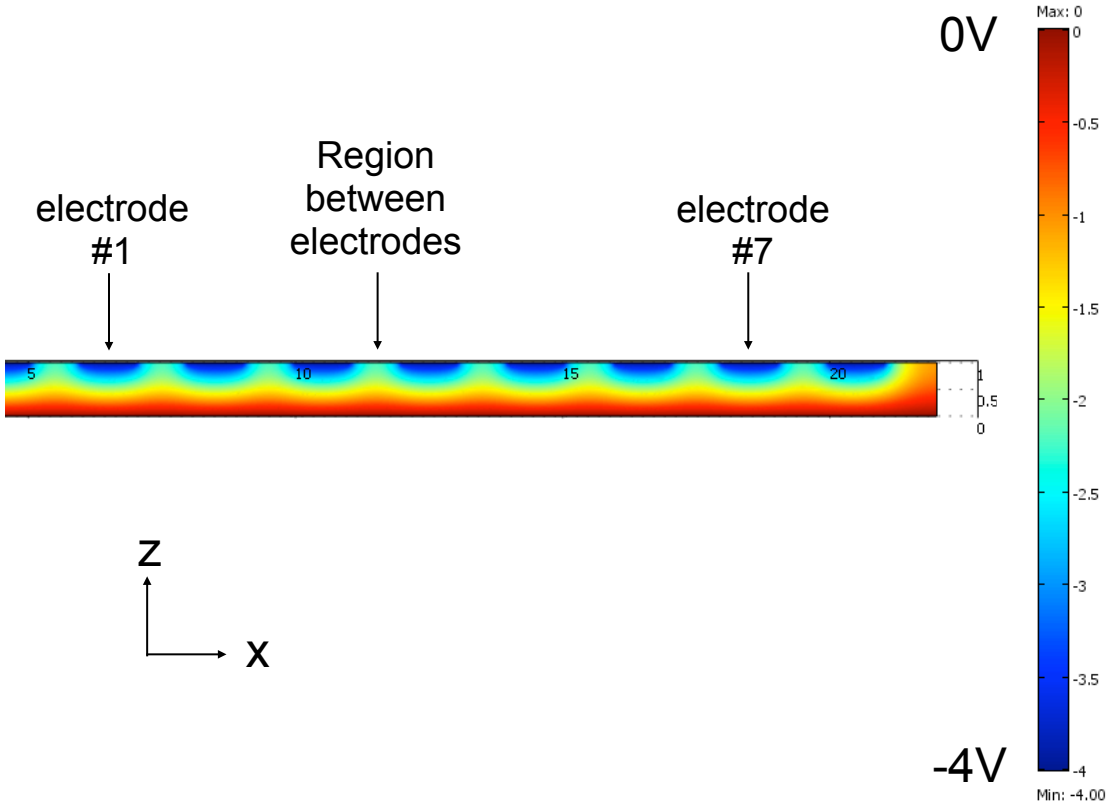

Figure 10.15: Plot of the electric potential $V(x, z)$ inside a portion of the conveyer sample, using actual electrode geometry, obtained by solution of Poisson's equation given the boundary conditions of -4 V on all top electrodes. (ie, V_{bias} only). Simulation calculated under COMSOL. Note that the potential on the top surface *in between* two electrodes (both at -4 V) is only $\sim$2 V, ie has been pulled halfway down to ground by the relatively close proximity of the ground electrode. The sample thickness, electrode width, and inter-electrode spacing are all 1 μm.

between two electrodes, not at the top surface $z = D$ but at the level of the CQW, $z = D/10$. The ground plane is relatively very much closer than the distant electrodes, and the electric potential close to zero. Thus, even with all electrodes set to the same voltage, the electric potential distribution $V(x, z)$ will be strongly dependent on x and the electric field ($F_z(x, z) = \textit{constant}$ for the ideal parallel plate capacitor) will depend everywhere on both x and z.

10.5.2 Simulation of the electric potential and field

Figure 10.15 is a plot of a simulation (in COMSOL) of $V(x,z)$ for the real electrode geometry, given zero conveyer amplitude but with V_{bias} present on all electrodes. Due the proximity of the ground plane, at the top surface the voltage between two electrodes is only (roughly) half of the voltage on either electrode. Even at the level of the CQW (10% above the ground plane) the voltage $V(x, z = D/10)$ retains a substantial x-dependence.

The quantity of interest is not the voltage but the electric field F_z at the level of the CQW, and the geometry of most interest is not the simple case of V_{bias}-only, but with the AC conveyer amplitude applied. Figure 10.16 is a plot of the electric field at $z = D/10$ as a function of distance x, for an instant in time with the electrodes driven by a 0.88 V-amplitude sine wave discretized in the usual fashion (ie, the voltage on electrode $\#n$ is $V_n = 0.88\,V\cos(n\frac{\pi}{7}) + 4.0\,V$, $n = 0\ldots6$). The proximity of the ground plane adds a very strong "ripple" to what ought to be a smooth-ish sinewave — the peak-to-trough height of the ripple is a considerable fraction of the peak-to-trough height of the overall sinewave!

It necessarily follows that attempts to simulate the physics of excitons in the presence of a conveyer ought to use the actual, more complicated potential which is strongly (perhaps unexpectedly strongly) perturbed by the electrode geometry.

10.5.3 Ripple model and empirical fit to the simulation

An empirical model can be constructed to include the ripple effects on the total conveyer (energy) potential.

$$
\begin{aligned}
U_{\text{total}} &= U_{\text{offset}} && (10.1)\\
&+ U_{\text{depth}}\cos(k_{\text{conveyer}}x - \omega t + \delta_{\text{conveyer}}) && (10.2)\\
&+ A_{\text{electrodes}}\cos(k_{\text{electrodes}}x + \delta_{\text{electrodes}}) && (10.3)\\
&\quad * \quad [U_{\text{depth}}\cos(k_{\text{conveyer}}x - \omega t + \delta_{\text{conveyer}}) + U_{\text{offset}}] && (10.4)
\end{aligned}
$$

The first term is just the energy offset due to the DC voltage V_{bias}. The second term is the desired sinusoidal conveyer, where U_{depth} is an empirically (e.g.

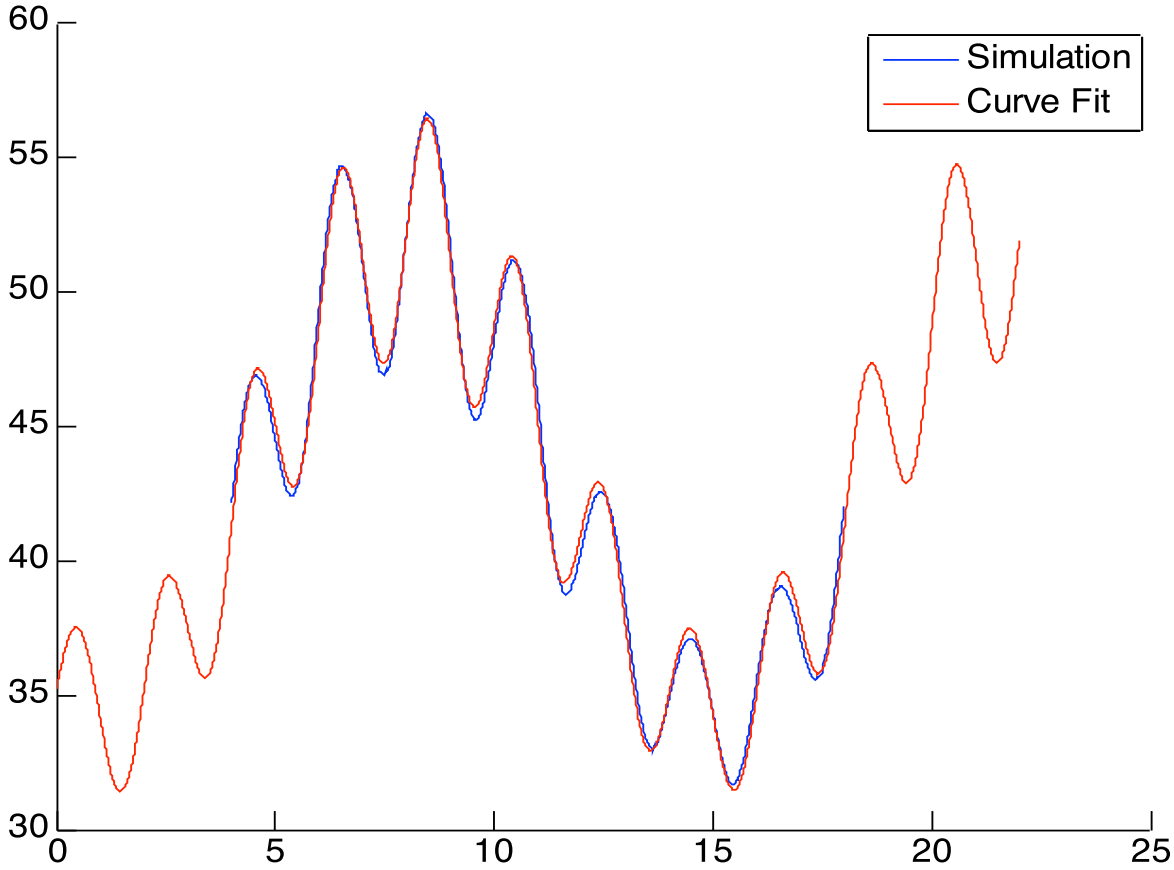

Figure 10.16: Plot of the electric field (vertical axis) as a function of x-position (horizontal axis, [μm]), at the z-level of the CQW, for an instant in time with the conveyer active (V_{bias}=4 V, V_{AC} = 0.88 V, ie the voltage sinewave of (true, semi-)amplitude 0.88 V is discretized across seven electrodes stepped $2\pi/7$ apart in phase.) The strong "ripple" effect is evident due to the 1 μm inter-electrode spacing being comparable to the 1 μm distance from the electrodes to the ground plane. The fit and fitted parameters are discussed in the text.

optically) measured amplitude. The product of the third and fourth terms construct the ripple effect. The third term models the electrode spacing geometry ($A_{\text{electrodes}}$ is a dimensionless "efficacy factor"), which modulates the fourth term, the "envelope function", which is essentially the desired conveyer potential all over again. The model is perhaps more easily understood when the fitted values are included and identified.

Table 10.2: Fit to the empirical ripple model.

Parameter		Value	Description
U_{depth}	=	9 meV	conveyer depth
U_{offset}	=	41 meV	energy offset due to V_{bias}
k_{conveyer}	=	$0.45/\mu\text{m} \approx 2\pi/14\,\mu\text{m}$	conveyer spatial wavenumber
δ_{conveyer}	=	2.7	spatial phase offset (sets which electrode is "first")
$A_{\text{electrodes}}$	=	0.088	"efficacy factor" of the geometry-induced ripple
$k_{\text{electrodes}}$	=	$3.14/\mu\text{m} \approx 2\pi/2\,\mu\text{m}$	stripe electrode spatial wavenumber
$\delta_{\text{electrodes}}$	=	-1.5336	spatial phase shift

This electrode ripple model is not needed for subsequent sections here, but it is necessary in ongoing efforts to model and numerically simulate the behavior of excitons in the presence of the conveyer potential.

10.6 Conveyance results examined with amplitude normalization

With some form of calibration in hand, it is feasible to replot the conveyer transport distance data of Figure 10.8 with the amplitudes of the different velocities normalized to that of a single velocity. Figure 10.17 is a plot for modes #1–#9 with all amplitudes rescaled and normalized to those of mode #1. (As is clear, not all curves were measured to the same equivalent voltage amplitude.)

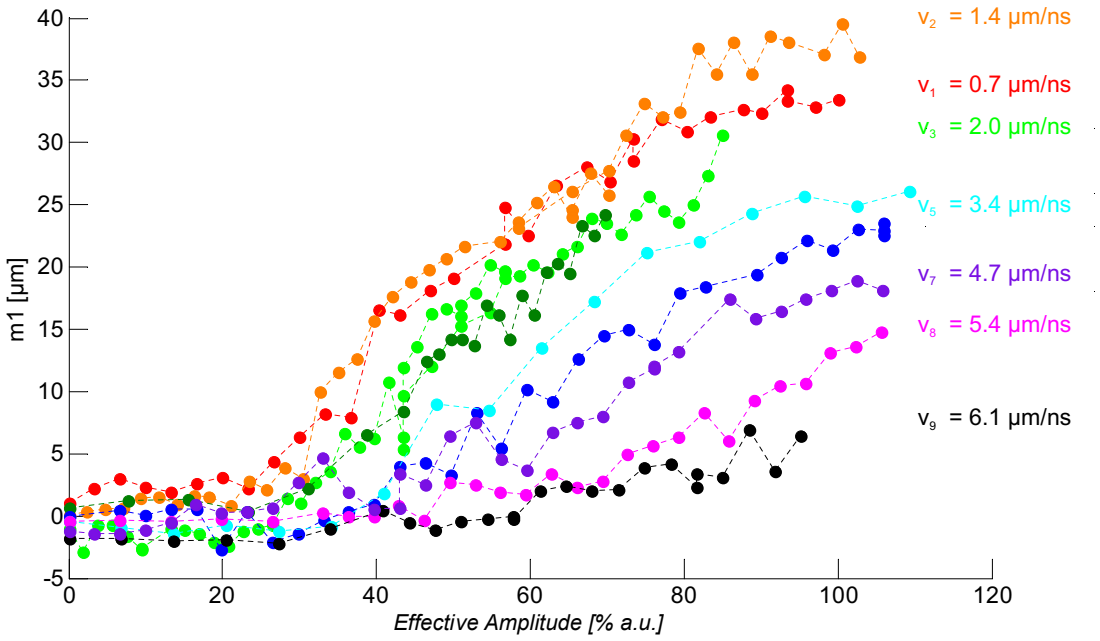

Figure 10.17: Exciton transport distance (as characterized by m_1) as a function of effective conveyer amplitude (normalized to mode #1), for all measured conveyer velocities v_1–v_9 (0.68 - 6.1 μm/ns).

The physics picture is now somewhat different than that seen without rescaling. In general, the highest velocities achieve shorter transport (m_1, ie *average*) transport distance, due perhaps in part to their lower collection efficiencies. There is a decent suggestion (though not conclusive given the apparent measurement noise) that v_2 does begin to overtake v_1 in transport distance. There is a hint that v_3 might even overtake v_1 and v_2 were the measurement extended farther. The amplitude for the onset of transport appears greater for the faster velocities, but the onset amplitudes for all modes are rather more tightly clustered. Lastly, there is some suggestion (most visibly for v_1, v_2, and v_5) that transport distance saturates. (Which would be expected in the presence of a downstream photolithography defect.)

10.6.1 Transport relative to sound velocity

Table 10.3: Studied conveyer frequencies and velocities. Velocities are measured in units of μm/ns $= 10^5$ cm/s, and also given as a percentage of the sound velocity, for a range of possible phonon modes (in bulk GaAs at $T \sim 1.5\,\mathrm{K}$). The [100] longitudinal-phonon mode is highlighted; for that case, modes #8 and #9 would be mildly supersonic.

		Conveyer operational frequency/velocity mode [#]								
		#1	**#2**	**#3**	**#4**	**#5**	**#6**	**#7**	**#8**	**#9**
Frequency [MHz]:		48.51	97.02	145.5	194.0	242.6	291.1	337	388	436.6
Conveyer velocity [um/ns]:		0.68	1.36	2.04	2.72	3.40	4.07	4.72	5.43	6.11
Phonon type (bulk GaAs, T~1.4K)	**Phonon velocity [um/ns]**	**Conveyer velocity normalized to sound velocity**								
[111] Longitudinal	**5.47**	12%	25%	37%	50%	62%	74%	86%	99%	112%
[110] Longitudinal	**5.31**	13%	26%	38%	51%	64%	77%	89%	102%	115%
[100] Longitudinal	***4.78***	***14%***	***28%***	***43%***	***57%***	***71%***	***85%***	***99%***	***114%***	***128%***
[100] Transverse	**3.40**	20%	40%	60%	80%	100%	120%	139%	160%	180%
[110] Transverse-1	**3.40**	20%	40%	60%	80%	100%	120%	139%	160%	180%
Typical SAW	**3.00**	23%	45%	68%	91%	113%	136%	157%	181%	204%
[111] Transverse	**2.84**	24%	48%	72%	96%	120%	143%	166%	191%	215%
[110] Transverse-2	**2.51**	27%	54%	81%	108%	135%	162%	188%	216%	243%

A natural velocity scale for comparison with the conveyer is the set of possible sound velocities. Perhaps the most obvious relevant mode is the longitudinal acoustic phonon, in bulk GaAs (at $T \approx 1.5\,\mathrm{K}$), in the $\langle 100 \rangle$ crystal direction. (The conveyer sample is MBE-grown as $\langle 100 \rangle$, ie the x, y, and z-axis as defined for experimental convenience in this research (Section 2.2) are all crystallographically-

identical in the bulk GaAs, and the x-axis is along the direction of conveyance.) Table 10.3 lists the the conveyer-potential velocities for the studied v_1–v_9 in both physical units and as as percentage of the sound velocity for the set of acoustic phonon modes in bulk GaAs. For the $\langle 100 \rangle$ LA-phonon ($v_{LA}^{\langle 100 \rangle} = 4.78\,\mu$m/ns), the studied transport curve v_7 is just barely subsonic, and v_8 and v_9 are 14% and 28%, respectively, above the sound velocity.

Other possibly-relevant sound velocities?

It is conceivable that other (acoustic) sound velocities may play a role. One would expect that a predominantly s-state exciton ought to couple predominantly to longitudinal phonons [Rössler, 2004]. If some portion of the exciton is in a p-state, it could couple to transverse phonons as well, and the $\langle 100 \rangle$ TA-phonon velocity is a good deal lower ($3.40\,\mu$m/ns) than the LA-case. Moreover, there are a number of material interfaces in the CQW sample, e.g. at the top surface, and also at the GaAs/$Al_{0.33}Ga_{0.67}$As interfaces of the CQW, which could in principle support surface modes. Surface acoustic waves (SAW) are combinations of both longitudinal and transverse modes, and their velocities are typically slightly lower than even the transverse mode [White, 1970]. The sample is fairly thin, $1\,\mu$m, and so low energy phonons could have wavelengths long enough for surface modes to extend to the depth of the quantum wells. However, this would require some degree of transverse coupling, which is a subject for future theoretical analysis.

(The exciton conveyer system discussed here appears quite different in nature from the SAW transport work mentioned briefly in Section 8.1.4. In those experiments, SAWs are deliberately excited directly by surface transducers, and electrons and holes or excitons are transported indirectly (via the quantum-confined Stark effect) by e.g. piezoelectric deformation of the crystal. For the conveyer, the moving electrostatic field is induced directly by the surface electrodes, and the potential velocity is not determined by the sound velocity.)

Evidence for a supersonic transition?

An initially curious feature of Figure 10.17 is that there is no immediately obvious signature of a change in transport behavior for the v_8 (or v_9) curves, which should be slightly above the $\langle 100 \rangle$-LA sound velocity. (If other transverse modes are relevant, than curve v_6 would also be supersonic, and in the case of SAW, perhaps v_5 also.) Inspection of the slopes of the transport curves or the effective conveyer amplitude threshold for the onset of transport reveals no dramatic difference above a particular velocity within the measured range. It is possible that subtle effects are present but masked by noise in the transport curves. In particular, for the $\langle 100 \rangle$-LA case, v_8 is only mildly (14%) supersonic, the v_9 curve is especially noisy (as a fraction of the signal), and the v_9 experimental data does not extend to the highest (effective) amplitudes reached by other measurements.

Some naive speculations on supersonic interaction

At present, we lack a complete theory of (indirect) exciton-phonon interactions. In the most naive 1-dimensional picture, for an exciton with initial velocity v_i^{x} emitting an LA-phonon of $E_{\mathrm{phonon}} = |p|v_s$, conversation of energy and momentum leads to the simple scattering relation

$$v_f^{\mathrm{x}} = 2|v_s| - v_i^{\mathrm{x}},$$

where v_s is the phonon velocity, and hence several scattering regimes

1. Excitons with $v_i^{\mathrm{x}} > 2v_s$ scatter backwards when emitting a phonon.
2. Excitons with $v_i^{\mathrm{x}} = 2v_s$ scatter to ground.
3. Excitons with $v_s < v_i^{\mathrm{x}} < 2v_s$ scatter to $0 < v_f^{\mathrm{x}} < v_s$
4. Excitons with $v_i^{\mathrm{x}} < v_s$ cannot emit a phonon.

(An important feature of this result (mentioned in Chapter 2) is that in bulk GaAs, hot excitons can only cool to the ground state by emission of phonons of energy $E^{\mathrm{ph}} = 2m_x v_s^2$; the timescale for that cooling process can be longer than the

exciton lifetime. In CQW systems, however, z-translation symmetry is violated, relaxing restrictions of momentum conservation, and cooling to the lattice happens much faster, well within the (indirect) exciton lifetime.)

This simple picture leads to particular behavior for excitons initially near v_s: Those with $v_i^{\mathrm{x}} = v_s + \delta v$ downscatter $\rightarrow v_f^{\mathrm{x}} = v_s - \delta v$, and those with $v_i^{\mathrm{x}} = v_s - \delta v$ do not scatter at all. Thus, for curve v_8 only mildly above the sound velocity, $v_i = 1.14 v_s$ would lead to $\rightarrow v_f = 0.86 v_s$; perhaps such a small velocity change may simply not have a strong effect on the transport result? (And the measurements in curve v_9 may simply not extend far enough.)

However, this picture is perhaps much too naive for a number of reasons: the excitons are in CQW, not 3D-bulk material, so momentum conservation is relaxed due to the z-translation noninvariance. The lattice bath temperature $T = 1.5\,\mathrm{K}$ puts the mean *thermal* exciton velocity $v = \sqrt{\frac{2k_BT}{m_x}} \approx 14\,\mu\mathrm{m/ns}$ much higher than these studied conveyer velocities. Thus, the actual picture is more akin to excitons moving randomly, thermally, in the presence of a comparatively slowly-moving conveyer potential, possibly actively emitting acoustic phonons and scattering among states much faster than $2v_s$. A complete theory of the indirect exciton-phonon interaction, in the presence of the conveyer potential, is a subject for future work.

10.7 Conclusion

We have demonstrated realization of electrostatic conveyers for indirect excitons, in a GaAs/$Al_{0.33}Ga_{0.67}$As coupled quantum well structure. The conveyer is a laterally moving lattice potential for excitons, generated by laterally modulated electrode voltages. The wavelength is set by the electrode periodicity, and the lateral velocity and potential depth are controlled *in situ* by, respectively, the frequency and voltage. Operation at RF frequencies corresponded to a range of conveyer potential velocities both slower and faster than the phonon velocity.

We observed exciton transport over several tens of microns, and studied the transport as a function of the conveyer potential amplitude and velocity and exciton density. We observed a dynamical localization-delocalization transition

for the excitons in the conveyer with varying exciton density and velocity and amplitude of the conveyer potential, a dynamical counterpart of the localization-delocalization transition for excitons in static lattices [Remeika et al., 2009]. In the localization regime, with a deeper potential and moderate exciton density, excitons are moved by the conveyer, following the moving lattice potential. In the delocalized regime, with shallower lattice potential or sufficiently high exciton density, excitons do not follow the conveyer motion. Generally, faster conveyer potential velocities (corresponding to appreciable fractions of or somewhat greater than the phonon velocity(ies)) lead to reduced transport, given the same conveyer potential depth and exciton density.

A theoretical model of the indirect exciton – phonon interaction in the presence of the conveyer potential are subjects of ongoing and future work. A number of possible future experiments, including time-resolved measurements, temporally-switched conveyer, and spin transport via the conveyer are briefly described in Section C.1.

Appendix A

Octopus CAD diagrams and machine drawings

A.1 Crown / Head section

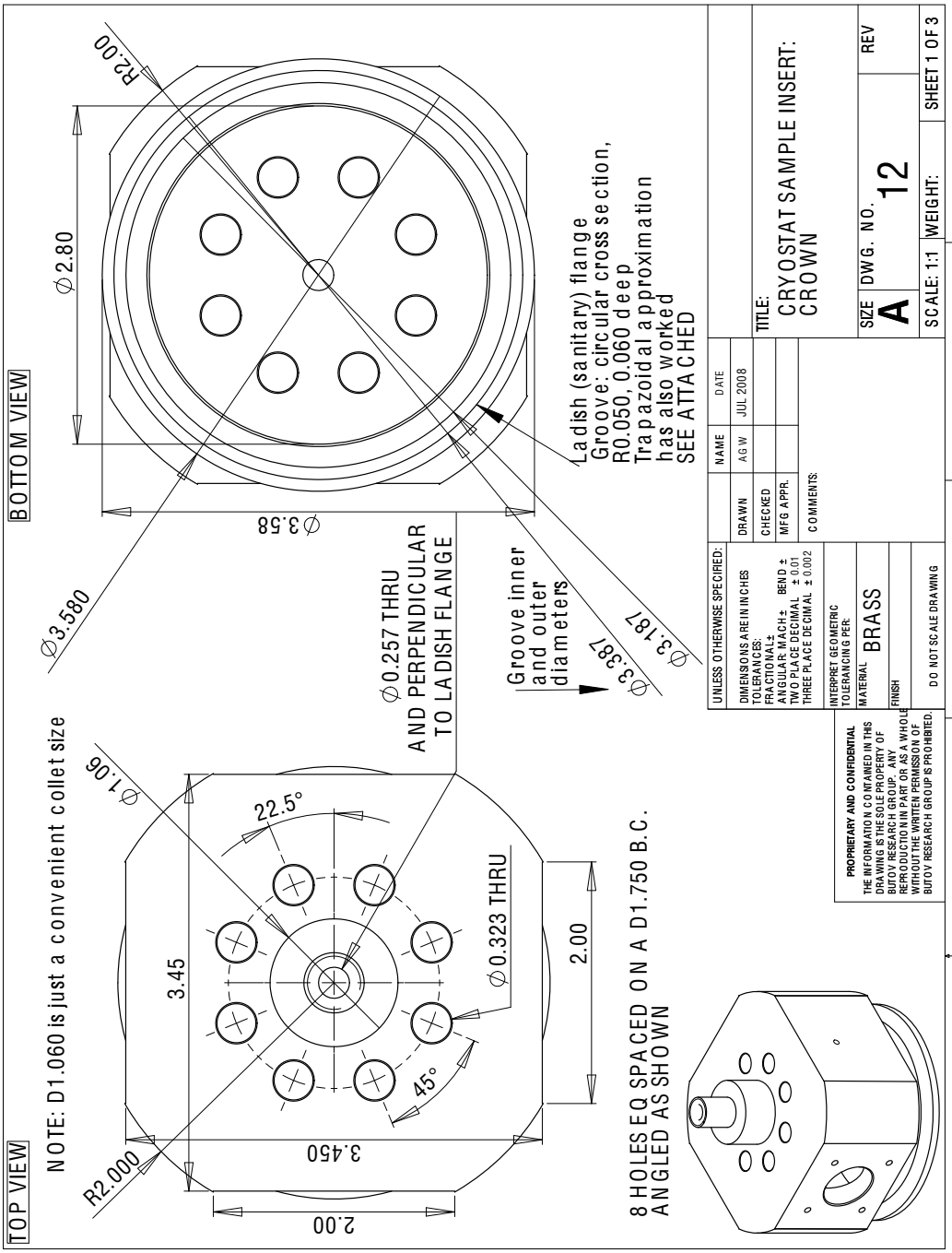

Figure A.1: fullcrown-Sheet1

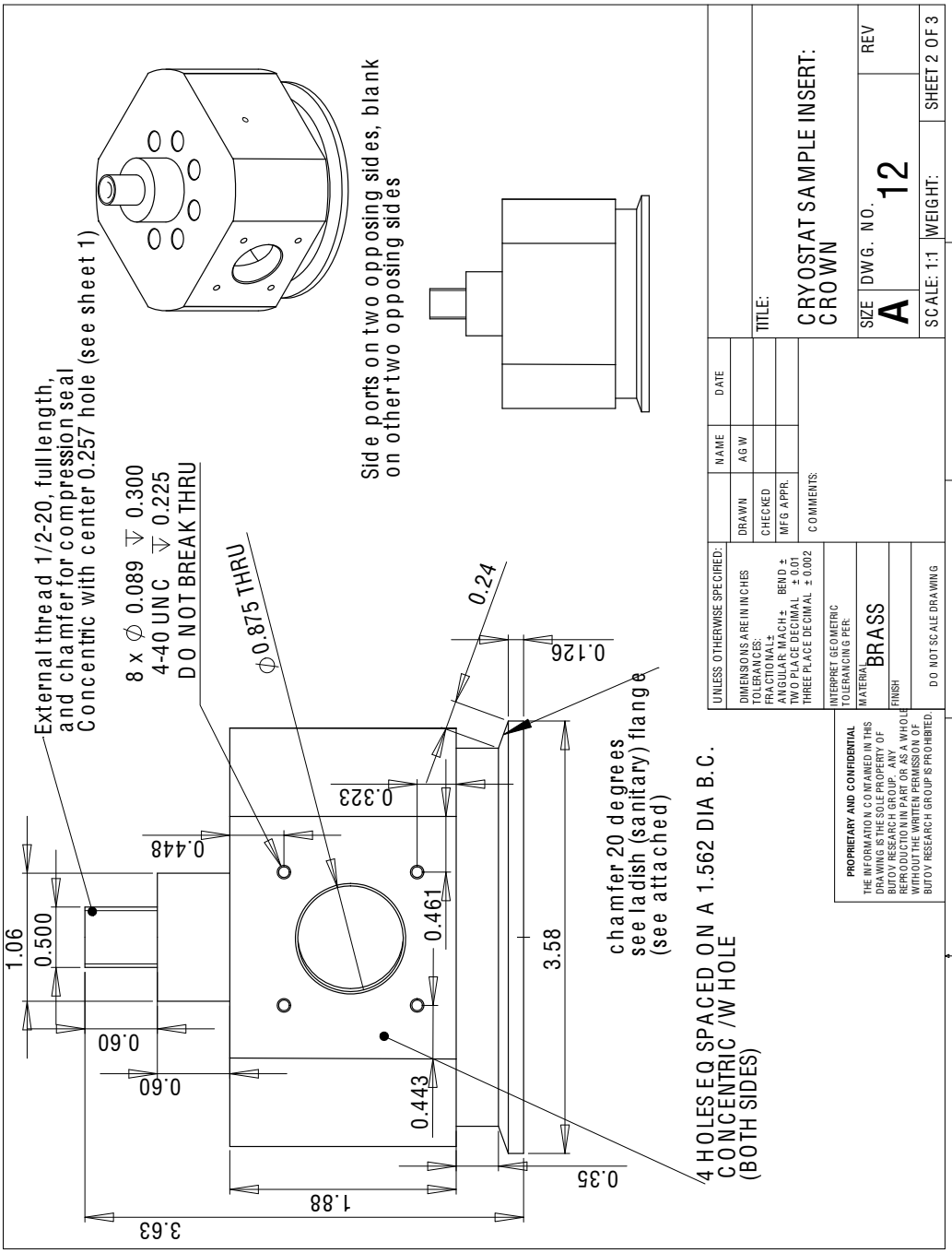

Figure A.2: fullcrown-Sheet2

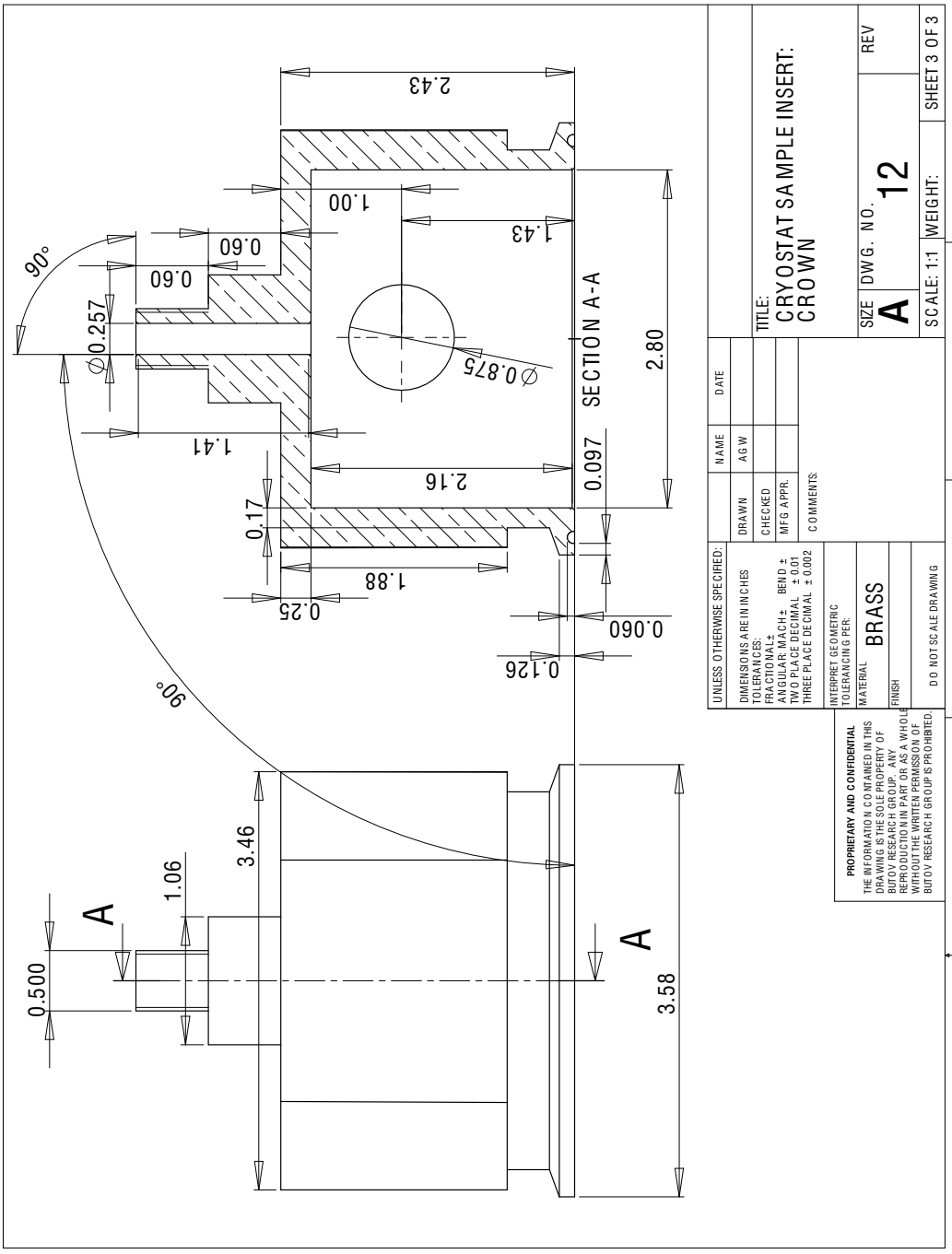

Figure A.3: fullcrown-Sheet3

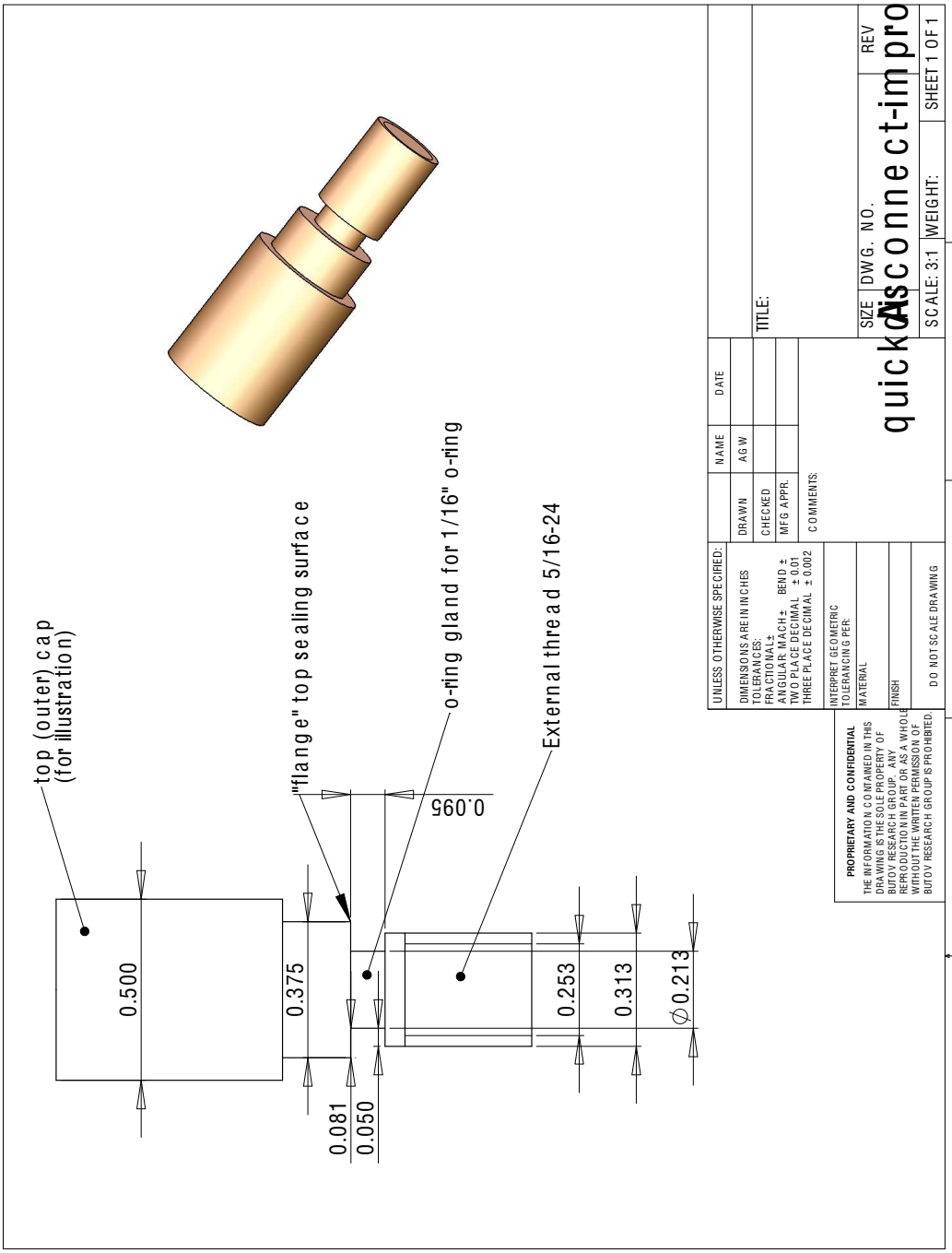

Figure A.4: quickdisconnect-improved-Sheet1

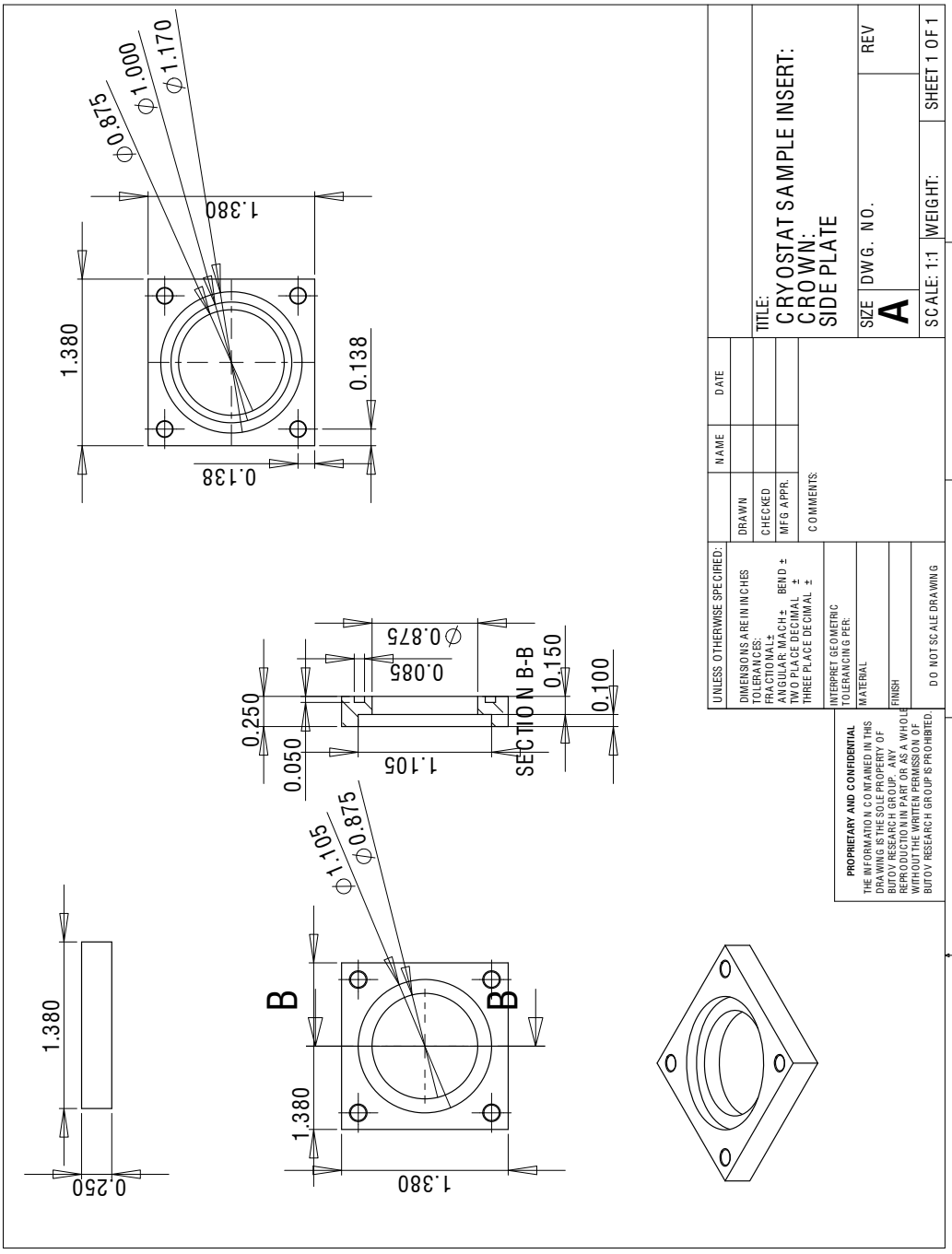

Figure A.5: sideplate-bigfeedthrough-Sheet1

A.2 Shaft

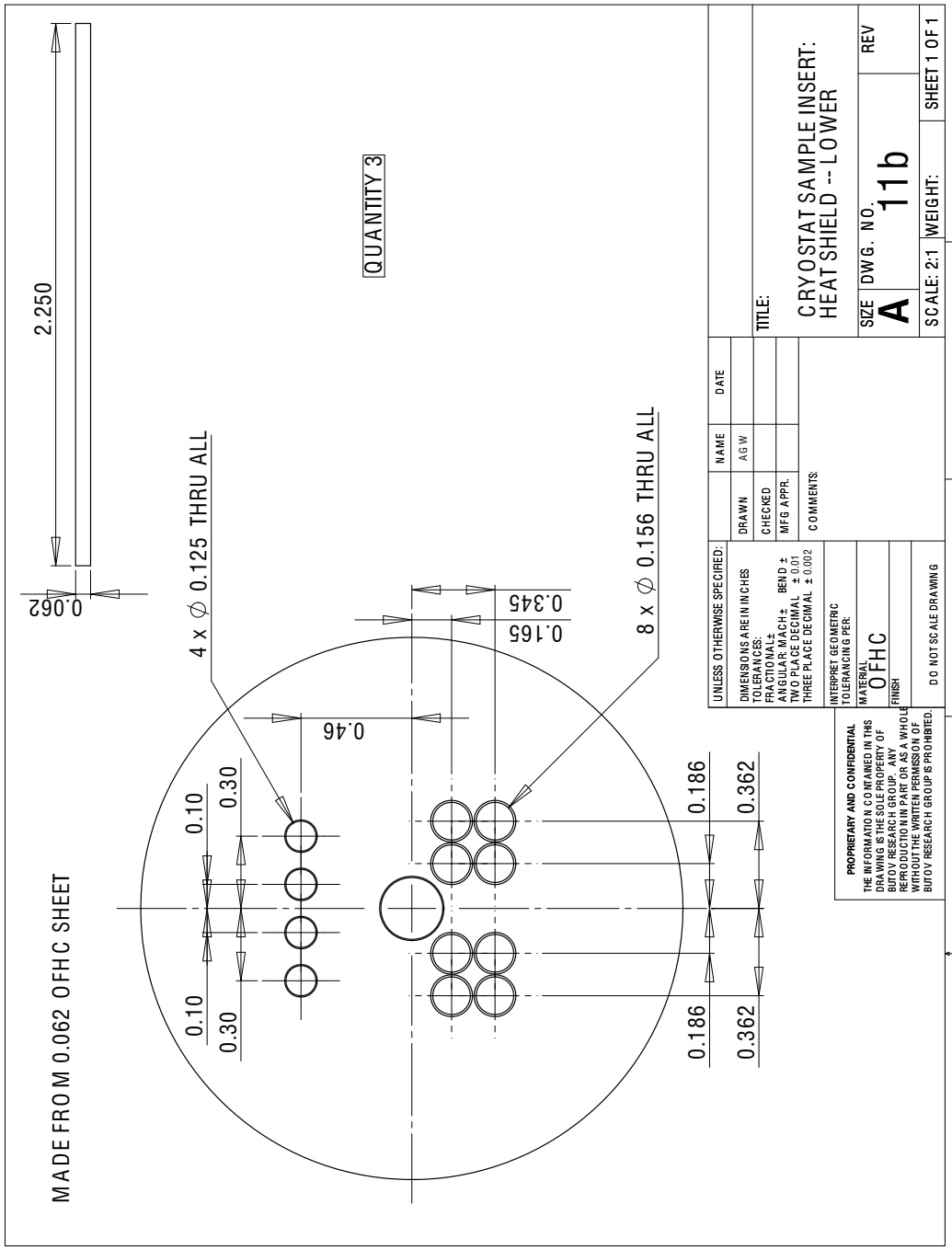

Figure A.6: heatshield-lower-Sheet1

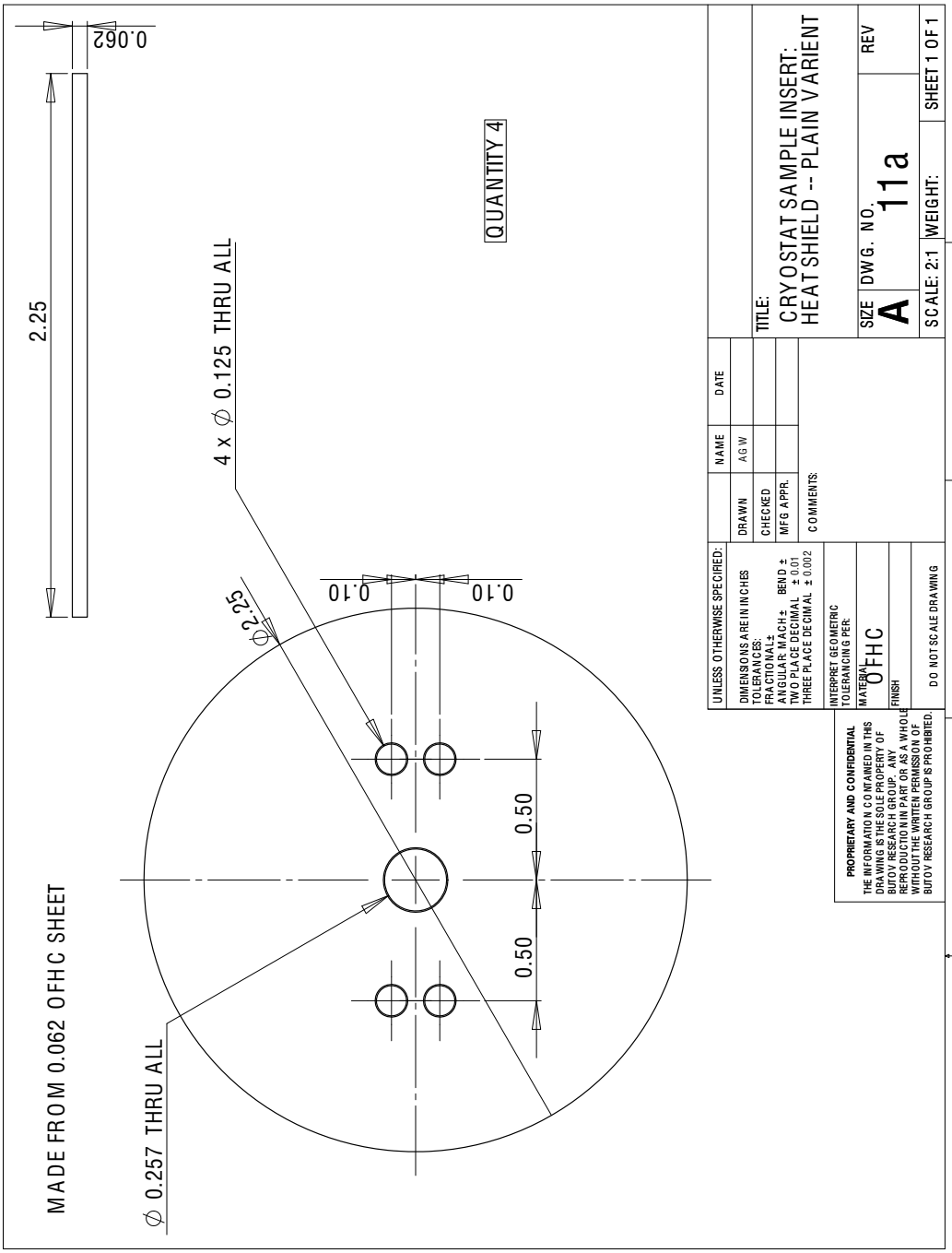

Figure A.7: heatshield-plain-Sheet1

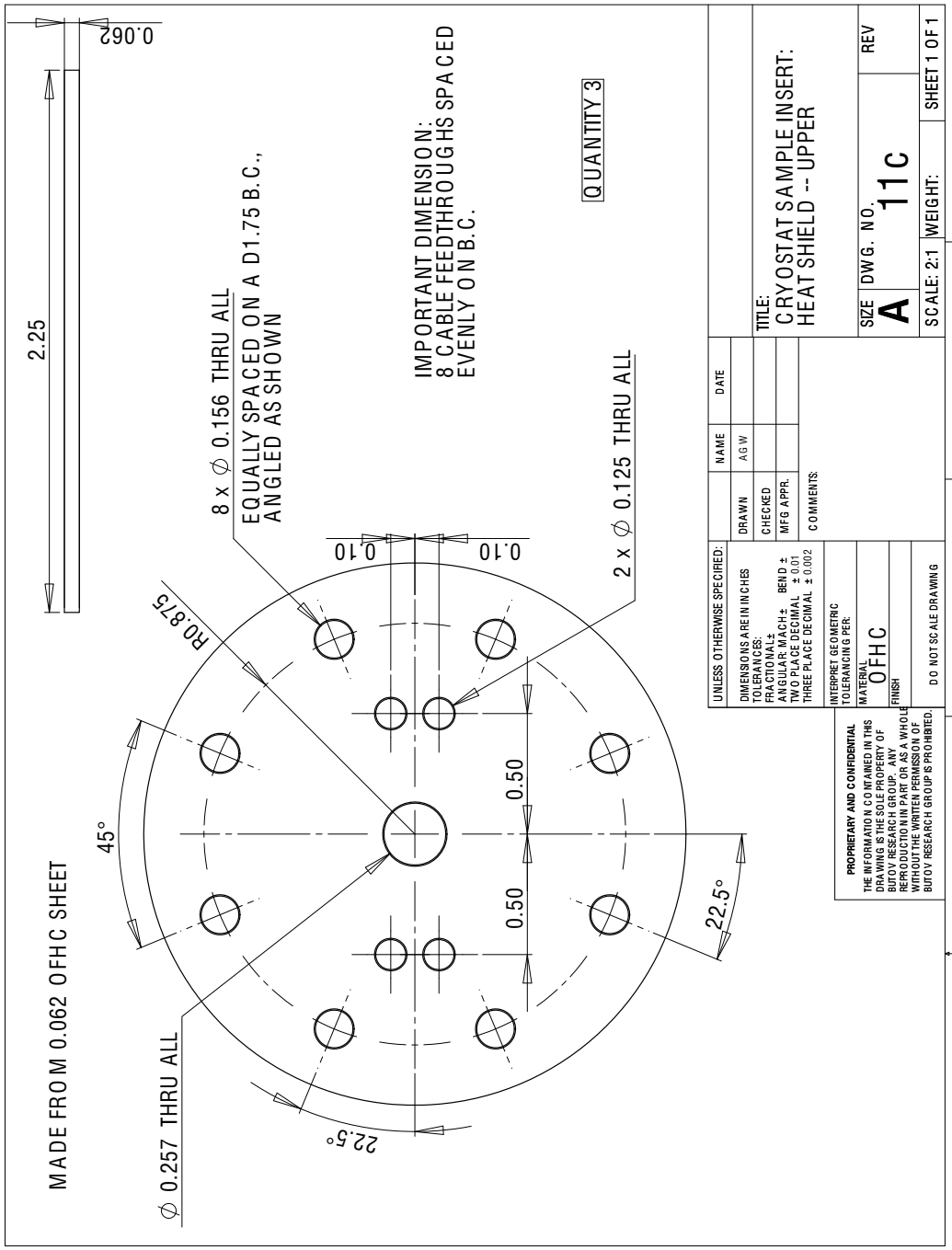

Figure A.8: heatshield-upper-Sheet1

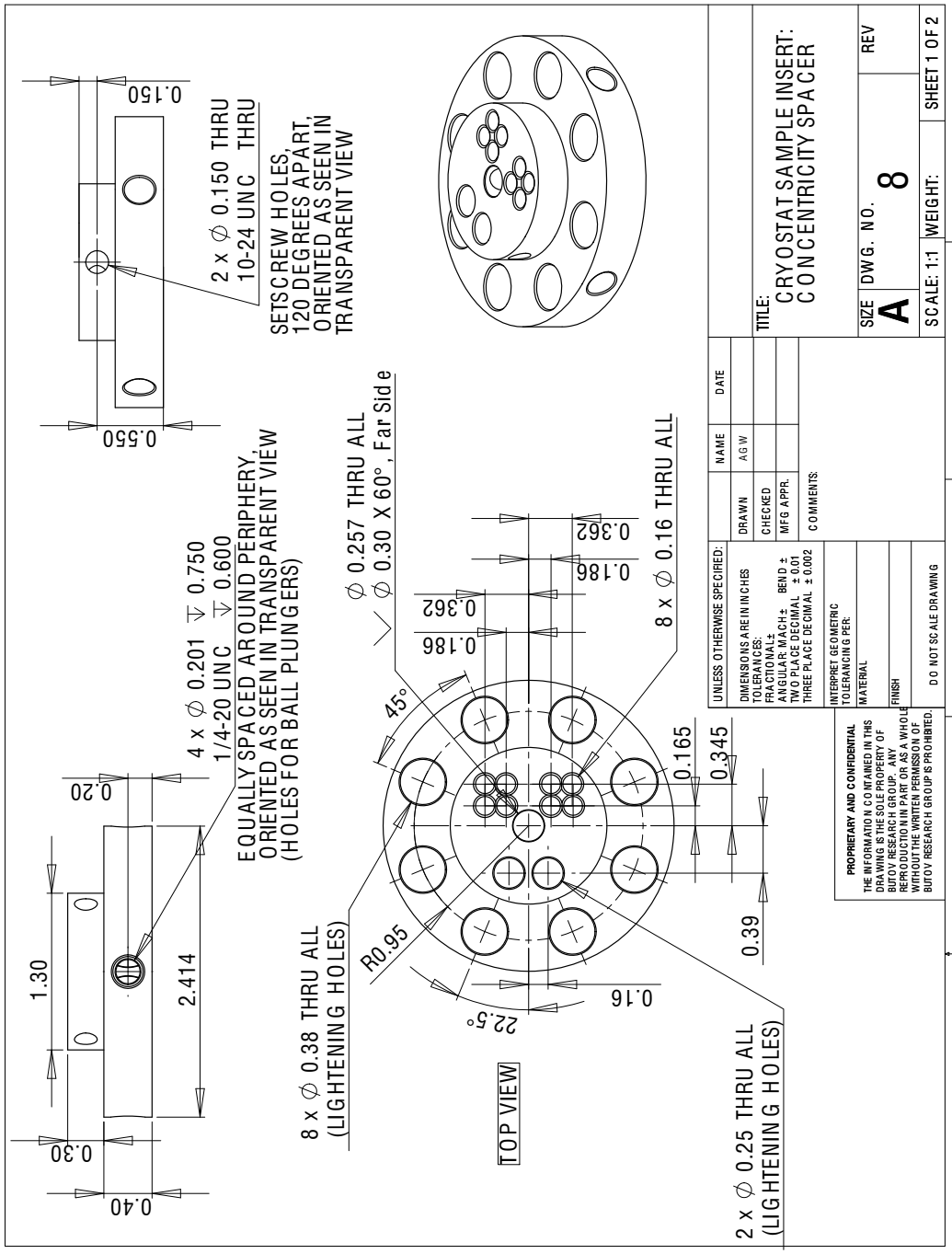

Figure A.9: concentricity-spacer-Sheet1

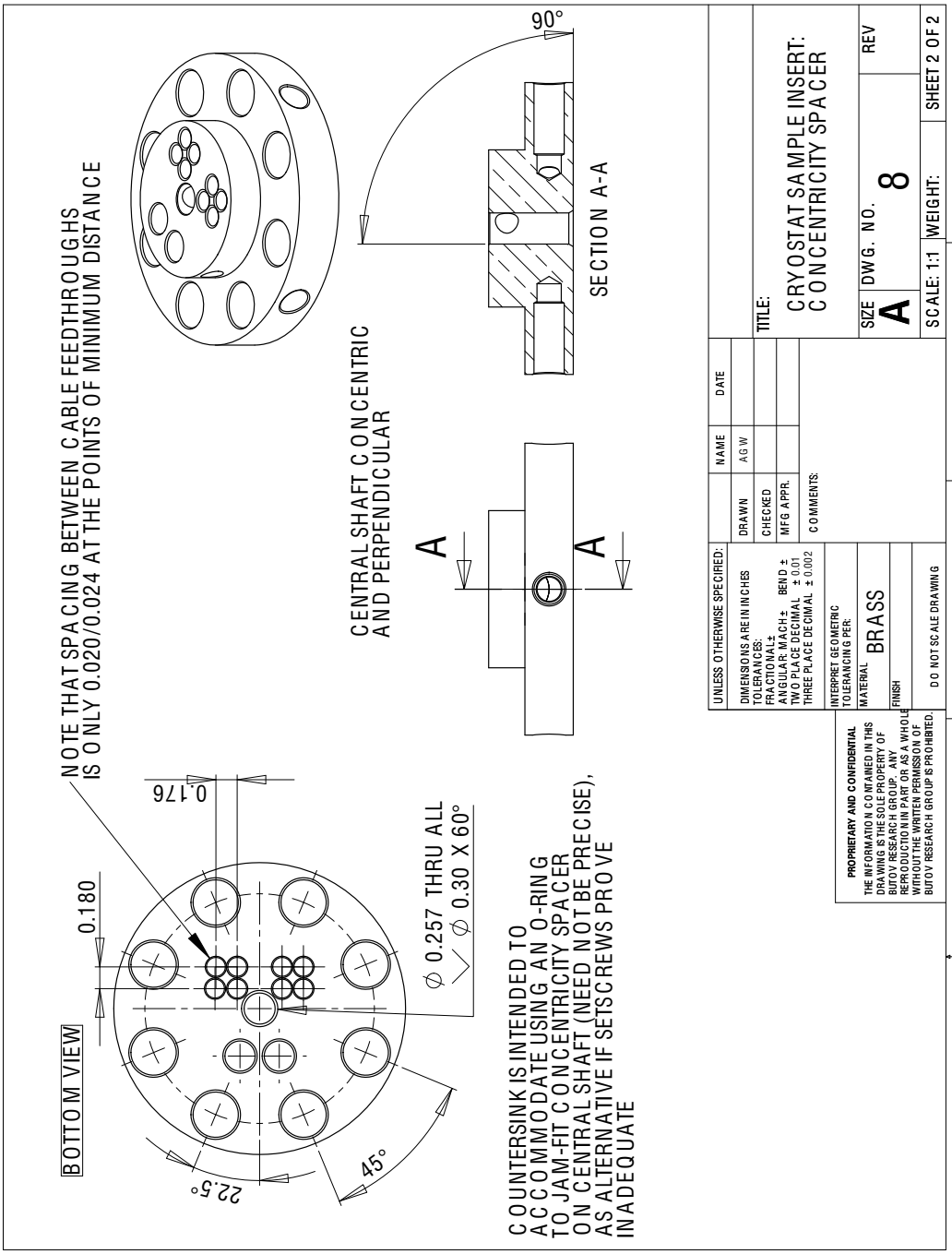

Figure A.10: concentricity-spacer-Sheet2

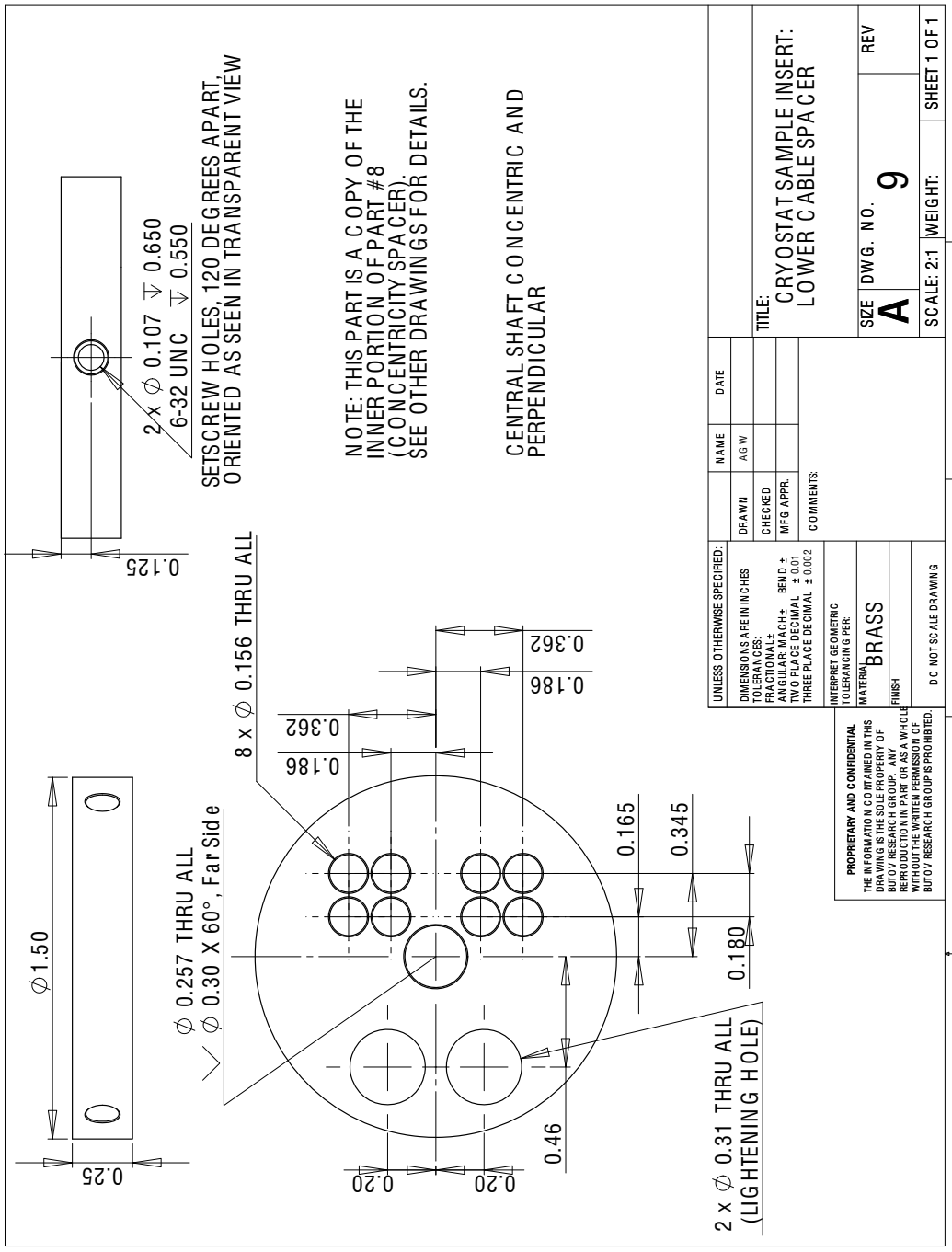

Figure A.11: lowercablespacer-Sheet1

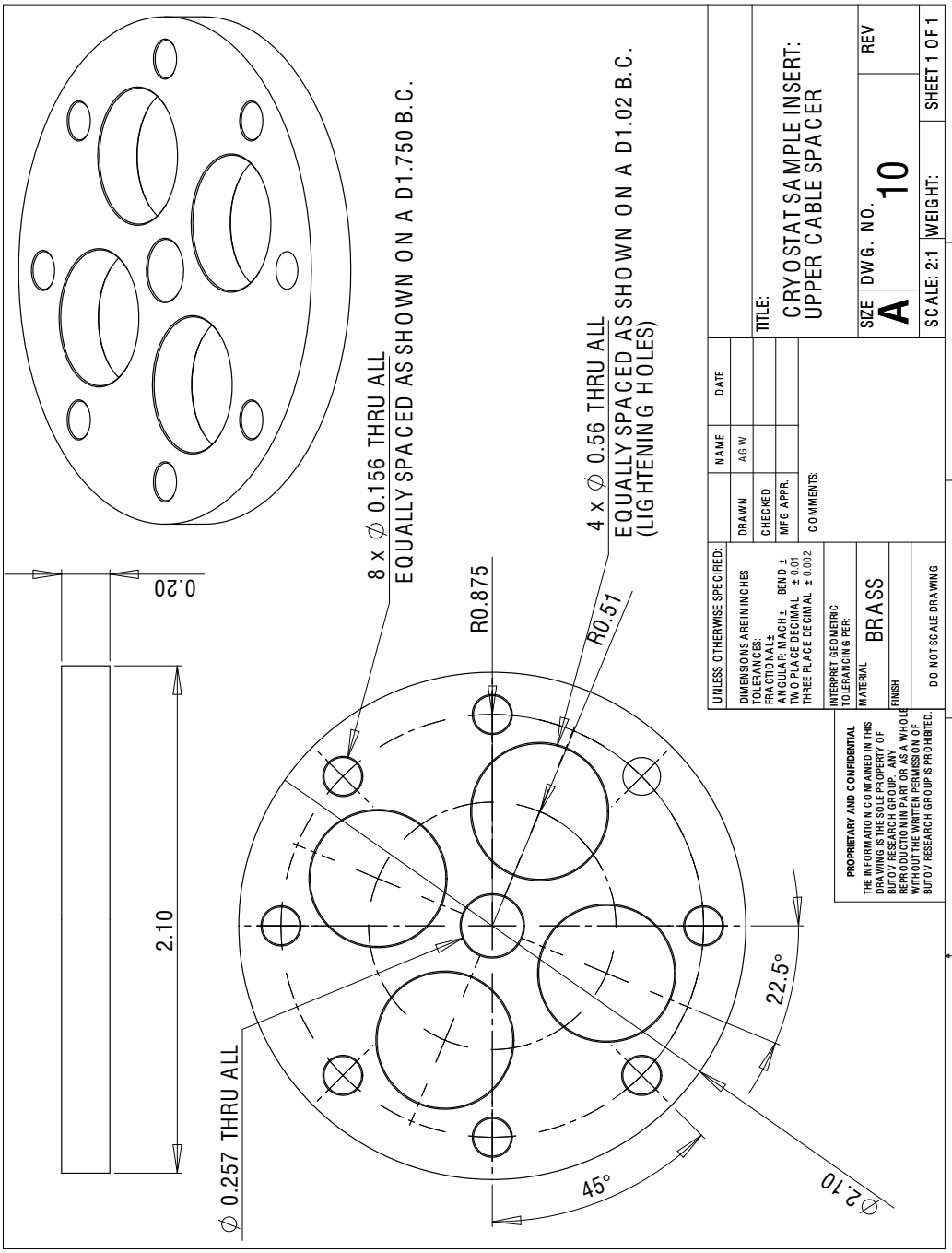

Figure A.12: uppercablespacer-Sheet1

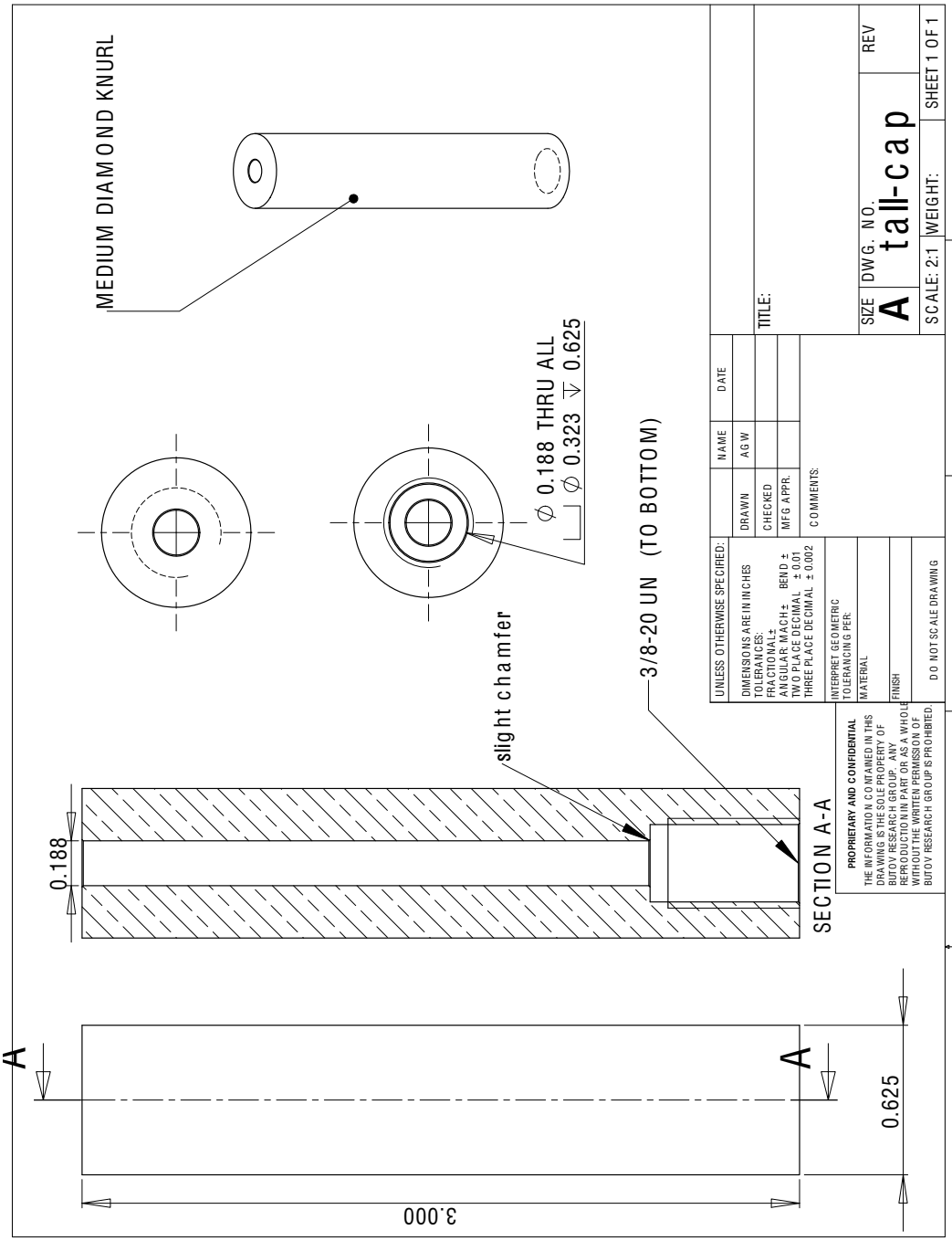

Figure A.13: tall-cap-Sheet1

A.3 Tail section

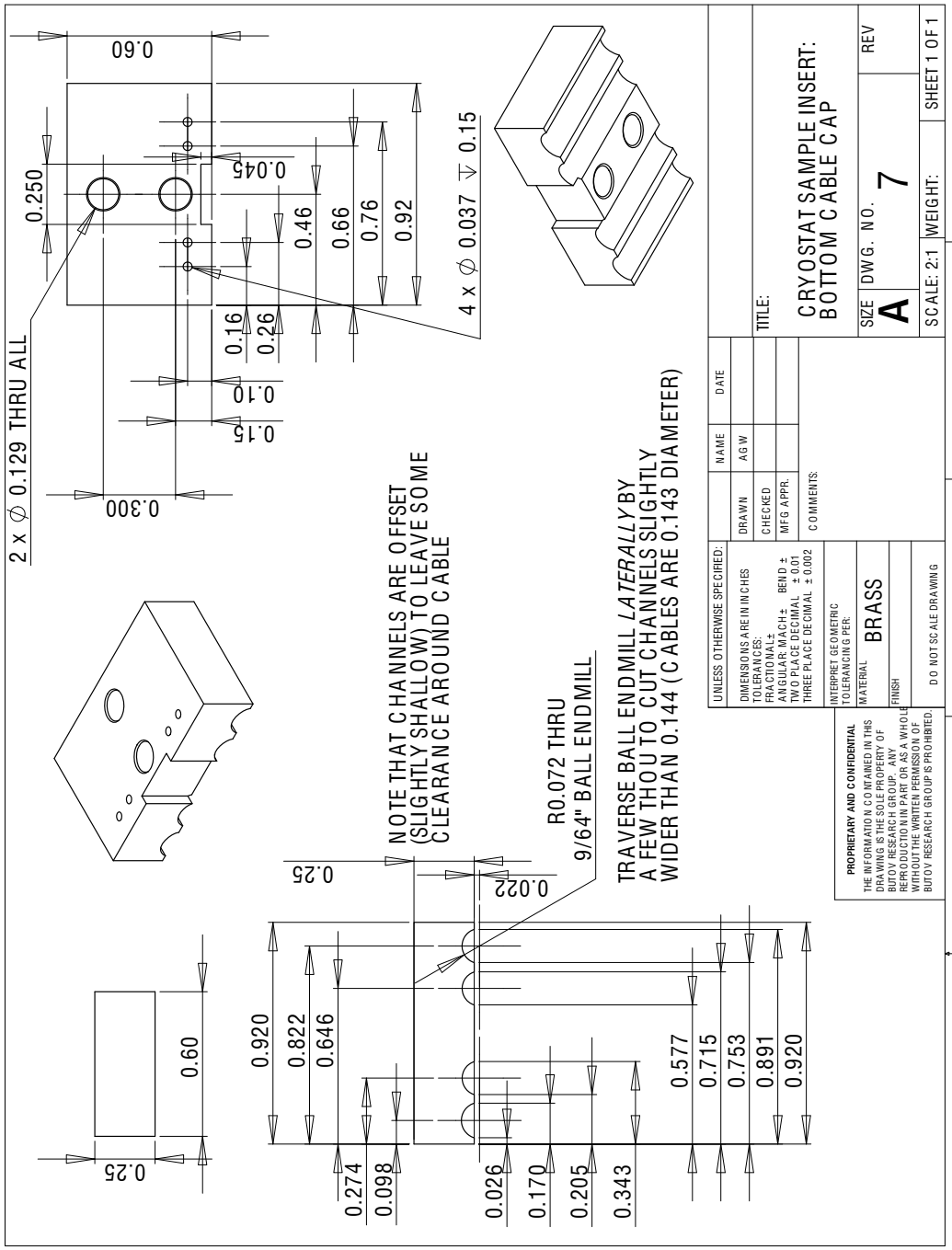

Figure A.14: bottomcablecap-revised-Sheet1

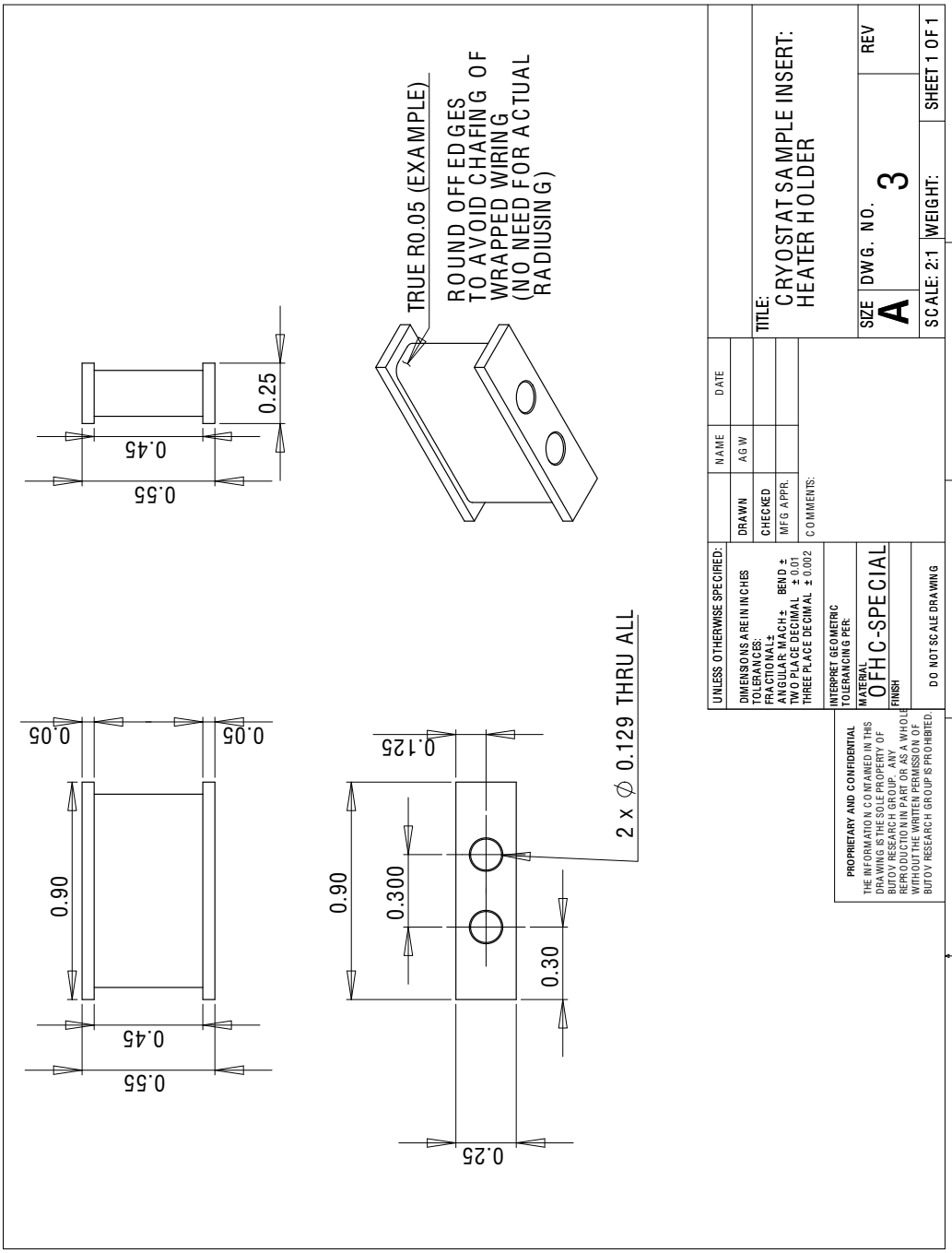

Figure A.15: heaterholder-Sheet1

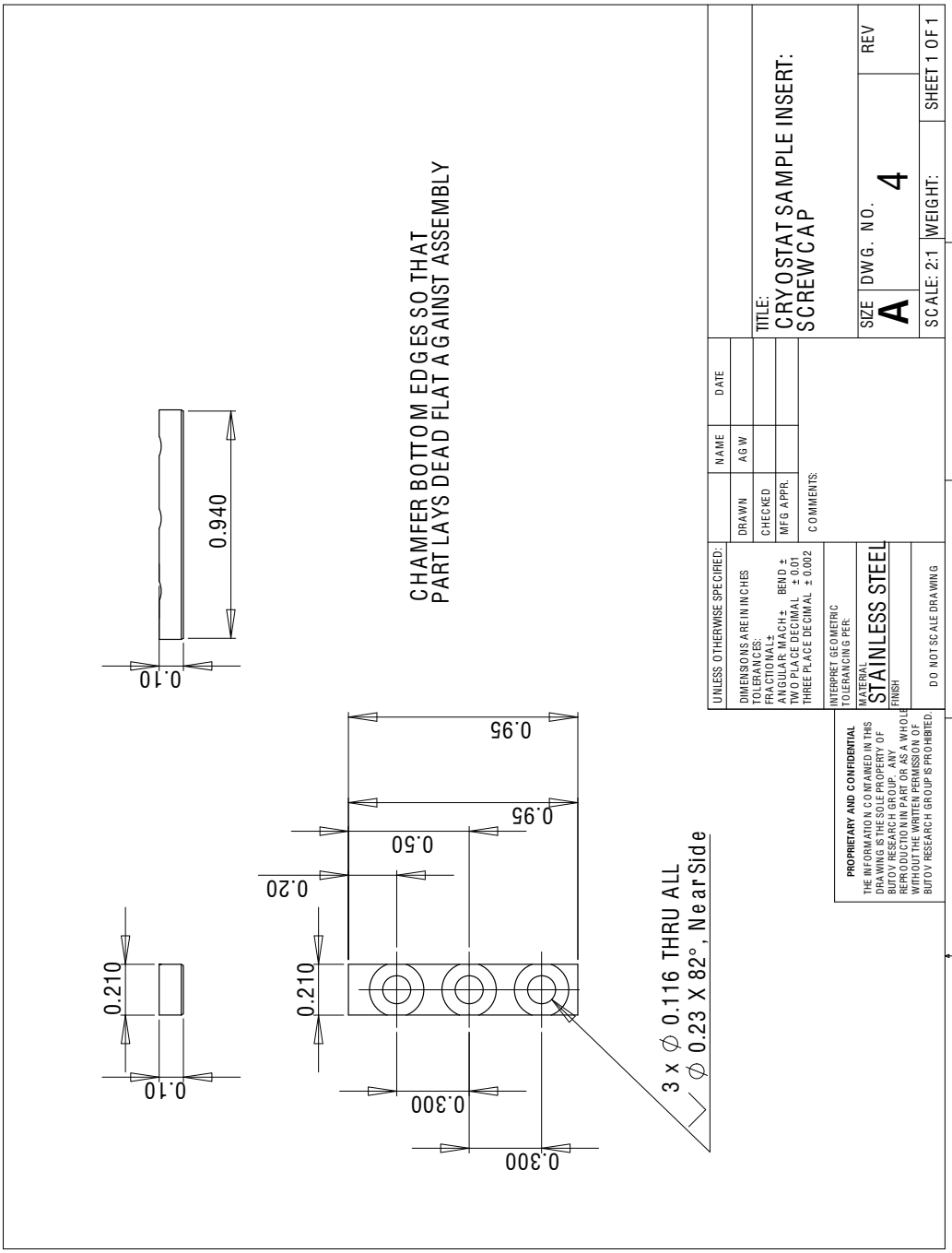

Figure A.16: screwcap-Sheet1

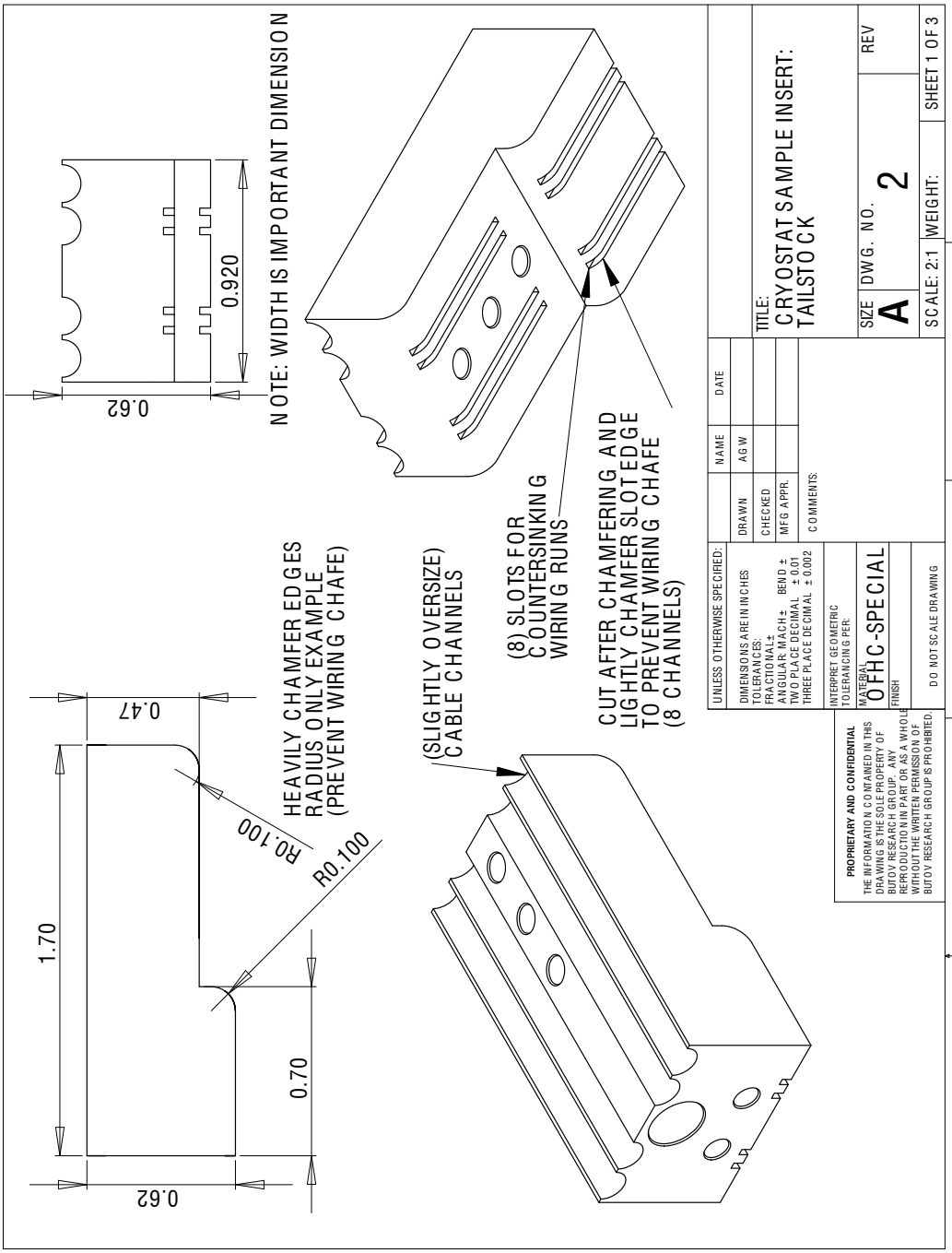

Figure A.17: tailstock-v4-Sheet1

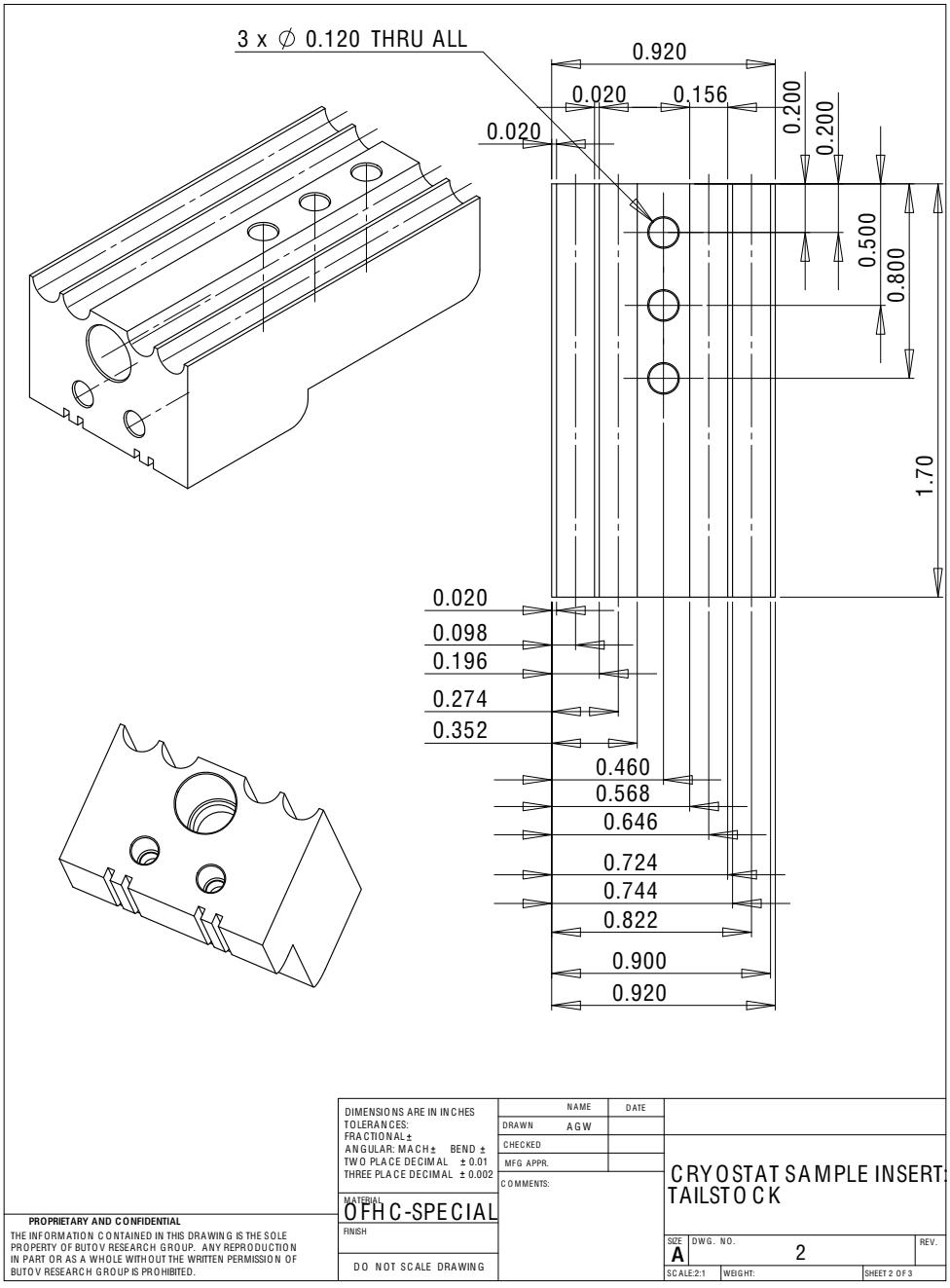

Figure A.18: tailstock-v4-Sheet2

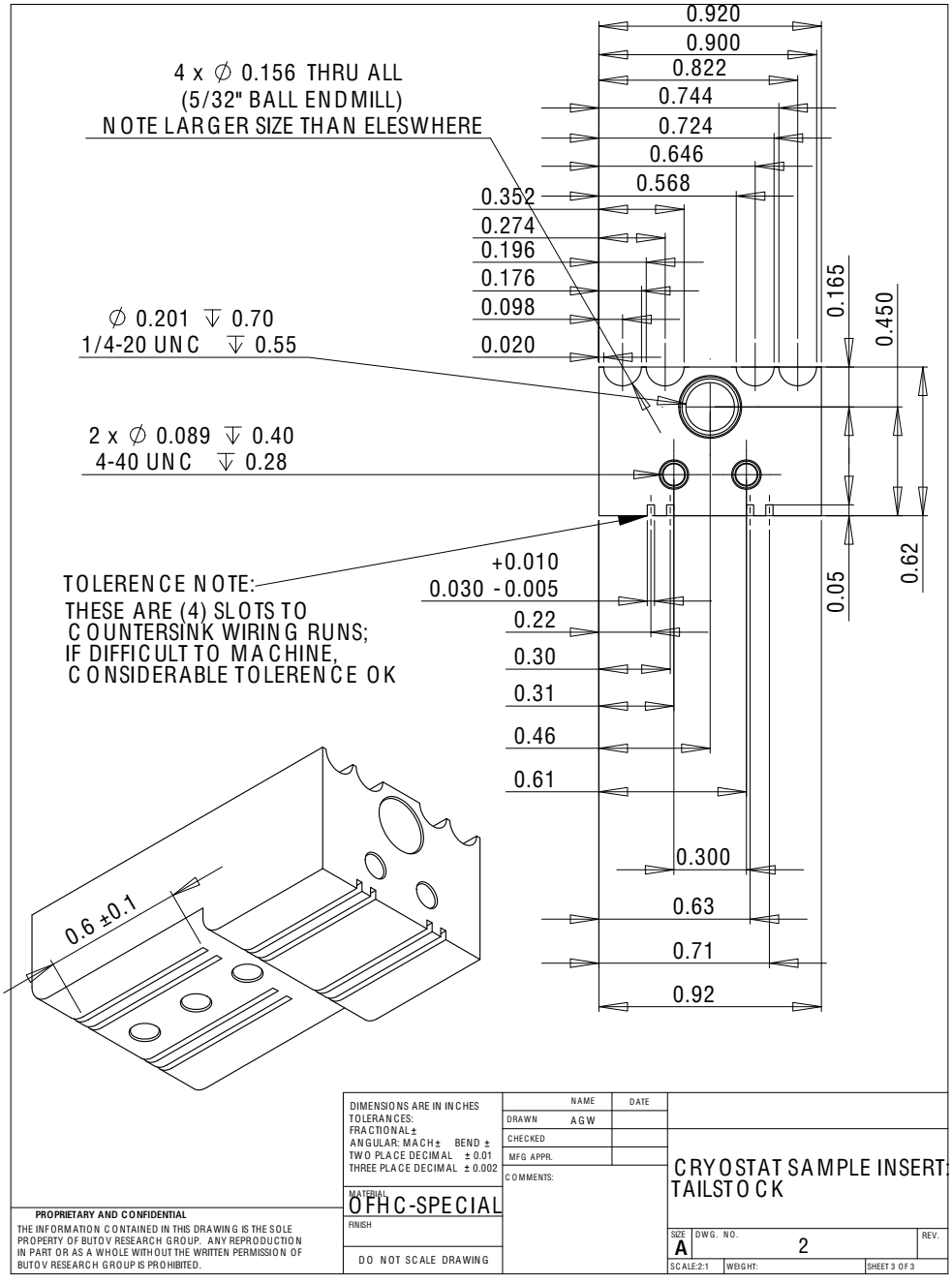

Figure A.19: tailstock-v4-Sheet5

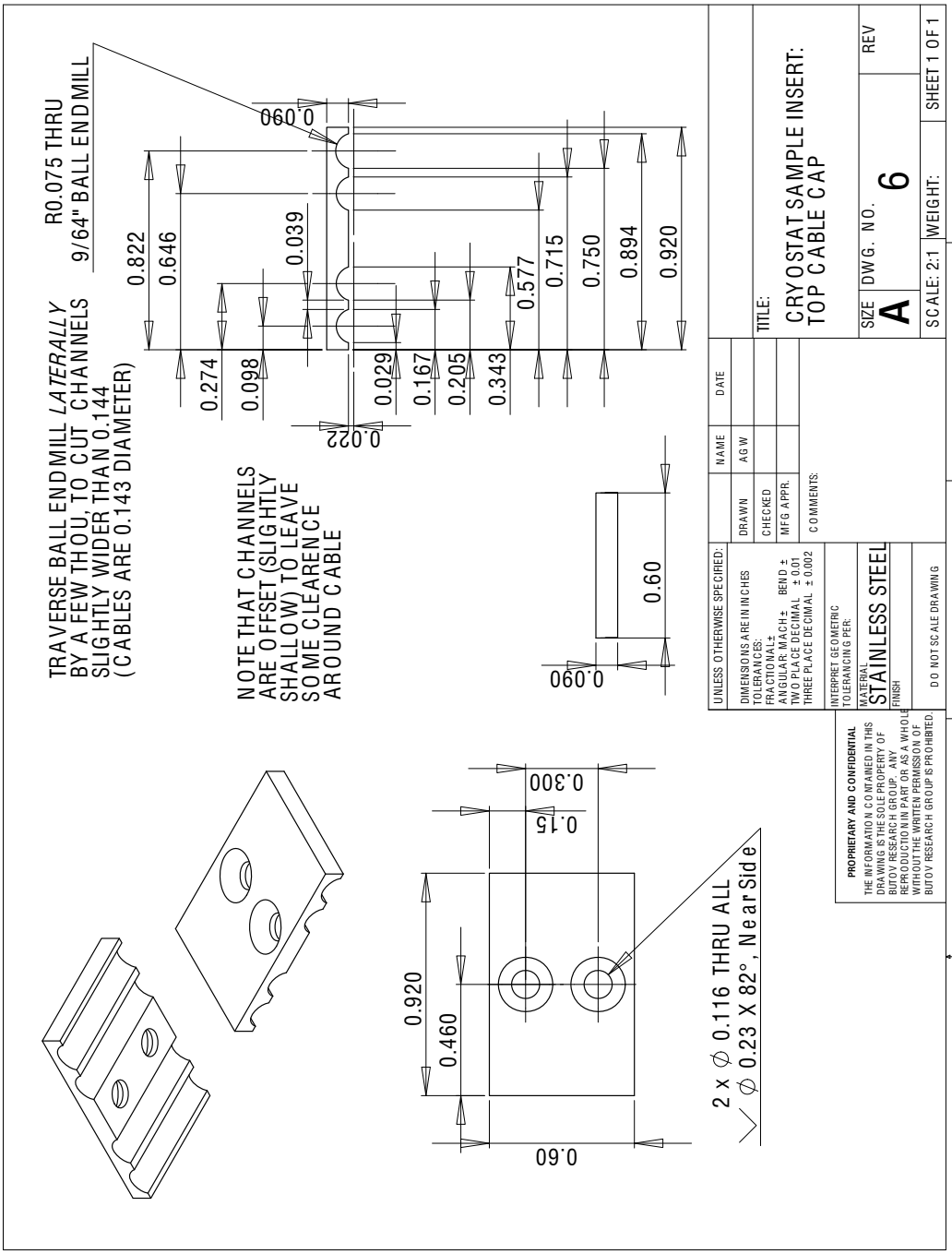

Figure A.20: topcablecap-Sheet1

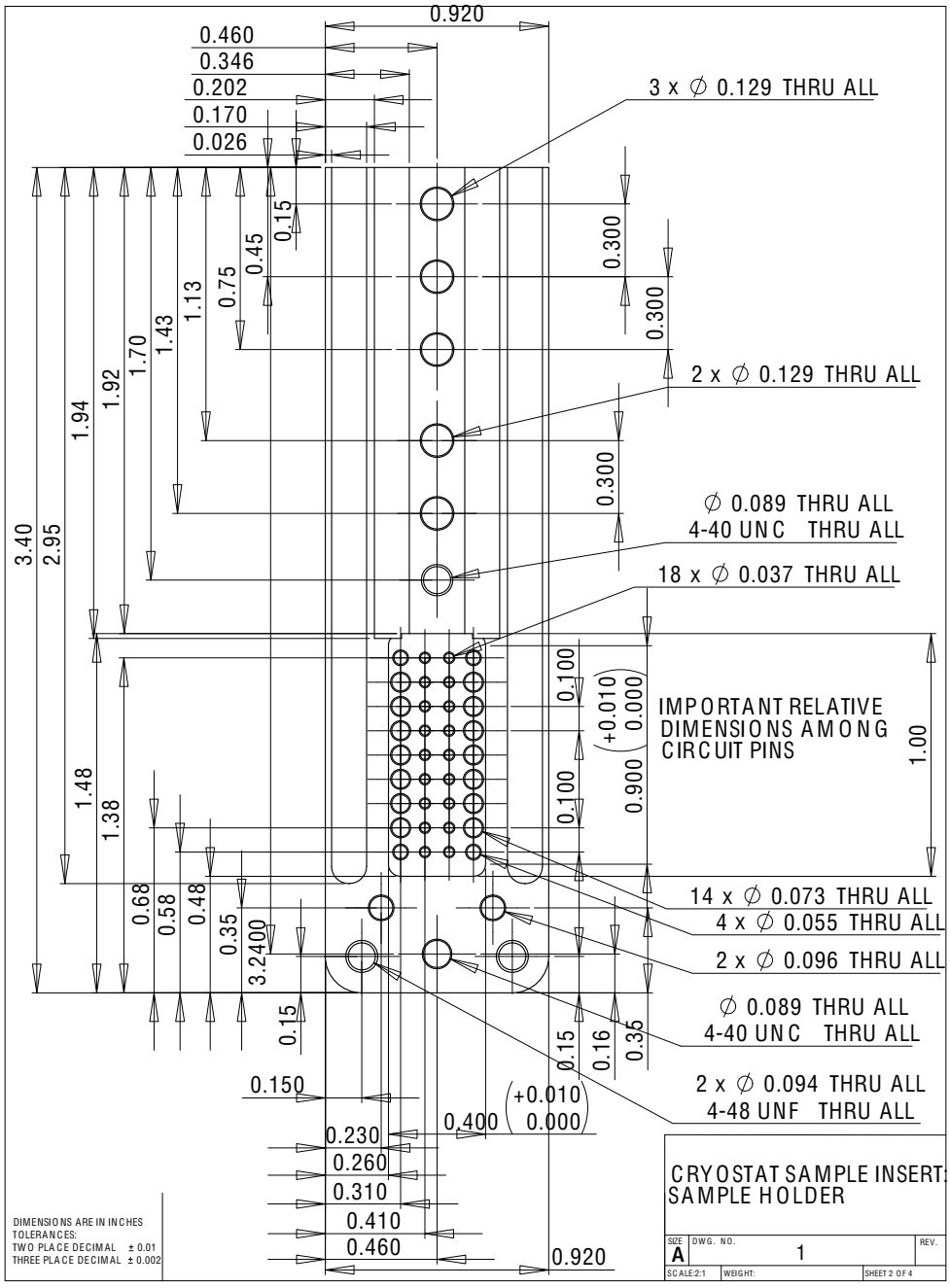

Figure A.21: sample-holder-v6c-Sheet2

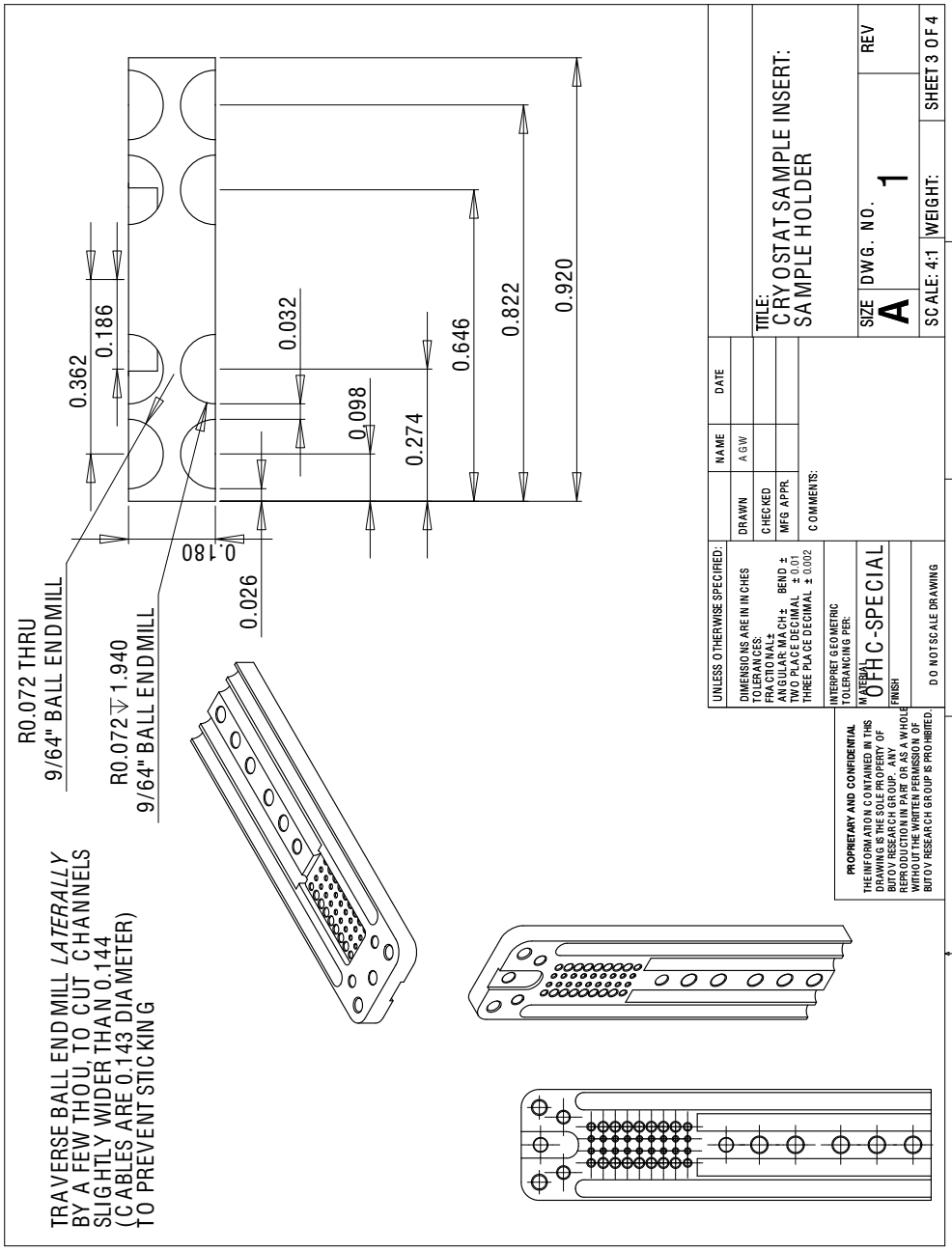

Figure A.22: sample-holder-v6c-Sheet4

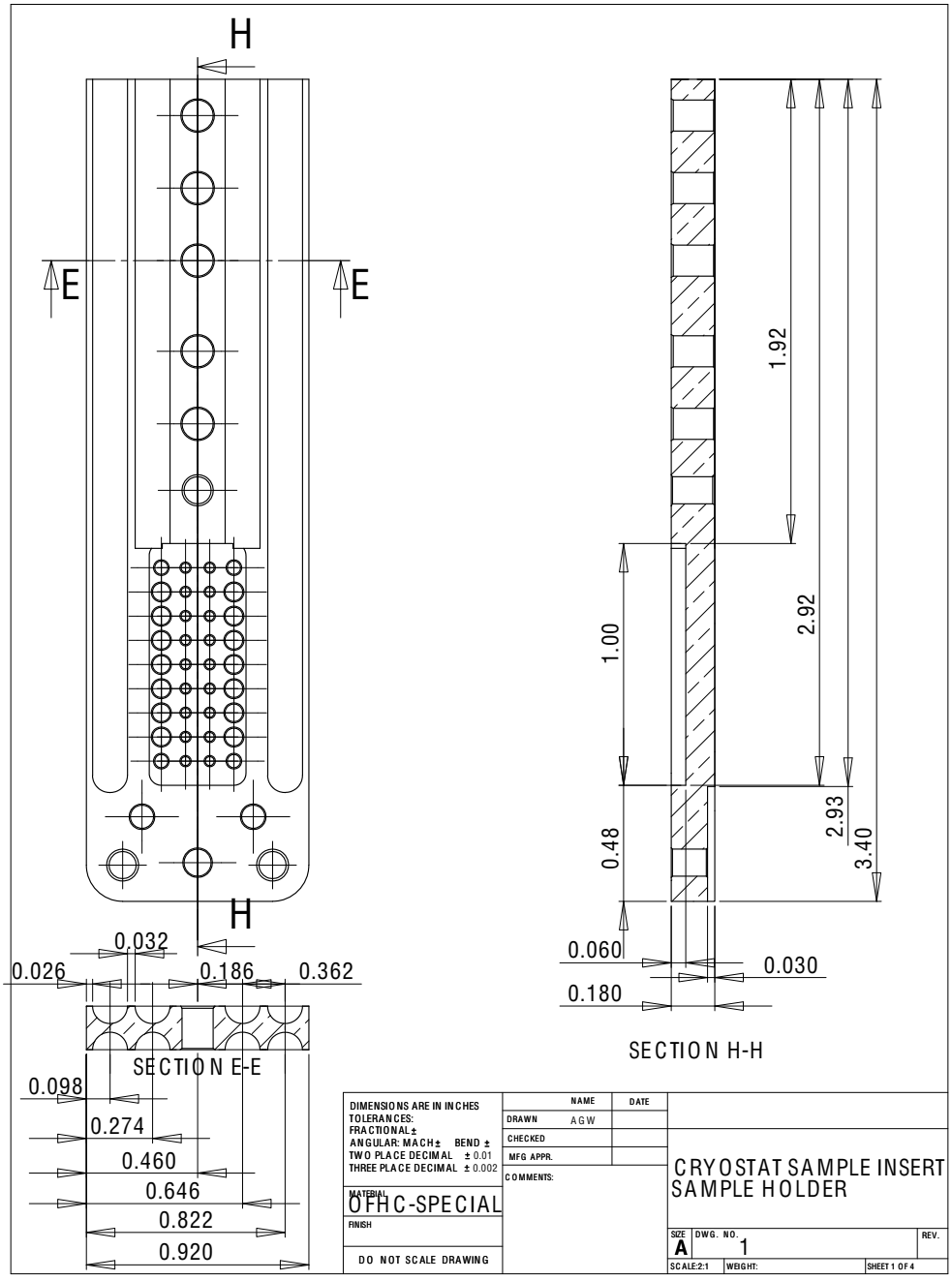

Figure A.23: sample-holder-v6c-Sheet6

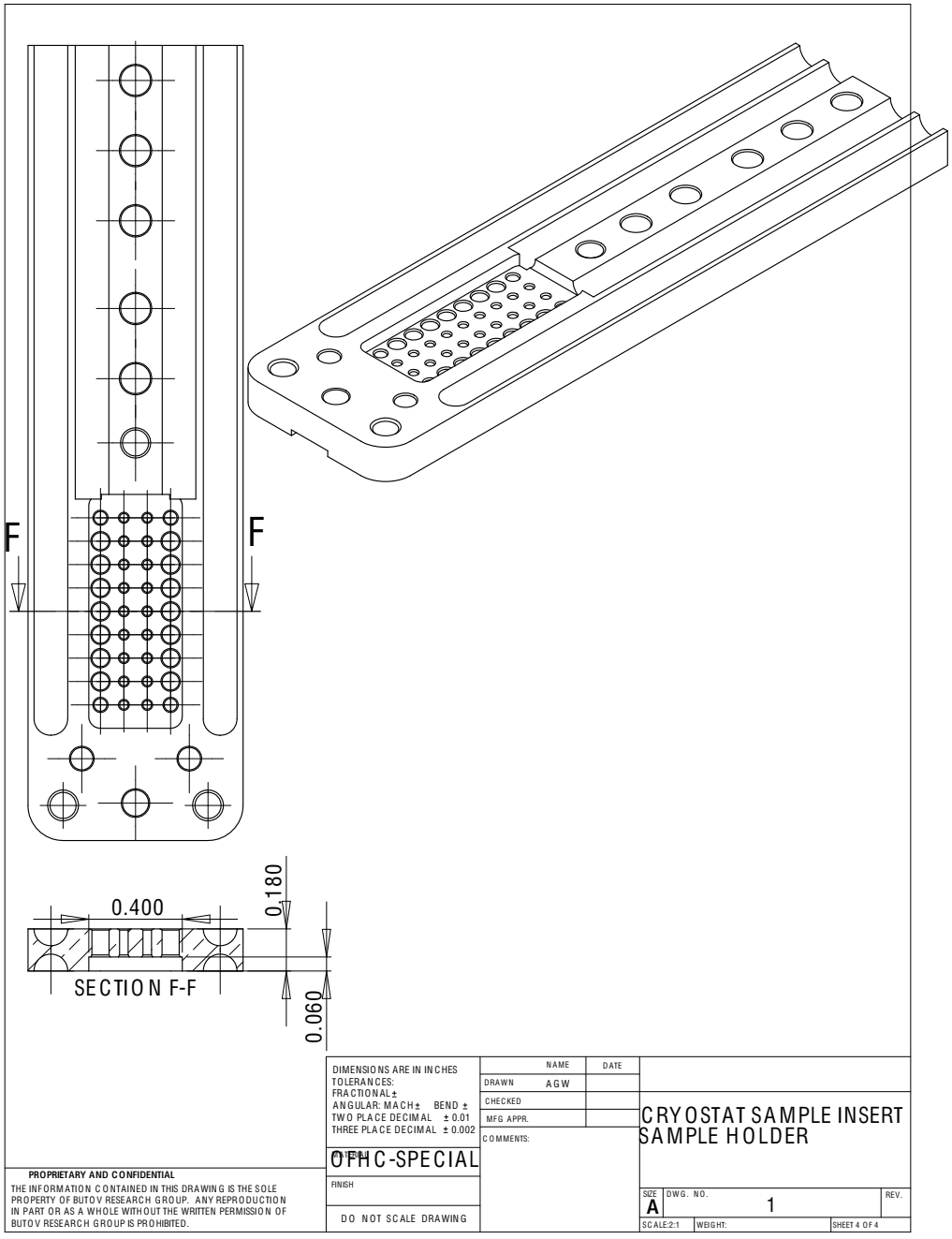

Figure A.24: sample-holder-v6c-Sheet7

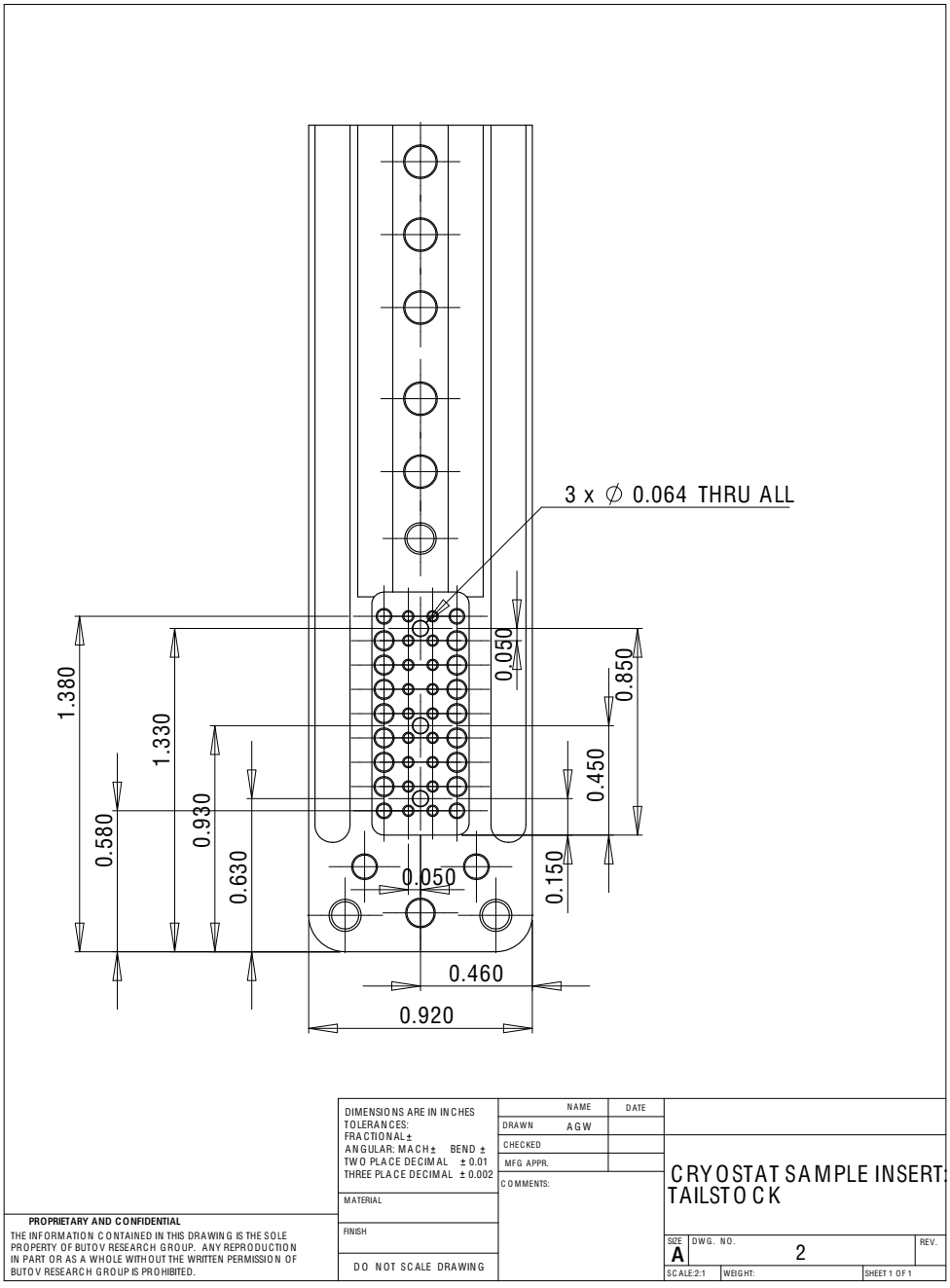

Figure A.25: sample-holder-v7-Sheet1

A.4 Sample holder assembly

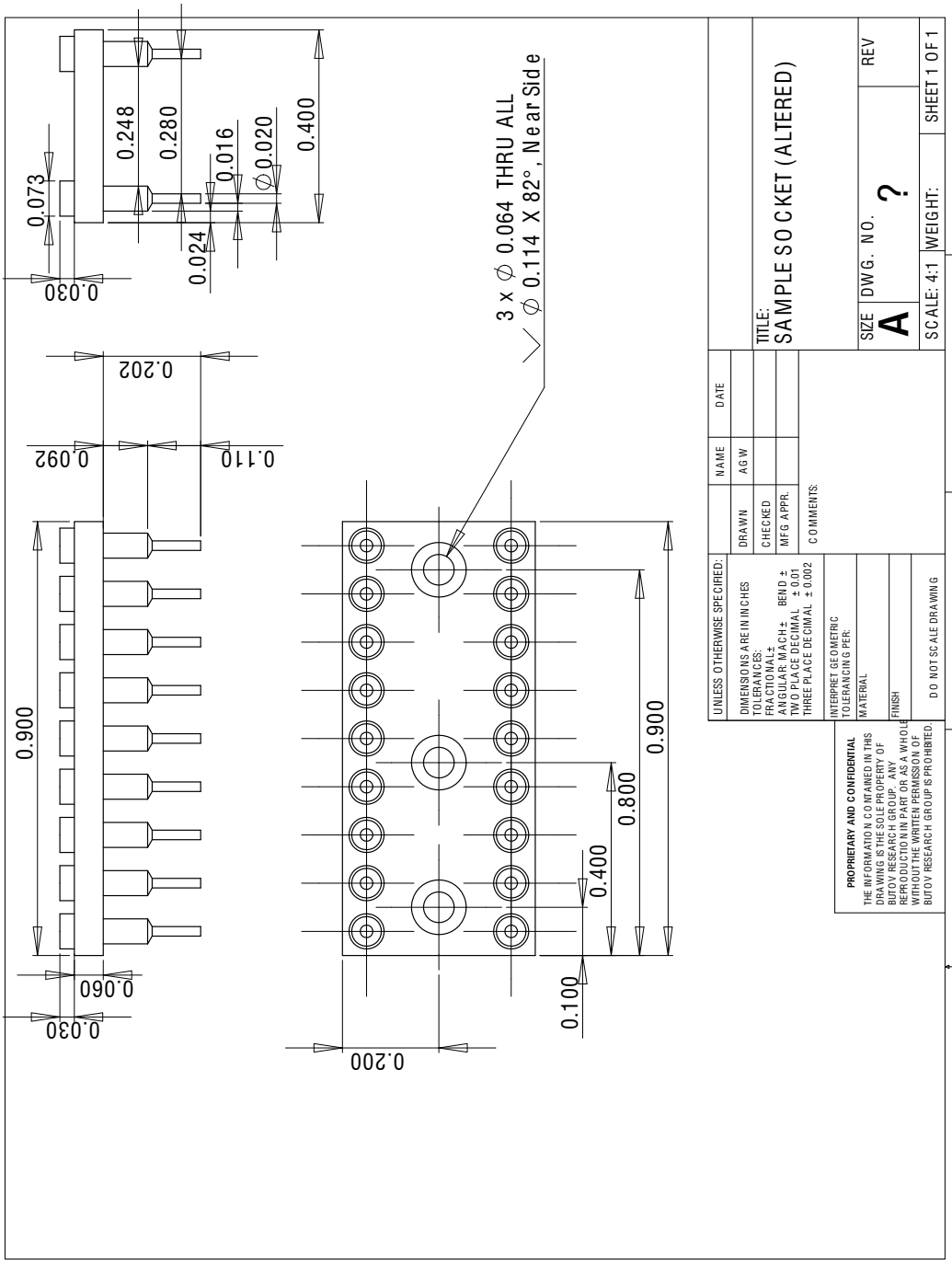

Figure A.26: ATHaltered-SampleSocket-Sheet1

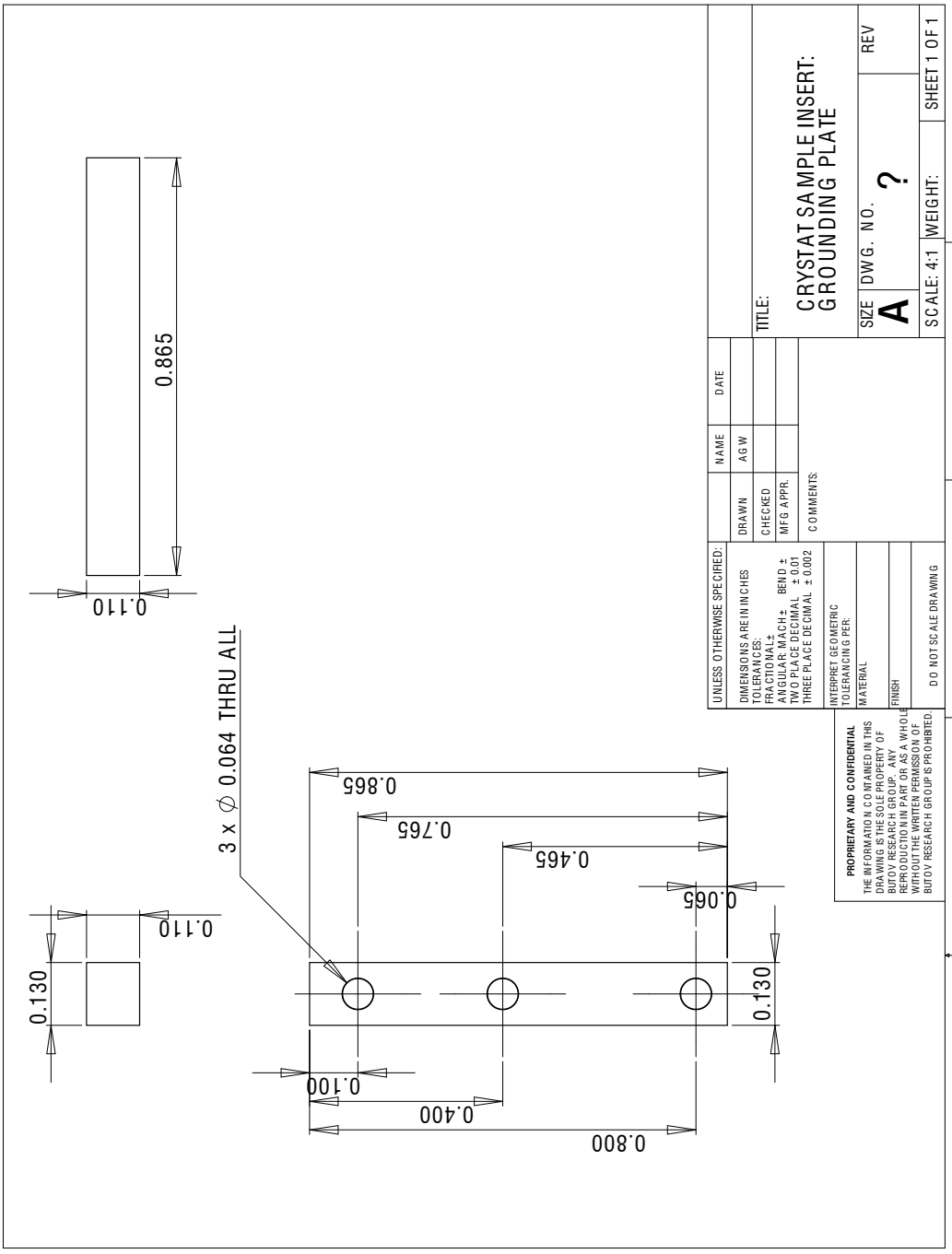

Figure A.27: groundingplate-Sheet1

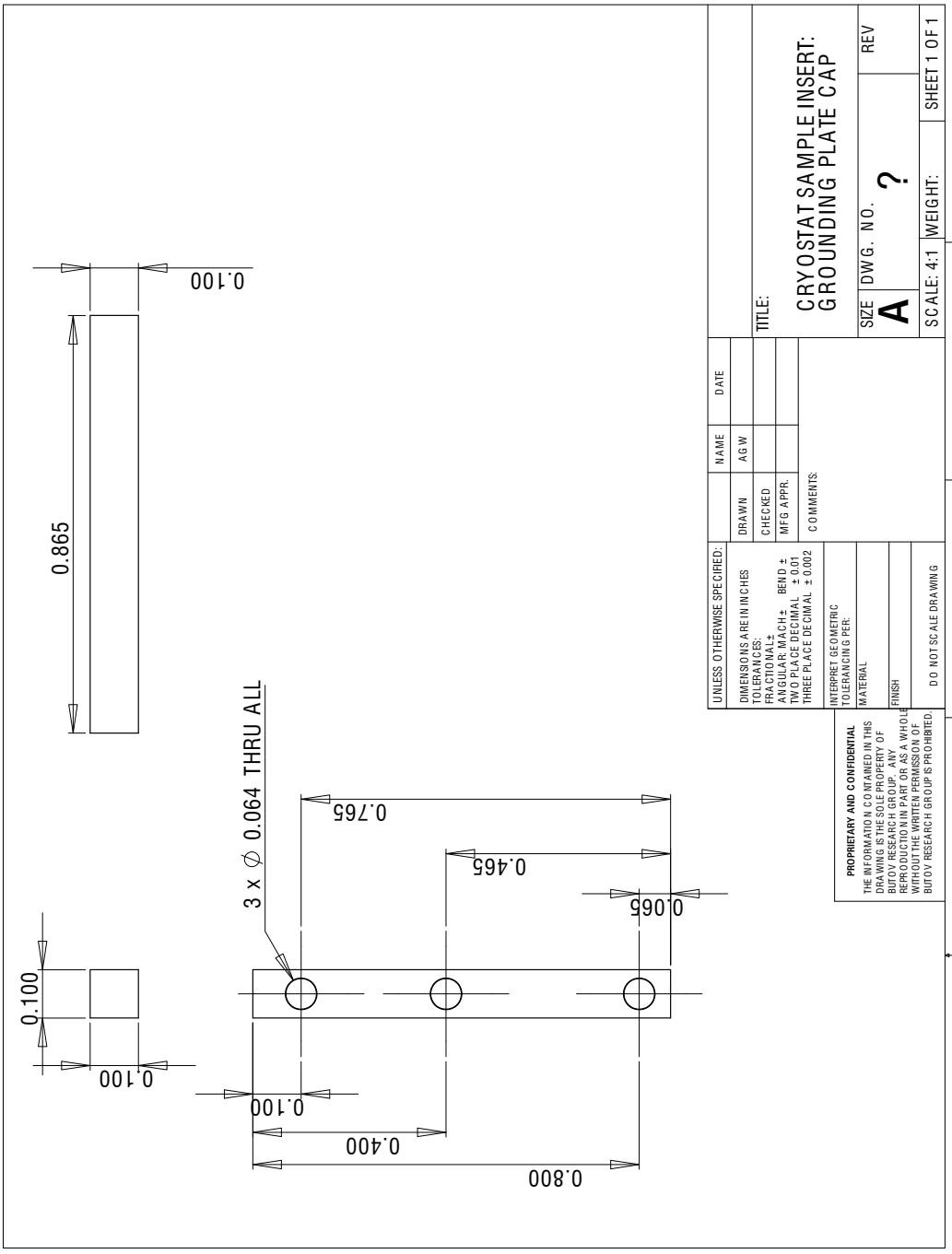

Figure A.28: groundingplatecap-Sheet1

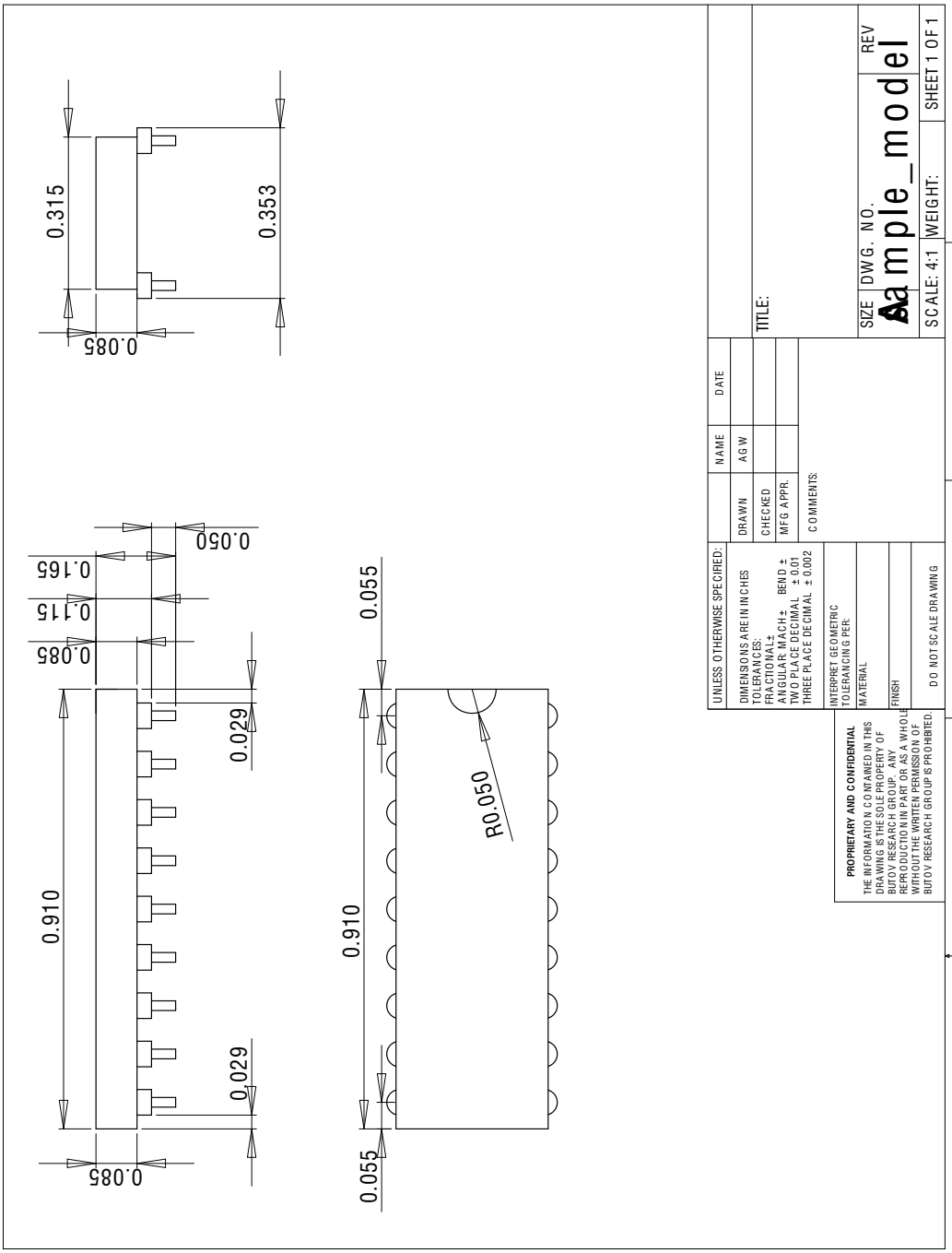

Figure A.29: sample-model-Sheet1

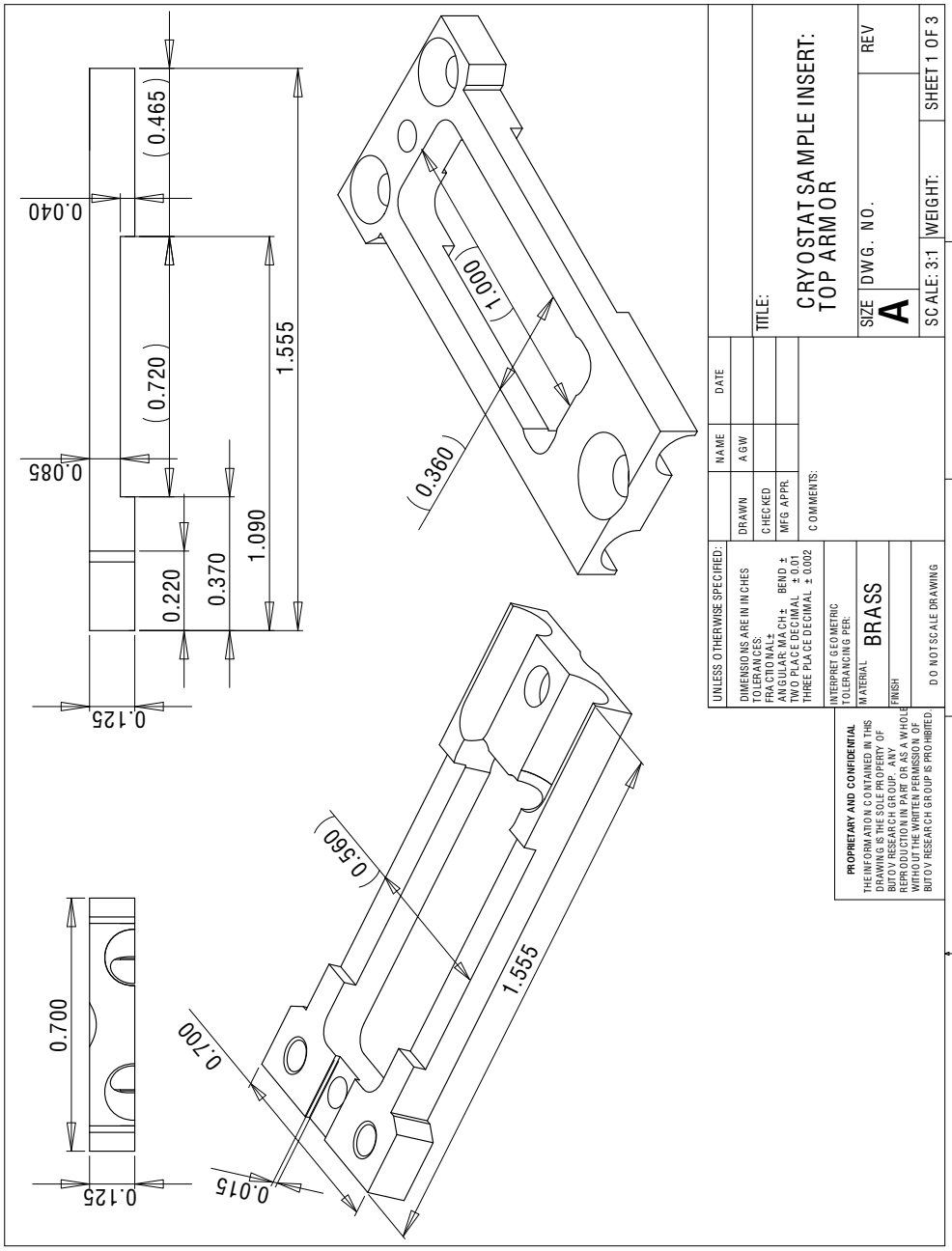

Figure A.30: toparmor-ring-Sheet1

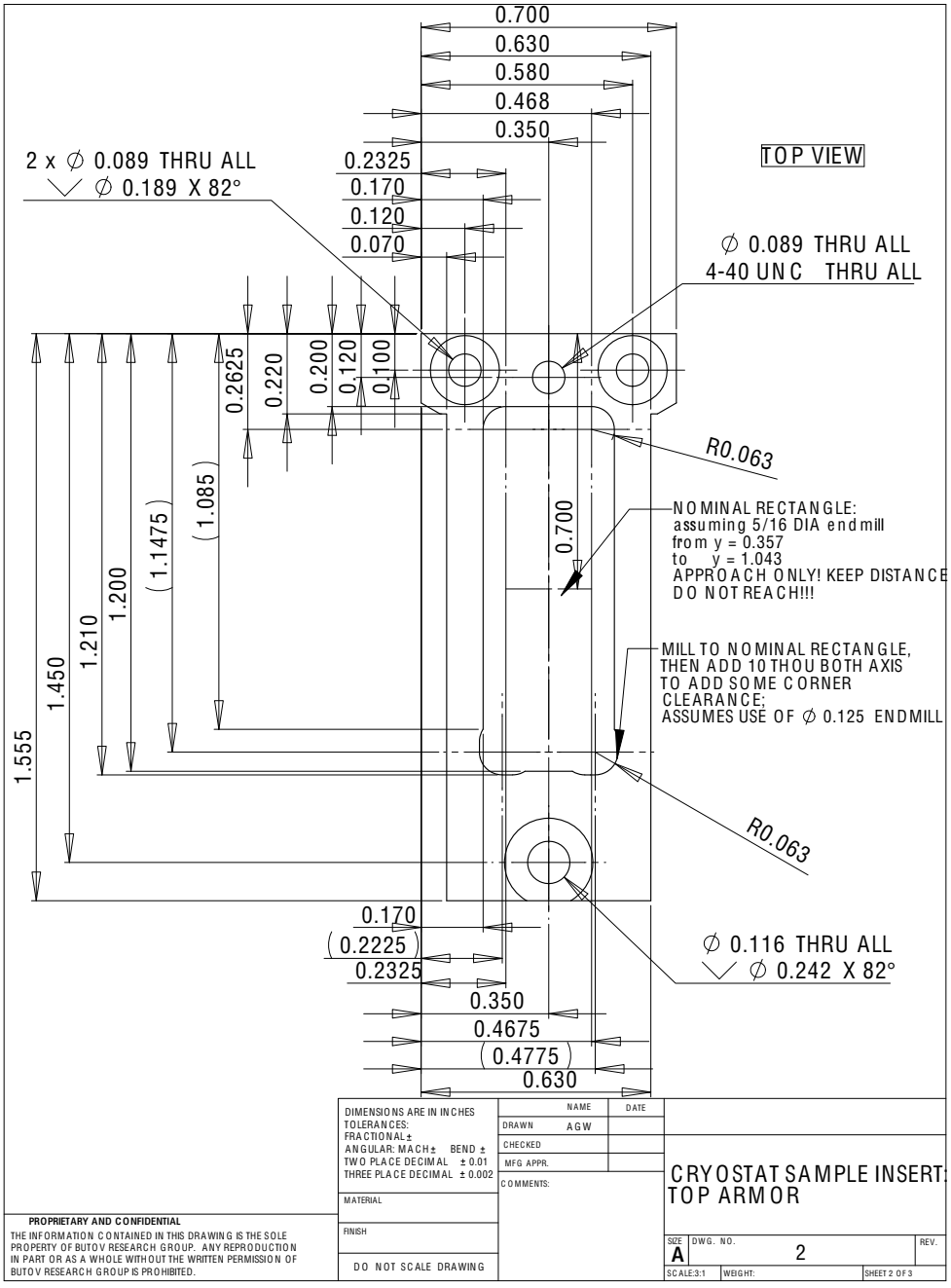

Figure A.31: toparmor-ring-Sheet2

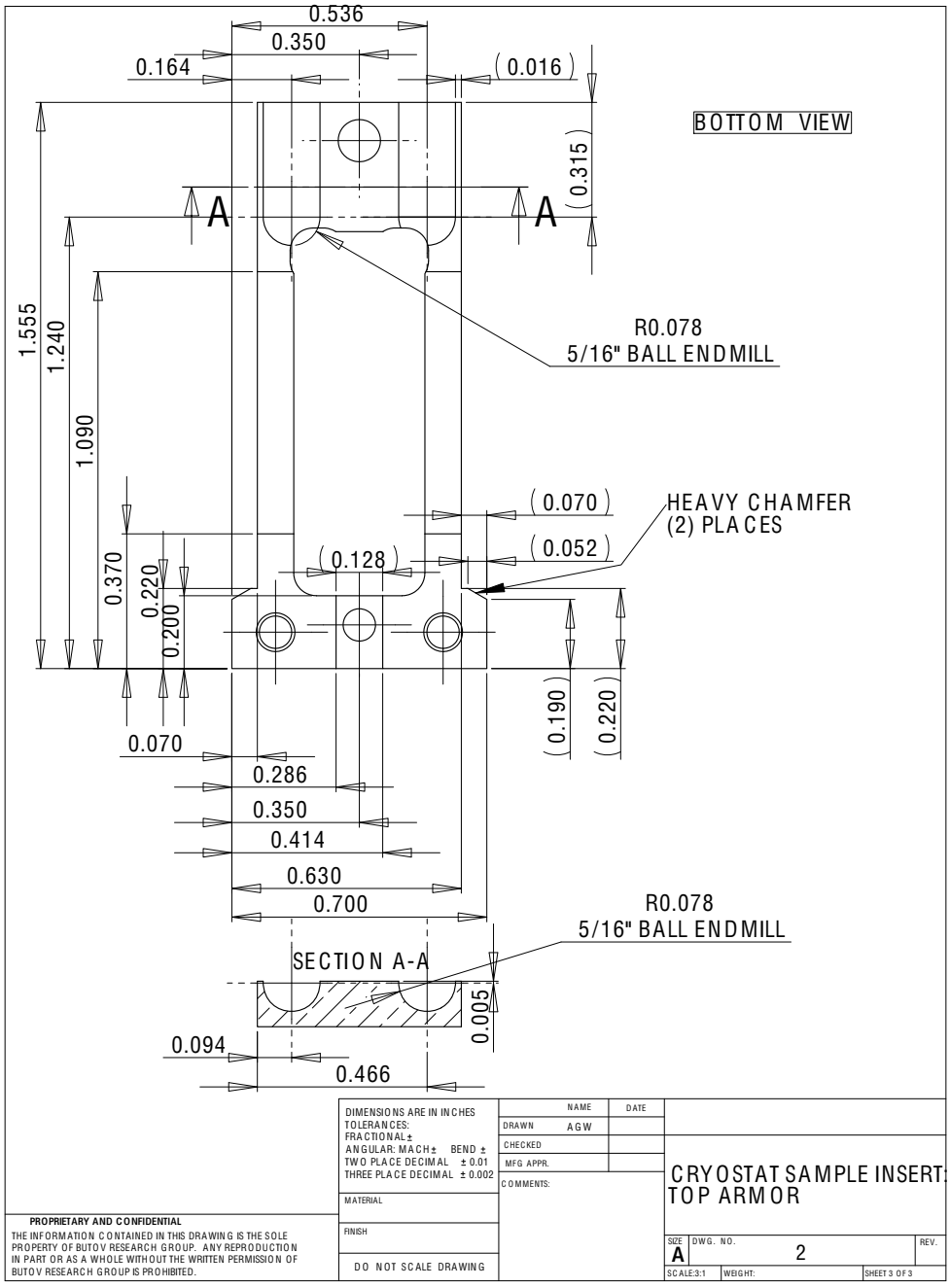

Figure A.32: toparmor-ring-Sheet3

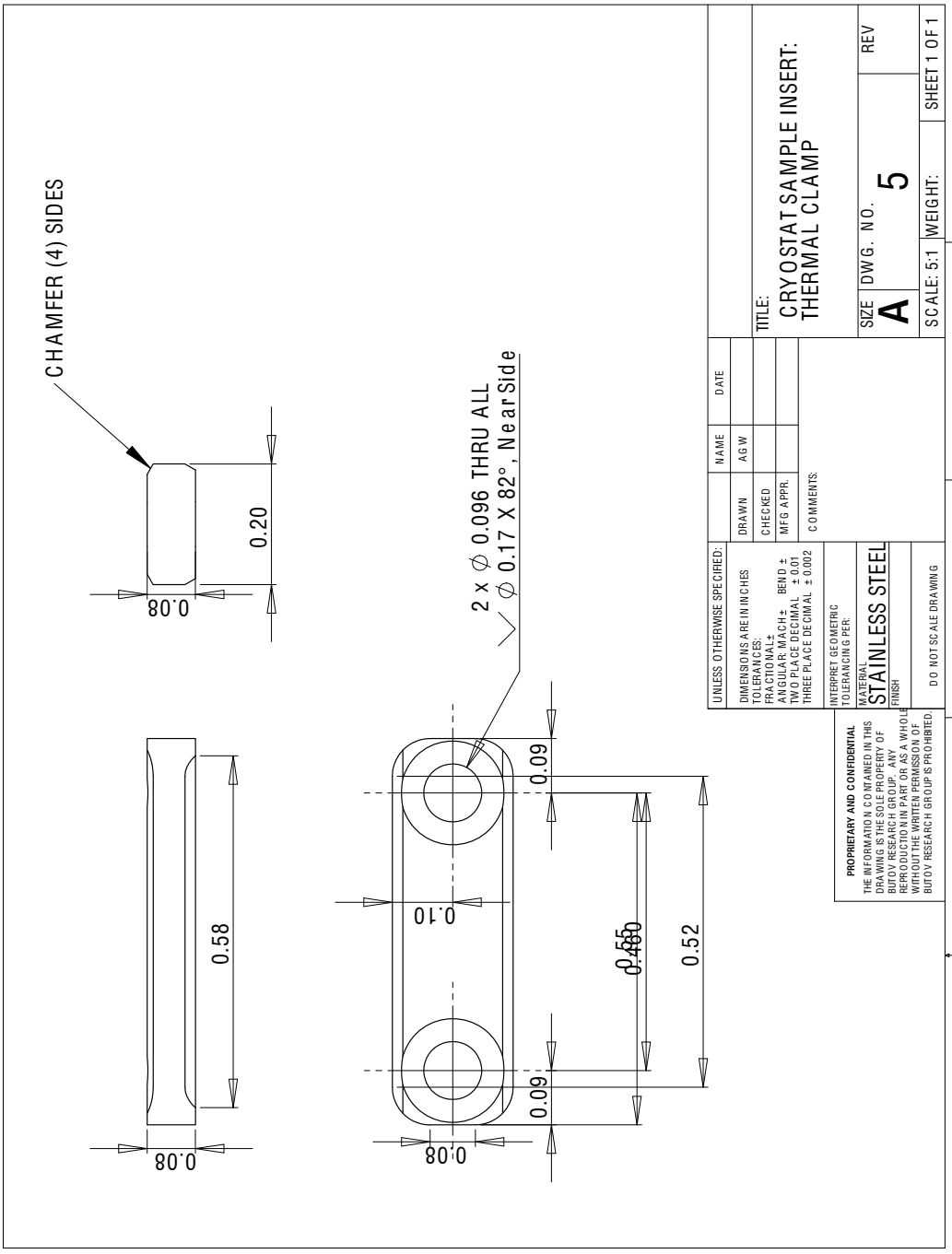

Figure A.33: thermal-clamp-revised-Sheet1

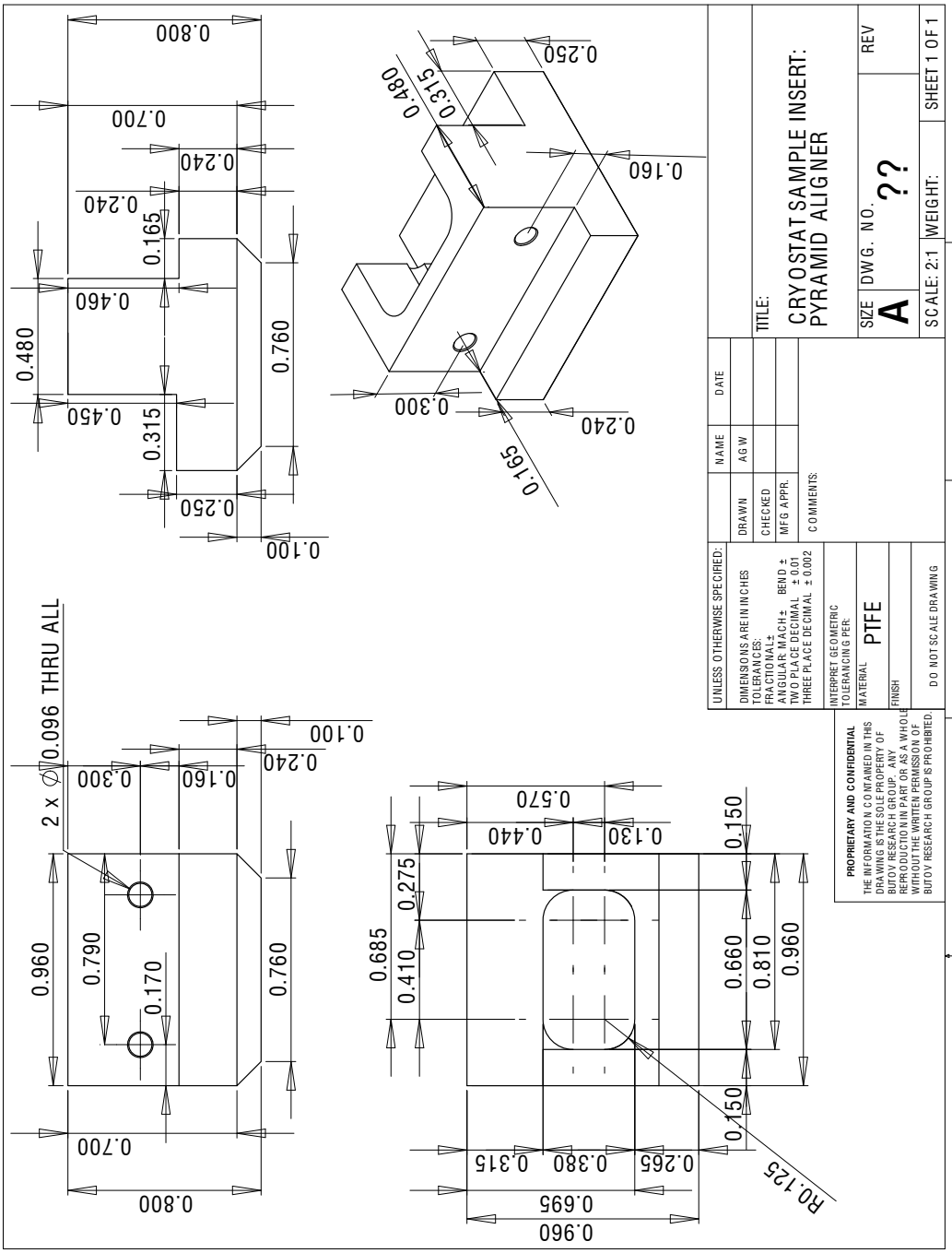

Figure A.34: pryamidaligner-Sheet1

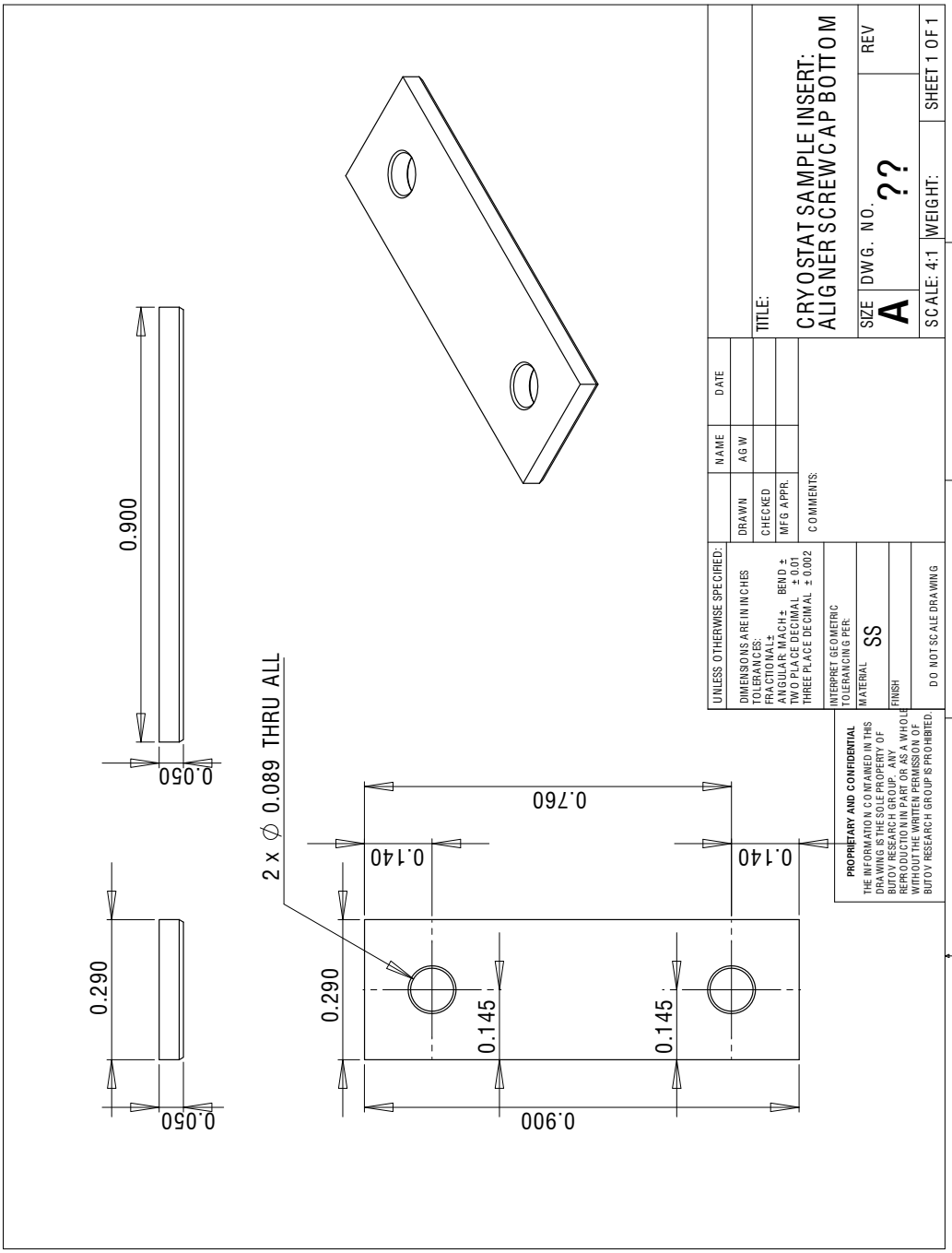

Figure A.35: alignerscrewcapbottom-Sheet1

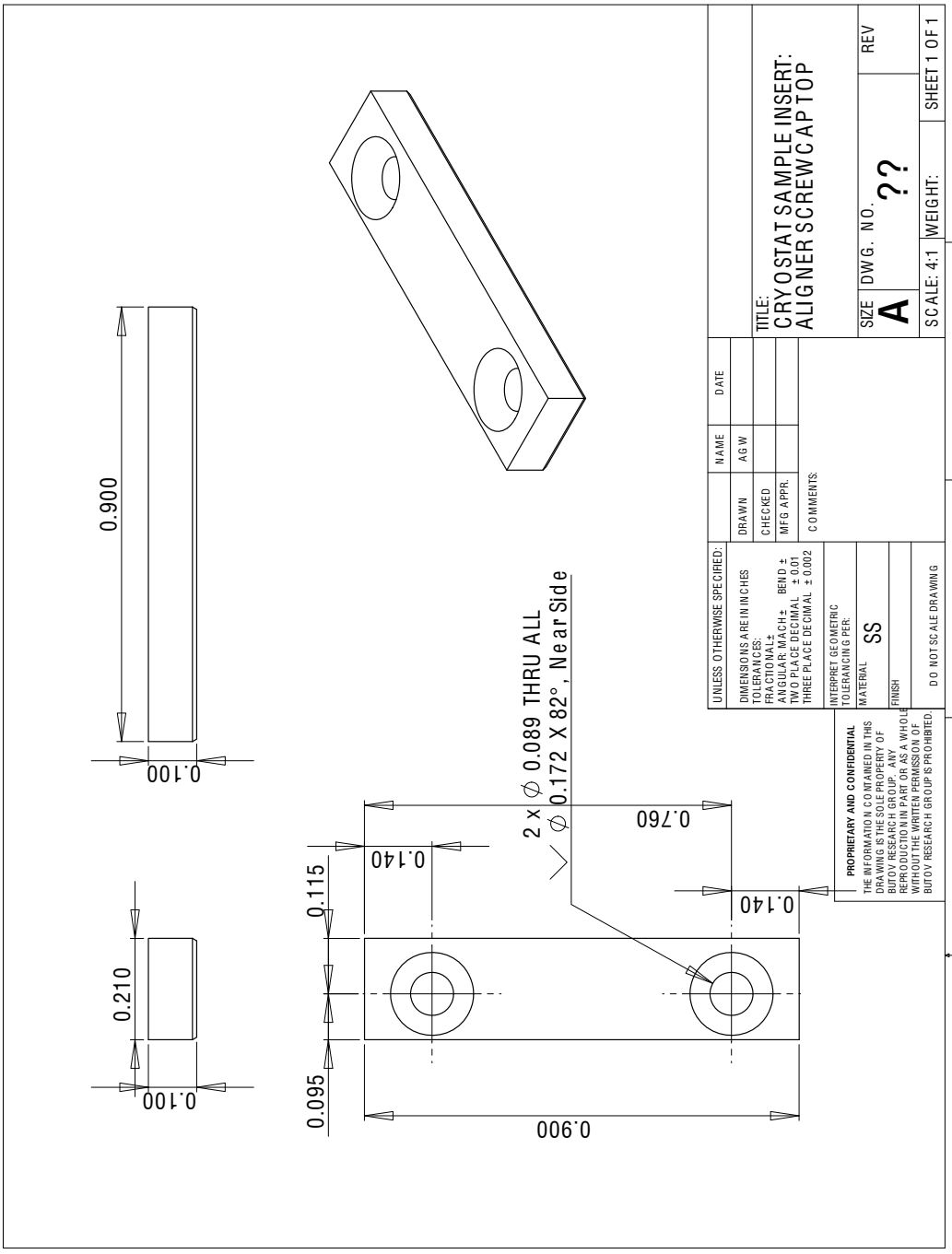

Figure A.36: alignerscrewcaptop-Sheet1

A.5 Printed circuit board

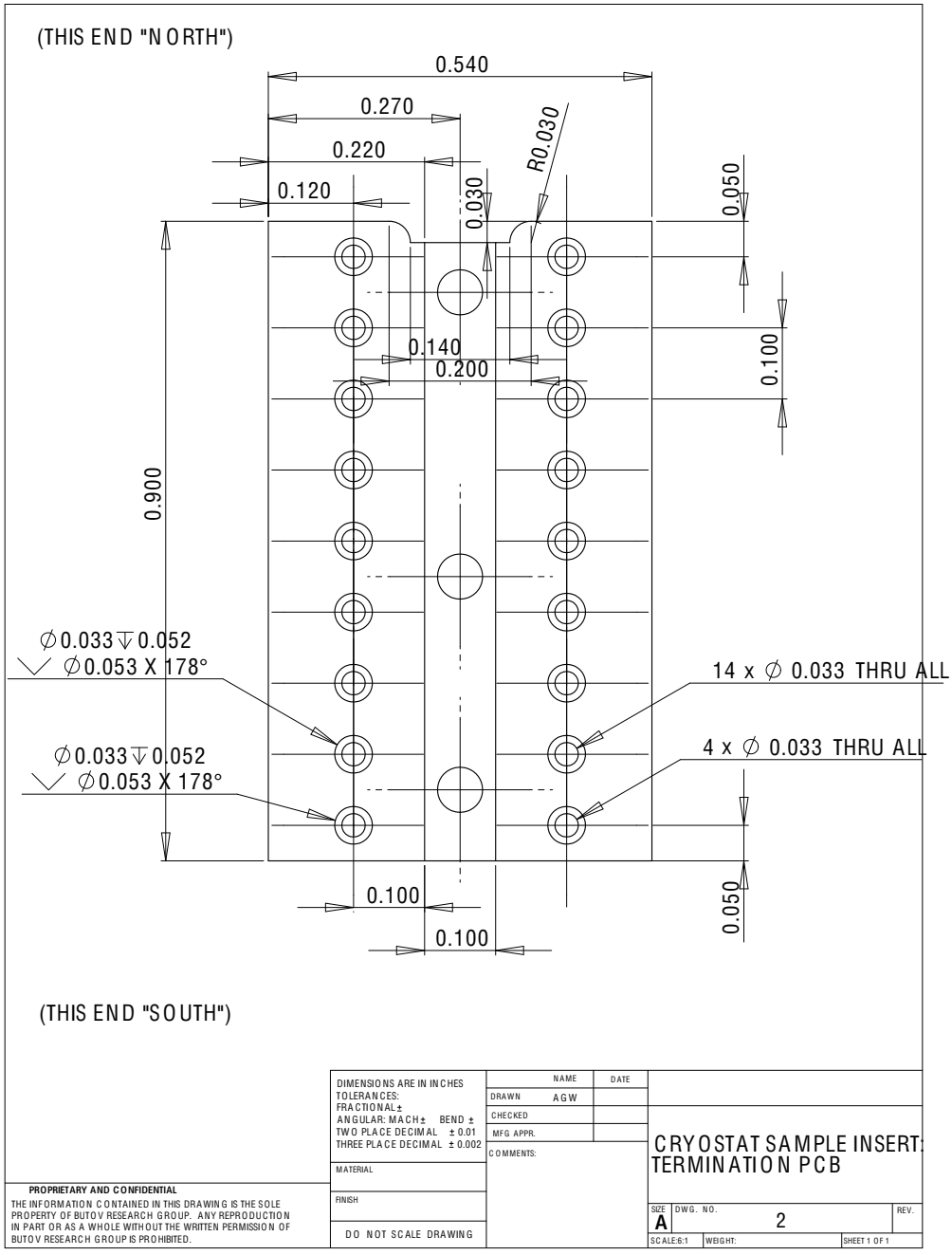

Figure A.37: pcb-Sheet1

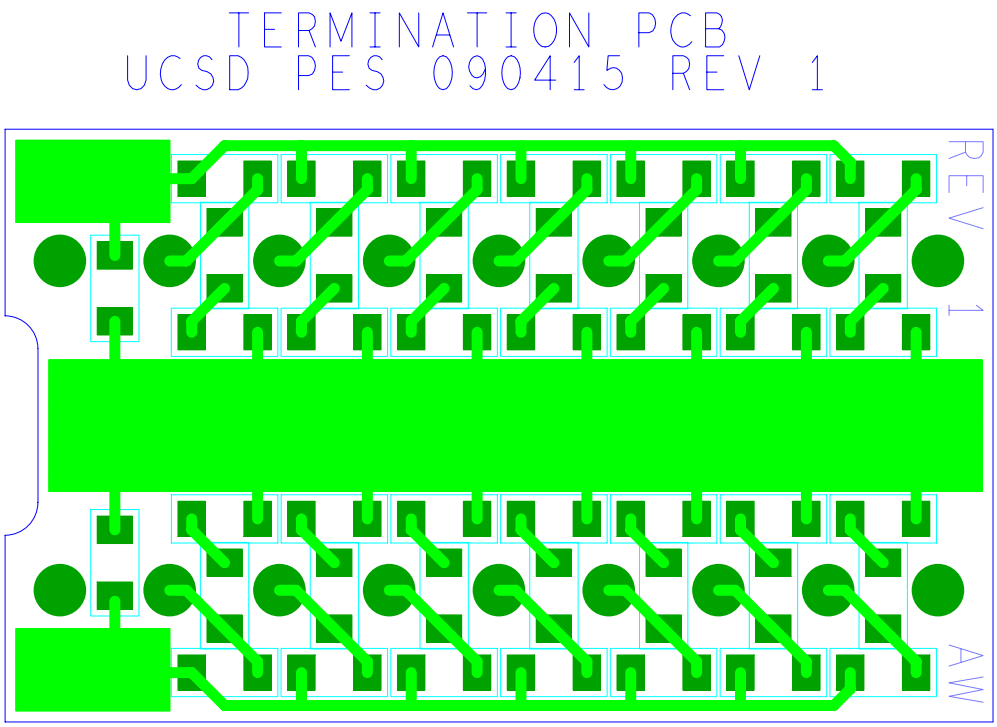

Figure A.38: PCB trace and SMT pad layout

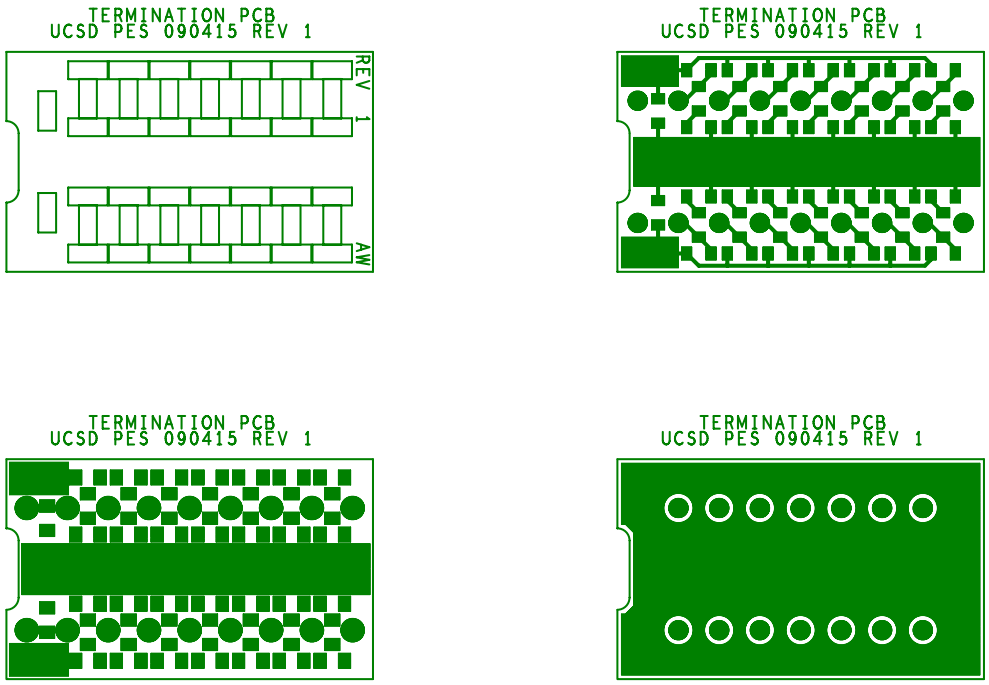

Figure A.39: PCB layers drawing

1. ALL LAYERS ARE VIEWED FROM TOP SIDE
2. HOLE DIAMETER IS AFTER PLATING
3. TYPE FR4 MATERIAL WITH 1 Oz. COPPER LAYERS
4. FINISHED BOARD THICKNESS 0.062 INCH
5. SILK SCREEN TOP SIDE USING WHITE EPOXY INK
6. FINISH: LEAD FREE SOLDER PLATED
7. SOLDER MASK TOP SIDE WITH LIQUID PHOTO IMAGEABLE MASK COLOR GREEN OVER BARE COPPER

DRILL CHART: TOP to BOTTOM			
ALL UNITS ARE IN MILS			
FIGURE	SIZE	PLATED	QTY
A	28.0	PLATED	18
◇	64.0	PLATED	3

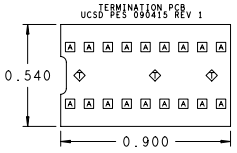

Figure A.40: PCB fabrication (drill and plating) drawing

Appendix B

Tips on cryogenic coax procedures

B.1 Successfully cutting semi-rigid coax

The cables are termed "semi-rigid" because they can be hand-formed into gentle curves. The tough stainless steel outer shield is difficult to cut without applying forces that crush the cable and destroy the desired electrical performance. The cable is best cut with a tubing cutter with appropriate roller diameter and fresh (sharp) circular blade, however clamping the cable with sufficient gripping force without crushing it, and cutting through the outer shell and subsequent Teflon without nicking the center conductor is awkward. The following procedure was found to work:

1. Mount the cable in a horizontal lathe using a 9/64 collet. It was usually necessary to pass the cable through the collet first, then mount the collet in the collet holder since the slight flexibility of the cable causes it to score on the jaws. If the cable end has been previously roughly cut, it will not pass through the collet jaws and may be necessary to gently file the end smooth on a beltsander while rotating it through the fingers. (If both ends of the cable have been previously supplied crushed by pliers, then a catch-22 is in effect, and at least one cable end will have to be roughly cut back by other means, for example clamping in "soft jaws" in a vise and using a tubing cutter or hacksaw and filing the end.) Inspect the collet jaws first for nicks or damage.

The next size larger collet, 5/32 is tempting for its clearance, but will not adequately clamp the 0.141" cable. Set the lathe gearing to a slowest speed, so that the transmission friction inhibits the lathe stock from rotating.

2. The cable should be positioned to protrude from the right side of the collet only far enough to give clearance to the tubing cutter from the collet, about 1", since the semi-flexible end will be unsupported during cutting. If the far end of the cable protrudes from the lathe headstock, support it level with boards or the like so that the droop does not permanently distort the cable.

3. Adjust the collet tension to adequately clamp the cable so that it cannot rotate against considerable finger torque. Steps 2 and 3 may need to be repeated several times to obtain satisfactory results.

4. With the tubing cutter set to slight cutting compression, rotate it about the cable taking light cuts. Progressively tighten the tubing cutter leadscrew and deepen the cut. It is vital to proceed with caution when cutting through the stainless steel into the Teflon, and practice is the best guide. It is possible to remove the tubing cutter and inspect the depth of cut, if subsequently put back into place with care.

5. After just cutting through the steel, continue to deepen the cut by practice and feel alone, through most but not all of the Teflon. If the Teflon is cut through, the center conductor will be damaged.

6. Remove the tubing cutter, and grasp the free piece of shield in large pliers. Rotate the shield back and forth while pulling it directly in-line away from the cable. The free shield may pull away from the almost-free Teflon, and the almost free-Teflon subsequently sheared away, but best results are obtained when the free shield and Teflon are removed simultaneously. Extraneous Teflon can be removed using "Hot Fingers" (in the electronics shop), but they usually do not produce a sufficiently clean edge for later soldering the SMA connector, and it is necessary to make a proper cut at this stage.

7. Inspect the center conductor for damage; if nicked, it should ordinarily not be used and the cable should be cut back again.

8. Cut back the center conductor using sharp pliers. If the end will later be soldered to an SMA connector, it will be necessary to cut the conductor to a specific protrusion length (measured to within 1 thou.) Use a caliper depth gage as needed. Make the cut clean.

> **Exercise caution if it should appear at all necessary to smooth the beryllium-copper center conductor by sanding or abrasion. Do not generate toxic dust. Do not use a belt sander or file.**

   One might try an approach such as using sandpaper soaked in machining oil, discarding the sandpaper as toxic waste.

9. Remove the cable from the lathe, and carefully sand the edge of the shield smooth with very light pressure against a belt sander whilst spinning it between the fingers. Clean the whole cable and cut end of machining oil and metal particulates with alcohol, and cap or guard the ends.

Repeated practice is recommended with a dummy cable before cutting an expensive cable to a particular final length. Note that if the dummy cable has different composition (e.g., the more common copper outer conductor instead of stainless steel), it will not provide a good guide to the critical step of cutting through the shield but not all the way through the Teflon.

B.2 Successfully soldering semi-rigid coax

Soldering UT-141B-SS semi-rigid coax is quite difficult. There are several challenges.

- Soldering to the stainless steel outer conductor requires removal of the oxide layer that protects and characterizes stainless steel

- The copper-based center conductor has tremendous thermal conductivity and wicks soldering iron heat away and upstream.
- The stainless steel outer conductor conducts heat very poorly.
- The center Teflon insulation is thermally vulnerable.

The end result is that solder won't wick to the shield, which stays cold, while soldering the center conductor causes the Teflon to thermally expand and extrude, destroying the careful tip geometry created by meticulously measuring and cutting the center conductor and dielectric.

The oxide layer must be removed by sanding and then meticulous cleaning shortly before soldering. A strong acid-based flux is still necessary for the solder to wick, and afterwards the acid may be removed by application of deionized water, weak NaOH, and buffer solutions.

B.3 Briefest remarks on RF electronics

RF electronics is surprisingly expensive and fraught with complexities for a physicist comfortable with a typical elementary analogue electronics background. There is not space here to provide an introduction to the principles and practices of electronics for operation from 10 MHz into the GHz. The reader is cautioned that the subject is large, rarely taught (even among many students in electrical engineering), and essentially constitutes an entire world of electronics quite different from the better-known worlds of elementary analogue or digital electronics.

Sources of information

An essential and excellent starting guide is Johnson and Graham [1993]. Microwaves101: Microwave Encyclopedia is also useful.

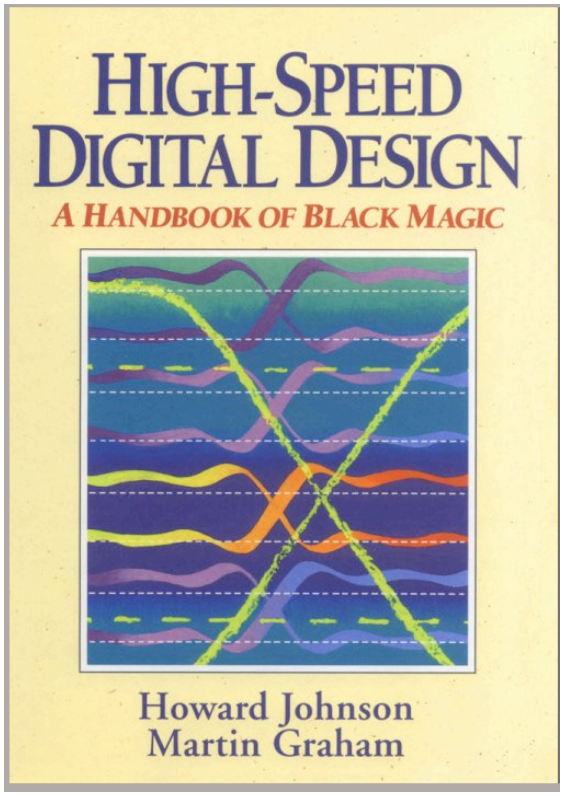

Figure B.1: "Black magic", indeed: a practical introduction to the widely-unfamiliar world beyond DC. [Johnson and Graham, 1993].

Appendix C

Future Steps

C.1 Physics experiments

C.1.1 Time-resolved exciton conveyer

Using the time-gated ICCD.[1] The timing signal ought to be extractable from the signal generator using e.g. (with strong attenuation) the Ortec discriminator as a level-crossing detector, and then triggering a pulse generator (NIM to voltage conversion), or else directly.

C.1.2 Stepped conveyer

Using a ns RF (absorptive) switch. Key issue is intermodulation frequencies; position centered in the passband; restricts on/off cycling. Delay lines suffer temporal propagation; may need 7 switches.

C.1.3 Spin conveyer optics

Use a quartz Wollanston prism & WPs; total beam symmetry and simultaneous readout separated on CCD surface. Must account for all polarization-sensitive dispersions in all optical elements. Obtains near real-time spin detection.

[1] Although it might not have the required time resolution for higher frequencies (e.g a $\tau/10$ window, probably yielding poor peak resolution, requires for v_9 a 230 ps integration window.)

C.1.4 Conveyer at higher velocities

C.1.5 Conveyer momentum-induced lifetime extension

C.1.6 Picosecond evolution of the indirect exciton emission

Need 100's ns high-quality delay; use LMR-240UF or separate delay gen; adapt NIM current/voltage signal.

C.1.7 GHz switching of the excitonic transistor

C.2 Improved cryogenic RF electronics

C.2.1 Device packaging

Switch to PLCC or LCC package; adapt new sample holder plate and use large PCB with proper trace geometry.

C.2.2 Characterization of device capacitance

Section 10.4 discusses how the sample capacitance is a principal limitation on the frequency response of the semiconductor heterostructure device; however, accurate direct measurement of this capacitance is difficult. In principle, direct measurements might be possible at room temperature in an RF probing station using lock-in techniques and extremely faint excitation voltages (e.g., nanoamperes, to avoid damage to the sample), or in liquid helium using a plain sample holder with transmission lines to make high-frequency measurements but without reactive elements. Even measurements with the factory Janis sample holder $\sim$1 MHz (for example, using a vector network analyzer in CW mode or an RF vector voltmeter and signal generator to construct a capacitance meter) might yield useful measurements.

C.2.3 Octopus-derived sample holder

C.2.4 RF electronics in dilution refrigerator

C.3 Octopus and sample minor modifications

C.3.1 Measurements vs. temperature

C.3.2 Octopus with pulsed RF

Swap caps for bridges, unless pulse edge slow enough.

C.4 Improved optics

C.4.1 Laser diode pulsing

C.4.2 Imaging optics throughput

Use properly-cut bandpass filter to avoid massive absorption caused by detuning; doubles/triples light throughput.

C.4.3 Exploiting polarization for filtering

Huge s/n gain. Polarizers much more efficient than steep filter edges.

C.4.4 Optical collimation

Use correct beam geometry, telescope, correct trunc. ratio for objective NA.

C.4.5 Diffuse illumination

Clear images of the sample surface under (pseudo) diffuse photoexcitation (employed in Section 10.4) can also be obtained by inserting a weak $f \sim 500\,\mathrm{mm}$) converging lens approximately 2–f upstream of the objective. Because the over-converged laser beam enters the front focal plane of the objective *diverging*, it exits the objective and illuminates the sample surface approximately collimated.

Appendix D

Conveyer RF system phase delay calibration

Table D.1: Phase deltas, page 1

Alex Winbow, Oct 2009 — Expected Phase Delays for Delay Lines — 1 of 6

			A	B	C	D	E	F	G
V_signal [cm/ns]	25.18								
Base frequency [MHz]	50	Length [in]	12	40.3125	68.625	96.9375	125.25	153.5625	181.875
		Length [in]	12	40 5/16	68 5/8	96 15/16	125 1/4	153 9/16	181 7/8
		Length [cm]	30.48	102.39375	174.3075	246.22125	318.135	390.04875	461.9625
EMPHASIZE		Delta length [cm]	0	71.91375	143.8275	215.74125	287.655	359.56875	431.4825
ALL		Delta time [ns]	0	2.85570019	5.71140038	8.567100571	11.42280076	14.27850095	17.13420114
VALUES		Shifting rate [deg/MHz]	0	1.028052068	2.056104137	3.084156205	4.112208274	5.140260342	6.168312411
THEORETICAL		Relative shifting rate []		1	2	3	4	5	6
BECAUSE									
DERIVED		**Zero #**	**Frequency of zero phase shifts relative to line 'A' [MHz]**						
FROM		1		350	175	117	88	70	58
CABLE		2		700	350	233	175	140	117
LENGTHS		3			525	350	263	210	175
AS		4			700	467	350	280	233
ORDERED		5			875	584	438	350	292
AND		6				700	525	420	350
THEORETICAL		7				817	613	490	409
VELOCITY									

Table D.2: Phase deltas, page 2

ALL VALUES THEORETICAL BECAUSE DERIVED FROM CABLE LENGTHS AS-ORDERED AND THEORETICAL VELOCITY

Frequency [MHz]	Mode [#]	Wavelength [cm]	A	B	C	D	E	F	G
			Phase shifts relative to line 'A' [degrees, 0 ⟷ 360]						
40.0	0.8	629.6	0	41	82	123	164	206	247
50.0	1.0	503.7	0	51	103	154	206	257	308
60.0	1.2	419.7	0	62	123	185	247	308	10
70.0	1.4	359.8	0	72	144	216	288	360	72
80.0	1.6	314.8	0	82	164	247	329	51	133
90.0	1.8	279.8	0	93	185	278	10	103	195
100.0	2.0	251.8	0	103	206	308	51	154	257
110.0	2.2	228.9	0	113	226	339	92	205	319
120.0	2.4	209.9	0	123	247	10	133	257	20
130.0	2.6	193.7	0	134	267	41	175	308	82
140.0	2.8	179.9	0	144	288	72	216	360	144
150.0	3.0	167.9	0	154	308	103	257	51	205
160.0	3.2	157.4	0	164	329	133	298	102	267
170.0	3.4	148.1	0	175	350	164	339	154	329
180.0	3.6	139.9	0	185	10	195	20	205	30
190.0	3.8	132.5	0	195	31	226	61	257	92
200.0	4.0	125.9	0	206	51	257	102	308	154
210.0	4.2	119.9	0	216	72	288	144	359	215
220.0	4.4	114.5	0	226	92	319	185	51	277
230.0	4.6	109.5	0	236	113	349	226	102	339
240.0	4.8	104.9	0	247	133	20	267	154	40
250.0	5.0	100.7	0	257	154	51	308	205	102
260.0	5.2	96.9	0	267	175	82	349	256	164
270.0	5.4	93.3	0	278	195	113	30	308	225
280.0	5.6	89.9	0	288	216	144	71	359	287
290.0	5.8	86.8	0	298	236	174	113	51	349
300.0	6.0	83.9	0	308	257	205	154	102	50
310.0	6.2	81.2	0	319	277	236	195	153	112
320.0	6.4	78.7	0	329	298	267	236	205	174
330.0	6.6	76.3	0	339	319	298	277	256	236
340.0	6.8	74.1	0	350	339	329	318	308	297
350.0	7.0	72.0	0	360	360	359	359	359	359
360.0	7.2	70.0	0	10	20	30	40	50	61
370.0	7.4	68.1	0	20	41	61	82	102	122
380.0	7.6	66.3	0	31	61	92	123	153	184
390.0	7.8	64.6	0	41	82	123	164	205	246
400.0	8.0	63.0	0	51	102	154	205	256	307
410.0	8.2	61.4	0	62	123	185	246	308	9
420.0	8.4	60.0	0	72	144	215	287	359	71
430.0	8.6	58.6	0	82	164	246	328	50	132
440.0	8.8	57.2	0	92	185	277	9	102	194
450.0	9.0	56.0	0	103	205	308	50	153	256
460.0	9.2	54.7	0	113	226	339	92	205	317
470.0	9.4	53.6	0	123	246	10	133	256	19
480.0	9.6	52.5	0	133	267	40	174	307	81
490.0	9.8	51.4	0	144	287	71	215	359	142
500.0	10.0	50.4	0	154	308	102	256	50	204
510.0	10.2	49.4	0	164	329	133	297	102	266
(n.b. manual fixup!)	***Phase shifting rate [degrees/MHz]***		***0***	***1.028052068***	***2.056104137***	***3.084156205***	***4.112208274***	***5.140260342***	***6.168312411***

Table D.3: Phase cal deltas, page 3

ALL VALUES THEORETICAL BECAUSE DERIVED FROM CABLE LENGTHS AS-ORDERED AND THEORETICAL VELOCITY

Frequency [MHz]	Mode [#]	Wavelength [cm]	A	B	C	D	E	F	G
			Phase shifts relative to line 'A' [degrees, -180 ←→ +180]						
40.0	0.8	629.6	0	-41	-82	-123	-164	154	113
50.0	**1.0**	**503.7**	**0**	**-51**	**-103**	**-154**	**154**	**103**	**52**
60.0	1.2	419.7	0	-62	-123	175	113	52	-10
70.0	1.4	359.8	0	-72	-144	144	72	0	-72
80.0	1.6	314.8	0	-82	-164	113	31	-51	-133
90.0	1.8	279.8	0	-93	175	82	-10	-103	165
100.0	**2.0**	**251.8**	**0**	**-103**	**154**	**52**	**-51**	**-154**	**103**
110.0	2.2	228.9	0	-113	134	21	-92	155	41
120.0	2.4	209.9	0	-123	113	-10	-133	103	-20
130.0	2.6	193.7	0	-134	93	-41	-175	52	-82
140.0	2.8	179.9	0	-144	72	-72	144	0	-144
150.0	**3.0**	**167.9**	**0**	**-154**	**52**	**-103**	**103**	**-51**	**155**
160.0	3.2	157.4	0	-164	31	-133	62	-102	93
170.0	3.4	148.1	0	-175	10	-164	21	-154	31
180.0	3.6	139.9	0	175	-10	165	-20	155	-30
190.0	3.8	132.5	0	165	-31	134	-61	103	-92
200.0	**4.0**	**125.9**	**0**	**154**	**-51**	**103**	**-102**	**52**	**-154**
210.0	4.2	119.9	0	144	-72	72	-144	1	145
220.0	4.4	114.5	0	134	-92	41	175	-51	83
230.0	4.6	109.5	0	124	-113	11	134	-102	21
240.0	4.8	104.9	0	113	-133	-20	93	-154	-40
250.0	**5.0**	**100.7**	**0**	**103**	**-154**	**-51**	**52**	**155**	**-102**
260.0	5.2	96.9	0	93	-175	-82	11	104	-164
270.0	5.4	93.3	0	82	165	-113	-30	52	135
280.0	5.6	89.9	0	72	144	-144	-71	1	73
290.0	5.8	86.8	0	62	124	-174	-113	-51	11
300.0	**6.0**	**83.9**	**0**	**52**	**103**	**155**	**-154**	**-102**	**-50**
310.0	6.2	81.2	0	41	83	124	165	-153	-112
320.0	6.4	78.7	0	31	62	93	124	155	-174
330.0	6.6	76.3	0	21	41	62	83	104	124
340.0	6.8	74.1	0	10	21	31	42	52	63
350.0	**7.0**	**72.0**	**0**	**0**	**0**	**1**	**1**	**1**	**1**
360.0	7.2	70.0	0	-10	-20	-30	-40	-50	-61
370.0	7.4	68.1	0	-20	-41	-61	-82	-102	-122
380.0	7.6	66.3	0	-31	-61	-92	-123	-153	176
390.0	7.8	64.6	0	-41	-82	-123	-164	155	114
400.0	**8.0**	**63.0**	**0**	**-51**	**-102**	**-154**	**155**	**104**	**53**
410.0	8.2	61.4	0	-62	-123	175	114	52	-9
420.0	8.4	60.0	0	-72	-144	145	73	1	-71
430.0	8.6	58.6	0	-82	-164	114	32	-50	-132
440.0	8.8	57.2	0	-92	175	83	-9	-102	166
450.0	**9.0**	**56.0**	**0**	**-103**	**155**	**52**	**-50**	**-153**	**104**
460.0	9.2	54.7	0	-113	134	21	-92	155	43
470.0	9.4	53.6	0	-123	114	-10	-133	104	-19
480.0	9.6	52.5	0	-133	93	-40	-174	53	-81
490.0	9.8	51.4	0	-144	73	-71	145	1	-142
500.0	**10.0**	**50.4**	**0**	**-154**	**52**	**-102**	**104**	**-50**	**156**
510.0	10.2	49.4	0	-164	31	-133	63	-102	94
(n.b. manual fixup!)	***Phase shifting rate [degrees/MHz]***		***0***	***-1.02805207***	***-2.05610414***	***-3.08415621***	***-4.11220827***	***-5.14026034***	***-6.16831241***

Table D.4: Phase cal deltas, page 4

Alex Winbow, Oct 2009 — Expected Phase Delays for Delay Lines — 4 of 6

	THEORETICAL VALUES	A-I	A-II	B	C	D	E	F	G-I	G-II
	Length [in]	*12*	*12*	*40.3125*	*68.625*	*96.9375*	*125.25*	*153.5625*	*181.875*	*181.875*
	Length [in]	*12*	*12*	*40 5/16*	*68 5/8*	*96 15/16*	*125 1/4*	*153 9/16*	*181 7/8*	*181 7/8*
	Length [cm]	*30.48*	*30.48*	*102.39375*	*174.3075*	*246.22125*	*318.135*	*390.04875*	*461.9625*	*461.9625*
	Delta length [cm]	*0*	*0*	*71.91375*	*143.8275*	*215.74125*	*287.655*	*359.56875*	*431.4825*	*431.4825*
	Delta time [ns]	*0*	*0*	*2.85570019*	*5.71140038*	*8.567100571*	*11.42280076*	*14.27850095*	*17.13420114*	*17.13420114*
	Shifting rate [deg/MHz]	*0*	*0*	*1.028052068*	*2.056104137*	*3.084156205*	*4.112208274*	*5.140260342*	*6.168312411*	*6.168312411*
	Relative shifting rate []		*0*	*1*	*2*	*3*	*4*	*5*	*6*	*6*

	Zero #	Frequency of zero phase shifts relative to line 'A-I' [MHz]				****** *AS MEASURED* ******			
	1		341.0	171.0	113.0	85.0	68.0	56.5	56.5
NEW CHOSEN	2	Shift @ Freq	681.0	343.0	226.3	170.0	136.0	113.2	113.2
MODE 7 (LOOP)	3	[deg] [MHz]		515.0	340.0	255.0	203.6	169.8	169.8
Frequency	4	<1 @ 400		687.0	453.3	340.0	271.6	226.7	226.6
[MHz]	5	~1.5 @ 500			566.5	425.0	339.7	283.4	283.3
340.02	6	~2.5 @ 1000			680.0	510.0	407.7	***340.02***	340.6
	7	(basically noise)				595.0	475.6	397.0	396.9
	MODE 20							*MODE 20:*	965

	Zero #	Delta frequencies between zeros			****** *AS MEASURED* ******			
	2	340.0	172.0	113.3	85.0	68.0	56.7	56.7
	3		172.0	113.7	85.0	67.6	56.6	56.6
	4		172.0	113.3	85.0	68.0	56.9	56.8
	5			113.2	85.0	68.1	56.7	56.7
	6			113.5	85.0	68.0	56.6	57.3
	7				85.0	67.9	57.0	56.3

NEW CHOSEN BASE Frequency [MHz]	**Averages**	340	172	113.4	85	67.93333333	56.75	56.73333333
	StddevP	0	0	0.178885438	0	0.159861051	0.141303456	0.298142397
48.57	**Shifting rate [deg/MHz]**	1.058823529	2.093023256	3.174603175	4.235294118	5.299313052	6.343612335	6.345475911
	Normalized rate	1	1.976744186	2.998236332	4	5.004906771	5.991189427	5.992949471
	Delta time [ns]	2.941176471	5.813953488	8.818342152	11.76470588	14.72031403	17.62114537	17.62632197
	Equiv. Delta length [cm]	74.06625882	146.4100465	222.0681481	296.2650353	370.6947203	443.7449868	443.8753467
NEW CHOSEN BASE PROPEGATION SPEED [cm/ns]	Normalized equiv. delta length	1	1.976744186	2.998236332	4	5.004906771	5.991189427	5.992949471
	Equiv. Overlength [cm]	2.152508824	2.582546512	6.326898148	8.610035294	11.12597031	12.26248678	12.39284665
	Frac. Equiv. Overlength	2.99%	1.80%	2.93%	2.99%	3.09%	2.84%	2.87%
	Suppose that THEORETICAL lengths are approximately correct; what equivalent value of c would account for observed frequencies?							
24.4866319	Equiv. 'c' [cm/ns]	24.450675	24.73833	24.46505775	24.450675	24.42670375	24.48663188	24.4794405
	% of free-space	81.6%	82.5%	81.6%	81.6%	81.5%	81.7%	81.7%

Table D.5: Phase cal deltas, page 5

FREQUENCIES DERIVED FROM MEASURED PHASE ZEROS → PREDICTED PHASE SHIFTS

Frequency [MHz]	Mode [#]	Wavelength [cm]	A	B	C	D	E	F	G
			Phase shifts relative to line 'A' [degrees, 0 ←→ 360]						
38.9	0.8	630	0	41	82	123	165	206	247
48.6	**1**	**504**	0	51	103	154	206	257	309
58.3	1.2	420	0	62	123	185	247	309	10
68.0	1.4	360	0	72	144	216	288	0	72
77.7	1.6	315	0	82	165	247	329	51	134
87.4	1.8	280	0	93	185	278	10	103	195
97.1	**2**	**252**	0	103	206	309	51	154	257
106.9	2.2	229	0	113	226	339	93	206	319
116.6	2.4	210	0	123	247	10	134	257	21
126.3	2.6	194	0	134	267	41	175	309	82
136.0	2.8	180	0	144	288	72	216	0	144
145.7	**3**	**168**	0	154	309	103	257	51	206
155.4	3.2	158	0	165	329	134	298	103	267
165.2	3.4	148	0	175	350	165	339	154	329
174.9	3.6	140	0	185	10	195	21	206	31
184.6	3.8	133	0	195	31	226	62	257	93
194.3	**4**	**126**	0	206	51	257	103	309	154
204.0	4.2	120	0	216	72	288	144	0	216
213.7	4.4	115	0	226	93	319	185	51	278
223.4	4.6	110	0	237	113	350	226	103	339
233.2	4.8	105	0	247	134	21	267	154	41
242.9	**5**	**101**	0	257	154	51	309	206	103
252.6	5.2	97	0	267	175	82	350	257	165
262.3	5.4	93	0	278	195	113	31	309	226
272.0	5.6	90	0	288	216	144	72	0	288
281.7	5.8	87	0	298	237	175	113	51	350
291.4	**6**	**84**	0	309	257	206	154	103	51
301.2	6.2	81	0	319	278	237	195	154	113
310.9	6.4	79	0	329	298	267	237	206	175
320.6	6.6	76	0	339	319	298	278	257	237
330.3	6.8	74	0	350	339	329	319	309	298
340.0	**7**	**72**	0	0	0	0	0	0	0
349.7	7.2	70	0	10	21	31	41	51	62
359.4	7.4	68	0	21	41	62	82	103	123
369.2	7.6	66	0	31	62	93	123	154	185
378.9	7.8	65	0	41	82	123	165	206	247
388.6	**8**	**63**	0	51	103	154	206	257	309
398.3	8.2	61	0	62	123	185	247	309	10
408.0	8.4	**60**	0	72	144	216	288	0	72
417.7	8.6	59	0	82	165	247	329	51	134
427.5	8.8	**57**	0	93	185	278	10	103	195
437.2	**9**	56	0	103	206	309	51	154	257
446.9	9.2	**55**	0	113	226	339	93	206	319
456.6	9.4	54	0	123	247	10	134	257	21
466.3	9.6	**53**	0	134	267	41	175	309	82
476.0	9.8	51	0	144	288	72	216	0	144
485.7	**10**	**50**	0	154	309	103	257	51	206
495.5	10.2	49	0	165	329	134	298	103	267
Phase shifting rate [degrees/MHz]			***0***	***1.028571429***	***2.057142857***	***3.085714286***	***4.114285714***	***5.142857143***	***6.171428571***

Table D.6: Phase cal deltas, page 6

FREQUENCIES DERIVED FROM MEASURED PHASE ZEROS → PREDICTED PHASE SHIFTS

Frequency [MHz]	Mode [#]	Wavelength [cm]	A	B	C	D	E	F	G
			Phase shifts relative to line 'A' [degrees, -180 ⟷ +180]						
38.9	0.8	630	0	-41	-82	-123	-165	154	113
48.6	**1**	**504**	**0**	**-51**	**-103**	**-154**	**154**	**103**	**51**
58.3	1.2	420	0	-62	-123	175	113	51	-10
68.0	1.4	360	0	-72	-144	144	72	0	-72
77.7	1.6	315	0	-82	-165	113	31	-51	-134
87.4	1.8	280	0	-93	175	82	-10	-103	165
97.1	**2**	**252**	**0**	**-103**	**154**	**51**	**-51**	**-154**	**103**
106.9	2.2	229	0	-113	134	21	-93	154	41
116.6	2.4	210	0	-123	113	-10	-134	103	-21
126.3	2.6	194	0	-134	93	-41	-175	51	-82
136.0	2.8	180	0	-144	72	-72	144	0	-144
145.7	**3**	**168**	**0**	**-154**	**51**	**-103**	**103**	**-51**	**154**
155.4	3.2	158	0	-165	31	-134	62	-103	93
165.2	3.4	148	0	-175	10	-165	21	-154	31
174.9	3.6	140	0	175	-10	165	-21	154	-31
184.6	3.8	133	0	165	-31	134	-62	103	-93
194.3	**4**	**126**	**0**	**154**	**-51**	**103**	**-103**	**51**	**-154**
204.0	4.2	120	0	144	-72	72	-144	0	144
213.7	4.4	115	0	134	-93	41	175	-51	82
223.4	4.6	110	0	123	-113	10	134	-103	21
233.2	4.8	105	0	113	-134	-21	93	-154	-41
242.9	**5**	**101**	**0**	**103**	**-154**	**-51**	**51**	**154**	**-103**
252.6	5.2	97	0	93	-175	-82	10	103	-165
262.3	5.4	93	0	82	165	-113	-31	51	134
272.0	5.6	90	0	72	144	-144	-72	0	72
281.7	5.8	87	0	62	123	-175	-113	-51	10
291.4	**6**	**84**	**0**	**51**	**103**	**154**	**-154**	**-103**	**-51**
301.2	6.2	81	0	41	82	123	165	-154	-113
310.9	6.4	79	0	31	62	93	123	154	-175
320.6	6.6	76	0	21	41	62	82	103	123
330.3	6.8	74	0	10	21	31	41	51	62
340.0	**7**	**72**	**0**	**0**	**0**	**0**	**0**	**0**	**0**
349.7	7.2	70	0	-10	-21	-31	-41	-51	-62
359.4	7.4	68	0	-21	-41	-62	-82	-103	-123
369.2	7.6	66	0	-31	-62	-93	-123	-154	175
378.9	7.8	65	0	-41	-82	-123	-165	154	113
388.6	**8**	**63**	**0**	**-51**	**-103**	**-154**	**154**	**103**	**51**
398.3	8.2	61	0	-62	-123	175	113	51	-10
408.0	8.4	60	0	-72	-144	144	72	0	-72
417.7	8.6	59	0	-82	-165	113	31	-51	-134
427.5	8.8	57	0	-93	175	82	-10	-103	165
437.2	**9**	**56**	**0**	**-103**	**154**	**51**	**-51**	**-154**	**103**
446.9	9.2	55	0	-113	134	21	-93	154	41
456.6	9.4	54	0	-123	113	-10	-134	103	-21
466.3	9.6	53	0	-134	93	-41	-175	51	-82
476.0	9.8	51	0	-144	72	-72	144	0	-144
485.7	**10**	**50**	**0**	**-154**	**51**	**-103**	**103**	**-51**	**154**
495.5	10.2	49	0	-165	31	-134	62	-103	93
		Phase shifting rate [degrees/MHz]	***0***	***-1.02857143***	***-2.05714286***	***-3.08571429***	***-4.11428571***	***-5.14285714***	***-6.17142857***

Appendix E

Misc. appendices

E.1 Octopus DIP pinout diagram

E.2 Copper purity report

Pinout configuration suggestions for samples to be used in the "Octopus" high-speed sample insert

Alex Winbow, May 2009. Rev. June 2009

Rationale: the coaxial cables cannot be positioned directly adject to pins 7, 8, 11, and 12. Cables for those pins end near the north end, and the pins connect via jumper wires that add stray inductance; the wires for pins 7 & 12 will be longest. These four pins are, ordinarily, permanently connected to coaxial cables. Additionally, the DIP chip package has long *internal* runs for pins 2, 8, 11, and 17, though degradation due to that may not be so bad since the internal runs appear to be close to the DIP chip's internal ground plane.

Among pins 2-6 and 13-17, only two cables are available per side, but they can be re-positioned as desired. (n.b. only 3 of 4 cables available as of May '09)

Pins 1, 9, 10, and 18 are permanently grounded via the holes in the copper sample holder. Any pins except the permanent grounds (including 7, 8, 11, and 12 if necessary), not connected to coaxial cables, can be used for DC signals or temporary ground points, depending on wiring and configuration of the termination PCB.

Suggestion: separate high-speed pins apart if possible to reduce crosstalk issues among the wiring once it exits the coaxial cables; ie, use non-adjacent pins if available.

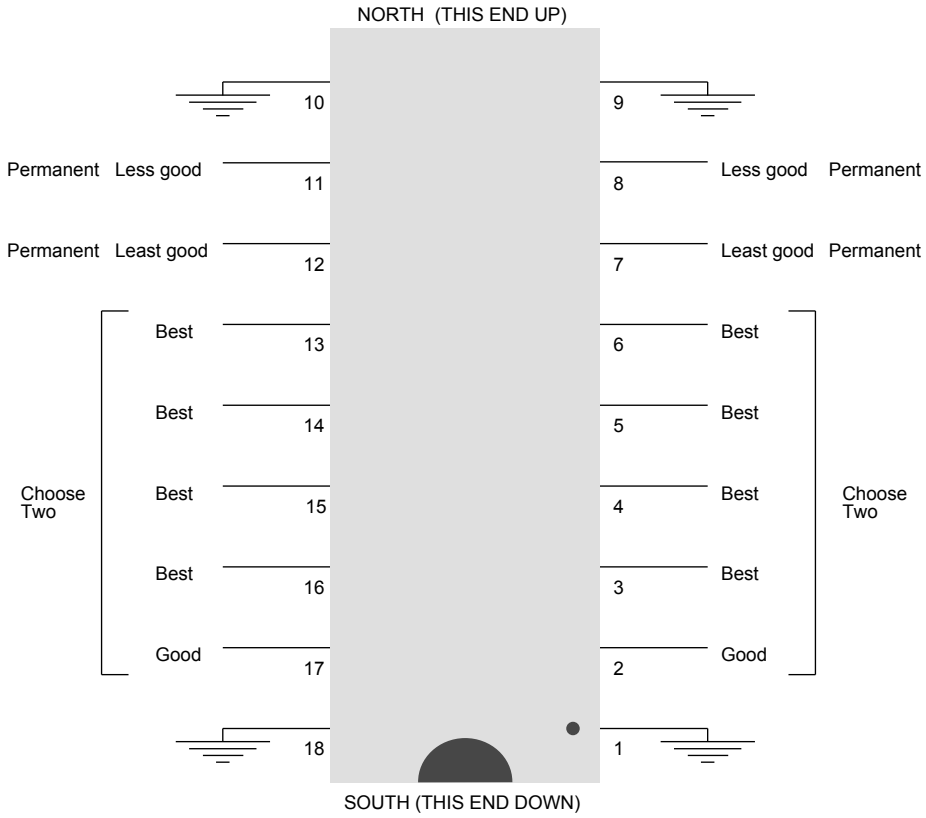

Figure E.1: Pinout diagram for Octopus DIP chip socket, as guide to wirebonding

INSPECTION REPORT

Hitachi Cable, Ltd.
Copper Products Quality Assurance Dept

Messrs. COPPER AND BRASS SALES/LOS ANGELES

No. CUBB-0806-125*

OrderNo. HCA-985*CBSP/ONO.W73957/139397-4

Date Jun.4,2008

ManufacturingNo.	Specification	Article	Size
91V5857	RB0170-249 ASTM F68-05	C1011BB-H (UNS C10100)	1/2"X12"-72"

Quantity Ordered	Quantity Delivered
2,000.0 lbs.	2,107.6 lbs. full

DIMENSION AND PHYSICAL PROPERTY

Item	Unit	Spec.Value Min.	Spec.Value Max.	Sample No. 1	Sample No. 2	Sample No. 3
Thickness	inch	1/2" - 0.0051	1/2" + 0.0051	0.5008	0.5012	0.5008
Width	inch	12" -- 0.063	12" + 0.063	11.960	11.955	11.959
Length	inch	72" 0	72" + 0.17	72.05	72.09	72.09
Chamfering Radius	mm	0	0.79	0.79	0.79	0.79
Tensile Strength	ksi	33	50	47		
Elongation	%	15	-	21		
Hardness Test	HRF	65	-	86.7		
Electric Conductivity at20℃	%	101	-	102.3		
After Embrittlement Repeated bending test		-	-	12		

Visual Inspection good

H2 Embrittlement Test
Blister good
Microscopic good

CHEMICAL COMPOSITION

Element	Specified Value (%) Min.	Specified Value (%) Max.	Measured Value (%)
Cu	99.990	-	99.995
	Max. (ppm)		Measured Value(ppm)
Bi	10		<1
Cd	1		<1
Pb	10		4
Hg	1		<1
O	5		2
P	3		2
Se	10		<1
S	15		8
Te	10		<1
Zn	1		<1

Mercury Free
Country of origin - Japan
This material is certified to be in accordance with specification

M. Kurita
Manager,Quality Assurance Gr

Figure E.2: Copper purity inspection report

Bibliography

M. Armigoda. Personal conversation, 2009. Ted Pella, Inc.

I. Bloch. Ultracold quantum gases in optical lattices. *Nat Phys*, 1(1):23–30, Oct. 2005. ISSN 1745-2473. doi:10.1038/nphys138.

O. Boser and V. Newsome. High frequency behavior of ceramic multilayer capacitors. *Components, Hybrids, and Manufacturing Technology, IEEE Transactions on*, 10(3):437 – 439, sep. 1987. ISSN 0148-6411. doi:10.1109/TCHMT.1987.1134747.

G. Burkard. Quantum information: Positively spin coherent. *Nat Mater*, 7(2): 100–101, Feb. 2008. ISSN 1476-1122. doi:10.1038/nmat2107.

L. V. Butov. Condensation and pattern formation in cold exciton gases in coupled quantum wells. *Journal of Physics: Condensed Matter*, 16(50):R1577, 2004. doi:10.1088/0953-8984/16/50/R02.

H. J. Caulfield and C. Tocci. *Optical interconnection : foundations and applications / Christopher Tocci and H. John Caulfield, editors*. Artech House, Boston :, 1994. ISBN 0890066329.

D. S. Chemla and D. A. B. Miller. Room-temperature excitonic nonlinear-optical effects in semiconductor quantum-well structures. *J. Opt. Soc. Am. B*, 2(7): 1155–1173, Jul 1985. doi:10.1364/JOSAB.2.001155.

G. Chen, R. Rapaport, L. N. Pfeiffer, K. West, P. M. Platzman, S. H. Simon, Z. Vörös, and D. W. Snoke. Artificial trapping of a stable high-density dipolar exciton fluid. *Phys Rev B*, 74(4):045309, 2006. doi:10.1103/PhysRevB.74.045309.

E. A. Cornell and C. E. Wieman. Nobel lecture: Bose-einstein condensation in a dilute gas, the first 70 years and some recent experiments. *Rev. Mod. Phys.*, 74 (3):875–893, Aug 2002. doi:10.1103/RevModPhys.74.875.

J. Ekin. *Experimental Techniques for Low-temperature Measurements: Cryostat Design, Material Properties and Superconductor Critical-current Testing*. OUP Oxford, October 2006. ISBN 0198570546.

A. Gärtner, A. W. Holleitner, J. P. Kotthaus, and D. Schuh. Drift mobility of long-living excitons in coupled gaas quantum wells. *Applied Physics Letters*, 89 (5):052108, 2006. doi:10.1063/1.2267263.

G. Grosso, J. C. Graves, A. T. Hammack, A. A. High, L. V. Butov, M. Hanson, and A. C. Gossard. Excitonic switches operating at around 100 k. *Nat Photonics*, 3 (10):577–580, 2009. doi:doi:10.1038/nphoton.2009.166.

M. Hagn, A. Zrenner, G. Böhm, and G. Weimann. Electric-field-induced exciton transport in coupled quantum well structures. *Appl. Phys. Lett.*, 67(2):232–234, 1995. doi:10.1063/1.114677.

A. T. Hammack. Personal communication, 2009.

A. T. Hammack. *Studies of transport and thermalization of excitons and the development of techniques for in-situ manipulation of excitons in coupled quantum wells*. PhD thesis, University of California, San Diego, 2010.

A. T. Hammack, N. A. Gippius, S. Yang, G. O. Andreev, L. V. Butov, M. Hanson, and A. C. Gossard. Excitons in electrostatic traps. *J Appl Phys*, 99(6):066104, 2006. doi:10.1063/1.2181276.

A. T. Hammack, L. V. Butov, L. Mouchliadis, A. L. Ivanov, and A. C. Gossard. Kinetics of indirect excitons in an optically induced trap in gaas quantum wells. *Phys Rev B*, 76(19):193308, 2007. doi:10.1103/PhysRevB.76.193308.

A. T. Hammack, L. V. Butov, J. Wilkes, L. Mouchliadis, E. A. Muljarov, A. L. Ivanov, and A. C. Gossard. Kinetics of the inner ring in the exciton emission pattern in coupled gaas quantum wells. *Phys Rev B*, 80(15):155331, 2009. doi:10.1103/PhysRevB.80.155331.

A. Hammoud, S. Gerber, R. Patterson, and T. MacDonald. Performance of surface-mount ceramic and solid tantalum capacitors for cryogenic applications. In *Electrical Insulation and Dielectric Phenomena, 1998. Annual Report. Conference on*, pages 572 –576 vol. 2, oct. 1998. doi:10.1109/CEIDP.1998.732962.

A. A. High. Personal communication, 2007.

A. A. High, A. T. Hammack, L. V. Butov, M. Hanson, and A. C. Gossard. Exciton optoelectronic transistor. *Opt Lett*, 32(17):2466–2468, 2007. doi:10.1364/OL.32.002466.

A. A. High, E. E. Novitskaya, L. V. Butov, M. Hanson, and A. C. Gossard. Control of exciton fluxes in an excitonic integrated circuit. *Science*, 321(5886):229–231, 2008. doi:10.1126/science.1157845.

A. A. High, A. T. Hammack, L. V. Butov, L. Mouchliadis, A. L. Ivanov, M. Hanson, and A. C. Gossard. Indirect excitons in elevated traps. *Nano Lett*, 9(5):2094–2098, 2009a. doi:10.1021/nl900605b.

A. A. High, A. K. Thomas, G. Grosso, M. Remeika, A. T. Hammack, A. D. Meyertholen, M. M. Fogler, L. V. Butov, M. Hanson, and A. C. Gossard. Trapping indirect excitons in a gaas quantum-well structure with a diamond-shaped electrostatic trap. *Phys Rev Lett*, 103(8):087403, 2009b. doi:10.1103/PhysRevLett.103.087403.

M. Hong, J. Baillargeon, J. Kwo, J. Mannaerts, and A. Cho. First demonstration of gaas cmos. In *Compound Semiconductors, 2000 IEEE International Symposium on*, pages 345 –350, 2000. doi:10.1109/ISCS.2000.947180.

T. Huber, A. Zrenner, W. Wegscheider, and M. Bichler. Electrostatic exciton traps. *Physica Status Solidi (a)*, 166(1):R5–R6, 1998. doi:10.1002/(SICI)1521-396X(199803)166:1<R5::AID-PSSA99995>3.0.CO;2-6.

R. A. Isaacson, C. Lulich, S. B. Oseroff, and R. Calvo. Coaxial coupler for a 9 ghz epr/endor cryostat. *Review of Scientific Instruments*, 51(10):1409–1411, 1980. doi:10.1063/1.1136084.

A. L. Ivanov. Quantum diffusion of dipole-oriented indirect excitons in coupled quantum wells. *Europhys Lett*, 59(4):586–591, 2002. doi:10.1209/epl/i2002-00144-3.

A. L. Ivanov, C. Ell, and H. Haug. Phonon-assisted boltzmann kinetics of a bose gas: Generic solution for $t \leq t_c$. *Physical Review E*, 55(6):6363–6369, 1997. doi:10.1103/PhysRevE.55.6363.

A. L. Ivanov, P. B. Littlewood, and H. Haug. Bose-einstein statistics in thermalization and photoluminescence of quantum-well excitons. *Phys Rev B*, 59(7):5032–5048, 1999. doi:10.1103/PhysRevB.59.5032.

H. Johnson and M. Graham. *High Speed Digital Design: A Handbook of Black Magic*. Prentice Hall PTR, 1993. ISBN 978-0133957242.

W. Ketterle. Nobel lecture: When atoms behave as waves: Bose-einstein condensation and the atom laser. *Rev. Mod. Phys.*, 74(4):1131–1151, Nov 2002. doi:10.1103/RevModPhys.74.1131.

J. Krauß, J. P. Kotthaus, A. Wixforth, M. Hanson, D. C. Driscoll, A. C. Gossard, D. Schuh, and M. Bichler. Capture and release of photonic images in a quantum well. *Appl. Phys. Lett.*, 85(24):5830–5832, 2004. doi:10.1063/1.1830676.

H. J. Krenner, C. E. Pryor, J. He, and P. M. Petroff. A semiconductor exciton memory cell based on a single quantum nanostructure. *Nano Letters*, 8(6):1750–1755, 2008. doi:10.1021/nl800911n.

M. Kroutvar, Y. Ducommun, J. J. Finley, M. Bichler, G. Abstreiter, and A. Zrenner. Wavelength selective charge storage in self-assembled ingaas/gaas quantum dots. *Appl. Phys. Lett.*, 83(3):443–445, 2003. doi:10.1063/1.1588368.

M. Kroutvar, Y. Ducommun, D. Heiss, M. Bichler, D. Schuh, G. Abstreiter, and J. J. Finley. Optically programmable electron spin memory using semiconductor quantum dots. *Nature*, 432:81–84, 2004. doi:doi:10.1038/nature03008.

Y. Y. Kuznetsova, A. A. High, and L. V. Butov. Control of excitons by laterally modulated electrode density. *Applied Physics Letters*, 97(20):201106, 2010a. doi:10.1063/1.3517444.

Y. Y. Kuznetsova, M. Remeika, A. A. High, A. T. Hammack, L. V. Butov, M. Hanson, and A. C. Gossard. All-optical excitonic transistor. *Opt. Lett.*, 35(10): 1587–1589, May 2010b. doi:10.1364/OL.35.001587.

Lakeshore Cryotronics, Inc. *Temperature Measurement and Control Catalog*, 2004.

J. R. Leonard, Y. Y. Kuznetsova, S. Yang, L. V. Butov, T. OstatnickÃ¡, A. Kavokin, and A. C. Gossard. Spin transport of excitons. *Nano Letters*, 9(12): 4204–4208, 2009. doi:10.1021/nl9024227.

R. Li, G. Berg, and D. Mast. Ceramic chip capacitors as low temperature thermometers. *Cryogenics*, 32(1):44 – 46, 1992. ISSN 0011-2275. doi:10.1016/0011-2275(92)90343-9.

Y. Lozovik and O. Berman. Phase transitions in a system of two coupled quantum wells. *JETP Letters*, 64:573–579, 1996. ISSN 0021-3640. doi:10.1134/1.567264.

T. Lundstrom, W. Schoenfeld, H. Lee, and P. M. Petroff. Exciton Storage in Semiconductor Self-Assembled Quantum Dots. *Science*, 286(5448):2312–2314, 1999. doi:10.1126/science.286.5448.2312.

Micro-coax, Inc. URL `http://www.micro-coax.com/pages/products/producttypes/cabletypes/semi-rigidcoaxial/Semi-RigidDetails.asp?ID=UT-141B-SS`.

Microwaves101: Microwave Encyclopedia. URL `http://www.microwaves101.com`.

D. A. B. Miller, D. S. Chemla, T. C. Damen, A. C. Gossard, W. Wiegmann, T. H. Wood, and C. A. Burrus. Electric field dependence of optical absorption near the band gap of quantum-well structures. *Phys. Rev. B: Condens. Matter*, 32 (2):1043–1060, Jul 1985. doi:10.1103/PhysRevB.32.1043.

Murata Manufacturing Co., Ltd. *Noise Suppression Techniques: Noise Suppression by Low-pass Filters: The Effect of Non ideal Capacitors*, 1998. URL `http://www.murata.com/products/emc/knowhow/index.html`.

E. Oberg, F. D. Jones, H. L. Horton, and H. H. Ryffel. *Machinery's handbook : a reference book for the mechanical engineer, designer, manufacturing engineer, draftsman, toolmaker, and machinist / by Erik Oberg, Franklin D. Jones, and Holbrook L. Horton ; Henry H. Ryffel, editor ; Robert E. Green, associate editor ; James H. Geronimo, associate editor*. Industrial Press, New York :, 23rd ed., rev. ed. edition, 1988. ISBN 083111200 0831109009.

M.-J. Pan. Performance of capacitors under dc bias at liquid nitrogen temperature. *Cryogenics*, 45(6):463 – 467, 2005. ISSN 0011-2275. doi:10.1016/j.cryogenics.2005.03.006.

R. Patterson, A. Hammond, and S. Gerber. Evaluation of capacitors at cryogenic temperatures for space applications. In *Electrical Insulation, 1998. Conference Record of the 1998 IEEE International Symposium on*, volume 2, pages 468 –471 vol.2, jun. 1998. doi:10.1109/ELINSL.1998.694835.

R. Rapaport, G. Chen, D. W. Snoke, S. H. Simon, L. N. Pfeiffer, K. West, Y. Liu, and S. Denev. Charge separation of dense two-dimensional electron-hole gases: Mechanism for exciton ring pattern formation. *Phys Rev Lett*, 92(11):117405, 2004. doi:10.1103/PhysRevLett.92.117405.

M. Remeika. Excitons in electrostatic lattices. `http://www-physics.ucsd.edu/~lvbutov/lattices.html`, 2009.

M. Remeika, J. C. Graves, A. T. Hammack, A. D. Meyertholen, M. M. Fogler, L. V. Butov, M. Hanson, and A. C. Gossard. Localization-delocalization transition of indirect excitons in lateral electrostatic lattices. *Phys. Rev. Lett.*, 102(18): 186803, May 2009. doi:10.1103/PhysRevLett.102.186803.

C. Rocke, S. Zimmermann, A. Wixforth, J. P. Kotthaus, G. Böhm, and G. Weimann. Acoustically driven storage of light in a quantum well. *Phys. Rev. Lett.*, 78(21):4099–4102, May 1997. doi:10.1103/PhysRevLett.78.4099.

U. Rössler. *Solid State Theory: An Introduction*. Advanced Texts in Physics. Springer, Berlin u.a., 2004. URL `http://epub.uni-regensburg.de/1324/`.

J. Rudolph, R. Hey, and P. V. Santos. Long-range exciton transport by dynamic strain fields in a gaas quantum well. *Phys. Rev. Lett.*, 99(4):047602, Jul 2007. doi:10.1103/PhysRevLett.99.047602.

P. V. Santos, M. Ramsteiner, and R. Hey. Spatially resolved photoluminescence in quantum wells with surface acoustic waves. *Phys. Stat. Sol. (b)*, 215(1):253–256, 1999.

C. Schindler and R. Zimmermann. Analysis of the exciton-exciton interaction in semiconductor quantum wells. *Phys. Rev. B*, 78(4):045313, Jul 2008. doi:10.1103/PhysRevB.78.045313.

M. Streibl, A. Wixforth, J. P. Kotthaus, A. O. Govorov, C. Kadow, and A. C. Gossard. Imaging of acoustic charge transport in semiconductor heterostructures by surface acoustic waves. *Applied Physics Letters*, 75(26):4139–4141, 1999. doi:10.1063/1.125562.

M. H. Szymanska and P. B. Littlewood. Excitonic binding in coupled quantum wells. *Phys. Rev. B*, 67(19):193305, May 2003. doi:10.1103/PhysRevB.67.193305.

Ted Pella, Inc. *Pelco Technical Notes: Colloidal Silver Paste #16032*. URL `http://www.tedpella.com/technote_html/16032%20TN.pdf`.

S. G. Tikhodeev. On the bose-einstein condensation of particles with finite lifetime – as demonstrated by excitons. *Solid state commun*, 72(11):1075–1079, 1989. doi:10.1016/0038-1098(89)90250-0.

S. G. Tikhodeev. Bose-einstein condensation of finite lifetime particles: Excitons as an example. *JETP*, 70:380, 1990.

G. K. White and P. J. Meeson. *Experimental Techniques in Low-Temperature Physics; 4th ed.* Monographs on the Physics and Chemistry of Materials. Clarendon Press, Oxford, 2002.

R. White. Surface elastic waves. *Proceedings of the IEEE*, 58(8):1238 – 1276, aug. 1970. ISSN 0018-9219. doi:10.1109/PROC.1970.7900.

A. Winbow, J. Leonard, M. Remeika, A. High, E. Green, A. Hammack, L. Butov, M. Hanson, and A. Gossard. Electrostatic conveyer for excitons. In *Quantum Electronics and Laser Science Conference*, page QFI3. Optical Society of America, 2010. URL `http://www.opticsinfobase.org/abstract.cfm?URI=QELS-2010-QFI3`.

A. G. Winbow, A. T. Hammack, L. V. Butov, and A. C. Gossard. Photon storage with nanosecond switching in coupled quantum well nanostructures. *Nano Lett*, 7(5):1349–1351, 2007. doi:10.1021/nl070386c.

A. G. Winbow, L. V. Butov, and A. C. Gossard. Photon storage with subnanosecond readout rise time in coupled quantum wells. *Journal of Applied Physics*, 104 (6):063515–+, Sept. 2008. doi:10.1063/1.2978214.

S. Yang, A. T. Hammack, M. M. Fogler, L. V. Butov, and A. C. Gossard. Coherence length of cold exciton gases in coupled quantum wells. *Phys Rev Lett*, 97(18): 187402, 2006. doi:10.1103/PhysRevLett.97.187402.

D. Yoshioka and A. H. Macdonald. Double quantum well electron-hole systems in strong magnetic fields. *Journal of the Physical Society of Japan*, 59(12):4211–4214, 1990. doi:10.1143/JPSJ.59.4211.

R. J. Young, S. J. Dewhurst, R. M. Stevenson, P. Atkinson, A. J. Bennett, M. B. Ward, K. Cooper, D. A. Ritchie, and A. J. Shields. Single electron-spin memory with a semiconductor quantum dot. *New J. Phys.*, 9(10):365, 2007. doi:10.1088/1367-2630/9/10/365.

S. K. Zhang, P. V. Santos, R. Hey, A. Garcia-Cristobal, and A. Cantarero. Microscopic carrier dynamics of quantum-well-based light storage cells. *Appl. Phys. Lett.*, 77(26):4380–4382, 2000. doi:10.1063/1.1336160.

W. Zhao, P. Stenius, and A. Imamoḡlu. Kinetics of condensation in trapped exciton gases. *Phys Rev B*, 56(9):5306–5315, 1997. doi:10.1103/PhysRevB.56.5306.

X. Zhu, P. B. Littlewood, M. S. Hybertsen, and T. M. Rice. Exciton condensate in semiconductor quantum well structures. *Phys. Rev. Lett.*, 74(9):1633–1636, Feb 1995. doi:10.1103/PhysRevLett.74.1633.

S. Zimmermann, A. O. Govorov, W. Hansen, J. P. Kotthaus, M. Bichler, and W. Wegscheider. Lateral superlattices as voltage-controlled traps for excitons. *Phys. Rev. B*, 56(20):13414–13421, Nov 1997. doi:10.1103/PhysRevB.56.13414.

S. Zimmermann, A. Wixforth, J. P. Kotthaus, W. Wegscheider, and M. Bichler. A Semiconductor-Based Photonic Memory Cell. *Science*, 283(5406):1292–1295, 1999. doi:10.1126/science.283.5406.1292.